Karlsruher Institut für Technologie

Institute of Meteorology and Climate Research

Atmospheric Aerosol Research

Chemical characterization and optical properties of brown carbon aerosol

Zur Erlangung des akademischen Grades einer

DOKTORIN DER NATURWISSENSCHAFTEN (Dr. rer. nat.)

von der KIT-Fakultät für

Bauingenieur-, Geo- und Umweltwissenschaften des

Karlsruher Instituts für Technologie (KIT)

genehmigte

DISSERTATION

von

M.Sc. Feng Jiang

aus

Anhui, China

Tag der mündlichen Prüfung: 03.07.2023

Referent: Prof. Dr. Stefan Norra

Korreferent: Prof. Dr. Jan Cermak

Erklärung

Hiermit erkläre ich, dass ich die vorliegende Dissertation, abgesehen von der Benutzung der angegebenen Hilfsmittel, selbständig verfasst habe.

Alle Stellen, die gemäß Wortlaut oder Inhalt aus anderen Arbeiten entnommen sind, wurden durch Angabe der Quelle als Entlehnungen kenntlich gemacht.

Diese Dissertation liegt in gleicher oder ähnlicher Form keiner anderen Prüfungsbehörde vor.

Karlsruhe, im April 2023

Feng Jiang

Acknowledgments

Time is the best answer for me and my dream. I remember the first time when I arrived at Karlsruhe. Everything is fresh for me e.g. S-Bahn, German house, church, and forest, etc., but I have no experience on how to live in Germany and start my Ph.D. Therefore, I met many problems and had puzzles about life and jobs in Germany. Due to these obstacles, I grow up from solving problems and answering questions. Thanks for myself to keep my dream and being brave in life and work. Hope is a good thing that can help you to fly anywhere. It is impossible for only me to solve problems and answer questions, and I also get much help from other people.

Firstly, I would like to appreciate my supervisor Dr. Harald Saathoff. He is patient and tolerant of young Ph.D. students. He has a really good attitude toward academy and his job. He also provides good ideas, advanced platforms, selfless jobs, and many opportunities to help Ph.D. students grow up. I learn a lot from his side, not only academy, but also life. He told me that shy boys will be dead, but brave boys can live anywhere. This sentence gives me many braves in Germany and the United States. Even though I will finish my study at KIT soon, his spirit about academy and jobs is still in my head and will have a positive impact on my life and job forever.

Thank you Prof. Stefan Norra who is my doctoral supervisor. He gives me a lot of advice about academy and life in Germany. He also supports me to do experiments at Potsdam University. It is a really happy experience in Potsdam doing experiments and drinking beer. He provides me with Aqualog to measure my samples. If without this instrument, it is hard to imagine how to start my work. In addition, thank you Prof. Thomas Leisner, who gives me much advice for academy and also host a course (Atmospheric Physics) to improve my background knowledge about atmosphere.

I appreciate many colleagues: Linyu Gao, Junwei Song, Hengheng Zhang, Yanxia Li, Yiwei Gong, Yuxuan Bian, and Linke Claudia from KIT-IMK-AAF. Thank you Linyu Gao for telling me how to operate FIGAERO-CIMS and how to analyze CIMS data. She is a nice and brave girl. Thank you to Junwei Song for teaching me AMS instrument and analyzing data. When I was a master student, we already know each other. He is a hard-working and clever colleague or friend. I wish Dr. Song and Dr. Gao a happy life and a successful job in Lyon. Thank you to Wei Huang for sharing Matlab scripts and teaching me CIMS data analysis. Furthermore, I appreciate AAF

technicians: Frank Schwarz, Vogt Steffen, Scheurig Georg, Bolz Susanne, Dombrowski Olga, Chudy Tomasz, and Nadolny Jens. They help me a lot during experiments.

I appreciate Prof. Laskin Alexander to give me an opportunity to study aboard at Purdue University. He is a patient and hard-working professor. During my visiting scholar at Purdue University, he provides me with a platform to analyze my samples by UPLC-PDA-MS and give me many suggestions for data analysis. I learn a lot from Alexander's group. His group has many interesting topics and helps me open my eye. Thank you to Kyla Siemens and Ana Morales to help me analyze samples by UPLC-PDA-MS and teach me to analyze the data. During the visiting scholar experience, I especially appreciate Xiaoli Shen. She gives me a lot of help with USA VISA applications and how to live USA. She shares her car with me and gives me many trips in the USA. And we eat delicious food in the USA. It is a really happy memory for me.

Thanks to my friends in Germany, Benchun Zhou, Huihuang Xia, Fan Yang, Jaroslav Storek, basketball teams, and gym teams. We did many fun and happy things in Germany, for example, playing basketball, drinking wine and beer, doing fitness, participating in Marathon, listening to concerts, riding bicycles, and holiday trips. Thanks to my friends in China, Xiaofan Xie, Hua Fan, and Jun Fang. They share many funning and happy things with me.

I would like to appreciate my parents, mother-in-law, father-in-law, and uncles. When I meet some problems, they always give me ideas and help. During my Ph.D. study, I did not go back to China due to the Covid-19 pandemic. Therefore, I often miss my hometown, especially when I am alone. They give me much motivation to live in Germany.

Finally, I appreciate my wife, Min Zhou. She is a brave, kind, beautiful, and hard-working girl. Even though I did not go back to China for more than three years, my wife gives me a happy family and a clean apartment in Germany. During the weekend, we generally meet together, cook delicious food, walk in forests, and forget jobs. Hope we could achieve our dream.

Hope is a good thing that can help you to fly.

Feng Jiang 江峰

Karlsruhe, in April 2023

Abstract

Brown carbon (BrC) aerosol has a significant impact on air quality and climate since it absorbs solar radiation in the near-ultraviolet and visible spectral ranges. Despite a large number of previous studies on BrC aerosol, especially the link between chemical composition and optical properties of BrC aerosol is still not well understood. Therefore, I conducted experiments on emissions and aging of BrC from combustion of various fuels, and on formation of BrC by atmospheric oxidation of toluene and indole as important anthropogenic and biogenic precursors. Furthermore, I measured characteristic properties of ambient BrC and determined sources during field campaigns in urban and rural areas.

I studied primary BrC emitted directly from combustion of straw, beech wood, plastic, and cow dung as well as its aging by photooxidation. Less oxygenated humic-like substances (LO-HULIS) and protein/phenol-like substances (PLS) dominate absorption and fluorescence intensities of BrC from primary emissions with 42% ± 7% and 42% ± 10%, respectively. Photooxidation of the primary BrC aerosol leads to a decrease of the PLS chromophore fraction from 47% to 11% and an increase of the highly oxygenated humic-like chromophore (HO-HULIS) from 12% to 32%. Overall, photo oxidation of the BrC aerosol lead to addition of lighter and less absorbing molecules to the particles. Consequently, the mass absorption coefficients of the primary brown carbon aerosol decreased with ongoing photo oxidation. The characteristic mass absorption spectra I have determined for the fresh as well as for aged BrC can now be used for a better representation of BrC in transport models.

I generated absorbing secondary organic aerosol (SOA with BrC) by oxidation of the major anthropogenic VOC toluene, with OH radicals at four different temperatures (313K, 293K, 273K, and 253K) in presence of NO_2., hence representing different regions of the polluted atmosphere. The SOA yields decrease with increasing temperature but the mass absorption coefficient MAC_{365} of toluene-SOA was highest at 313K with 0.17 ± 0.03 $m^2\ g^{-1}$ and only 0.11 ± 0.02 $m^2\ g^{-1}$ for the lower three temperatures. Increasing formation temperatures correspond to lower oxidation states and higher aromaticity of particle phase molecules. Furthermore, I studied secondary BrC from the oxidation of indole, an important aromatic biogenic VOC including one nitrogen atom, in presence/absence of NO_2 and with/without different seed particles. The major chromophore of indole SOA formed without NO_2 was $C_8H_7O_3N$ contributing 20–30% of the light absorption of

indole SOA. However, 3-nitroindole, $C_8H_6O_2N_2$, was the dominating chromophore for indole SOA formed in presence of NOx contributing around 50% of the total absorption at 365 nm. Based on yields and optical properties of SOA from toluene and indole, I calculated that this secondary BrC can have a substantial contribution to aerosol absorption at least on a regional scale including the corresponding impact on climate and visibility.

In addition, I analyzed BrC at a kerbside in downtown Karlsruhe during winter and summer. I quantified five nitroaromatic compounds and classified 316 potential BrC molecules contributing 0.3 ± 0.1% and 32 ± 15% of the absorption at 365 nm, respectively. The average absorption coefficients and MAC at 365 nm (Abs_{365} and MAC_{365}) of methanol-soluble BrC (MS-BrC) were lower in the summer period (1.6 ± 0.5 Mm^{-1}, 0.5 ± 0.2 $m^2\ g^{-1}$) than in the winter period (2.8 ± 1.9 Mm^{-1}, 1.1 ± 0.3 $m^2\ g^{-1}$). Two different groups of HO-HULIS dominated in summer and contributed 96 ± 6% of total fluorescence intensity. In contrast, less oxygenated-HULIS (LO-HULIS) dominated the total fluorescence intensity in winter with 57 ± 12%, followed by HO-HULIS with 31 ± 18%. The LO-HULIS comprised a high contribution of nitrogen-containing molecules originating from biomass burning in winter. The HO-HULIS had fewer nitrogen-containing molecules and was low-volatility oxygenated organic aerosol from regional transport and oxidation of biogenic volatile organic compounds (VOC) especially in summer.

Furthermore, I conducted a field campaign at the rural area, KIT Campus Nord, during winter. I identified 178 BrC molecules in the particle phase contributing on average 2.3 ± 1.5% of the total organic particle mass, but explaining 14 ± 9% of total BrC absorption at 370 nm, assuming an average MAC_{370} value of 9.5 $m^2\ g^{-1}$. Primary emissions from biomass burning accounted for 39 ± 21% of the total BrC but secondary formation dominates the mass fraction of BrC with 61 ± 7% during the whole winter campaign.

My findings clearly demonstrate that a small mass fraction of absorbing organic molecules dominates the absorption properties of ambient aerosol, and that biomass burning and secondary formation are major BrC sources in the atmosphere.

Zusammenfassung

Absorbierende kohlenstoffhaltige Aerosole (BrC) haben einen erheblichen Einfluss auf die Luftqualität und das Klima, da sie die Sonnenstrahlung im nahen ultravioletten und sichtbaren Spektralbereich absorbieren. Trotz zahlreicher früherer Studien über BrC ist insbesondere der Zusammenhang zwischen der chemischen Zusammensetzung und den optischen Eigenschaften von BrC noch immer nicht gut verstanden. Daher habe ich Experimente zur Emission und Alterung von BrC aus der Verbrennung verschiedener Brennstoffe sowie zur Bildung von BrC durch atmosphärische Oxidation von Toluol und Indol als wichtige anthropogene und biogene Vorläufer durchgeführt. Darüber hinaus habe ich bei Feldkampagnen in städtischen und ländlichen Gebieten die charakteristischen Eigenschaften und Quellen von BrC in der Atmosphäre bestimmt.

Ich untersuchte primäres BrC, das direkt aus der Verbrennung von Stroh, Buchenholz, Kunststoff und Kuhmist stammt, sowie seine Alterung durch Photooxidation. Weniger sauerstoffhaltige humusähnliche Substanzen (LO-HULIS) und protein-/phenolähnliche Substanzen (PLS) dominieren die Absorptions- und Fluoreszenzintensitäten von BrC aus primären Verbrennungsemission mit 42 % ± 7 % bzw. 42 % ± 10 %. Die Photooxidation des primären BrC führt zu einem Rückgang des PLS-Chromophoranteils von 47 % auf 11 % und zu einem Anstieg des hochoxidierten humusartigen Chromophors (HO-HULIS) von 12 % auf 32 %. Insgesamt führte die Photooxidation des BrC zu einer Anreicherung der Partikel mit leichteren und weniger absorbierenden Molekülen. Folglich nahmen die Massenabsorptionskoeffizienten des primären BrC mit fortschreitender Photooxidation ab. Die charakteristischen Absorptionsspektren, die ich sowohl für das frische als auch für das gealterte BrC bestimmt habe, können nun für eine bessere Beschreibung von BrC in Transportmodellen verwendet werden.

Ich habe absorbierendes sekundäres organisches Aerosol (SOA mit BrC) durch Oxidation der wichtigsten anthropogenen flüchtigen organischen Verbindung (VOC) Toluol mit OH-Radikalen bei vier verschiedenen Temperaturen (313 K, 293 K, 273 K und 253 K) in Gegenwart von NO_2 erzeugt und damit verschiedene Regionen der verschmutzten Atmosphäre abgedeckt. Die SOA-Ausbeute nimmt mit steigender Temperatur ab, aber der Massenabsorptionskoeffizient MAC_{365} von Toluol-SOA war bei 313 K mit 0.17 ± 0.03 $m^2\ g^{-1}$ am höchsten und bei den drei niedrigeren Temperaturen nur 0.11 ± 0.02 $m^2\ g^{-1}$. Steigende Bildungstemperaturen entsprechen niedrigeren Oxidationsstufen und höherer Aromatizität der Moleküle in den Aerosolpartikeln. Außerdem

untersuchte ich sekundäres BrC aus der Oxidation von Indol, einem wichtigen aromatischen biogenen VOC mit einem Stickstoffatom, in Anwesenheit/Abwesenheit von NO_2 sowie mit/ohne verschiedener Kondensationskeime. Das Hauptchromophor von Indol-SOA, das ohne NO_2 gebildet wird, ist $C_8H_7O_3N$, das 20-30 % der Lichtabsorption von Indol-SOA ausmacht. 3-Nitroindol, $C_8H_6O_2N_2$, ist jedoch das dominierende Chromophor für Indol-SOA, welches in Gegenwart von NOx gebildet wurde und etwa 50 % der Gesamtabsorption bei 365 nm beiträgt. Auf Grundlage der Ausbeuten und optischen Eigenschaften von SOA aus Toluol und Indol habe ich berechnet, dass dieses sekundäre BrC zumindest auf regionaler Ebene einen wesentlichen Beitrag zur Aerosolabsorption leisten kann, einschließlich der entsprechenden Auswirkungen auf das Klima und die Sichtweite.

Weiterhin analysierte ich BrC an einem Straßenrand in der Karlsruher Innenstadt im Winter und im Sommer. Ich konnte fünf nitroaromatische Verbindungen quantifizieren und 316 potenzielle BrC-Moleküle klassifizieren, die 0.3 ± 0.1% bzw. 32 ± 15% der Absorption bei 365 nm ausmachen. Die durchschnittlichen Absorptionskoeffizienten und MAC bei 365 nm (Abs_{365} und MAC_{365}) von in Methanol löslichem BrC (MS-BrC) waren im Sommer niedriger (1.6 ± 0.5 Mm-1, 0.5 ± 0.2 m2 g^{-1}) als im Winter (2.8 ± 1.9 Mm^{-1}, 1.1 ± 0.3 m^2 g^{-1}). Zwei verschiedene Gruppen von HO-HULIS dominierten als Chromophore im Sommer und trugen zu 96 ± 6 % der gesamten Fluoreszenzintensität bei. Im Gegensatz dazu dominierten im Winter die weniger oxidierten HULIS (LO-HULIS) mit 57 ± 12 % die Gesamtfluoreszenzintensität, gefolgt von den HO-HULIS mit 31 ± 18 %. Dabei enthielten LO-HULIS einen hohen Anteil von stickstoffhaltigen Molekülen, die aus der Biomasseverbrennung im Winter stammten. HO-HULIS enthielten weniger stickstoffhaltige Moleküle sondern stammt als schwererflüchtiges oxidiertes organisches Aerosol aus dem regionalen Transport und der Oxidation biogener flüchtiger organischer Verbindungen (VOC) insbesondere im Sommer.

Darüber hinaus habe ich im Winter eine Feldkampagne im ländlichen Raum, am KIT Campus Nord, durchgeführt. Ich identifizierte 178 BrC-Moleküle in der Partikelphase, die im Durchschnitt 2.3 ± 1.5 % der gesamten organischen Partikelmasse ausmachten, aber 14 ± 9 % der gesamten BrC-Absorption bei 370 nm erklärten, wenn man einen durchschnittlichen MAC_{370}-Wert von 9.5 m^2 g^{-1} annimmt. Die Primäremissionen aus der Verbrennung von Biomasse machten 39 ± 21 % des gesamten BrC aus, aber die sekundäre Bildung dominierte den Massenanteil des BrC mit 61 ± 7 % während der gesamten Winterkampagne.

Meine Ergebnisse zeigen deutlich, dass ein kleiner Massenanteil absorbierender organischer Moleküle die Absorptionseigenschaften des Umgebungsaerosols dominiert und dass die Biomasseverbrennung und die sekundäre Bildung wesentliche BrC-Quellen in der Atmosphäre sind.

Contents

List of Figures

List of Tables

Abbreviations

OA	Organic Aerosol
Abs	Light Absorption
AAE	Absorption Ångström Exponents
AMS	Aerosol Mass Spectrometer
AE33	Aethalometer
AIDA	Aerosol Interaction and Dynamics in the Atmosphere
AS	Ammonium Sulfate
BC	Black Carbon
BrC	Brown Carbon
BBOA	Biomass Burning Organic Aerosol
CIMS	Chemical Ionization Mass Spectrometer
CHARON	CHemical Analysis of aerosol ONline inlet
CPC	Condensation Particle Counter
COA	Cooking-related Organic Aerosol
DMA	Differential Mobility Analyzer
DBE	Double Bond Equivalent
$\mathbf{d_{va}}$	Vacuum Aerodynamic Diameter
$\mathbf{d_m}$	Mobility Diameter
EEM	Excitation Emission Matrix
EI	Electron Ionization
FIGAERO	A Filter Inlet for Gases and AEROsols
FI-ICR-MS	Fourier-Transform Ion Cyclotron Resonance Mass Spectrometry
GC-MS	Gas Chromatography coupled with Mass Spectrometry
HULIS	Humic-like Substances
HRMS	High-Resolution Mass Spectrometry
HO-HULIS	Highly Oxygenated HULIS
HOA	Hydrocarbon-like Organic Aerosol
LO-HULIS	Less-Oxygenated HULIS

LV-OOA	Less-volatility Oxygenated Organic Aerosol
MAC	Mass Absorption Coefficient
MSOC	Methanol-Soluble Organic Carbon
NFV	Normalized Fluorescence Volume
$NO_3^{\bullet}$	Nitrate Radicals
NACs	Nitro Aromatic Compounds
NO_2	Nitrogen Dioxide
OA	Primary Organic Aerosol
O/C	Oxygen-to-Carbon Ratio
O_3	Ozone
OPC	Optical Particle Counter
PTR-MS	Proton-Transfer-Reaction Mass Spectrometer
PAHs	Polycyclic Aromatic Hydrocarbon
PDA	Photodiode Array Detector
PAS	PhotoAcoustic Spectrometer
PARAFAC	PARAllel FACtor analysis
PMF	Positive Matrix Factorization
RH	Relative Humidity
SMPS	Scanning Mobility Particle Sizer
SO_2	Sulfur Dioxide
SOA	Secondary Organic Aerosol
SV-OOA	Semi-volatility Oxygenated Organic Aerosol
UPLC	Ultra-Performance Liquid Chromatography
VOC	Volatile Organic Compounds
λ	Wavelength
ρ_{eff}	Effective Density

1. Introduction

Atmospheric aerosol is a suspension of fine solid particles or liquid droplets in the air with particle diameters in the range of 10^{-9}–10^{-4} m (Seinfeld and Pandis, 2006; Poschl, 2005). It consists of dust, sea salt, pollen, bacteria, black carbon, organic compounds, water, and various other compounds (Poschl, 2005; Chan and Yao, 2008). These particles play an important role in cloud formation, human health, air quality, and climate (Seinfeld and Pandis, 2006). Aerosol particles indirectly affect the earth's climate by influencing formation and properties of clouds (Fan et al., 2016; Herckes et al., 2013). In addition, aerosol particles also directly scatter and absorb solar and terrestrial radiation (Poschl, 2005). Therefore, atmospheric aerosol particles have an important impact on global energy balance and climate.

1.1 Organic aerosol, black carbon, and brown carbon aerosol

Organic aerosol (OA) is a complex mixture comprising thousands of organic species (Goldstein and Galbally, 2007). There are two main types of OA sources. One is the direct emission of OA into the atmosphere, known as primary OA (POA). POA can be emitted from human activities such as traffic emissions, industrial emissions, biomass burning, or cooking emissions, but also from biogenic sources like pollen, and fungal spores, etc. Secondary organic aerosol (SOA) is formed in the atmosphere by the oxidation of biogenic/anthropogenic volatile organic compounds (VOCs). Their oxidation products of lower volatility either nucleate new aerosol particles or condense on existing particles. This process is called gas-to-particle portioning (Jimenez et al., 2009). OA is quite abundant and can make up between 20%–90% of the total fine aerosol mass concentration (Jimenez et al., 2009; Zhang et al., 2007). Initially, OA was considered to be non-light-absorbing, or "white", hence only contributing to scattering of the solar radiation. The best-known type of light-absorbing carbonaceous aerosol is "black carbon" (BC), which represents soot-like particulates generated by biomass burning, traffic emissions, and fossil fuel combustion (Bond et al., 2013). And the BC absorbs solar radiation over a broad spectral range, from ultraviolet all the way into the infrared range (IR). However, coloured OA compounds, known as brown carbon (BrC), also absorb solar radiation in the near-ultraviolet (300–400 nm) and visible spectral ranges (Wu et al., 2016; Saleh, 2020; Yan et al., 2018; Moise et al., 2015; Laskin et al., 2015). As shown in Figure 1, the geographic distributions of simulated BrC can have

the annual mean BrC column densities often exceeding 1–2 mg m^{-2}, and the fraction of BrC in total organic carbon can be above 40%–50% (Feng et al., 2013). With this model simulation, the annual mean contribution of BrC to aerosol particle absorption is estimated to be 7%–19% (Feng et al., 2013). Using a 3-D global chemical transport model (GEOS-Chem), Park et al. (2010) found that the mean radiative forcing of BrC aerosol is -0.43 W m^{-2} at the surface and 0.05 W m^{-2} at the top of the atmosphere, accounting for about 15% of total radiative forcing by the absorbing aerosols (Park et al., 2010). A global field campaign finds the BrC accounting for approximately 7%–48 % of direct radiative forcing by comparing all absorbing carbonaceous aerosol (Zeng et al., 2022).

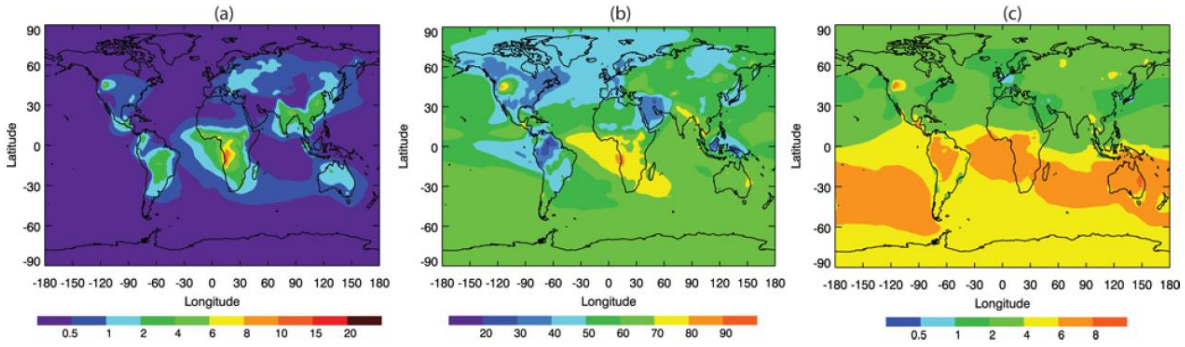

Fig. 1. The estimated **(a)** annual mean atmospheric burden (mg m^2) of BrC, **(b)** percentage (%) of BrC in total OC, and **(c)** ratio of BrC to BC.

Figure 1. A global model simulation estimated the atmospheric burden (mg m^{-2}), the fraction in total organic carbon (b) and ratio of BrC to black carbon (c). This is adapted with permission from Figure 1 in (Feng et al., 2013) © 2013, European Geosciences Union.

1.2 Sources of brown carbon

There are many studies which have investigated BrC due to its impact on the global climate, human health, and air quality. The sources of BrC are quite complex. There are two main types of BrC sources. One is the primary BrC from direct emissions, e.g. biomass burning, fossil fuel combustion, and forest fires (Wu et al., 2016; Laskin et al., 2015). The other secondary BrC is formed from the oxidation of VOCs in the atmosphere. A typical example is the oxidation of aromatic VOC at high NOx levels (Li et al., 2021b; Liu et al., 2021b; Lin et al., 2015). Figure 2 gives a brief illustration of sources, transport, and deposition of BrC, as well as its effects on the climate (Wu et al., 2016). In the following section, I will briefly introduce the primary emissions of brown carbon (1.2.1) and secondary formation of brown carbon (1.2.2).

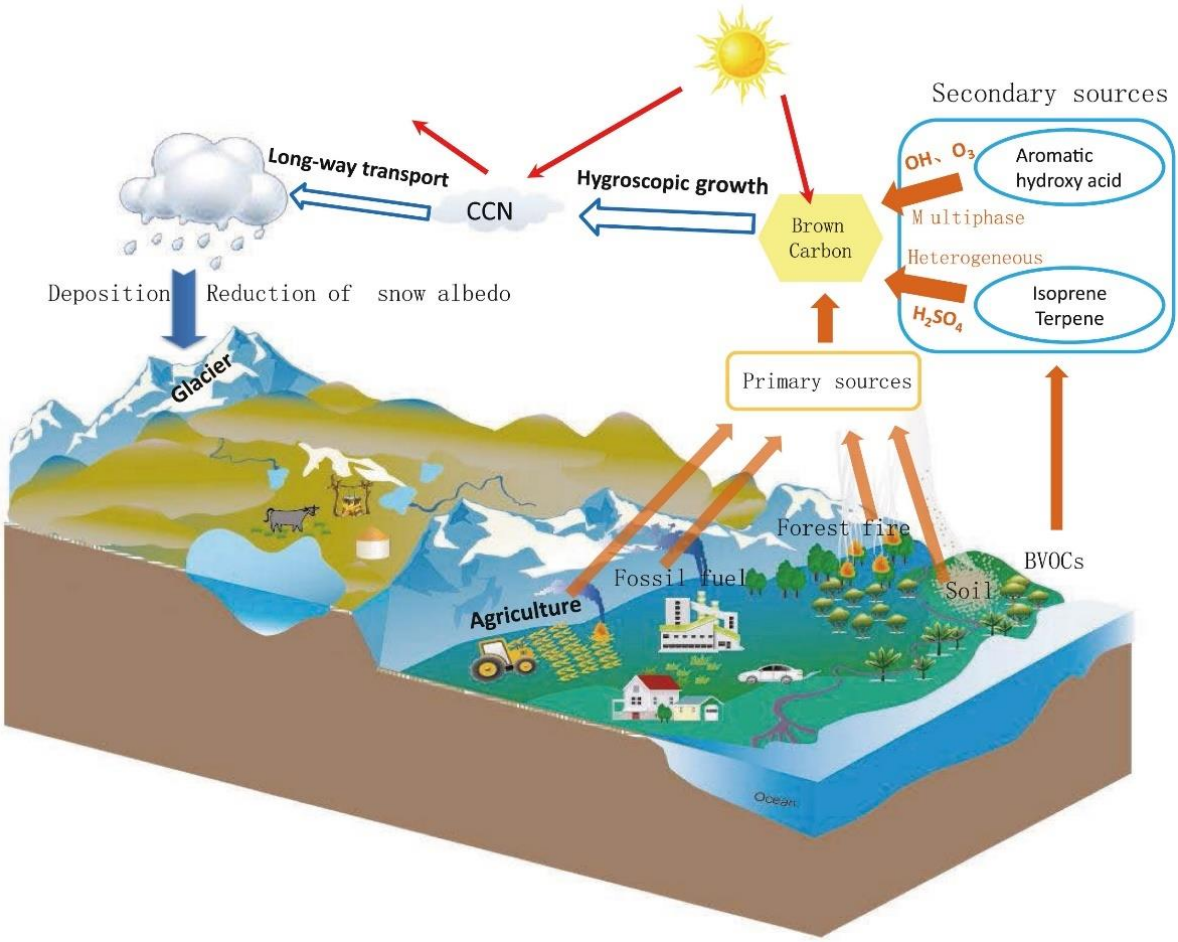

Figure 2. A schematic overview on the sources, transport, and radiative forcing of BrC, as well as its impact on the snow and glaciers after deposition. This is adapted with permission from Figure 1 in Wu et al. (2016) © 2016, ELSEVIER.

1.2.1 Primary emissions of brown carbon

As shown in Figure 2, there are many primary emissions potentially contributing to BrC. The global total primary BrC emissions from natural and anthropogenic sources in 2010 were estimated to 7.26 Tg (Xiong et al., 2022). On a global scale, biomass burning is considered as one of the most important sources for BrC. Strong BrC emissions are often caused by uncontrolled and disastrous events, such as large-scale forest fires, but also by prescribed smoldering fires used in forest management or agriculture, and extensive use of wood for heating and cooking (Laskin et al., 2015; Ramanathan et al., 2007; Liu et al., 2021a; Saleh et al., 2018). Smog chamber experiments showed that BrC in emission from biomass burning are associated with organic compounds of extremely low volatility (Saleh et al., 2014). A majority of BrC aerosol mass is associated with biomass burning dominating BrC absorption in rural southeastern United States

(Washenfelder et al., 2015). Fossil fuel is also an important source for BrC in some areas. For example, residential coal combustion contributes to increasing light-absorbing organic carbon in Beijing in winter (Yan et al., 2017). Through observation-constrained modeling, it showed that BrC, originated from fossil fuel combustion in the mid-to-high latitudes of the Northern Hemisphere (32%), can be a strong warming agent in the Arctic region (Yue et al., 2022). In addition, natural sources can also contribute to the brown carbon e.g. biogenic aerosol (e.g. plant debris and fungi) as well as dispersed soil humic matters (Rizzo et al., 2013).

1.2.2 Secondary formation of brown carbon

Both primary organic particulate emissions and SOA can contribute to BrC. Secondary BrC contains many different species which can be formed from multiple precursors and a variety of reaction pathways. As illustrated in Figure 3, secondary BrC can be formed by oxidation of biogenic and anthropogenic VOCs. For anthropogenic VOCs, especially oxidation of aromatic compounds like toluene e.g. in presence of NOx can lead to formation of brown carbon molecules (e.g. nitro aromatic compounds) (Xie et al., 2017; Lin et al., 2015; Liu et al., 2021b; Li et al., 2021b). Other anthropogenic VOCs, like naphthalene and ethylbenzene, can also form nitro aromatic chromophores contributing to secondary BrC in presence of NOx (Siemens et al., 2022; He et al., 2022; Yang et al., 2022). Nitrogen-containing heterocyclic VOCs (pyrrole, 1-methylyrrole, 2-methylpyrrole, and furan) typically emitted from wildfire emissions may react with nitrate radicals ($NO_3^{\bullet}$) to form the secondary BrC (Mayorga et al., 2022; Jiang et al., 2019). Indole, another nitrogen containing aromatic compound, emitted from biomass burning, animal husbandry and agriculture plants like maize is also an important precursor for secondary BrC (Montoya-Aguilera et al., 2017; Li et al., 2021a; Baboomian et al., 2023). Oxidation of the most abundant aerosol forming from biogenic VOC (isoprene, monoterpenes, and sesquiterpenes) only contributes very little to light absorption or brown carbon (Yang et al., 2022; Xie et al., 2017).

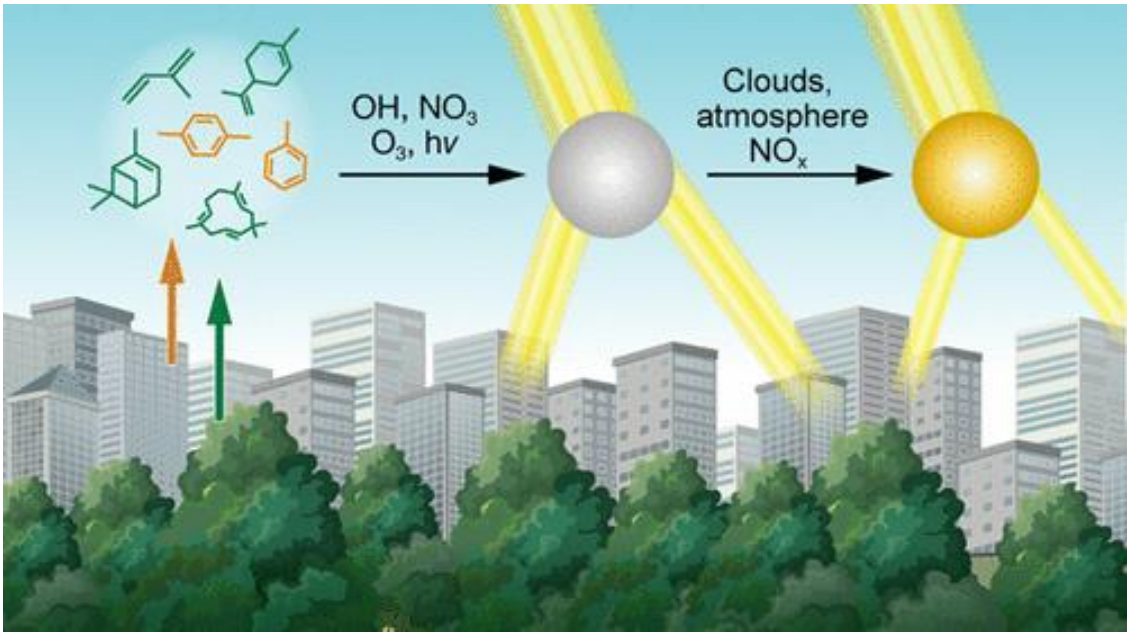

Figure 3. A schematic view of secondary BrC formation. The figure is adapted from (Moise et al., 2015) © 2015, America Chemistry Unit.

Furthermore, the reaction of ammonia or amino acids with SOA that contain carbonyl products can contribute to secondary BrC formation. The light absorption and chemical composition of brown carbon were studied for aerosol particles generated by reaction of NH_4^+, NH_3, and amino acids with terpene SOA as well as aqueous-phase reactions of glyoxal and methylglyoxal with ammonium sulfate and amino acids (Nguyen et al., 2013; Updyke et al., 2012; De Haan et al., 2020). In addition, BrC can be also formed from bond-forming reaction between SOA constituents generating dimers and larger oligomers e.g. oligomerization processes like acid-catalyzed aldol condensation of volatile aldehydes (De Haan et al., 2009; Bond et al., 2013).

1.3 Chemical characteristic of brown carbon

The chemical composition of BrC is extremely complex due the multiple sources. Nevertheless, in terms of chemical speciation, BrC is generally divided into humic-like substances (HULIS) and tar ball. (Wu et al., 2016; Moise et al., 2015; Laskin et al., 2015; Yan et al., 2018).

1.3.1 Humic-like substances

Atmospheric humic-like substances are class of macromolcular organic compounds prevalent in diverse environmental media, which can be easily isolated and recognized as important components of BrC, as shown in Figure 4 (Zheng et al., 2013; Laskin et al., 2015). HULIS were

found to differ from Humic substances. HULIS were generally more surface active, less acidic, and having much smaller molecular weight and lower aromaticity than Humic substances (Graber and Rudich, 2006). They can be emitted directly during the process of biomass burning which are accretion reactions of smaller molecules or by breakdown of larger molecules (Graber and Rudich, 2006). In addition, humic-like substances also were from complex secondary reaction from anthropogenic/biogenic VOCs (Zheng et al., 2013). According to the oxidized level, the HULIS can be separated as highly oxygenated HULIS and less oxygenated HULIS (Chen et al., 2016). HULIS dominated total BrC absorption with 73%–81% in the Indo-Gangetic Plain (Mukherjee et al., 2020).

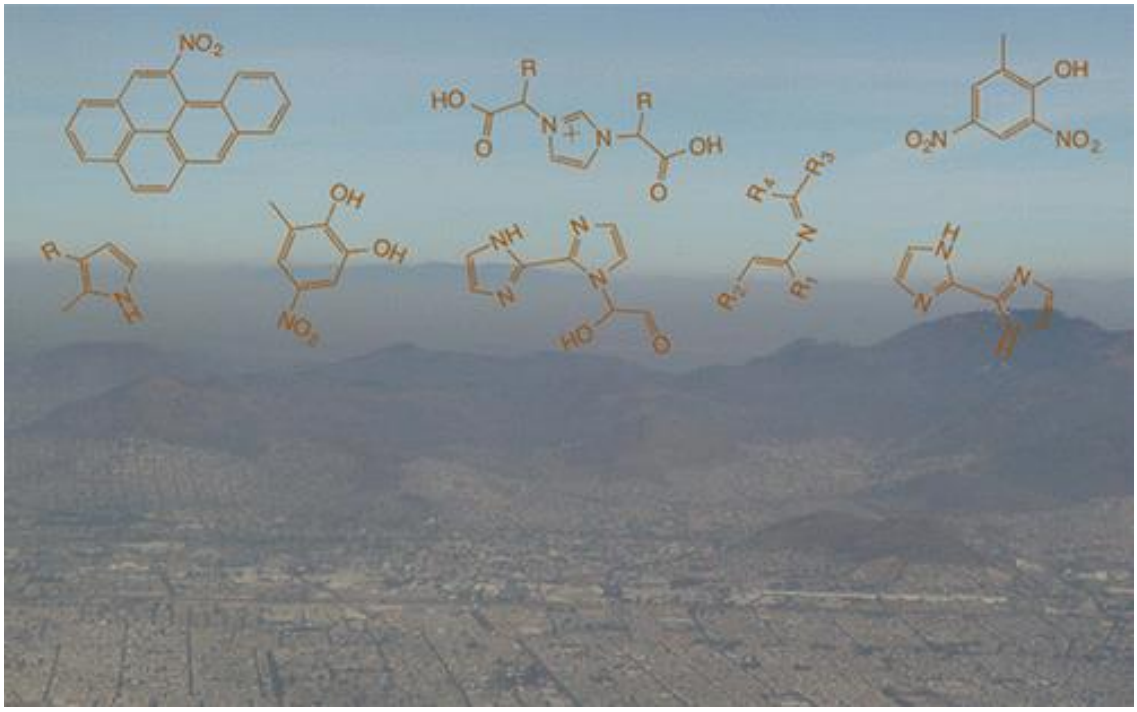

Figure 4. An overview of chemical compounds typical for brown carbon. The figure is adapted from (Laskin et al., 2015) © 2015, American Chemistry Unit.

Nitro-aromatic compounds (NACs) are classes of nitro-derivated phenols or heterocyclic compounds, including nitrophenols, nitrocatechols, nitrosalicylic acids, nitroguaiacols, and heterocyclic nitrated compounds. These are important species of BrC. The sources of NACs consist of primary emissions and secondary chemistry. The primary emissions can be from human activities and natural emissions, including biomass burning (Salvador et al., 2021; Mohr et al., 2013; Teich et al., 2017), fossil fuel combustion (Morville et al., 2004), and forest fire (Palm et al., 2020). In addition, secondary formation can also contribute to NACs. For example, the oxidation

of aromatic VOCs (e.g. toluene, naphthalene, and benzene, etc.) at high NOx levels can contribute to NACs formation which dominated the BrC absorption at UV wavelengths (Palm et al., 2020; Lin et al., 2015; Liu et al., 2021b; Li et al., 2021b; Siemens et al., 2022). Other heterocyclic VOCs (pyrrole, furan, and thiophene etc.) reacted with nitrate radicals ($NO_3^{\bullet}$) and then lead to nitro-aromatic products which play a significant role for BrC absorption (Mayorga et al., 2022; Jiang et al., 2019; Montoya-Aguilera et al., 2017).

Polycyclic aromatic hydrocarbon (PAHs) are light-absorbing species in atmospheric brown carbon aerosol (Laskin et al., 2015). PAHs compounds are a class of complex organic chemicals, which include carbon and hydrogen with a fused ring structure containing at least 2 benzene rings. PAHs may also contain additional fused rings that are not six-sided. For example, the known PAHs are benz [a] anthracene and chrysene [$C_{18}H_{12}$]; benzo [b] fluoranthene, benzo [j] fluoranthene, benzo [k] fluoranthene and B [a] P [$C_{20}H_{12}$]; indeno [1,2,3-cd] pyrene [$C_{22}H_{12}$]; and dibenz [a,h] anthracene [$C_{20}H_{14}$] (Ravindra et al., 2008). PAHs are mainly formed from natural and anthropogenic combustion processes e.g. biomass burning, fossil fuels, and forest fire (Ravindra et al., 2008). Typically, PAHs dominate the total BrC absorbance up to 90%, if the BrC was generated from hydrocarbon fuel combustion (West et al., 2020). The measured PAHs and carbonyl-OPAHs account for on average ~1.7% of the overall absorption of methanol-soluble BrC, about 5 times higher than their mass fraction in total organic carbon (Huang et al., 2018).

1.3.2 Tar ball

Tar ball aerosol is a prominent type of largely homogeneous BrC particles commonly detected in smoke emissions from smoldering burns of biofuel and biomass burning plumes (Laskin et al., 2015; Yuan et al., 2021). They can absorb light in the visible range of the solar spectrum. The contribution of tar ball to the number concentrations of particles can be as high as 80% in the vicinity of biomass burning sources (Posfai et al., 2003). Tar ball aerosol account for 4% of all observed particles in the Himalaya (Cong et al., 2009). If HULIS only contributed to a few percent of solar absorption of brown carbon, the main fraction of BrC absorption was attributed to tar ball (Hoffer et al., 2006). A laboratory study found that the mass absorption coefficients of tar ball ranged between 0.8–3.0 m^2g^{-1} at 550 nm, with average absorption Ångström exponents (AAE) of 2.9 in the wavelength range of 467–652 nm (Hoffer et al., 2016).

1.4 Optical properties of BrC

BrC strongly absorbs solar radiation in the near-ultraviolet (300–400 nm) and visible spectral range. The absorption characteristics are typically described by the light absorption (Abs), the mass absorption cross section (MAC), and Absorption Ångström exponents (AAE) reflecting the wavelength dependence. The Abs, MAC, and AAE were shown in method sections as equations (1), (2), and (3). The light absorption of BrC has large variety. The Abs of BrC at 370 nm during winter in Leipzig and Waldstein, Germany, were 5.4 Mm^{-1} and 6.0 Mm^{-1}, respectively (Teich et al., 2017). Abs_{365} of lipid-soluble organic matter in non-heating seasons in Beijing, China was 0.9 ± 1.3 Mm^{-1} (Li et al., 2020). The light absorption coefficient of BrC has typically a much stronger wavelength dependence (λ^{-2}–λ^{-6}) than BC with absorption increasing sharply from the visible to the UV range. The AAE of BrC from incomplete combustion of biomass typically ranges from 1 to 3 (Martinsson et al., 2015). When BrC was oxidized, the AAE can even increase further from 3 to 7, indicating that the wavelength dependence of secondary BrC is higher, and the ability of secondary BrC to absorb radiation decreases with wavelength (Shen et al., 2017). AAE values as high as 7.4–8.3 were observed for BrC collected from combustion of straw, pine needles, and sesame (Du et al., 2014). In addition, the AAE values of water-soluble organic carbon of aerosol samples was observed to range from 6 to 8 in urban and rural areas (Jiang et al., 2022; Budisulistiorini et al., 2017). The MAC give the specific BrC absorption per unit mass. The MAC values of BrC from incomplete biomass burning and fossil fuel combustion was relatively high (West et al., 2020). High MAC_{365} values were observed for the methanol-soluble organic carbon collected from biomass burning (2.3 ± 1.1 m^2 g^{-1}) and bituminous coal combustion (3.2 ± 1.1 m^2 g^{-1}) (Tang et al., 2020). According to typical MAC and AAE values in Table 1, Saleh (2020) proposed an optical framework to clarify BrC by grouping BrC into four broad categories: very weakly absorbing BrC (VW-BrC), weakly absorbing BrC (W-BrC), moderately absorbing BrC (M-BrC), and strongly absorbing BrC (S-BrC).

Table 1. The proposed brown optical-based carbon classes. The table is adapted from (Saleh, 2020) © 2020, springer.

BrC class	k_{550}	w	MAC_{550}*(m^2/g)	**AAE***
Very weakly absorptive BrC (VW-BrC)	10^{-4}–10^{-3}	6–9	1.3×10^{-3}–1.3×10^{-2}	7–10
Weakly absorptive BrC (W-BrC)	10^{-3}–10^{-2}	4–7	1.3×10^{-2}–0.13	5–8
Moderately absorptive BrC (M-BrC)	10^{-2}–10^{-1}	1.5–4	0.13–1.3	2.5–5
Strongly absorptive BrC (S-BrC)	> 10^{-1}	0.5–1.5	> 1.3	1.5–2.5

1.5 Recent advances in aerosol instrumentation

To get profound insights into brown carbon aerosol, it is important to measure their chemical composition and their optical properties, e.g. the molecular identification and light absorption of major chromophores. In this section I will briefly summarize the advanced mass spectrometric techniques which recently became available for aerosol particle chemical characterization (1.5.1), for corresponding gas phase measurements (1.5.2), and state-of-the-art optical methods (1.5.3).

1.5.1 Aerosol particle measurements

Recently, various online and offline mass spectrometers have been developed to characterize and quantify OA or brown carbon particles. The aerosol mass spectrometer (AMS) is able to quantify non-refractory particle composition by utilizing electron ionization (EI) e.g. total organics, sulfate, nitrate, ammonium, and chloride (DeCarlo et al., 2006). Even though AMS can quantify the OA mass, it cannot provide molecular information of OA since the high ionization energy (70eV) results in substantial fragmentation (Canagaratna et al., 2007). A chemical ionization mass spectrometer can minimize or avoid fragmentation and provide molecular information. A filter inlet for gases and aerosols coupled to a high-resolution time-of-flight chemical ionization mass spectrometer (FIGAERO–HR-ToF-CIMS, Aerodyne Research Inc, hereafter CIMS) employing iodide ions for chemical ionization can provide brown carbon molecular compositions of gas and particle phase (Lopez-Hilfiker et al., 2014). However, the subsequent thermal desorption of the particle from filters requires more time, thus FIGAERO-CIMS only provides semi-continuous measurements of OA with a time resolution of less than 40 minutes (Lopez-Hilfiker et al., 2014).

Furthermore, FIGAERO-CIMS is capable to detect thousands of oxygenated organic molecules and to determine their volatility. Typically, authentic standards are only available for a few of them which is limiting the potential to determine the concentrations of the various oxygenated organic molecules. The sensitivity of the instrument varies over several orders of magnitude for different molecules (Lee et al., 2014). However, a very sensitive method for the online measurement of oxidized aerosol particle compounds and brown carbon molecules was recently realized by extractive electrospray ionization time-of-flight mass spectrometry (EESI-ToF-MS) (Stefenelli et al., 2019). EESI-ToF-MS allows the continuous measurement of particle composition without pre-collection of particles, but thermal desorption and volatility information are not available. Recently, the chemical analysis of aerosol online inlet (CHARON) coupled to the proton-transfer-reaction mass spectrometer (PTR-MS) has been developed to measure the chemical composition of aerosol particles (Eichler et al., 2015). Although the PTR-MS is a relatively soft ionization technique, significant fragmentations in the CHARON-PTR-MS still occur during transfer reactions (Blake et al., 2009). However, this method allows a better quantification of the gas phase and also particle phase compounds since the sensitivities for different compounds vary typically only by a factor of two. Offline techniques are based on the filter collection and subsequent laboratory analysis including an ultra-performance liquid chromatography (UPLC) coupled with high-resolution (HR) Q-Exactive HF-X hybrid quadrupole Orbitrap mass spectrometer equipped with an electrospray ionization (ESI) source (UPLC-ESI/HRMS) and fourier-transform ion cyclotron resonance mass spectrometry (FT-ICR-MS). The UPLC-MS first separates individual components or isomers and provides mass spectral information that can help to identify each separated component by its very high mass resolution (Siemens et al., 2022). The UPLC can also be coupled to and on-line absorption measurement allowing to determine the absorption spectra of the separated individual chromophores (Lin et al., 2015). The FI-ICR-MS can provide detailed information of brown carbon aerosol such as molecular compositions and functional groups (Tang et al., 2020). However, offline techniques generally have lower time resolution of hours or days depending on sample collection, sensitivities, and laboratory analysis.

1.5.2 Gas phase measurements

To determine concentrations of VOCs, the PTR-MS is a versatile, sensitive, and quantitative instrument for less oxidized compounds (Yuan et al., 2017), such as hydrocarbons (toluene, indole, isoprene, and terpenes) and slightly oxidized organics (aldehydes, alcohols, etc.). As mentioned

above, the PTR-MS is a relatively soft ionization technique but still significant fragmentation occurs in the PTR-MS (Blake et al., 2009). Other instrument for VOCs is gas chromatography coupled with mass spectrometry (GC-MS). The GC can be used to separate many different compounds based on their retention times in the chromatographic columns. However, the time resolution of GC-MS is relatively low with more than 1 hour during to sample collection and laboratory analysis. Recently, iodide-CIMS is very useful for the very sensitive detection of oxygenated organic molecules in the gas phase (Lopez-Hilfiker et al., 2016). However, it can't measure the pure hydrocarbons and only for few of the higher oxygenated compounds authentic standards are available which allow quantification with this technique.

1.5.3 Optical measurements

Several different online and offline optical instruments are available to measure the optical properties of aerosol particles and especially the light absorption which is characteristic for BrC aerosol (Laskin et al., 2015). For online measurement, a filter-based instrument, the Aethalometer (AE33 and MA200) (Sandradewi et al., 2008b) and multi-angle absorption photometry (MAAP) , can derive the absorption coefficient by measuring the change in light attenuation due to aerosol loading on a filter. The time resolution of the AE33 (Magee Scientific) is 1 second or 1 minute. And it provides light absorption for 7 wavelengths (370, 470, 520, 590, 660, 880, and 980 nm). However, due to light measurement based on particle loading on filter, it has artifacts from aerosol scattering and loading effect. Therefore, the Aethalometer is mainly suitable for strongly absorbing compounds like black carbon but has high uncertainties for weaker absorbers like BrC. The photoacoustic spectrometer (PAS) has been developed to directly measure the aerosol absorption on-line. The in-situ measurement of aerosol absorption using PAS has less biases and lower uncertainties compared to filter-based instrument, but, on the other hand, the PAS has not a very high sensitivity, are more complex, and thus require more care during operation and calibration. Offline techniques are based on the filter collection. These filter samples can be extracted by different solvents like water, methanol, or acetonitrile to extract the soluble BrC molecules (Laskin et al., 2015). The filter extracts can then be analyzed e.g. by photometers to measure their absorption spectra. Furthermore, excitation-emission spectra can be recorded e.g. using an instrument called Aqualog (HORIBA Scientific, USA). The excitation-emission spectra can then be analyzed for characteristic chromophore signatures (Chen et al., 2016). The light absorption from offline UV-vis spectrometer measurement has typically a high accuracy. However, offline

techniques generally have low time resolution with hours or days depending on sample collection and laboratory analysis. As introduced above, each instrument has its own advantages and disadvantages. The combination of different online and offline techniques can improve the optical properties and chemical characterization of brown carbon.

1.6 Research questions for my thesis

Brown carbon aerosol has a significant effect on air quality and climate. It absorbs solar radiation in the near-ultraviolet and visible spectral range. There are many sources contributing to brown carbon including primary emissions e.g. incomplete combustion and secondary formation e.g. oxidation of volatile organic compounds. The different sources of brown carbon lead to extremely complex chemical compositions (PAH, NAC, HULIS, and tar ball). In addition, the optical properties of brown carbon have a large variety due to the multiple sources and complex chemical compositions. Even though many previous studies investigated brown carbon, their chemical characteristics and especially the link between optical properties and chemical composition are still not well understood. Furthermore, there is still little known about chemical characterization and optical properties of brown carbon from combustion emissions. It is also unclear about the chemical compositions and light absorption of secondary brown carbon at different conditions, e.g. temperatures, NO_2, and seed particles. Finally, formation mechanisms and loss pathways of brown carbon aerosol in the atmosphere are not well understood. In this context, this dissertation aims to provide a comprehensive and substantial contribution to a better understanding of the chemical composition and the optical properties of brown carbon aerosol from primary emissions of burning different fuels (combustion), secondary formation with anthropogenic and biogenic precursors (simulation chamber experiments), and field campaigns in rural and urban areas for different seasons. My major research questions are listed as follows:

(1) What are the chemical compositions and optical properties of brown carbon from different combustion sources, from the oxidation of major VOCs, and from mixed sources in field studies?

(2) What is the link between chemical composition and optical properties of brown carbon aerosol?

(3) How do the presence of NO_2, temperatures, and seed particles affect formation and optical properties of secondary brown carbon aerosol?

(4) What are the formation mechanisms and loss pathways of brown carbon aerosol in ambient environment? And what is the evolution of brown carbon aerosol from primary emissions after photooxidation.

To answer these research questions, I have applied various methods which will be described in detail in the following section. To study emissions from major combustion sources and to study secondary BrC I conducted dedicated laboratory experiments. Then I related these results to observations in the ambient rural and urban atmosphere. In section, 3.1, the chemical composition, chromophores and optical properties of brown carbon emitted from combustion (straw, beech, cow dung, and plastic) will be presented. In section 3.2, the yields and characteristics of secondary brown carbon from oxidation of toluene and indole oxidation will be discussed for different experimental boundary conditions (NO_2, temperature, and seed particles). In section 3.3, chromophores and chemical composition of brown carbon will be discussed at an urban kerbside based on excitation-emission spectroscopy and mass spectrometry results. Please note that I have published these results as a first-author (Jiang et al., 2022). In section 3.4, the brown carbon molecules in a rural area in southwest Germany as well as their optical properties, sources, and loss pathways will be discussed.

2. Methodology

To achieve the research objectives and answer the open questions, I conducted several simulation chamber experiments and field campaigns. These experiments are helpful to understand the chemical characteristics and optical properties of brown carbon aerosol from primary emissions, secondary formation, and mixed sources in ambient air. During the experiments, I mainly used two mass spectrometers (FIGAERO-CIMS and AMS) and two optical instruments (AE33 and Aqualog) to measure the aerosol chemical composition and the corresponding optical properties. The major chamber experiments and field campaigns that I performed during my Ph.D. study are summarized in Figure 5. Section 2.1 of this chapter describes the techniques and calibration of the main instruments as well was the data analysis tools. Sections 2.2 and 2.3 describe how I did the simulation chamber experiments and field campaigns, respectively. Sections 2.4 and 2.5 describe how to calculate aerosol densities, aerosol yields, and how to identify potential brown carbon molecules, respectively.

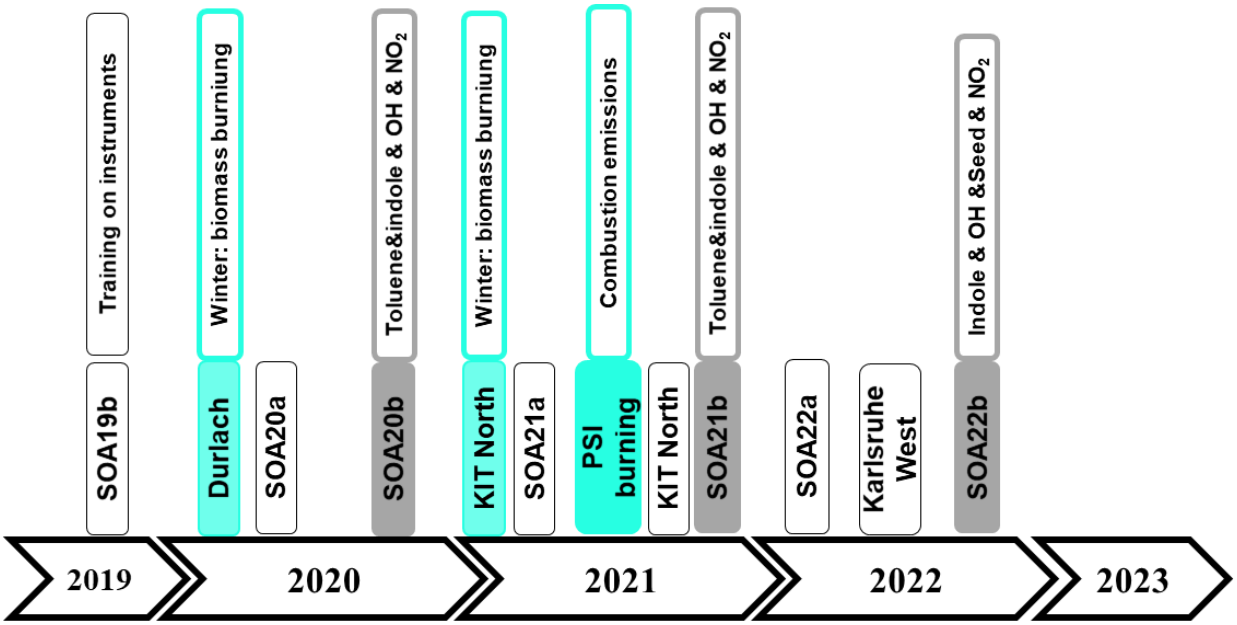

Figure 5. Timeline of the major campaigns I performed or participated in during my Ph.D. study from October 2019 to July 2023. The campaigns are marked grey (AIDA chamber) and light blue (field) colors. The vertical boxes give my contributions or research interest in these activities.

2.1 Instrumentation and software

2.1.1 HR-TOF-AMS technique and calibration

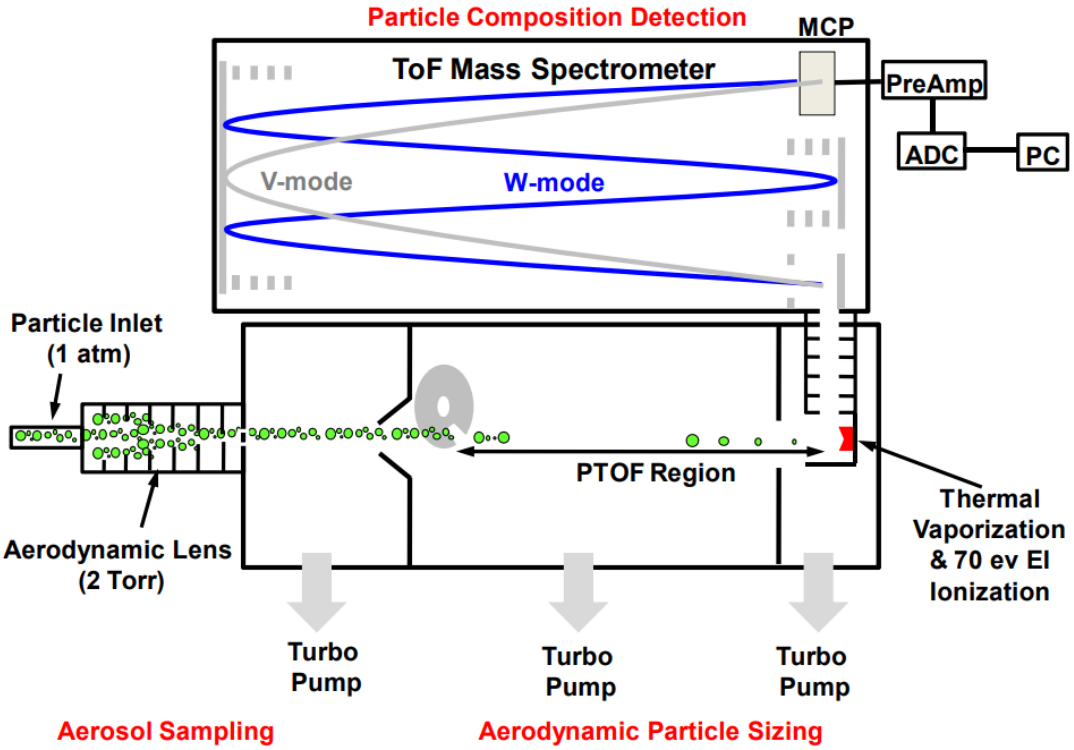

Figure 6. A schematic of the HR-ToF-AMS, adapted from DeCarlo et al. (2006).

A high-resolution time of flight aerosol mass spectrometer (HR-ToF-AMS, Aerodyne Inc.) is a really powerful instrument to obtain the size-resolved real-time composition of non-refractory submicron aerosols including organic aerosol, sulfate (SO_4^{2-}), nitrate (NO_3^-), ammonium (NH_4^+), and chloride (Chl^-) (Canagaratna et al., 2007). As shown in Figure 6, the instrument includes several parts: sample introduction system, sizing region, and vaporization and ionization systems. During the measurement, aerosol particles with typical sizes ranging between 35 nm and 2.5 μm are sampled through a critical orifice into the aerodynamic lens. In the aerodynamic lens, the particles are gradually concentrated into a narrow beam at the exit of the lens using six apertures, and most sample gases are removed by turbo pumps. At the exit of the lens, a supersonic expansion accelerates the particle into the sizing region (particle time-of-flight, PToF), where particle size is determined by measuring particle flight time across a fixed distance. When the particles reach the thermal vaporization and ionization region, there are vaporized by impaction on a resistively heated tungsten surface (~ 600) °C and ionized by electron ionization (EI). The AMS can be

operated alternatingly in V mode for determining the particle mass concentration and size distribution, and in W mode for measuring the highest resolution mass spectra. Then the ions travel to the ToF region and are separated based on their *m/z* value before reaching the multichannel plate (MCP) detector. Therefore, AMS detect the nonrefractory compounds e.g. organic species, nitrate, sulfate, and ammonium, but cannot measure the refractory compounds e.g. crustal material, sea salt, and black carbon.

The AMS data were analyzed by the data analysis software package SQUIRREL (version 1.60C) and PIKA (version 1.2C). For the HR-ToF-AMS data analysis, I followed the steps listed on the Jimenez Research group (http://cires1.colorado.edu/jimenez-group/wiki/index.php/ToF-AMS_Analysis_Software): raw data loading, mass calibration, baseline calibration, parameter corrections (e.g. air beam, ionization efficiency, collection efficiency and particle size), unit resolution data of nonrefractory compounds, peak width and peak shape for high resolution fitting in PIKA, peak identification, and generating graphs with high resolution. Parameters for ionization efficiency correction and size calibration (using ammoniate nitrate). Operation and calibration of the AMS in the chamber and field campaigns were performed by me and my colleague Junwei Song. My colleague Junwei Song also did a positive matrix factorization (PMF) analysis of the organic aerosol mass spectra resulting in characteristic source factors with the ME2 engine (see Song et al., 2022 for further details). According to PMF analysis, OA can be separated into e.g. hydrocarbon-like OA (HOA), cooking-related OA (COA), biomass burning OA (BBOA), semi-volatile oxygenated OA (SV-OOA), and low-volatility oxygenated OA (LV-OOA) (de Sa et al., 2019).

2.1.2 FIGAERO-CIMS technique and calibration

FIGAERO-CIMS (Aerodyne Inc.) is a really powerful instrument to enable online measurements of both gas-phase and particle-phase chemical constituents of aerosols (Lopez-Hilfiker et al., 2014; Le Breton et al., 2019; Salvador et al., 2021). The iodide-adduct ionization is selective toward polar organic compounds (Lee et al., 2014). Detailed schematics, operations, and design of FIGAERO (Filter Inlet for Gas and Aerosols) were provided by Lopez-Hilfiker et al. (2014), as shown in Figure 7A. Briefly, gases are directly sampled through an inlet and the gas sample flow is controlled by a pin hole to 2 SLM during measurement. During the gas measurement, the particles are collected onto a Teflon (Polytetrafluoroethylene, PTFE) filter via a separate sampling port (Figure 7B). After collection, the linear actuator moves the filter to the

desorption port (Figure 7C). Then, the particulate compounds were thermally desorbed from the filter by a flow of ultra-high-purity (UHP) N_2 heated from room temperature to 200 °C (Yang et al., 2021).

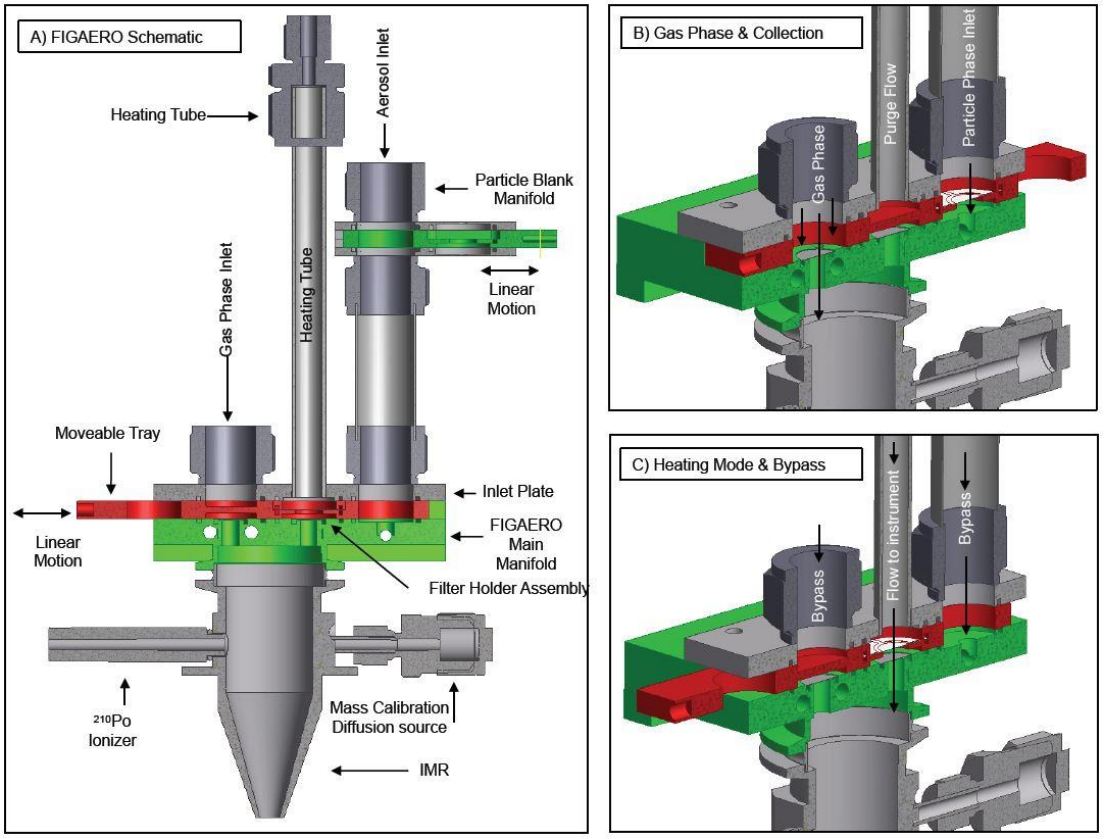

Figure 7. A schematic of FIGAERO inlet (A), FIGAERO in gas phase & particle collection mode (B), FIGAERO in heating mode (C).

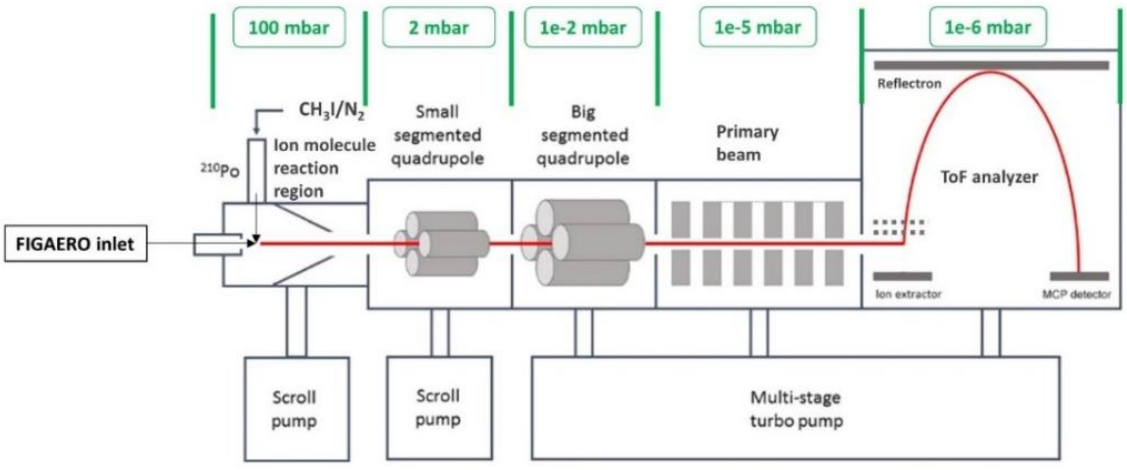

Figure 8. A schematic of a HR-ToF-CIMS with FIGAERO inlet (Sanchez et al., 2016) with the different pressure zones.

As shown in Figure 8, the sample molecules reach the ion molecule reaction (IMR) region at a pressure of 100 mbar where they react with an excess of iodide ions (I^-) forming iodide clusters. The reagent ions are formed by flowing UHP nitrogen over a permeation tube with methyliodide (CH_3I) through a radioactive polonium-210 source. Then the cluster ions travel to the ToF analyzer region through the small segmented quadrupole region (SSQ), big segmented quadrupole (BSQ) region, and primary beam (PB) region. The ions form an air beam with increasing vacuum. The air beam ions are detected by a multichannel plate (MCP) detector. The time of flight of lighter ions are less than those of heavier ions in the TOF channel. Thus, the instrument resolves all ions by their mass-to-charge ratios (m/z, Th), according to different flying time with a resolution of about 4000.

The sensitivity of a CIMS is fundamentally limited by the collision frequency between reagent ions and molecules, known as the collision limit, the ion-molecule reaction time, and the transmission efficiency of product ions to the detector. The sensitivity of the CIMS (I^-) can vary over about 4 orders of magnitude for different molecules. Therefore, I did calibrations to determine the sensitivity of typical brown carbon molecules e.g. nitro aromatic compounds. I calibrated the CIMS for 4-nitrophenol, 4-nitrocatechol, 2-methyl-4-nitrophenol, and 2-methyl-4-nitrocatechol. Each nitro aromatic compound (NAC) was dissolved into methanol to about 10 ng/μL as a standard NACs solution. Different volumes (1, 2, and 5 μL) of the standard NACs solution were deposited on a PTFE filter using an accurate syringe. The loaded filter was analyzed by FIGAERO-iodide-CIMS by a standard thermal desorption. The filters were then desorbed in the same way as for the field samples. Every analysis of the standard solution was repeated three times. The average sensitivity factor of the four NACs was 1.7 ± 0.06 (Figure 15).

FIGAERO-CIMS data was analyzed by using the toolkit Tofware (v3.1.2, Tofwerk, Thun, Switzerland, and Aerodyne, Billerica) with the Igor Pro software (v7.08, Wavemetrics, Portland, OR). Here are my workflows for FIGRAERO-CIMS data analysis: a) average the 1s time of raw data into 10s data, b) mass axis calibration by using I-, H_2OI^-; $CH_2O_2I^-$, and I_3^- as reference masses, c) define reference spectrum by using potential ions detected in samples, d) refine baseline, e) refine peak with and peak shape with a nominal resolution of about 4000, d) do peak lists. After obtaining signal intensities of ions, I use MATLAB to calculate the molecular mass concentrations with scripts written by myself. For the simulation chamber experiments and a field campaign at downtown Karlsruhe, I used Teflon filters to collect particles and then stored the sample filters in

a freezer at -20 ºC until analysis by FIGAERO-CIMS. For the field campaign at KIT Campus Nord, the FIGEARO-CIMS was used to measure the particle and gas phase intermittently. During the gas-phase measurement, gases were sampled via a fluorinated ethylene propylene (FEP) tube. At the same time, particles were collected via a stainless steel tube and a $PM_{2.5}$ inlet on a Teflon filter. At a regular interval of 30 minutes, the gas-phase measurement was switched off and particles collected on the filter were desorbed by heated nitrogen from room temperature to 200 ºC over the course of 35 min. The operations and data analysis of the FIGAERO-CIMS were mainly performed by me but especially at the beginning of my PhD work with substantial support by my colleague Linyu Gao.

2.1.3 Aqualog

Aqualog (Horiba Scientific) simultaneously measures both absorbance spectra and fluorescence excitation-emission matrices (EEM) (Figure 9a and b). To measure absorbance, the detector measures the transmission of light through the sample in a quartz cuvette. The absorption wavelength ranges from 239 to 800 nm with a resolution 3 nm. Methanol-soluble organic carbon (MSOC) was extracted from the quartz filters with 5mL methanol (for analysis purity, Merck) via ultrasonication of filter punches for 30 min. All the extracts were filtered through a 0.45 μm polytetrafluoroethylene membrane into a glass bottle to remove the insoluble materia. The light absorption coefficients of e.g. methanol-extracted brown carbon were calculated through the absorption (A_λ) of the solution:

$$Abs_\lambda = (A_\lambda - A_{700}) \times \frac{V_{extract}}{V_{air} \times L} \times \ln(10) \quad (1)$$

Where A_{700} and A_λ are measured by Aqualog, $V_{extract}$ (m^3) is the solvent volume, V_{air} (m^3) is the sampling volume corresponding to the extracted filter, and L is the optical path length of the quartz cuvette (1 cm).

The mass absorption coefficient (MAC; $m^2\ g^{-1}$) of the methanol-soluble BrC (MS-BrC) fractions in the extracts as a function of the wavelength was calculated according to Hecobian et al. (2010):

$$MAC_\lambda = \frac{Abs_\lambda}{C} \quad (2)$$

Where Abs_λ (Mm^{-1}) is the light absorption coefficient. C ($\mu g\ m^{-3}$) represents the atmospheric concentration of organic aerosol detected by AMS, assuming that all organic aerosol components can be dissolved into methanol.

The absorption Ångström exponent (AAE) is an important parameter to characterize the wavelength dependence of light absorption which fits a power law as follows:

$$Abs_\lambda = K \times \lambda^{-AAE} \quad (3)$$

Where K is a concentration- and composition-related constant. In my work, AAE was typically fitted in the range of 300–450 nm.

To measure the excitation-emission matrices, a monochromatic excitation light is directed into the sample (e.g. methanol solution) which emits luminescence. At 90º-angles to the excitation beam, the sample's luminescence is directed into a multichannel charge-coupled detector, which measures the fluorescence spectrum. I used an excitation wavelength range from 239–500 nm and an emission wavelength range from 247–700 nm to have ranges comparable to Tang et al. (2020). The wavelength increments of the scans for excitation were 3 nm and the emission wavelength increments used were 2.33 nm. The resulting excitation–emission spectra were analyzed with the PARAFAC model to identify potential chromophoric components in the methanol soluble organic carbon (MSOC). I used the staRdom package for R version 4.0.5 of the PARAFAC model (Pucher et al., 2019; Murphy et al., 2013) which was downloaded from https://cran.r-project.org/web/packages/staRdom/vignettes/PA-RAFAC_analysis_of_EEM.html (2021 October 8). The details of the data analysis procedure are given by Pucher et al. (2019) and Murphy et al. (2013). In brief, light absorption measurements were used to correct the excitation emission matrix (EEM) for inner-filter effects. The highest absorbance was not greater than 2 (mostly below 0.5 at 237 nm), which is appropriate for inner-filter corrections of the EEMs. Afterwards, all EEMs were normalized to the Raman peak area of water so that their unit is in Raman units (RU) whose excitation wavelength was 350 nm. Additionally, an interpolation method was used to remove the signals of the first-order Rayleigh and Raman scattering as well as the second-order Rayleigh scattering in the EEMs. The integral fluorescence volume (FV, RU-nm^2) of the methanol extracts was calculated for the excitation wavelengths of 239–500 nm and in the emission wavelength range of 247–700 nm. The integral fluorescence volume was normalized by the organic concentration of the extracts obtained e.g. from AMS measurements to the normalized fluorescence volume (NFV, RU nm^2 [mg L^{-1}]$^{-1}$). During analyzing samples collected at downtown

Karlsruhe, the emission wavelength increments used were 4.66 and 2.33 nm in summer and winter, respectively. However, the increments of EEM spectra can be changed by the function (eem_extend2largest) in RStudio staRdom. I used this function to reduce the wavelength increments for the summer samples and ensured the same wavelengths for all samples.

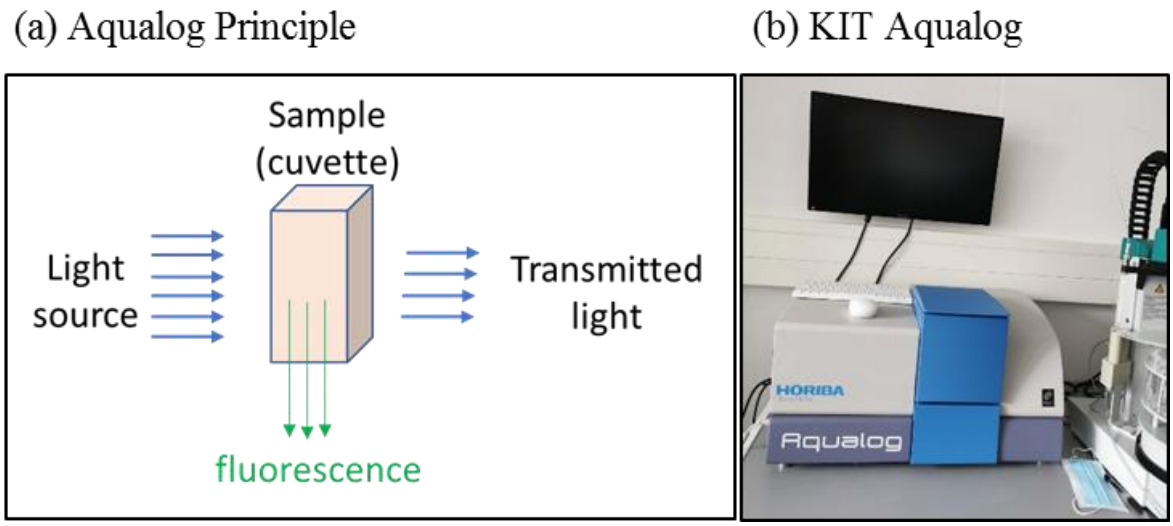

Figure 9. A schematic of (a) the Aqualog principle and (b) a photo of the Aqualog at KIT (Photo: F., Jiang, 06.2020).

2.1.4 Aethalometers (AE33)

In the aethalometer AE33 (Magee Scientific), aerosol particles are continually sampled on a quartz filter and the optical attenuation is measured with time resolutions 1 second or 1 minute at seven wavelengths (370, 470, 520, 590, 660, 880, and 950 nm) (Drinovec et al., 2015). The light absorption at seven wavelengths was calculated from the measured attenuation as shown in Figure 10. Attenuation is measured on two spots with different sample flows and on the reference spot without sample flow (Figure 10a). The two loading spots with different flows are used to allow for loading effect corrections. The light absorption of aerosol particles on the filter is also influenced by scattering of light within filter which will enhance the light absorption. In this dissertation, I used the default value (1.57) to do the scattering correction (Drinovec et al., 2015). The BC mass concentration is calculated from the change in optical attenuation at 880 nm in the selected time interval using the mass absorption cross section 7.77 m^2 g^{-1} (Gundel et al., 1984), since other aerosol particles (organic aerosol or mineral) have less absorption at this wavelength and major absorption is contributed from BC alone.

I assumed negligible absorption by dust and thus, Abs_{λ} can be divided into BC and BrC absorption. Therefore, the $Abs_{BrC}(\lambda)$ can be calculated as follows:

$$Abs_{BrC}(\lambda) = Abs(\lambda) - Abs(880) \times (\frac{\lambda}{880})^{-AAE_{BC}} \quad (4)$$

Where $Abs_{BrC}(\lambda)$ is the absorption caused by BrC at λ = 370, 470, 520, 590, or 660 nm, the $Abs(\lambda)$ is total absorption by AE33, the Abs(880) is the light absorption at 880 nm, and the AAE_{BC} is 1.

The fraction of wood burning black carbon (BCwb) was calculated by using the Aethalometer model (Sandradewi et al., 2008a):

$$BC_{wb} = [\frac{b_{abs}(470nm) - b_{abs}(950nm) * \left(\frac{470}{950}\right)^{-\alpha ff}}{\left(\frac{470}{950}\right)^{-awb} - \left(\frac{470}{950}\right)^{-\alpha ff}}]/b_{abs}(950nm) * BC \quad (5)$$

Where two pairs of Ångström exponents values were utilized to obtain BC associated with fossil fuel (BC_{ff}) and wood burning (BC_{wb}): αff and αwb of 0.95 and 1.60 were applied (Saarikoski et al., 2021). The operations and data analysis of the AE33 was done by me.

(a) Optical chamber in the AE33 (b) KIT AE33

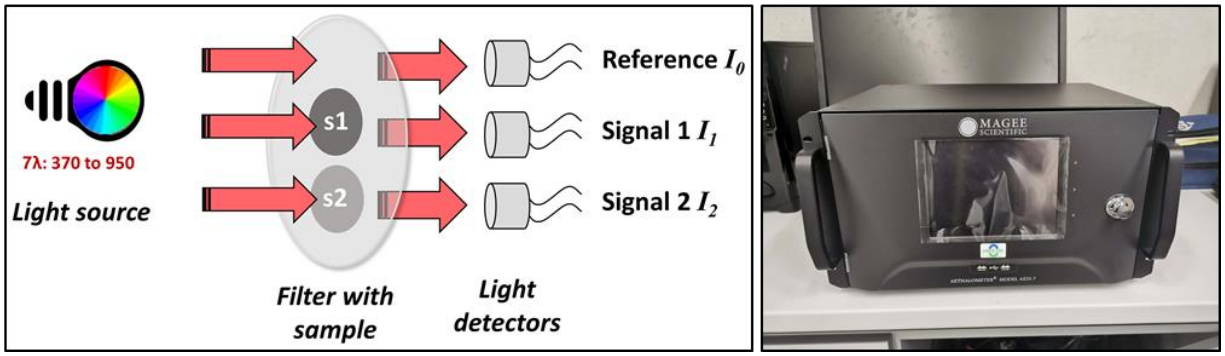

Figure 10. A Schematic representation of (a) the optical chamber in the Aethalometer AE3, adapted from Cuesta-Mosquera et al. (2021), and (b) a photo of the AE33 at the KIT (Photo: F, Jiang, 10.2020).

2.1.5 Auxiliary instruments

In all chamber experiments and field campaigns during my Ph.D. study, a series of auxiliary instruments for particle, gas, and meteorological measurements were also used and are briefly introduced here.

PTR-ToF-MS: During the experiments, the volatile organic compounds e.g. toluene, indole, and phenol etc. were measured by a proton-transfer-reaction time-of-flight mass spectrometer (PTR-ToF-MS 4000, Ionicon Analytic GmbH) equipped with the CHARON (Chemical Analysis of Aerosol Online) particle inlet. Data were analyzed using PTR viewer 3.3.12 (Ionicon Analytic GmbH). During the period of VOC injection and oxidation in simulation chamber, the PTR-ToF-

MS was operated for measuring gaseous VOCs only. The gas phase was measured at a flow rate of 40 SCCM via a PEEK (polyether ether ketone) tube. Furthermore, a flow rate of 3.9 L min^{-1} was added to the total flow to minimize the residence time in the sampling tube. For measuring gases, the drift tube of the PTR-MS was kept at 353.15 K and 2.7 mbar, with an electric field (E/N) of 92 Td. For the indole simulation chamber studies, I calibrated the PTR-MS with indole as aqueous solution using a liquid calibration unit (LCU-a, Ionicon Analytic GmbH). I obtained an indole sensitivity of 200 ± 21 ncps ppb^{-1} (ncps: normalized counts per second). A gas standard (Ionicon Analytik GmbH) was used to calibrate the PTR-ToF-MS for toluene. I obtained a toluene sensitivity of 608 ± 60 ncps ppb^{-1}. Please note that operation and data analysis of the PTR-ToF-MS were mainly performed by my colleagues Junwei Song, Yanxia Li, and only partially by me.

UPLC-PDA-HRMS: A quartz filter loaded with aerosol particles in each experiment was extracted with 8 mL acetonitrile (Optima LC/MS grade, Fisher Chemical) under sonication. As shown in Figure 11, the 8 mL sample solution was dried to 2 mL with pure nitrogen. 1 mL concentrated solution was used to measure its light absorption by Ocean Optics spectrophotometer. Another 1 mL concentrated solution was further dried to 200 μL and then analyzed using an ultra-performance liquid chromatography (UPLC) system coupled with a photodiode array detector (PDA), both from Thermo Vanquish, and a high-resolution (HR) Q-Exactive HF-X hybrid quadrupole Orbitrap mass spectrometer equipped with an electrospray ionization (ESI) source (UPLC-PDA-ESI/HRMS, Thermo Scientific, Inc). Detailed information of samples analysis by UPLC-PDA-ESI/HRMS is given in previous studies (Siemens et al., 2022; He et al., 2022). Briefly, around 0.3 ug of organic aerosol was injected into the UPLC for each sample. The analytes were separated on a reversed-phase column (Luna C18, 150 × 2 mm, 5 μm particles, 100 Å pores, Phenomenex, Inc.) using a 400 μL min^{-1} binary solvent mixture containing water (A) and acetonitrile (B), with both solvents containing 0.1% (v/v) formic acid. A 36 min LC gradient was programmed as follows: 0–0.5 min at 5% of B, 0.5–26 min at a linear gradient to 100% of B, 26–30.5 min B held at 100%, 30.5–31 min decreased to 5% of B, and 31–36 min held at 5% of B to re-equilibrate the column. The UV-vis absorption spectra were recorded using the PDA detector over the wavelength range of 300–680 nm. Mass spectra were acquired for the m /z range of 80–1200 Da at a mass resolution of $m/\Delta m$ = 240 000 at 200 m /z. The raw data were acquired using Xcalibur software (Thermo Scientific) and were further processed using MZmine 2.38 (He et al.,

2022). Please note that operations and data analysis of the UPLC-PDA-ESI/HRMS were mainly performed by Kyla Siemens (Purdue University) and me.

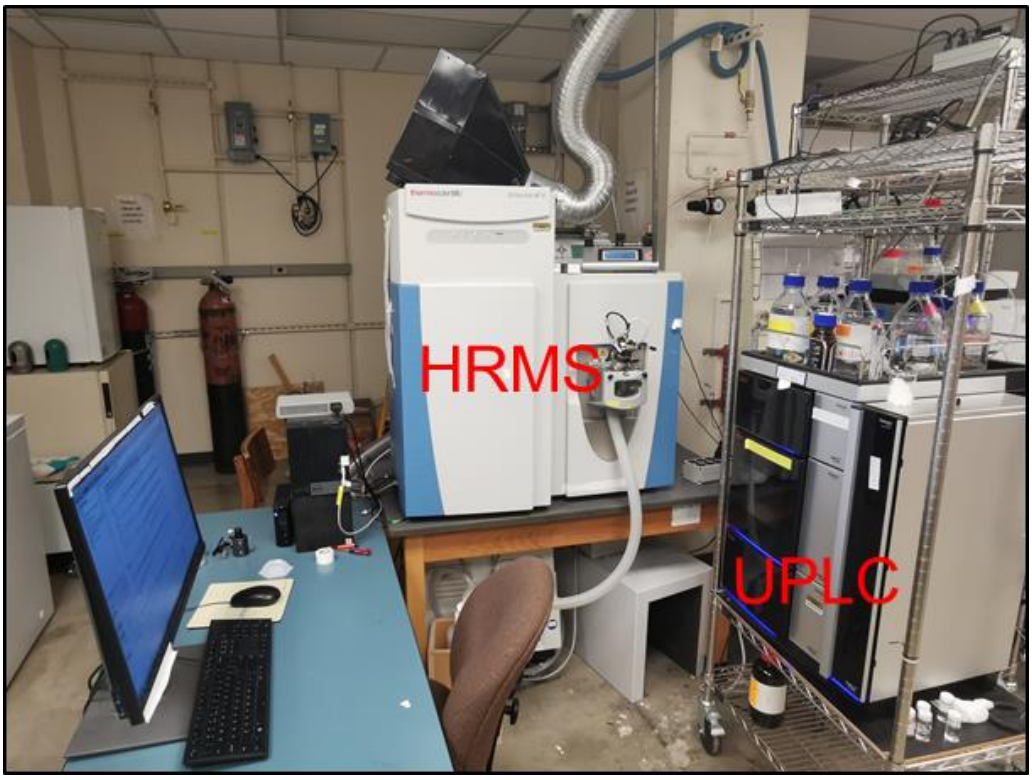

Figure 11. A photo of the UPLC-HRMS at Purdue University (Photo: F., Jiang, 11/2022).

Photoacoustic spectroscopy: The absorption measurement by the photoacoustic method is initiated by a modulated laser (Linke et al., 2016). Due to the absorption of light by particles within the laser beam, the carbonaceous material gets energetically excited and heats up. The deposited thermal energy is subsequently released into the surrounding gas. Due to the periodic thermal expansion caused by a laser modulation, a pressure or sound wave is generated in the gas. This sound wave is amplified in an acoustic resonator and is detected by a microphone. The photoacoustic signal correlates directly the light absorption (Linke et al., 2016). The photoacoustic spectroscopy (PAS, Schnaitec Gmbh) measures the light absorption of aerosol particles at three wavelengths (405, 515, and 660 nm). Please note that operation and data analysis of the PAS were mainly performed by my colleague Dr. Claudia Linke (IMK-AAF).

Optical Particle Counter (OPC): the OPC Fidas200 (Palas, Germany) measured aerosol particles in the ambient air in the size range of 0.18–18 µm. Based on the measured size distribution and some assumptions, it calculates particulate mass concentrations like PM_1, $PM_{2.5}$ and PM_{10}. The

actual aerosol sensor is an optical aerosol spectrometer which determines the particle size using Lorenz-Mie scattered light analysis of single particles. The sample flow of Fidas200 is approximately 0.3 $m^3 h^{-1}$. Please note that operations and data analysis of the Fidas200 were mainly performed by Dr. Harald Saathoff and me.

Condensation Particle Counter (CPC): During my Ph.D. study, the particle number concentrations were measured by CPCs (CPC3022A and CPC3776, TSI Inc., USA). The aerosol sample is drawn continuously through a heated saturator where butanol is vaporized and diffuses into the aerosol sample stream. Once the butanol condenses into the particles, the particles quickly grow into larger droplets and pass through an optical detector. The minimum particles sizes were detected by CPC3022A and CPC3776 are >2.5 nm and >7 nm, respectively. The operations and data analysis of the CPCs were mainly performed by Dr. Harald Saathoff.

Scanning Mobility Particle Sizer: During my experiments, a SMPS consisting of a differential mobility analyzer (DMA, TSI 3080) and a CPC (CPC3022) was used to measure the particle size distributions in a range of 13.6–700 nm. The SMPS uses a bipolar aerosol charger to keep particles within a known charge distribution. Charged particles are classified according to their electrical mobility, using a long-column DMA. The particle concentration is measured with a CPC. The time resolution of the SMPS measurement was about 7 min. Operations and data analysis of the SMPS were mainly performed by Buschbacher Rainer and me.

Gas Monitors and Meteorological Data: Trace gases were measured via the FEP sampling tubes with different gas monitors i.e., ozone (O_3, O341M, Environment SA), nitrogen dioxide (NO_2, AS32M, Environment SA), and sulfur dioxide (SO_2, AF22M, Environment). Meteorological data like ambient air temperature, relative humidity, atmospheric pressure, global radiation, wind direction, wind speed, and precipitation were mainly obtained from a compact sensor (WS700, Lufft). Operation and data analysis of the gas monitors and meteorological sensors were mainly performed by Dr. Harald Saathoff.

2.2 Simulation chamber experiments

2.1.1 AIDA simulation chamber experiments

A schematic of the AIDA (Aerosol Interaction and Dynamics in the Atmosphere) simulation chamber at the Karlsruhe Institute of Technology and the main instrumentation used in this work are shown Figure 12. Experiments were conducted in AIDA simulation chamber operated at dark conditions, at relative humidities (RH) of 20%–60%, and at temperatures between 253–313 K. The core instrumentation used in my work is shown in Figure 12. A detailed description of the AIDA chamber, its operation modes, and the associated measurement techniques were published elsewhere (Gao et al., 2022; Saathoff et al., 2009).

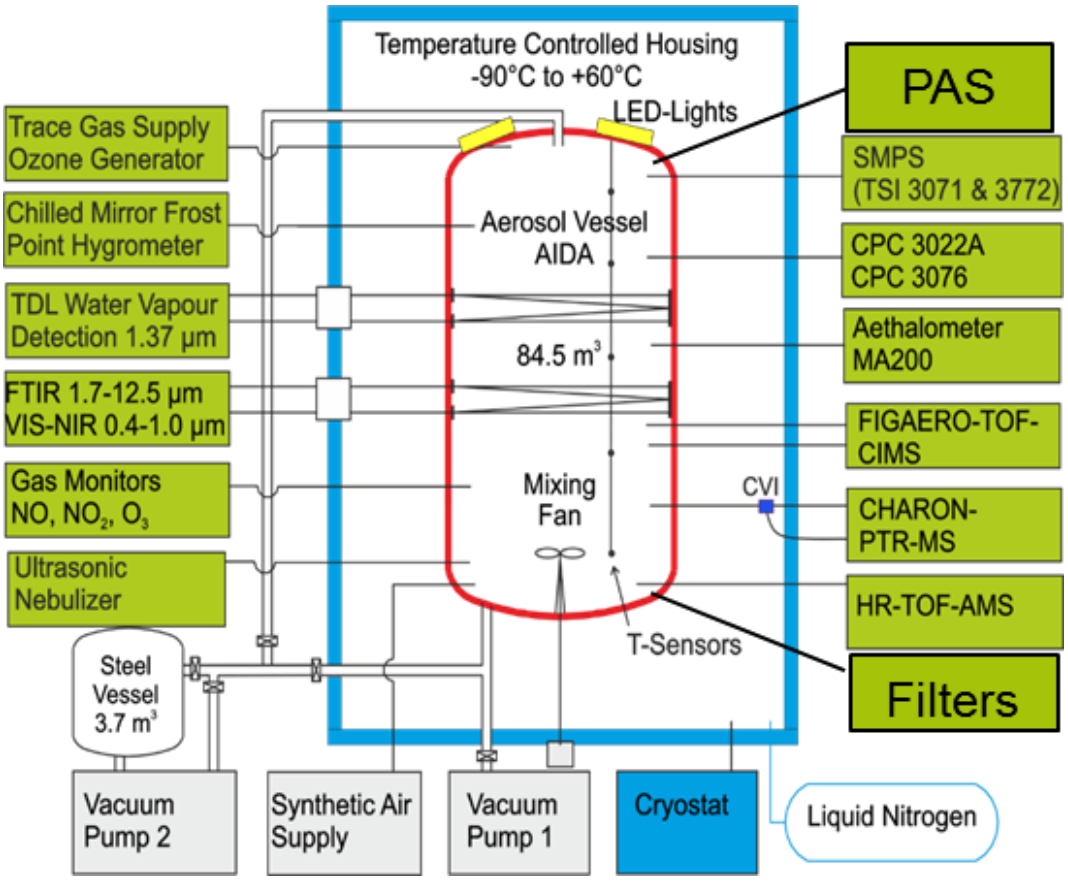

Figure 12. Schematic of the AIDA simulation chamber and its instrumentation used in this work.

Toluene SOA: The experimental conditions are listed in Table 2. The toluene-SOA was produced from OH radical oxidation of toluene at 4 different temperatures (253, 273, 293, 313 K) in presence of NO_2. Briefly, a dedicated amount of toluene was added into the AIDA chamber with a flow of 10 SLM of synthetic air. After toluene reaching ~230 ppb, 88 ppb of NO_2 (1000 ppm of 99.5%

purity in nitrogen 99.999 %; Basi Schöberl GmbH) was added into the AIDA chamber. When the toluene and NO_2 concentrations were stable, ozone generated by a silent discharge generator (Semozon 030.2, Sorbios) in pure oxygen (99.9999 %) was injected into chamber up to ~900 ppb. Subsequently, 2,3-dimethyl-2-butene (7000ppm in N_2, TME) was injected continuously with a flow of 50 SCCM and reacted with the excess of O_3 forming one OH radical per TME molecule added. Toluene was oxidized by OH radicals to form toluene SOA. The O_3 and NO_2 concentrations in the chamber were recorded in real-time by gas monitors (Environment S.A).

Table 2. Summary of toluene SOA samples and experimental conditions.

Toluene	NO_2	RH	Temperature	SOA density (g cm^{-3})*
201 ppb	80 ppb	60%	253 K	1.7± 0.2
215 ppb	81 ppb	60%	273 K	1.5 ± 0.2
230 ppb	80 ppb	30%	293 K	1.3 ± 0.1
244 ppb	82 ppb	20%	313 K	1.2 ± 0.1

*Calculate from AMS and SMPS sizers (see section 2.4)

Indole SOA: SOA was produced by oxidation of indole in presence/absence of NO_2 and $(NH_4)_2SO_4$ seed particles. The experimental conditions are listed in Table 3. Indole (≥ 99% purity, Sigma-Aldrich) was dissolved in methanol (HPLC grade, Honeywell) and the solution was used to coat a glass tube with indole. After evaporation of the methanol, a flow of 10SLM of synthetic air was send through the glass tube into the AIDA chamber to obtain 90–150 μg m^{-3} of initial indole mass concentrations (Montoya-Aguilera et al., 2017). Then the ozonolysis was started by adding 600–800 ppb of O_3 in 293 K at the 84.5 m^3 AIDA chamber. Subsequently, 2,3-dimethyl-2-butene (7000 ppm in N_2, TME) was injected continuously with 50 SCCM and reacted with the excess of O_3 to form OH radicals, (Lambe et al., 2007) for which calculated concentrations ranged between $0.2–1.0\times10^7$ molecules cm^{-3} (Salo et al., 2011). Following injection of OH radicals, rapid growth of *ind*-SOA was observed in each experiment. For experiments in the presence of $(NH_4)_2SO_4$ seed particles, (Figure S1b and d), ammonium sulfate (Merck, 99.5%) in ultra-pure water was aerosolized using an ultrasonic nebulizer (Synaptec), introduced into the AIDA chamber to reach mass loadings of ~50 ug m^{-3} (Figure S1b and d), before injecting indole. The number concentration and mobility mode size of the AS seed particles were ~2000 cm^{-3} and ~230 nm, respectively. For experiments with NO_2 present, NO_2 (99.5% purity, Basi Schöberl GmbH) was

injected into the chamber up to ~ 60 ppb after finishing indole injection, and followed by adding 100 ppb of O_3. However, the indole was oxidized only slowly, compared to oxidation by OH radicals. After 30 minutes, the products were further oxidized by adding more O_3 and TME, hence OH radicals. The O_3 and NO_2 concentrations in the chamber were recorded in real-time by gas monitors (Environment S.A). I also did oxidation of indole at different temperatures (313 K and 273K) and different seed particles (NaCl and BC), as shown in Table 3. Data analysis of indole SOA at different temperatures and seed particles is still going on.

Table 3. Summary of indole SOA samples and experimental conditions.

Experiment ID	Temperature	Indole (ppb)	NO_2 (ppb)	Seed particles	RH (%)	SOA density (g cm^{-3})	Filter loadings (μg)
REF	293 K	20.5	_	_	29	0.8 ± 0.2	30.9
AS	293 K	24.5	_	$(NH_4)_2SO_4$	28	0.9 ± 0.2	30.6
NO_2	293 K	23.3	66	_	29	1.1 ± 0.2	9.52
AS-NO_2	293 K	18.6	60	$(NH_4)_2SO_4$	29	1.3 ± 0.3	16.2
273	273 K	~20	_	_	60	_	_
313	313 K	~20	_	_	9	_	_
NaCl-NO_2	293 K	~40	60	NaCl	30	_	_
BC-NO_2	293 K	~40	60	BC	30	_	_

Before starting AIDA experiments, background samples from the AIDA chamber were collected on filters and by the online mass spectrometers. After the mass concentrations of indole or toluene SOA became stable inside the chamber, the aerosol samples were collected onto a Teflon filter (polytetrafluorethylene (PTFE), 1 μm, SKC Inc) and parallel quartz filters (47 mm diameter, Whatman) for each experiment. The Teflon filter was analyzed by FIGAERO-CIMS to obtain the chemical composition and volatility of the particle phase compounds. One quartz filter was analyzed by Aqualog to obtain the optical properties and excitation emission matrices. Another one quartz filter from *ind*-SOA was analyzed by UPLC-PDA-HRMS to identify the chromophores and the chemical composition. The particle number size distributions were monitored by a scanning mobility particle sizer (SMPS). SMPS and CPC data analysis was done

as in the previous studies (Gao et al., 2022). The chemical composition and aerodynamic size of toluene or indole SOA were characterized by a high-resolution time-of-flight aerosol mass spectrometer (HR-ToF-AMS, Aerodyne Inc. hereafter AMS). The toluene or indole concentrations and lowly oxygenated gaseous oxidation products were measured by the proton-transfer reaction time-of-flight mass spectrometer (PTR-ToF-MS 4000, Ionicon Analytic GmbH). Besides, highly oxygenated gaseous oxidation products were measured with a filter inlet for gases and aerosols coupled to a high-resolution time-of-flight chemical ionization mass spectrometer (FIGAERO-HR-ToF-CIMS, Aerodyne Research Inc. hereafter CIMS) employing iodide (I^-) as the reagent ion.

2.1.2 PSI smog chamber experiments

During a visit at the Paul Scherrer Institute (PSI, Villigen, Switzerland), I participated in several experiments conducted in their atmospheric simulation chamber. A schematic setup of this experiment is shown in Figure 13 and a list of the experiments is given in Table 4. Emissions originated from the combustion of the beech, straw, plastic, and cow dung were first collected in a steel container (holding chamber). I collected samples from the primary organic aerosol (POA) in the holding chamber. Subsequently, the aerosol was injected into a smog chamber (5.5 m^3) where it was oxidized by O_3 and OH radicals to form secondary organic aerosol. After the oxidation was completed, filters of the POA-SOA mixture were collected as well. There were several instruments connected the smog chamber (Figure 13b), e.g. size distributions from SMPS, chemical composition from EESI-CIMS, chemical composition from AMS, and black carbon and light absorption from AE33. Since the experiments were mainly done by the colleagues at PSI, the detailed information on the experimental methods can be found in their references (Bruns et al., 2015) and will not be repeated here in detail. The online measurement instruments (EESI-CIMS, AMS, AE33, and SMPS) were mainly operated by PSI colleagues. The data analysis from online measurements is still going on. Filter samples were collected as shown in Table 4, and I brought these filters to KIT and then analyzed them at our laboratory by Aqualog and FIGAERO-CIMS. The CIMS analysis provides chemical compositions and thermogram of oxygenated organic aerosol components. The quartz filters were analyzed by Aqualog. This analysis provides light absorption and excitation-emission matrices. The methanol extraction steps of quartz filters are given in section 2.1.3. The mass loading of organic aerosol on filters were calculated by combining AMS data, sampling times and flows.

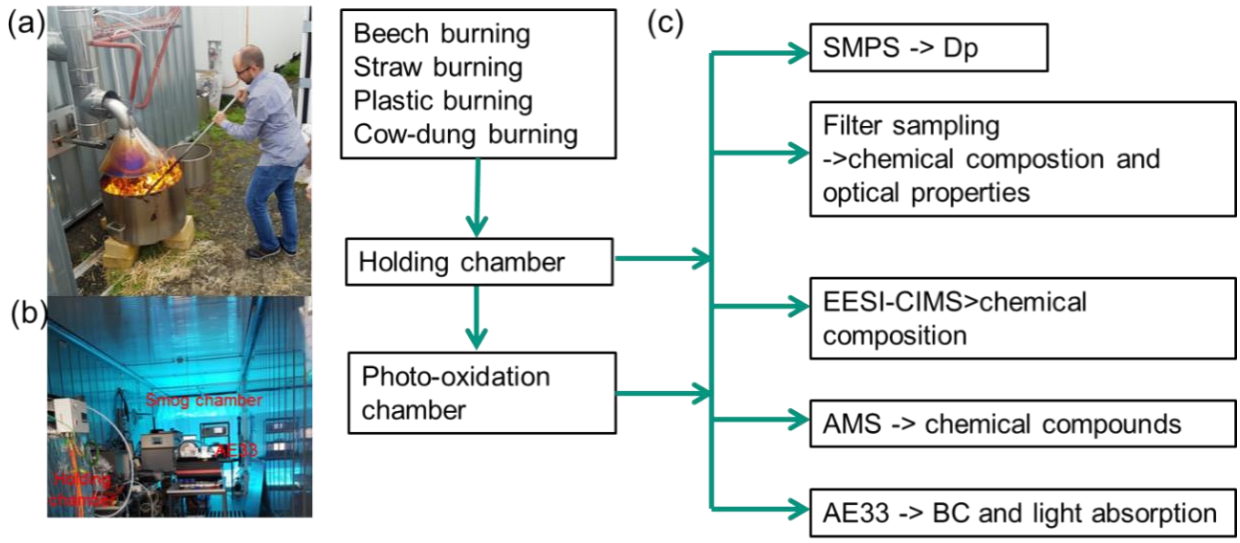

Figure 13. Schematic of the combustion experiment and instrumentations at PSI, Switzerland. (a) An example of straw combustion was controlled by Dr. David Bell. (b) Instrumentations (AE33 and SMPS) and chambers (a holding chamber and a smog chamber) in a container. (c) Setup of the experiments and instrumentations.

Table 4. List of the filter collection and particle types in the PSI combustion campaign.

Fuel types	Aerosol type	Particle types	Quartz filter No.	Teflon filter No.
Straw	Directing emission	Straw POA	1	1
	Photooxidation	straw POA+SOA	2	2
Beech	Directing emission	Beech POA	3	3
	Photooxidation	Beech POA+SOA	4	4
Cow dung	Directing emission	Cow dung POA	5	5
	Photooxidation	Cow dung SOA	6	6
Plastic	Directing emission	Plastic POA	7	7
	Photooxidation	Plastic SOA	8	8

2.3 Field campaigns at urban and rural sites

To investigate the chemical compositions and optical properties of brown carbon aerosol, I have participated in four field campaigns at an urban location in downtown Karlsruhe and a rural site 10 km north of Karlsruhe as shown in Figure 14. During the field campaigns at an urban kerbsite in downtown Karlsruhe near Durlacher Tor, I mainly used filters to collect particles and analyzed them by FIGAERO-CIMS and Aqualog in the laboratory. For the measurements at KIT Campus Nord, I mainly used online measurement to characterize chemical composition and optical properties of brown carbon employing the FIGAERO-CIMS and Aethalometer (AE33).

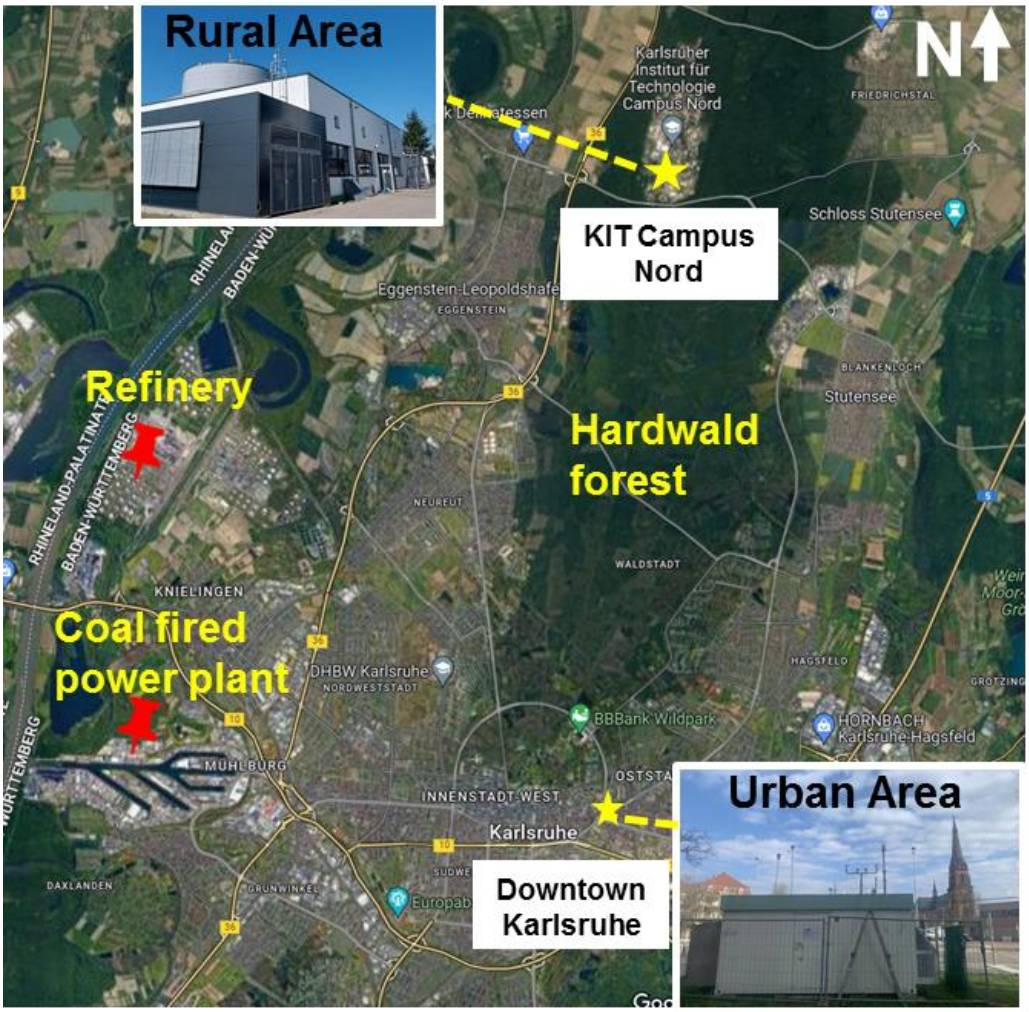

Figure 14. The map of sampling sites for field campaigns at urban kerbsite of Karlsruhe (Durlacher Tor) and rural site in north Karlsruhe (KIT Campus Nord), western Germany. Background map courtesy of © Google Maps.

Field campaigns in city of Karlsruhe during summer and winter: I performed particle and trace gas measurements from 6–26 July 2019 and 26 February–25 March 2020 in downtown

Karlsruhe, Germany (49°00'33.9"N 8°25'02.3"E), a city with a population of about 300 000. The measurement site at the Durlacher Tor is located at a central traffic junction with a three-lane road and a street crossing. Therefore, it can be classified as a typical urban kerbside. As shown in Figure 14, there are also several industrial emission sources within ~10 to 15 km of the measurement site, including a refinery with a capacity of 15.5 Mt yr^{-1} in the southwest and a 1450 MW hard coal-fired power plant in the west (Hagemann et al., 2014). The largest part of the city, including larger residential areas, is located southwest of the measurement site and may be expected to be a source of biomass burning emissions, especially in the heating season. The Hardtwald forest, an area surrounding Karlsruhe, is ~3km to the north and northeast and ~10km southwest of the measurement site. This forest emits biogenic volatile organic compounds, especially in summer. During the two measurement periods in summer and winter, I collected filters to analyze the aerosol particle chemical composition by CIMS and their optical properties by Aqualog. The filter number was shown in Table S1 and Table S2. And the main instruments used are listed in Table 5. To understand the chemical composition and the major chromophore types that contribute to BrC at different seasons at a typical urban environment in western Europe, I combined the aforementioned methods. Firstly, the seasonal variation of optical properties of BrC extracted by methanol were investigated. Secondly, the chromophoric types and sources were identified by excitation-emission spectroscopy and aerosol mass spectrometer measurements. Thirdly, absorption contributions from typical chromophore molecules were estimated, which were detected by chemical ionization mass spectrometry. Correlations of chromophore types and chemical composition will be discussed in section 3. I published some results of these field measurements already: Jiang et al. (2022) "Chromophores and chemical composition of brown carbon characterized at an urban kerbside by excitation-emission spectroscopy and mass spectrometry".

Field campaigns at a rural site 10 km north of Karlsruhe: I also performed particle and trace gas measurements from February 20th–March 16th March 2021 and July 16th to August 16th, 2021 at KIT Campus Nord, a rather rural area in Germany (49°05'43.1"N 8°25'45.6"E). The sampling site is located at the building of the IMK-AAF on KIT Campus Nord. The samples were collected above the roof top about 8 m above ground level via stainless steel tubes and a $PM_{2.5}$ and a TSP inlet as well as FEP tubes for the VOC measurements. The campus is mostly surrounded by the Hardward forest dominated by pine trees. The sampling site is also near some villages e.g. 3–4 km

east of the village “Eggenstein-Leopoldshafen”, 6–7 km northeast of the village “Neureut”, 3–4 km east of the village “Friedrichstal”, and 5–6 km southeast of the village “Linkenheim”. Therefore, there are biomass burning emissions from wood stove combustion in rural residential areas during winter time (Thieringer et al., 2022). Furthermore, the downtown of Karlsruhe is 10 km south of the measurement site including industrial areas with the coal-fired power plants “Rheinhafen” and a refinery “MIRO”. Therefore, the measurement site is affected by different aerosol sources. The main instruments used for the field measurements are listed in Table 5. During these campaigns, I used the FIGAERO-CIMS to measure the oxygenated organic aerosol compounds in the gas and particle phase online. I operated AMS and a series of auxiliary instruments (OPC, SMPS, CPC, AE33) to measure the particle composition, size, number and absorption. Junwei Song operated CHARON-PTR-MS and analyzed the data on VOC concentrations and less oxidized aerosol particle compounds. In this dissertation, the major results from the winter campaign are given in section 3.4. I am preparing a publication about these field measurements Jiang et al., “Light absorption, chemical characterization, and loss pathways of brown carbon molecules in rural Germany”.

Table 5 The Main instruments used for the four field campaigns.

Measured parameter	**Instrument**	**Downtown Karlsruhe Campaigns**		**KIT Campus Nord Campaigns**	
		Summer	**Winter**	**Winter**	**Summer**
Ambient temperature	WS700 (Lufft GmbH)	×	×	×	×
Container temperature	WS700 (Lufft GmbH)	×	×	×	×
Relative humidity	WS700 (Lufft GmbH)	×	×	×	×
Pressure	WS700 (Lufft GmbH)	×	×	×	×
Wind speed	WS700 (Lufft GmbH)	×	×	×	×
Wind direction	WS700 (Lufft GmbH)	×	×	×	×
Precipitation	WS700 (Lufft GmbH)	×	×	×	×
Global radiation	WS700 (Lufft GmbH)	×	×	×	×
O_3	O341M (Environment SA)	×	×	×	×
NO_2	AS32M (Environment SA)	×	×	×	×
Particle optical diameter (0.18-18 µm)	OPC FIDAS200 (Palas GmbH)	×	×	×	×

Black carbon (BC)	AE51 Aethalometer (Aethlabs Inc.)	×	×		×
Black carbon (BC)	MA200 Aethalometer (Aethlabs Inc.)		×	×	×
Black carbon (BC) and brown carbon (BrC)	AE33 Aethalometer (Magee Inc.)			×	×
Particle composition	AMS (Aerodyne Research Inc.)	×	×		×
Light absorption and emission excitation spectroscopy (offline analysis of filters extracts)	Aqualog (Horiba Inc.)	×	×		
Particle-phase oxygenated organic molecules (offline analysis of filters)	FIGAERO-CIMS (Aerodyne Research Inc.)	×	×	×	
Particle-phase oxygenated organic molecules (intermittent online analysis of filters)	FIGAERO-CIMS (Aerodyne Research Inc.)			×	×
Gas phase oxygenated organic molecules (online)	CIMS (Aerodyne Research Inc.)			×	×
VOCs/semi-volatile particles	CHARON-PTR-MS (IONCON Analytik GmbH)			×	×
Profiles of aerosol and/or cloud backscatter	LIDAR (Raymetrics Inc.)			×	
Particle number	CPC (TSI Inc.)	×	×	×	×

2.4 Aerosol density and yield calculation

Effective densities of indole SOA were derived from comparisons of the aerodynamic size distributions from AMS and the mobility size distributions from SMPS (Saathoff et al., 2009). Briefly, the mass distribution vs. vacuum aerodynamic diameter is from AMS. And volume distribution vs. mobility diameter is from SMPS. The density was calculated as:

$$\rho_{eff} = \frac{d_{va}}{d_m}\rho_0 \quad (6)$$

Where $\boldsymbol{\rho}_{\text{eff}}$ is the effective density, d_{va} the vacuum aerodynamic diameter, dm the mobility equivalent diameter and $\boldsymbol{\rho}_0$ is the unit density (DeCarlo et al., 2004)

The SOA yield was calculated as follows:

$$Yield = \frac{\Delta SOA}{\Delta VOC} \quad (7)$$

Where ΔSOA is the SOA mass concentration e.g. measured by SMPS or AMS and ΔVOC is the corresponding VOC concentration consumed as measured by PTR-MS.

2.5 FIGAERO-CIMS calibration

For all compounds detected by FIGAERO-CIMS for which I couldn't do a calibration e.g. because of missing standards, I calculated their potential mass concentration by assuming an average sensitivity of the CIMS of 22 cps/ppt (Lopez-Hilfiker et al., 2016). To determine absolute concentrations of important chromophores like nitroaromatic compounds (NAC), I calibrated the FIGAERO-CIMS for 4-nitrophenol, 4-nitrocatechol, 2-methyl-4-nitrophenol, and 2-methyl-4-nitrocatechol. Each NACs was dissolved into methanol to about 10 ng/μL as a standard NACs solution. Different volumes (1, 2, and 5 μL) of the standard NACs solution were deposited on a PTFE filter using an accurate syringe. The loaded filter was heated by ultra-high purity nitrogen following a thermal desorption and measurement by FIGAERO-iodide-CIMS. The filters were desorbed in the same way as for the field samples. Every concentration of the standard solution was measured three times. The sensitivities for all four compounds were very similar. The average sensitivity factor of the four NACs was 1.7 ± 0.06 (Figure 15).

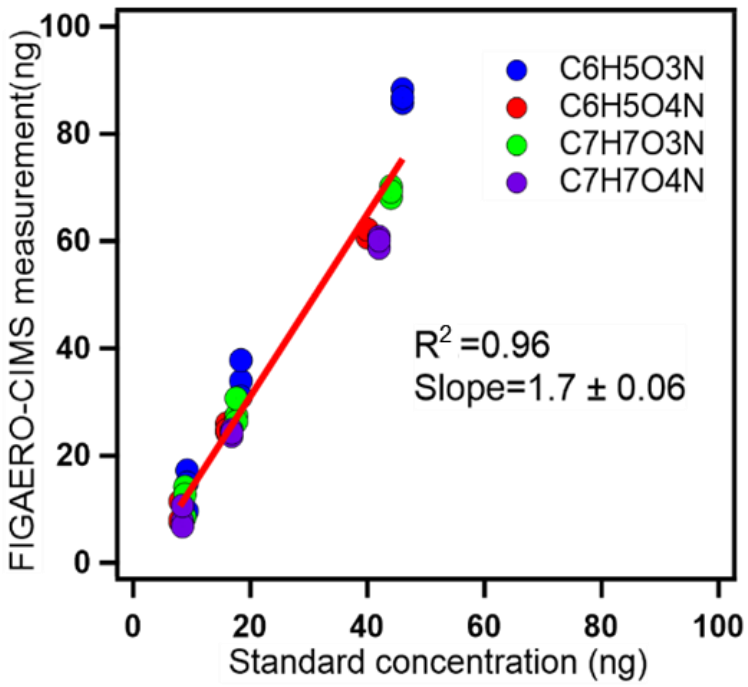

Figure 15. A calibration of FIGAERO-CIMS with NACs. Blue: $C_6H_5O_3N$; Red: $C_6H_5O_4N$; Green: $C_7H_7O_3N$; Purple: $C_7H_7O_4N$.

2.6 Identification of potential brown carbon molecules.

I observed typically about 2000 mass peaks corresponding to different oxygenated organic compounds in particles by using FIGAERO-CIMS. Individual compounds were assigned to the mass peaks by fitting, $C_cH_hO_oN_n$, different numbers of atoms: c carbon, h hydrogen, o oxygen, n nitrogen (Lopez-Hilfiker et al., 2014). Molecules with absorption in the visible should have higher double bond equivalents. A double bond equivalent (DBE) can be calculated as follows (Yassine et al., 2014):

$$DBE = \frac{n-h}{2} + c + 1 \quad (8)$$

Lin et al. (2018) assigned potential brown carbon compounds by plotting of DBE vs. the number of carbon atoms per molecule. They employed high-resolution mass spectrometry to analyze biomass burning organic aerosol. I used this method to find potential BrC molecules, as shown in Fig. S15. After this classification of the potential brown carbon molecules from around 2000 molecules, I calculated their potential mass concentration and mass fraction by assuming an average sensitivity of the CIMS of 22 cps/ppt (Lopez-Hilfiker et al., 2016) and dividing their mass by the total organic aerosol mass measured by AMS.

Modified Aromaticity Index (AI_{mod}) was calculated for each molecular formula according to the formula proposed by Koch and Dittmar (2006) as shown the below equation:

$$AI_{mod} = \frac{1+C-\frac{1}{2}O-S-\frac{1}{2}(N+H)}{C-\frac{1}{2}O-N} \quad (9)$$

The extent of oxidation is expressed in term of the oxidation state of the carbon atom (Kroll et al., 2011) as shown the below equation:

$$OSc = \frac{2O}{C} + \frac{3N}{C} - \frac{H}{C} \quad (10)$$

3. Results and Discussion

The chemical composition, chromophores, and optical properties of brown carbon from combustion emissions are presented in section 3.1. The chemical compositions and optical properties of secondary brown carbon from oxidation of indole and toluene at different conditions are discussed in section 3.2. Optical properties, chromophores, and chemical compositions of brown carbon in urban aerosol from downrown Karlsruhe are shown in section 3.3. In the final results section (3.4) I present optical properties, sources, and loss pathways of brown carbon at a rural site at KIT Campus Nord.

3.1 Primary brown carbon from combustion emissions

In this chapter, I will compare the chemical composition of organic particles directly emitted from combustion of beech wood, straw, plastic, and cow dung (POA) but also formed subsequently in smog chamber oxidation experiments (SOA) (3.1.1). Furthermore, I will compare the chromophores identified in POA and SOA from combustion of the four different fuels (3.1.2), as well as the resulting optical properties of the organic aerosol (3.1.3). These sections are mainly to answer these scientific questions: 1) What are the chemical compositions and optical properties of brown carbon from different combustion sources? 2) What is the evolution of brown carbon aerosol from primary emissions after photooxidation? Detailed information on methods used in combustion emission experiments can be found in section 2.1.2 on PSI smog chamber experiments.

3.1.1 Chemical composition of aerosol particles from combustion emissions

Primary emitted particles (POA) from combustion of beech wood, straw, plastics, and dried cow dung as well as those formed in smog chamber oxidation experiments (SOA) with the primary emissions were collected on Teflon filters as shown in Table 4 and analysed by FIGAERO-CIMS for the oxygenated organic compounds. Average mass spectra for particles formed for these eight cases are presented in Figure 16. The highest signal intensity was observed for levoglucosan ($C_6H_{10}O_5$) accounting for 10%–20% of the total signal intensities from FIGAERO-CIMS. This is consistent with previous studies in which levoglucosan was considered as a typical tracer for biomass burning (Bhattarai et al., 2019). Methyl-butanetricarboxylic acid ($C_8H_{12}O_6$) and glutaric acid ($C_5H_8O_4$) had also an important contribution to the signals of particles with 2%–4% in beech wood, straw, and cow dung POA. Kong et al. (2021) also found that $C_8H_{12}O_6$ and $C_5H_8O_4$ from

biomass burning aerosol had important signals in CIMS measurement. However, these two molecules showed smaller contributions in plastic POA. Interestingly, comparing the combustion products from the four fuels, dimers (m/z including I-:450–550) and trimers (m/z including I-:550–650) were formed mainly from straw, cow dung, and plastic. For example, the dimers ($C_{22}H_{44}O_2$ and $C_{27}H_{54}O_2$) as well as the trimer ($C_{30}H_{60}O_2$ and $C_{30}H_{60}N_2O_2$) showed higher mass contributions in POA from straw-burning. The dimer ($C_{18}H_{32}O_2$) and trimers ($C_{28}H_{56}O_2$ and $C_{29}H_{60}NO$) also showed high contributions to cow dung POA. Nitro-aromatic compounds ($C_7H_7NO_4$, $C_6H_5NO_4$, and $C_8H_9NO_4$) had low mass fraction (0.3%–0.9%) on the burning products from primary emissions and secondary formation. Even though the nitro-aromatic compounds were considered as typical brown carbon molecules in biomass burning, the major burning products were still levoglucosan or methyl-butanetricarboxylic acid.

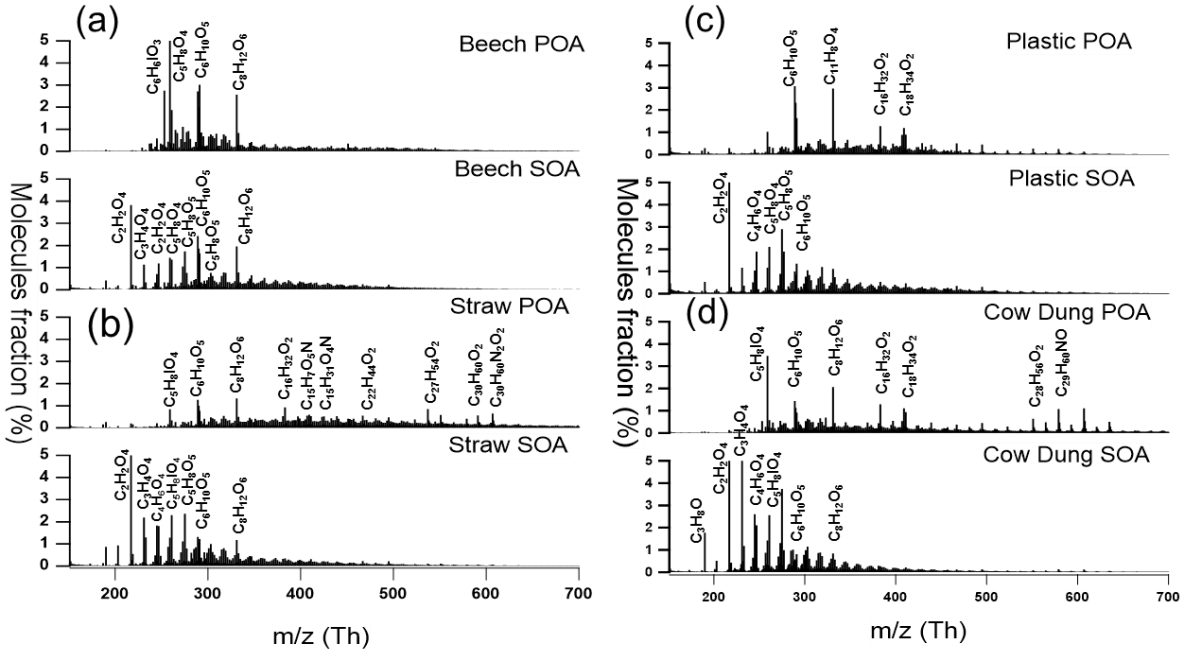

Figure 16. Mass spectra of particles from combustion emission from FIGAERO-CIMS measurement. (a) particles from combustion/oxidation of beech wood; (b) straw; (c) plastics; (d) cow dung. Please note that the signal intensity of $C_6H_{10}O_5$ was multiplied by 0.1. The x axis, mass to charge ratio (m/z), includes mass of iodide ion; m/z 126.9050 Th.

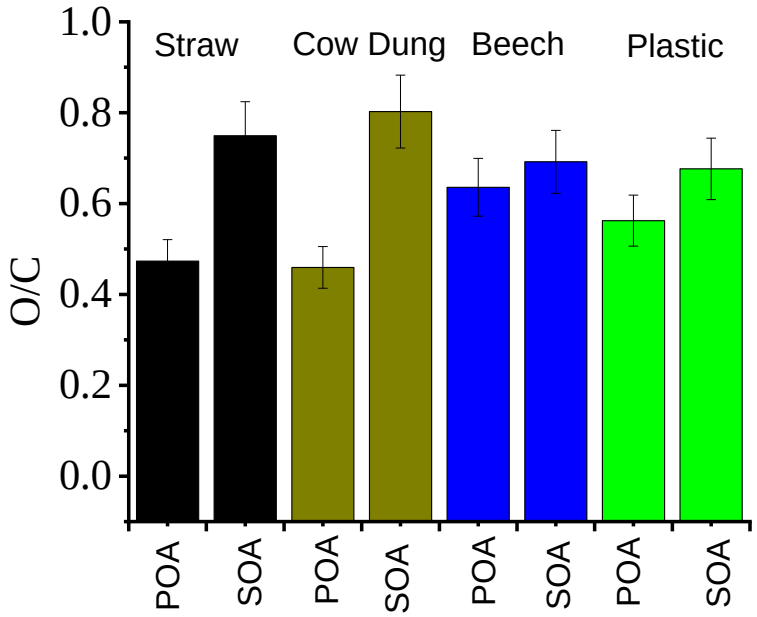

Figure 17. The O/C ratio of POA and SOA from FIGEARO-CIMS measurement (black: straw, brown: cow dung, blue: beech wood, and green: plastic.

Figure 16 shows also the major SOA molecules formed by subsequent oxidation of the primary emissions from burning the four different fuels. The mass fraction of heavier molecules was reduced and lighter more oxidized compounds like organic acids increased. This indicates that after O_3 injecting into the PSI smog chamber and light on, the heavier molecules, e.g. $C_{22}H_{44}O_2$, $C_{27}H_{54}O_2$, and $C_{30}H_{60}N_2O_2$, decomposed and smaller organic acids e.g. $C_2H_2O_4$, $C_3H_4O_4$, and $C_4H_6O_4$ were formed. As shown in Figure 17, after photooxidation of the POA, all O/C ratios increased by between 0.1–0.4 with the largest increases for straw and cow dung. This is consistent with observations by Kodros et al. (2022). They showed that the oxidation of biomass burning aerosol leads to an increase in O/C ratios ranging from 0.09–0.23 (enhancement of 1.2–1.58) after the injection of NO_2 and O_3 for 3 hours. The higher enhancement of O/C ratio in straw and cow dung compared to beech wood and plastic is caused by the higher contributions of heavier compounds with low O/C in straw and cow dung which could be oxdized by photooxidation.

3.1.2 Chromophore identification

I dissolved the filter samples collected for the eight different cases in methanol and measured their absorption and excitation-emission spectra. The filter was listed in Table 4. The methanol extraction and optical properties measurements by Aqualog were discussed in the methodology

section 2.1.3. Then I used the PARAFAC model to investigate the major chromophores in methanol-soluble organic carbon extracted from the biomass-burning aerosol particles (Chen et al., 2020). With this approach, four different characteristic chromophore components were identified and named C1, C2, C3, and C4 hereafter (Figure 18). The peaks of excitation/emission (Ex/Em) values for C1 were below 240 nm and 375 nm. Correlation analysis of PARAFAC components and AMS data was shown that a similar water-soluble chromophore component can be considered as less-oxygenated humic-like substances (Chen et al., 2016). The maximum emission wavelength of C2 ranges above 400 nm. Similar components as C2 were found in water-soluble organic carbon and were considered to consist of highly oxygenated humic-like substances (Yan and Kim, 2017; Chen et al., 2016). The maximum emission wavelength of C3 and C4 was less than 350 nm. It was located at the protein-like region which contains phenol and naphthalene compounds (Jiang et al., 2022), since the peaks of shorter excitation wavelength (<250 nm) and shorter emission wavelength (<350 nm) were associated with aromatic proteins like tyrosine (Cory and McKnight, 2005). Jiang et al. (2022) found that phenol- and naphthalene-like components had a good correlation (r = 0.7) with phenol, which most likely originates from biomass burning and fossil fuel combustion. Compared with the significant similarity of the characteristic spectra identified using the PARAFAC model with literature data, C1 was a less-oxygenated HULIS (LO-HULIS) component; C2 was a highly oxygenated HULIS (HO-HULIS) component; C3 was a protein/phenol-like substance (PLS) component; C4 was a second PLS component.

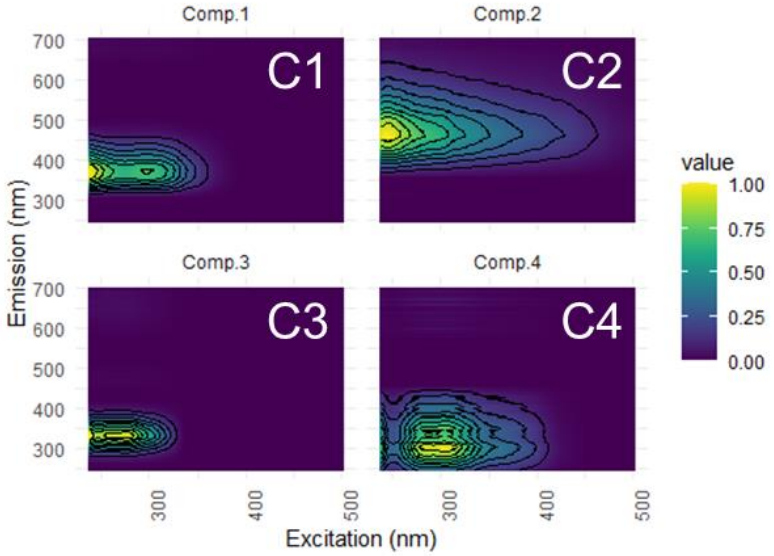

Figure 18. Relative contribution of four different components identified by the PARAFAC model analysis to total fluorescence for a methanol extract of particles from combustion of beech wood, straw, cow dung, and plastic.

Figure 19 shows that there were different relative contributions of chromophore components from burning the four different fuels. The LO-HULIS component (C1) has a relatively high contribution of (42% ± 7%) in biomass-burning POA. The LO-HULIS component was also identified as chromophore in brown carbon from biomass burning (straw, pinewood, and corn straw) with about 15%–25% (Fan et al., 2020). The relative contribution of C1 was with 54% ± 7% higher for beech wood than for the other three fuels with all nearly 40%. However, compared to LO-HULIS, the HO-HULIS component C2 in four different fuels shows only lower contributions to fluorescence with 15% ± 8%. This is in contrast to findings by Jiang et al. (2022) who found that the HO-HULIS components dominated (96 ± 6) % in summer and had much less but still substantial contributions of (31 ± 8) % in winter, both for urban aerosol. However, the findings of this study somewhat agree with the HO-HULIS component fraction of about 10% of brown carbon POA from pinewood burning (Fan et al., 2020). In contrast to C2, the relative contribution of the PLS-1 component C3 in four different fuels was higher with 42% ± 10% which has an important contribution to the chromophore. This is consistent with a previous study where a similar component dominated the fluorescence in biomass-burning aerosol with about 35%–45% (Fan et al., 2020). The protein/phenol-like substance component (PLS-2, C4) shows only minor contributions with (1 ± 0.6) % in POA for all four burned substances.

Variations of the relative chromophore contributions for the oxidized primary emissions (SOA) of the four fuels are displayed in Figure 19 as well. After aging with ozone and OH radicals, the relative contribution of C3 (PLS-1) significantly decreased, from 56% to 7% for plastic, from 33% to 6% for straw, from 53% to 10% for beech wood, and from 45% to 19% for cow dung. These findings suggest that the protein/phenol-like component is easily susceptible to photooxidation. The component C2 exhibits a significant increase with photooxidation from 5% to 45% for plastic, from 23% to 34% for straw, from 12% to 31% for beech wood, and from 8% to 19% for cow dung. Overall, after photo-oxidized aging of the primary BrC aerosol, PLS chromophore decreased from 47% to 11% and the highly oxygenated humic-like chromophore (HO-HULIS) increased from 12% to 32%. This indicates that the HO-HULIS was generated by further oxidation reactions and accompanied by the decomposition of PLS. In comparison, the LO-HULIS (C1) also moderately increased, especially, from 35% to 57% for straw. Taken together, the relative contributions of humic-like fluorophores (LO-HULIS and HO-HULIS) accounted for 77%–91% of the aged combustion BrC (SOA), which is much higher than the range of 44%–55%

observed for the primary samples (POA). Consistently, after photooxidation, the heavier molecules were oxidized and lighter organic acids were formed either by fragmentation or oxidation of remaining gas-phase components (Figure 16). Correspondingly, the O/C ratio increased with an enhancement of 0.1–0.4 (Figure 17). Compared with previous studies, the O_3 oxidation of oxyaromatics could produce polyhydroxylated aromatics (Fan et al., 2020). Fan et al. (2020) also found that a similar as C3 (PLS-1) component was predominantly decomposed by O_3 aging, while the relative fraction of highly oxygenated humic-like components significantly increased.

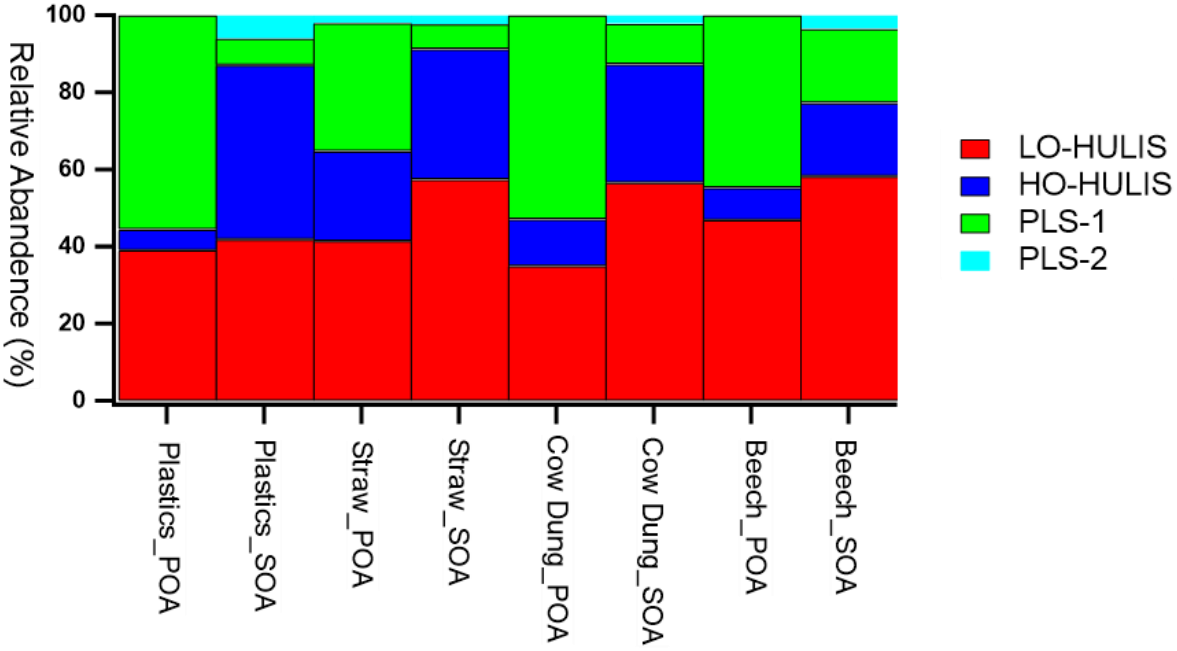

Figure 19. Relative contribution of the four chromophore components identified by PARAFAC model analysis to total fluorescence. Comparison of relative contributions from POA and SOA from combustion of the four different fuels.

3.1.3 Optical properties of combustion aerosol

Figure 20 shows the mass absorption coefficients (MAC) of methanol extracts of aerosol particles formed by burning the four different fuels and their subsequent aging in presence of ozone. The filter was listed in Table 4. The methanol extraction and optical properties measurements by Aqualog were discussed in the methodology section 2.1.3. The MAC decreased in the following order from POA form plastics to straw, to beech wood and cow dung. Aging in presence of ozone and OH radicals lead to a strong decrease of the MAC especially for SOA from plastics and beech wood and especially in the UV. By photooxidation, the MAC_{250}/MAC_{365} ratios significantly decreased from 7.6 to 5.3 for straw, from 6.9 to 5.2 for beech, from 7.6 to 5.7 for cow dung, and from 9.0 to 3.5 for plastic, respectively. Furthermore, after photooxidation, more lighter organic

acids were present which may be formed by gas phase oxidation and gas to particle partitioning as well as fragmentation of POA compounds (Figure 16). In addition, the Angström absorption exponent $AAE_{300–400}$ decreased from 6.8 to 5.2 for straw, from 7.8 to 6.1 for beech wood, from 7.5 to 5.5 for cow dung, and from 7.9 to 3.8 for plastic, respectively, by photooxidation. It indicates that after photooxidation, the absorption of brown carbon decreased. Consistently, Fan et al. (2020) found that the UV absorption values gradually declined, especially during the first hours of aging, implying a significant decrease in aromatic fraction during O_3 aging.

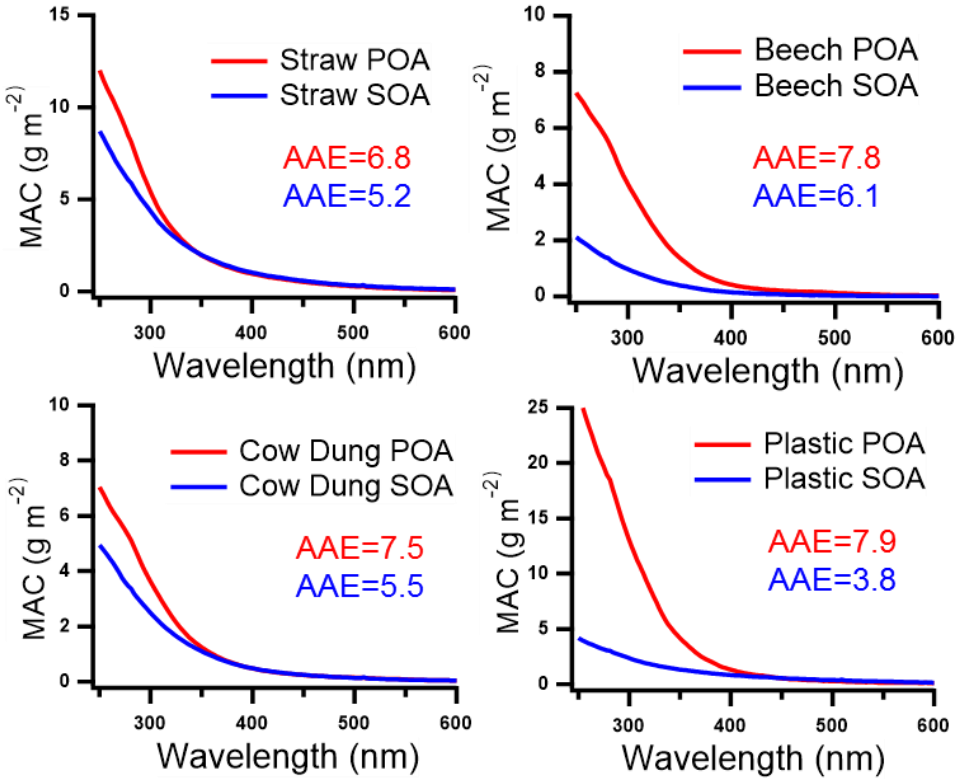

Figure 20. Mass absorption coefficients (MAC) of methanol-soluble brown carbon in fresh (POA) and aged (SOA) aerosol particles from combustion of straw, beech wood, cow dung, and plastic. Red: POA, blue: SOA. Angström absorption exponents (AAE) reported in this work are calculated for a wavelength range of 300–450 nm.

3.1.4 Summary

The chemical composition and the corresponding optical properties of aerosol particles from combustion of straw, beech wood, plastic, and cow dung and their subsequent aging by oidation with ozone were comprehensively characterized using mass spectrometry (FIGAERO-CIMS) and excitation emission spectroscopy (Aqualog) as well as a series of supplementary instruments.

Nitro-aromatic compounds ($C_7H_7NO_4$, $C_6H_5NO_4$, and $C_8H_9NO_4$) had lower mass fractions of 0.3%–0.9% in primary and secondary organic aerosol. Humic-like substances (LO-HULIS) and protein/phenol-like substances (PLS) dominates fluorescence intensities of BrC from primary emission with 42% ± 7% and 42% ± 10%, respectively. After aging of the primary BrC aerosol by photooxidation, PLS chromophores decreased and the highly oxygenated humic-like chromophore (HO-HULIS) increased. In addition, after photooxidation, the heavier molecules e.g. dimers (m/z 450–550) and trimers (m/z 550–650) were less abundant partially due to fragmentation but also due to gas to particle partitioning of lighter molecules formed by oxidation reactions in the gas phase e.g. $C_2H_2O_4$ and $C_3H_4O_4$. In addition, the O/C ratio increased by 0.1–0.4. Aging of the primary combustion emissions in presence of ozone and OH radicals lead to an increasing O/C ratio and a larger fraction of smaller organic acids.Furthermore, by photooxidation, the fraction of protein/phenol-like components decreased and that of highly-oxygenated humic-like substance increased, the MAC decrease especially in the UV with corresponding decreasing AAEs shown as Table 6.

Table 6: Comparison of typical mass absorption coefficients at 300 nm and Angstrom absorption exponents from 300 to 400 nm of fresh and aged BrC from flaming combustion of four different fuels.

Fuel	MAC (fresh) ($m^2\ g^{-1}$)	MAC (aged) ($m^2\ g^{-1}$)	AAE (fresh)	AAE (aged)
Straw	5.5 ± 1.6	4.4 ± 1.3	6.8	5.2
Beech wood	4.1 ± 1.2	1.0 ± 0.3	7.8	6.1
Plastic	13.3 ± 4.0	2.4 ± 0.7	7.9	3.8
Cow dung	3.7 ± 1.1	2.5 ± 0.8	7.5	5.5

3.2 Secondary brown carbon from oxidation of toluene and indole

In this chapter, I present the yields and chemical composition of toluene secondary organic aerosol as a function of temperature (3.2.1), optical properties and chromophores of toluene secondary organic aerosol (3.2.2), yields and chemical composition of indole secondary organic aerosol (3.2.3), and optical properties and chromophores of indole secondary organic aerosol (3.2.4). These sections are mainly to answer these scientific questions: 1) What are the chemical compositions and optical properties of brown carbon from the oxidation of major VOCs? 2) What is the link between chemical composition and optical properties of brown carbon aerosol? 3) How do the presence of NO_2, temperatures, and seed particles affect formation and optical properties of secondary brown carbon aerosol? Detailed information on methods used in AIDA simulation chamber experiments can be found in section 2.1.1.

3.2.1 Chemical composition and yields of toluene SOA

Figure 21 presents yields and densities of toluene SOA (*tol*-SOA) formed at four different temperatures (313 K, 293 K, 273 K, and 253 K) in presence of 80 ppb of NO_2. The experimental steps are described in section 2.1.1 with temperatures covering the main regions of the troposphere. The yield of *tol*-SOA was 1.01 ± 0.01 at the lowest temperature (253 K), followed by 0.56 ± 0.06 at 273 K and 0.19 ± 0.02 at 293 K, while the lowest yield of 0.08 ± 0.01 was measured at the highest temperature of 313 K (Figure 21a). Liu et al. (2021b) found that the SOA yield increased from 28.1% in the absence of NH_3 to 34.7% in the presence of NH_3 but decreased to 19.5% in the presence of NOx. Hinks et al. (2018) found that higher relative humidity reduced the *tol*-SOA yields. Hildebrandt et al. (2009) found that the yields of *tol*-SOA were increased from 0.12 to 0.66 with decreasing NOx concertation from 1300ppb to <5ppb at a total organic mass of 20 µg m^{-3}. Yields of *tol*-SOA were 0.29 at low NOx conditions and 0.19 at high NOx conditions (Ng et al., 2007). Several factors affect *tol*-SOA yields. As shown in (Figure 21b), the yields of *tol*-SOA increased with decreasing temperature as expectable. The β-caryophyllene SOA yields increased from 0.16 ± 0.05 to 0.37 ± 0.11, with temperatures decreasing from 313 K to 243 K at a total organic mass of 10 µg m^{-3} (Gao et al., 2022). A study with a chemistry-transport model found that yields of *tol*-SOA increased from around 0.1 to 0.3 for temperature decreasing from 310 K to 250 K (Svendby et al., 2008). Therefore, the yield of *tol*-SOA has a significant temperature dependence. At lower temperatures, the semivolatile species partition into the particle phase and lead to

increasing the *tol*-SOA yields. As shown in Figure 20c, the density of *tol*-SOA particle decreased from 1.72 ± 0.2 to 1.18 ± 0.1 with increasing temperature from 253 K to 313 K. Consistently, during isoprene photo-oxidation experiments done in the presence of NOx, SOA density is observed to decrease slightly with increasing reaction temperature (Clark et al., 2016). The semivolatile species partitioning into the particle phase at lower reaction temperatures may contribute to a higher particle density.

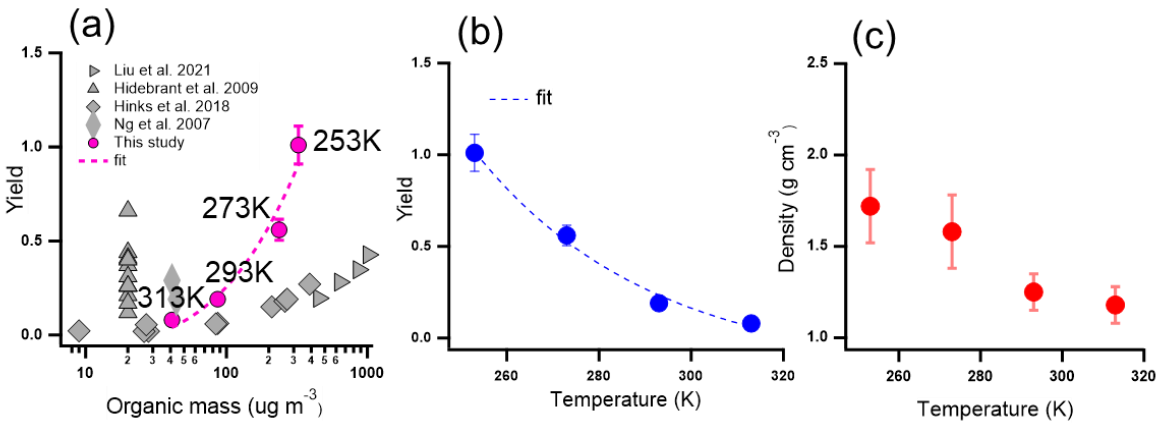

Figure 21. Yields for toluene SOA as a function of organic aerosol particle mass (a) and as a function of temperature density (b) and densities (c)of toluene SOA in at four temperatures (313 K, 293 K, 273 k, 253 k).

Figure 22 shows mass spectra of $C_xH_yO_z$ and $C_xH_yO_zN_n$ containing compounds as fractions of all compounds measured by FIGAERO-CIMS at the four different temperatures: 313, 293, 273, and 253 K. The $C_xH_yO_z$ compounds dominated the *tol*-SOA products with 80%–92% of the total organic mass. The compounds $C_7H_8O_7$, $C_7H_{10}O_7$, $C_7H_{10}O_6$, and $C_7H_8O_5$ are the major products at 313, 293, and 273 K (Figure 22 a, b, and c). They account for 8%–13% of the total ogranic mass concentration estimated from CIMS measurements. In contrast, at the lowest temperature (253 K), the major products significantly changed with major produts being $C_7H_{10}O_6$, $C_7H_{10}O_5$, $C_7H_8O_5$, $C_7H_8O_4$, $C_6H_8O_4$, and $C_5H_6O_4$, accounting for 27% of the total organic mass measured by CIMS (Figure 22d). With the temperature decreasing, the most abundant individual products were $C_7H_8O_7$ at 313 K, $C_7H_8O_5$ at 293 K, $C_7H_8O_5$ at 273 K, and $C_7H_8O_4$ at 253 K. Lower temperatures favor less oxidized products and larger oligomers. Remarkably, the dimer ($C_{16}H_{24}O_6$) appeared in *tol*-SOA products with 0.5%–1% of the total organic mass measured by CIMS. At 273 K and 253 K more dimers were formed in *tol*-SOA. Cheng et al. (2021b) found that $C_7H_8O_6$, $C_7H_{10}O_5$, and $C_7H_{10}O_7$ are major products from oxidation of bicyclic peroxy radicals ($C_7H_9O_5$) in *tol*-SOA. $C_7H_8O_6$ and $C_7H_8O_6$ are the main closed-shell monomers that might be carbonyls that are produced

by the termination of $C_7H_9O_7$ and $C_7H_9O_7$ by reaction with HO_2 or RO_2, respectively (Cheng et al., 2021b). Therefore, the major products are mainly secondary or third formation products from bicyclic peroxy radicals.

The total $C_xH_yO_zN_n$ accounts only for 8%–20% of *tol*-SOA mass concentration. The products, methyl-nitrocatechol ($C_7H_7O_4N$), methyl-nitrophenol ($C_7H_7O_3N$), $C_7H_7O_5N$, and 4-nitrocatechol ($C_6H_5O_4N$) dominated the $C_xH_yO_zN_n$ mass fraction with 8%–10% at 313, 293, and 273 K (Figure 22e, f, and g). $C_7H_9O_8N$ and $C_7H_{11}O_6N$ had important contributions to *tol*-SOA products only at 253 K (Figure 22h). With the temperature decreasing, the most abundance of individual products was methyl-nitrocatechol at 313, 293, and 273 K and methyl-nitrophenol at 253 K. Therefore, also nitrogen-containing products were less oxidized at lower temperatures and showed a higher relative fraction of oligomers. Lin et al. (2015) found that methyl-nitrophenol and methyl-nitrocatechol are important BrC chromophores in *tol*-SOA formed at high NOx concentrations.

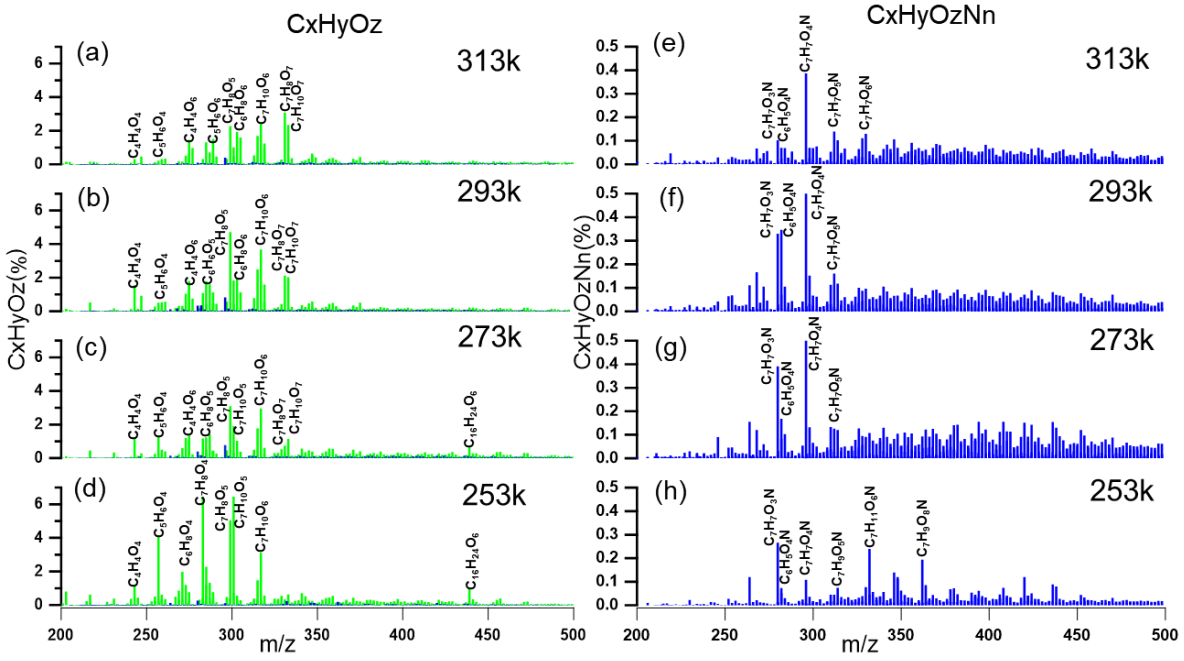

Figure 22. CIMS mass spectra as a relative fraction of particle-phase compounds for the four different temperatures 313 K, 293 K, 273 K, and 253 K. The left panels refer to all $C_xH_yO_z$ molecules and the right panels refer to all $C_xH_yO_zN_n$ molecules.

Figure 23 shows the variation of oxidation state (OSc) and modified aromaticity index (AI_{mod}) as a function of formation temperature of *tol*-SOA. The OSc and AI_{mod} are not linear correlation with temperature. However, the OSc and AI_{mod} were significantly different at 313 K. For example, the OSc was lower at 313 K than in any one (Figure 23a). And the AI_{mod} was higher at 313 K than

for any other experiment (Figure 23b). Therefore, *tol*-SOA products were less oxidized and had higher aromaticity at 313 K compared with the other temperatures.

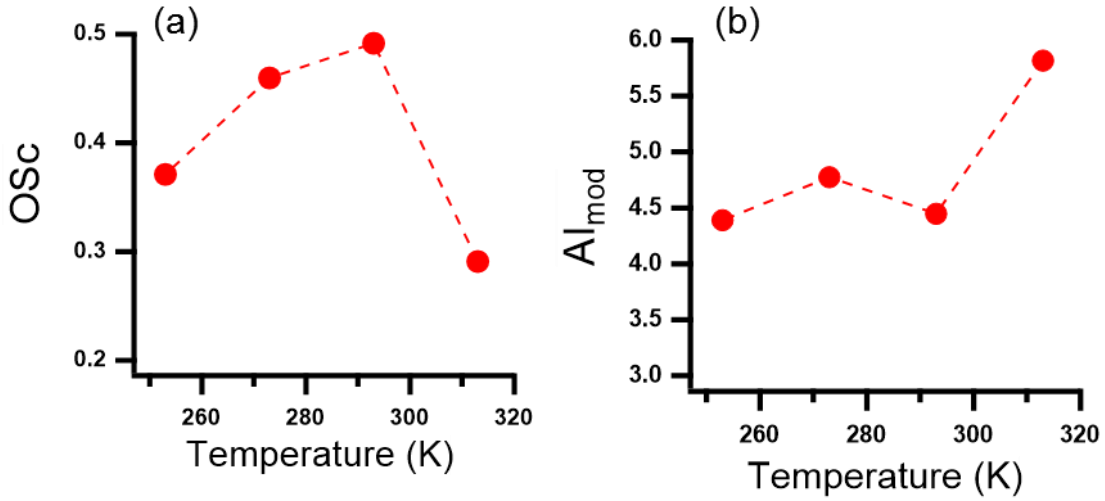

Figure 23. Oxidation state (OSc) (a) and aromaticity index (AI_{mod}) (b) of *tol*-SOA at four different formation temperatures (313 K, 293 K, 273 K, 253 K).

3.2.2 Optical properties of toluene SOA

Figure 24 presents the mass absorption coefficients (MAC) of *tol*-SOA for four different formation temperatures (313, 293, 273, and 253 K). The absorption coefficient at 365 nm (MAC_{365}) was highest with 0.17 $m^2\ g^{-1}$ at 313 K, followed by 0.12 $m^2\ g^{-1}$ at 293 K and 253 K, and lowest value was 0.09 $m^2\ g^{-1}$ at 273 K. Yang et al. (2022) found that average $MAC_{300–700}$ of ethylbenzene SOA at high NOx level was 0.29 $m^2\ g^{-1}$. Lin et al. (2015) found that the MAC_{365} of *tol*-SOA was 0.78 $m^2\ g^{-1}$ under high-NOx conditions (defined here as initial NOx/toluene of 5/1). The MAC of tol-SOA in this study was lower than Lin et al. (2015), since the NOx concentrations in this study were 20 times lower than the previous study. The MAC_{365} had no linear correlation with temperature, but especially in the range between 300 and 370 nm the MAC was higher at 313 K than for the other three temperatures. The highest temperature facilitated *tol*-SOA product formation with higher AI_{mod} and lower OSc and exhibiting higher absorption. Therefore, these lead to increasing *tol*-SOA absorption also at 365 nm.

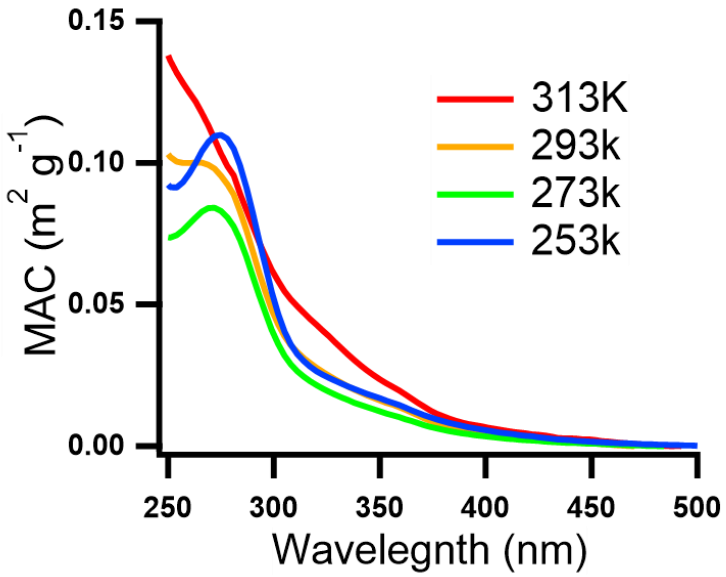

Figure 24. MAC of methanol-soluble BrC in *tol*-SOA at 300–600 nm as measured by Aqualog.

Mean concentrations of toluene were 16 μg m^{-3} in the atmosphere of Balikesir, Turkey, during the winter (Yalcin et al., 2020). This is a relatively typical concentration for urban areas (USEPS, 1988). To estimate the potential contribution of *tol*-SOA to average SOA absorption in the atmosphere, I used the following simplified approach as follow:

$$Abs_{SOA} = VOC \times Y_{SOA} \times MAC \quad (11)$$

Where VOC is the average atmospheric toluene concentration (Yalcin et al., 2020). Y_{SOA} is the *tol*-SOA yield at 293 K condition, MAC was the mass absorption coefficient of *tol*-SOA at 365nm at 293 K condition by Aqualog measurement. Therefore, the potential $Abs_{tol\text{-}SOA}$ can be estimated to 0.6 ± 0.06 Mm^{-1} at 365 nm which is a similar level as light absorption (0.5 ± 0.1 Mm^{-1} at 370 nm) of brown carbon observed in the ambient atmosphere in Waldstein (Teich et al., 2017). Therefore, SOA from toluene in regions with NOx, can have a significant impact on aerosol absorption, visibility, and climate.

3.2.3 Chemical composition and yields of indole SOA

Figure 25 presents yields and densities of indole (*ind*) SOA measured in four different experiments: REF (indole oxidation), AS (indole oxidation in presence of seed particles), AS-NO_2 (indole oxidation in presence of seed particles and NO_2), and NO_2 (indole oxidation in presence of NO_2). The experiment steps were shown in section 2.1.1. The yield of *ind*-SOA recorded in the

REF experiment was highest with 0.5 ± 0.1, while the lowest yield of 0.13 ± 0.02 was detected in the NO_2 experiment (Figure S2). These observations are consistent with previously reported yields of SOA from oxidation of aromatic volatile organic compounds (AVOCs), which tend to show lower yield values in the presence of NOx. (NO_2 and NO) (Liu et al., 2021b; Yang et al., 2022) The AVOCs oxidation products, organic peroxyl radicals (RO_2), mainly react with hydroperoxyl radicals (HO_2) at low-NOx conditions to form oxygenated low volatility species which readily partition into particle phase, providing growth of the SOA mass (Ng et al., 2007; Xu et al., 2014). In the presence of NO_2, gas-phase RO_2 intermediates react with NO_2 to produce fragmented products with higher volatility. The volatile fragmented products remain in the gas phase, and therefore, inhibit the *ind*-SOA formation. Notably, the yield of *ind*-SOA in the absence of NOx was reported 1.3 ± 0.3 in a previous study, using a higher initial indole concentration (200 ppb) (Montoya-Aguilera et al., 2017). In that study, formation of lower volatility oligomers was facilitated by higher VOC concentrations, resulting in greater partitioning into particle phase and higher yield values. The highest density of *ind*-SOA in our study was determined as 1.3 ± 0.3 g m^{-3} in the AS-NO_2 experiment; while the lowest density of 0.8 ± 0.2 g m^{-3} was observed for the REF experiment. This suggests that the heavier products were preferentially formed in *ind*-SOA at conditions of the AS-NO_2 experiment. Similarly, Ng et al. (2007) found that the effective density of m-xylene SOA in the presence of high-NOx and AS seed particles was 1.5 g cm^{-3}, significantly higher than the value of 1.3 g cm^{-3} determined for low-NOx conditions.

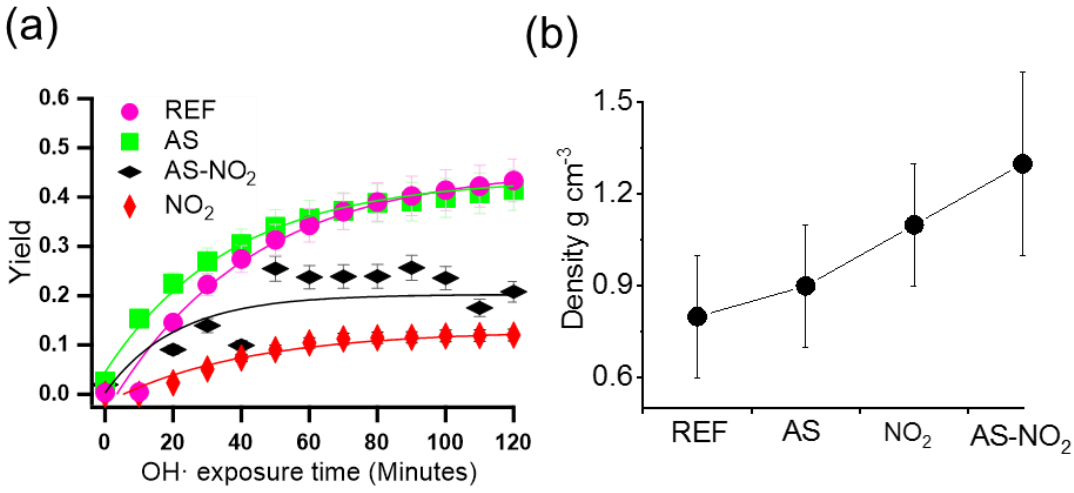

Figure 25. Evolution (a) of indole SOA yield with OH radical oxidation time and density (b) of indole SOA. REF (pink), AS (green), AS-NO_2 (black) and NO_2 (red).

Figure 26 presents the FIGAERO-CIMS mass spectra, O/C ratios, and fractions of $C_xH_yO_zN_{1-2}$ intensities for *ind*-SOA generated in the REF, AS, NO_2, and AS-NO_2 experiments. In the REF and AS experiments (Figure 26a and b), $C_8H_7O_4N$ appears as the major product, accounting for ~10% of the total organic mass (OM) concentration estimated from CIMS measurements. The second abundant product in the same mixtures is $C_8H_7O_3N$, which contributes to 6%–8% of OM. $C_8H_5O_3N$ is the third abundant product with accounting for 5%–6 of all $C_xH_yO_zN_{1-2}$. However, the *ind*-SOA products are significantly different in presence of NO_2 and AS-NO_2 experiments (Figure 26c and d). $C_8H_5O_3N$ is the third abundant product with accounting for 5%–6 of total OM. In the NO_2 experiment (Figure 26c), the first abundant product is still $C_8H_7O_4N$ with accounting for 16% of total OM. Interestingly, a new product, not appearing in the REF and AS experiments, is $C_8H_6O_2N_2$ (3-nitroindole) which accounts for 7% of total OM. In the AS-NO_2 experiment (Figure 26d). Remarkably, 3-nitroindole significantly dominates indole SOA products with 76%. Consistently, the 3-nitroindole has the highest cumulative intensity with 1×10^9 measured by UPLC-PDA-MS (Figure 27e). Furthermore, a dimer product, $C_{16}H_{12}O_4N_4$, accounts for 3.4% of total OM. Consistently, high intensities of fragments ($C_{13}H_6^+$, $C_5H_6NO_3^+$, $C_7H_5^+$, C_6H_4+, and C_5H_3+, etc.) of larger compounds like 3-nitroindole or $C_{16}H_{12}O_4N_4$ were measured by AMS (Figure S3). Due to the high mass contribution from 3-nitroindole and $C_{16}H_{12}O_4N_4$, *tol*-SOA has lower O/C ratios and higher mass fractions from nitrogen-containing molecules in the AS-NO_2 experiment. Please note that the concentrations of VOC and oxidants in my experiments were more comparable with atmospheric conditions, which are remarkably different from all previous studies with indole (Montoya-Aguilera et al., 2017). To compare our experiments to Montoya-Aguilera et al. (2017) studies, they found that $C_8H_7O_3N$ and $C_8H_5O_3N$ were the first and second abundant products in *ind*-SOA measured by LC-MS. 3-nitroindole was also identified but with a low fraction (Montoya-Aguilera et al., 2017). The different abundance compared to my results may be caused by different experimental conditions and measurement techniques. In addition, low mass fractions of dimers and trimers in my study were not consistent with the previous report (Montoya-Aguilera et al., 2017). They used ten times higher initial concentrations of indole (200 ppb) leading to the formation of larger fractions of dimers and trimers. In a computational study, Xue et al. (2022) predicted that $C_8H_7O_2N$ (N-(2-formylphenyl)formamide) should be an important product from OH radical oxidation of indole using a computational study. This molecule only accounts for 0.01%–

0.2% of the organic mass in particle phase, but a high mass fraction (0.1%–3%) in the gas phase measured by FIGAERO-CIMS.

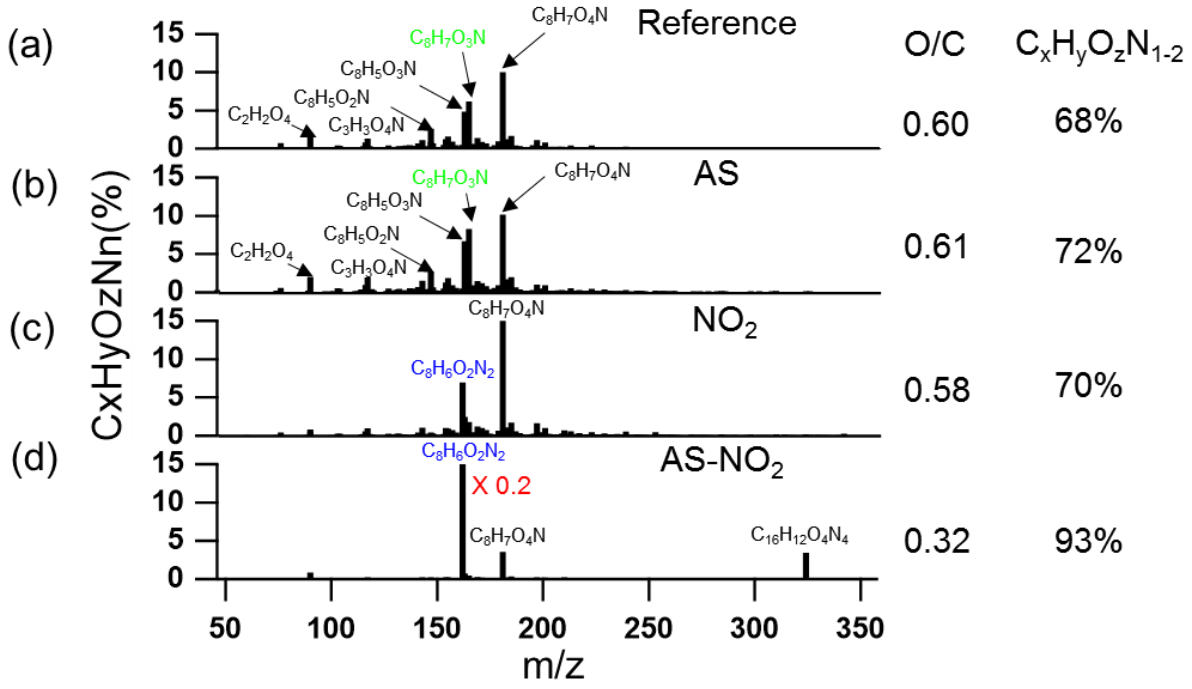

Figure 26. CIMS mass spectra of particle-phase indole SOA (products generated in the REF, AS, NO_2, and AS-NO_2 experiments). The CI source employs reactions of I- ions, which convert analyte molecules into [M+I]- ions, Legends above MS features correspond to neutral molecules. The blue and green legends indicate the most abundant features of $C_8H_6O_2N_2$ and $C_8H_7O_3N$. The mass fraction of $C_8H_6O_2N_2$ was multiplied by 0.2 since the fraction was too high. The O/C ratios were calculated based on the intensity-weighted sum of all compounds. The Y-axis scale shows the fraction of $C_xH_yO_zN_{1-2}$ of the total ion intensities.

The UPLC-PDA-ESI/HRMS results were used to identify the individual BrC chromophore in the *ind*-SOA samples and assess their contributions to the overall light-absorbing properties of *ind*-SOA formed in the four different experiments of our study. Figure 27 summarizes the BrC molecular characterization results observed for the NO_2 and AS-NO_2 experiments, while those for the REF and AS experiments are included in the supplemental information (Figure S4 and Figure S5). In the *ind*-SOA sample from the NO_2 experiment, the abundant $C_8H_7NO_3$ product shows strong UV-vis feature absorbing in the range of 250–350 nm with ~5×10^4 μAU signal intensity (Figure 27a). This $C_8H_7NO_3$ product has been also detected as a high intensity $[M-H]^-$ ion (Figure 27b), consistent with the FIGAERO-CIMS measurements discussed above. Remarkably, this individual $C_8H_7NO_3$ chromophore account for 20–35% of overall BrC absorption by the *ind*-SOA generated in the REF, AS, and NO_2 experiments (Figure 27c, S6c, and S7c), while its contribution is less prominent in the AS-NO_2 case. The latter is heavily influenced by the different $C_8H_6N_2O_2$

chromophore with strong absorption band in 300–400 nm detected with 5.5~×10^4 μAU signal intensity (Figure 27d). In this case, contribution of the individual $C_8H_6N_2O_2$ chromophore is even higher, it accounts for ~50% of the total BrC absorption (Figure 27f). Consistent with the FIGAERO-CIMS measurement, $C_8H_6N_2O_2$ product was detected as the very abundant [M-H]- ion with intensity approximately two orders of magnitude higher than all other components present in the mixture (Figure 27e). It follows that presence of both NO_2 and seed particles has effects on the formation of 3-nitroindole product, responsible for the BrC absorption in *ind*-SOA.

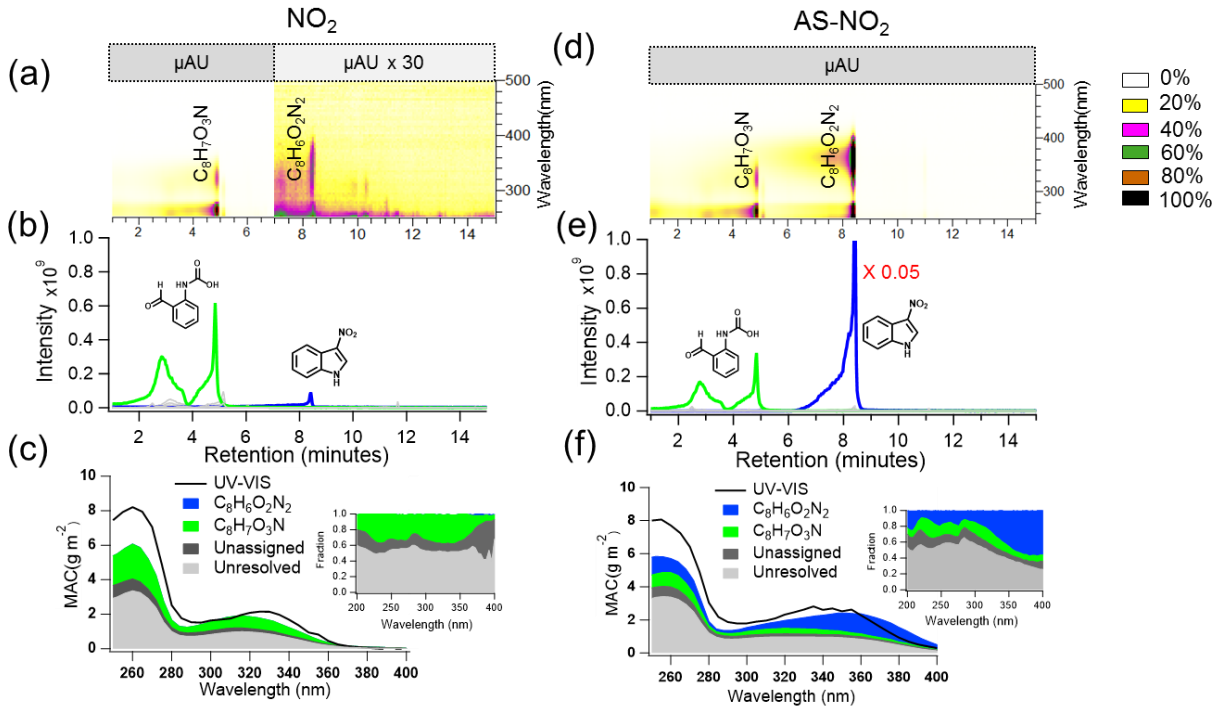

Figure 27. Molecular characteristics of individual components identified in the indole SOA at NO_2 (left panels) and AS-NO_2 (right panels). The panels (a, d) are the normalization of UPLC-PDA chromatograms and identified chromophore molecules. The top marker areas of pane (a) are two levels of chromatograms and left one is 30 times lower that the right area. The panels (b, e) show a compilation of the selected extracted ion chromatograms (EICs) and molecular structures of the most abundant peaks. The panels (c, d) show the MAC from UV-visible spectrometer and UPLC-PDA measurement. The UPLC-PDA contained unresolved chromophores (grey), unassigned absorbing chromophores (red), $C_8H_7NO_3$ (green), and $C_8H_6N_2O_2$ (blue).

The observed difference between *ind*-SOA products formed in different experiments allows to elucidate reaction mechanisms behind their formation as summarized in Figure 28. The reaction sequences start by subtraction of a hydrogen atom by either OH radicals or NO_3 radicals, which predominantly takes place in position 3 of the molecules and leads to formation of an indole radical ($C_8H_6N^{\bullet}$). Consistently, the attack of an electrophile at position 3 in indole generates carbocation which does not disturb the aromaticity of benzene ring (Sundberg, 2012). However, the attack of

an electrophile at other positions in the indole would generate a carbocation which would disrupt the aromatic character by delocalizing the positive charge over the benzene ring (Sundberg, 2012). Therefore, the position 3 of indole was preferentially attacked. In absence of NO_2, C_8H_6N radical was added O_2 to form peroxyl radicals ($C_8H_6O_2N^{\bullet}$). Afterwards, the nitrogen-containing ring is opened by subsequent reactions with OH radicals leading to formation of aldehyde ($C_8H_7O_2N$). In agreement with this, $C_8H_7O_2N$ measured by CIMS accounts for 0.2% of total organic mass. The organic mass measured by FIGAERO-CIMS was shown in section of 2.1.2. And $C_8H_7O_2N$ is also an important product from OH radical oxidation of indole predicted by a computational study (Xue et al., 2022). Furthermore, the aldehyde group in $C_8H_7O_2N$ can be further oxidized by OH radicals forming $C_8H_7O_3N$ and $C_8H_7O_4N$ with carboxyl groups. The proposed mechanism is also consistent with the results that the $C_8H_7O_3N$ and $C_8H_7O_4N$ account for a high fraction of total OM measured by CIMS. It is similar with aromatic VOC oxidation by OH radicals where organic acids were formed in low NOx conditions (Montoya-Aguilera et al., 2017; Siemens et al., 2022).

In presence of NO_2, NO_2 can add to the C_8H_6N radical forming directly the 3-nitroindole with accounting for 8% of total OM measured by CIMS. This is similar as observed for OH radical oxidation of toluene (Lin et al., 2015), naphthalene (Siemens et al., 2022), and pyrrole (Mayorga et al., 2022) leading to nitro-aromatic compounds in presence of NO_2. Remarkably, in presence of ammonium sulphate (AS) and NO_2, 3-nitroindole is formed in a much larger quantity and dominates *ind*-SOA products with 76% of all organic mass measured by CIMS. The proposed mechanism is also consistent with the result that 3-nitroindole led to strong light absorption of *ind*-SOA in the AS-NO_2 experiment. Therefore, seed particles and NO_2 seem to have a synergetic effect on 3-nitroindole formation of *ind*-SOA.

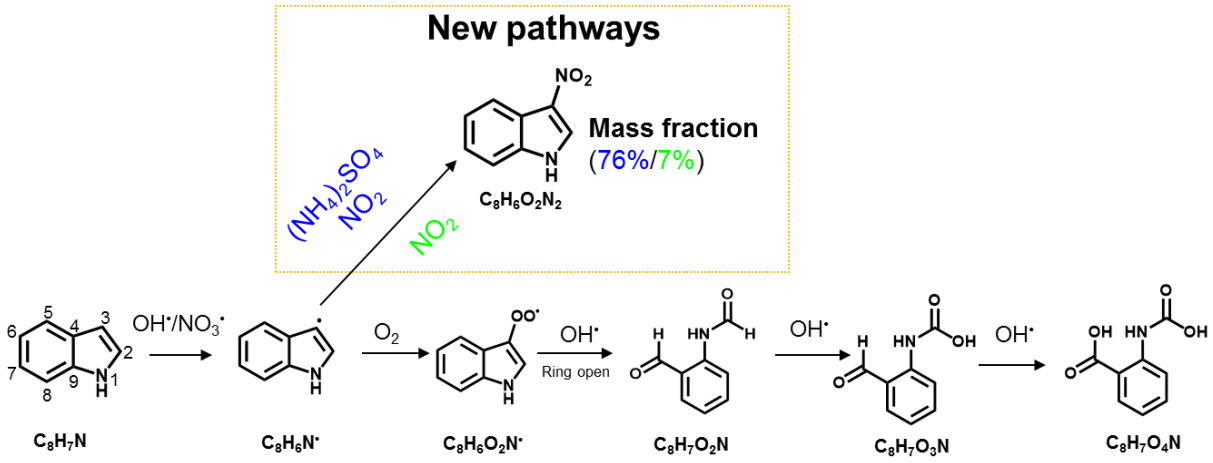

Figure 28. Proposed chemical reaction mechanisms for major products of indole SOA in particle phase and new pathways of indole oxidation in presence of NO_2 and $(NH_4)_2SO_4$ seed particles**.**

3.2.4 Optical properties of indole SOA

As shown in Figure 29a, the indole precursor itself dissolved in methanol is non-absorbing even at shortest visible wavelengths (e.g. 365 nm). However, all *ind*-SOA samples exhibit appreciable values of $MAC_{365nm,\ offline}$ with highest values of 4.3 ± 0.4 $m^2\ g^{-1}$ in the AS-NO_2 experiment, followed by 1.2 ± 0.1 $m^2\ g^{-1}$ in the NO_2 experiment. $MAC_{365nm,\ offline}$ values in the AS and REF experiment are very similar with 0.8 ± 0.1 and 0.7 ± 0.1 $m^2\ g^{-1}$ respectively. Overall, *MAC* values reported here are higher than those published for secondary BrC generated by atmospheric oxidation of other VOC, e.g. 0.29 $m^2\ g^{-1}$ ($MAC_{300–700nm}$) of ethylbenzene SOA formed at high-NOx conditions (Yang et al., 2022), 0.35 $m^2\ g^{-1}$ (MAC_{375nm}) of pyrrole SOA formed by NO_3 radical oxidation, (Mayorga et al., 2022) and 0.01 $m^2\ g^{-1}$ (MAC_{365nm}) of β-pinene SOA. (Yang et al., 2022) Therefore, *ind*-SOA shows a strong BrC absorbing capacity of all known secondary BrC. The highest *MAC* values were detected in the AS-NO_2 experiment, indicating that NO_2 and seed particles may have a synergetic effect on the formation of BrC chromophores and corresponding light-absorption by *ind*-SOA. Liu et al. (2021b) also found that presence of NH_3 and NOx had synergetic effects on the production of BrC chromophores in toluene SOA which were attributed to formation of imidazole and its derivatives. Consistently, $MAC_{405,\ online}$ by PAS measurements in the AS-NO_2 experiment also showed highest values of ~3.5 ± 0.4 $m^2\ g^{-1}$, higher than in the REF (0.6 ± 0.2 $m^2\ g^{-1}$), AS (0.9 ± 0.3 $m^2\ g^{-1}$), and NO_2 (0.4 ± 0.2 $m^2\ g^{-1}$) experiments (Figure 29b). The MAC values in REF, AS, and NO_2 were similar between online-PAS and offline-Aqualog measurements. However, for AS-NO_2 experiments, PAS shows higher MAC values at

405 nm than the methanol extraction. This difference may be caused by the uncertainties of both measurement techniques but may also be caused by an enhancement pf the aerosol particle absorption in a core shell structure as can be demonstrated by corresponding Mie scattering calculations for particles with a core-shell structure.

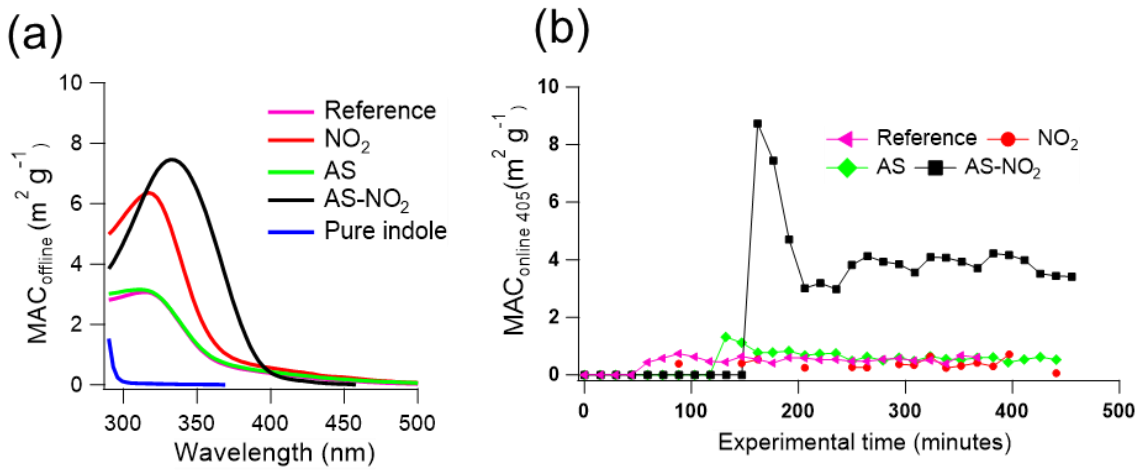

Figure 29. (a): $MAC_{offline}$ of methanol-soluble BrC from *ind*-SOA at 300–600 nm from Aqualog measurements. (b): temporal evolution of $MAC_{405nm,\ online}$ of *ind*-SOA measured by photoacoustic spectrometry (PAS).

Atmospheric indole concentrations were ~1.8 and ~2.6 ppb at daytime and nighttime, respectively during the spring flowering (Gentner et al., 2014). To estimate the potential contribution of *ind*-SOA to average SOA absorption in the atmosphere, I used the following simplified approach as equation (11). Where VOC is the average atmospheric indole (Gentner et al., 2014), Y_{SOA} is the *ind*-SOA yield at AS-NO_2 condition, MAC was the mass absorption coefficient of *ind*-SOA at 405 nm at AS-NO_2 condition by PAS measurement. Therefore, the potential average absorption by *ind*-SOA ($Abs_{ind\text{-}SOA}$) can be estimated to 2.3 ± 0.2 Mm^{-1} and 3.2 ± 0.3 Mm^{-1} at 405 nm at daytime and nighttime, respectively. The $Abs_{ind\text{-}SOA}$ estimated is very similar to total light absorption (1.6 ± 0.5 Mm^{-1} in summer and 2.8 ± 1.9 Mm^{-1} in winter) of brown carbon aerosol observed in downtown Karlsruhe (Jiang et al., 2022). Therefore, SOA from indole in regions with NOx, can have a significant impact on aerosol absorption, visibility, and climate. Detailed transport model calculation would allow to substantiate these findings and to identify potentially susceptible regions.

3.2.5 Summary

Chemical composition and optical properties of *tol*-SOA were investigated at four different temperatures (313 K, 293 K, 273 K, and 253 K) in presence of NO_2 as representatives of different polluted regions in the troposphere. The yields of *tol*-SOA increased with decreasing temperature. At lower temperatures, semi-volatile organic compounds partition into the particle phase and lead to increasing *tol*-SOA yields. Consistently, the density of *tol*-SOA decreased from 1.7 ± 0.2 g cm^{-3} to 1.2 ± 0.1 g cm^{-3} with temperature increasing from 253 K to 313 K. The $C_xH_yO_z$ compounds dominated the *tol*-SOA products with a mass fraction of 80%–92%. The oxidation state of the products was lowest at the 313 K experiment. The most abundance of individual nitrogen containing products were methyl-nitrocatechol ($C_7H_7O_4N$) at 313, 293, and 273 K and methyl-nitrophenol ($C_7H_7O_3N$) at 253 K. Increasing the formation temperature of *tol*-SOA to 313 K leads also to lower oxidation states and higher aromaticity compared with the lower temperatures and consequently the highest MAC_{365} of *tol*-SOA was 0.17 m^2 g^{-1}. Based on yield and optical properties of toluene SOA, the potential $Abs_{tol\text{-}SOA}$ can be estimated to 0.6 ± 0.06 Mm^{-1} at 365 nm.

This work also provides the first data linking formation mechanism, chemical composition, and optical properties of SOA from oxidation of indole with/without NO_2 and seed particles for realistic atmospheric scenarios. $C_8H_7O_4N$, $C_8H_7O_3N$, and 3-nitoindole were identified as major constituents of *ind*-SOA with 3-nitroindole dominating in presence of ammonium sulfate seed particles and NO_2 resulting in also a mass absorption coefficient of 4.3 ± 0.4 m^2g^{-1}, This is among the highest values observed for secondary brown carbon. Based on yield and optical properties of indole SOA, the potential average absorption by *ind*-SOA ($Abs_{ind\text{-}SOA}$) can be estimated to 2.3 ± 0.2 Mm^{-1} and 3.2 ± 0.3 Mm^{-1} at 405 nm at daytime and nighttime, respectively. Therefore, indole has the potential to dominate the aerosol absorption regionally.

3.3 Brown carbon at an urban site in downtown Karlsruhe

In this chapter, I present an overview of field observations in downtown Karlsruhe (3.3.1) and optical properties of methanol-soluble brown carbon (3.3.2). Furthermore, I present chromophore identification (3.3.3) and source of chromophore and organic aerosol (3.3.4). Finally, I present the molecular composition of brown carbon during winter (3.3.5). These sections are mainly to answer these questions: 1) What are the chemical compositions and optical properties of brown carbon from mixed sources in field studies? 2) What is the link between chemical composition and optical properties of brown carbon aerosol? Detailed information on methods used at this field campaign in downtown Karlsruhe can be found in section 2.3.

3.3.1 Overview of the field observations

Figure 30, Figure S7, and Figure S8 give an overview of meteorological parameters, trace gases, and particle concentrations during the campaigns. In the summer 2019 and winter 2020, the major wind directions were northeast and southwest (Figure 30) caused by the channeling of the wind in the Rhine Valley. The average wind speeds were 3.6 ± 1.8 (average ± standard deviation) and 6.6 ± 1.8 m s^{-1}, respectively. Depending on meteorological conditions, local sources and regional transport had an impact on air quality in Karlsruhe (Shen et al., 2019). As shown in Figure S7 and Figure S8, temperature showed diurnal variations with an average of (21.7 ± 6.7) ˚C in summer and (9.5 ± 1.5) ˚C in winter. Furthermore, the temperatures slowly increased from the beginning to the end of both campaigns. The relative humidity (RH) showed diurnal variations in summer with peaks at nighttime. In contrast, the RH had high values before the middle of the campaign in winter due to windy conditions with almost continuous rain. Therefore, general air pollution including $PM_{2.5}$ and black carbon was low before 14 March 2021 because of precipitation scavenging of aerosol particles (Song et al., 2022; Zikova and Zdimal, 2016). NO_2 and O_3 were typically anti-correlated with peaks of NO_2 in the night and peaks of O_3 in the afternoon. The average concentrations of NO_2 and O_3 were higher in summer (18.6 ± 12.5, 66.5 ± 37.2 µgm^{-3}) than in winter (9.6 ± 7.4, 27.3 ± 10.6 µgm^{-3}). Please note that the lower NO_2 concentrations in this winter period may not be typical as this was a relatively windy and rainy period.

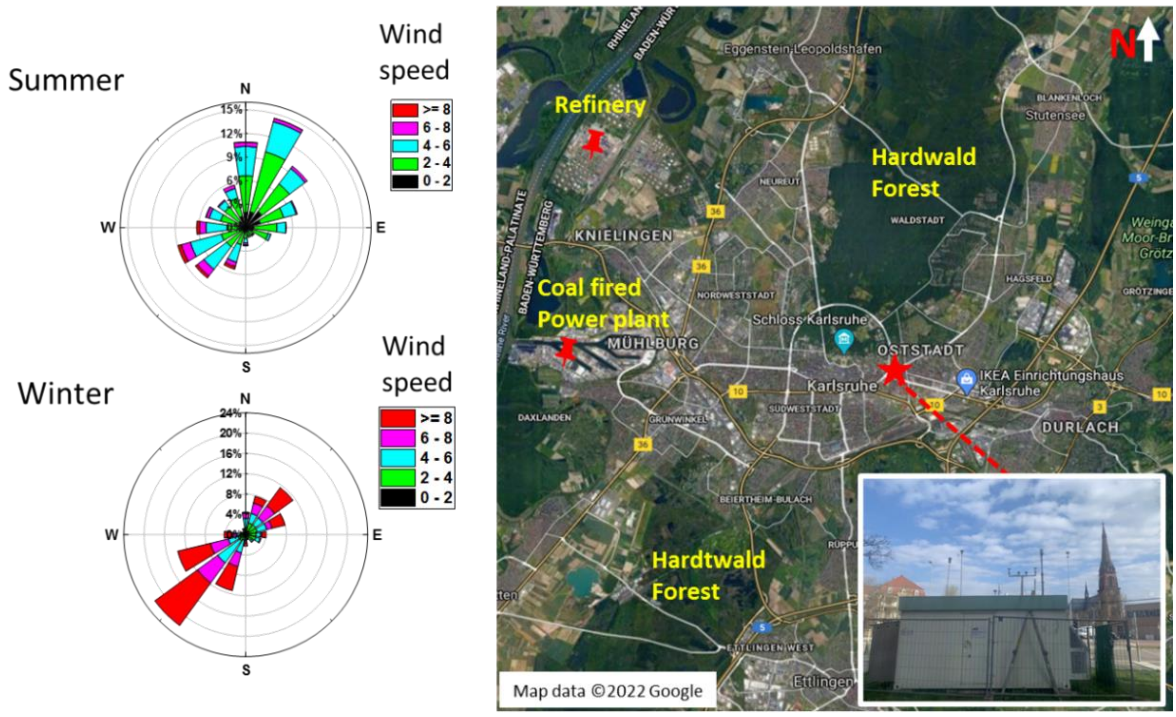

Figure 30. Wind roses (left) pattern, and measurement location map and container picture (right) pattern. Background map courtesy of © Google Maps

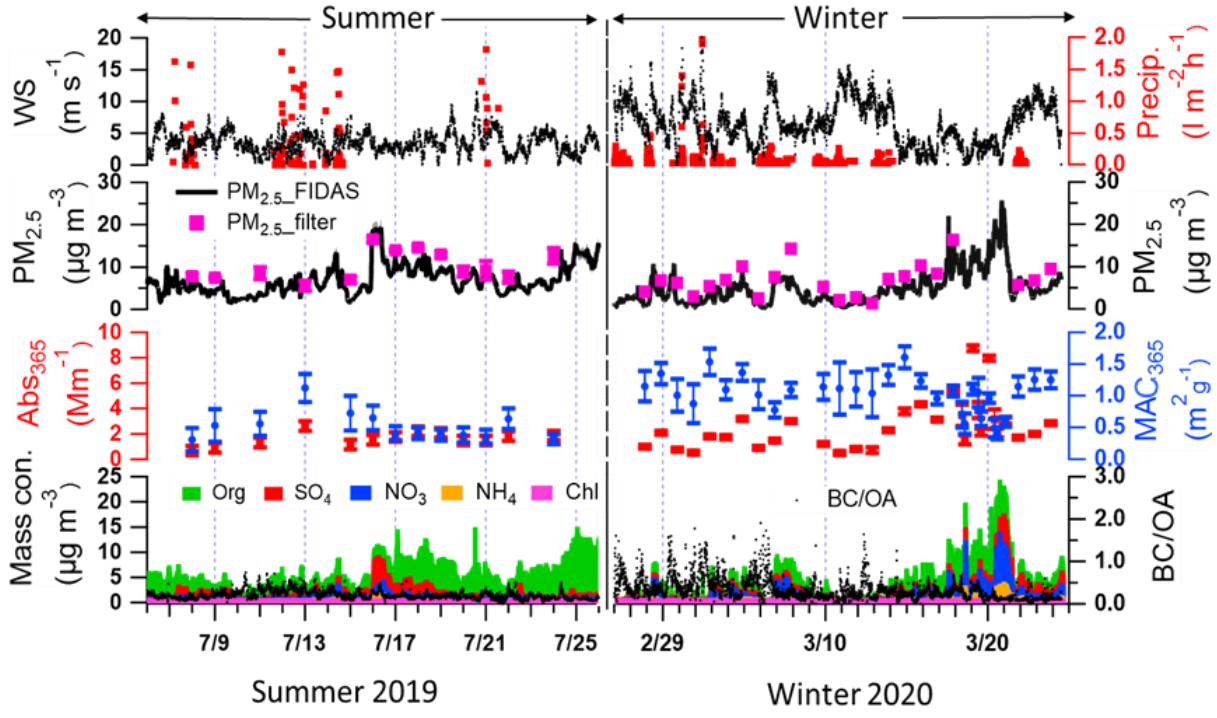

Figure 31. Time series of wind speed, precipitation, $PM_{2.5}$ mass concentrations from FIDAS optical particle sizer and gravimetric analysis of filter samples, optical properties of methanol-soluble aerosol particle compounds (Aqualog),

concentrations of non-refractory aerosol particle compounds (AMS), and ratios of BC/OA in summer 2019 and the following winter.

3.3.2 Optical properties of methanol-soluble brown carbon

Figure 32 shows the time series of wind speeds, precipitations, particle mass concentrations, absorption coefficient, and mass absorption efficiency of methanol-soluble particle components at 365 nm (Abs_{365} and MAC_{365}), non-refractory aerosol particle compounds, and BC-to-OA ratios (BC / OA) in summer and winter at this measurement site. The third panel shows the temporal variation of Abs_{365} and MAC_{365} in summer and winter. The MAC_{365} had higher values (0.6–1.1 $m^2\ g^{-1}$) from 13–16 July 2019 and lower values (0.3–0.4 $m^2\ g^{-1}$) towards the end of the summer period. In contrast, MAC_{365} showed higher values during the whole winter campaign. The MAC_{365} had a relatively good correlation (Pearson's r = 0.4) with the BC/OA ratio (Figure S10), indicating BrC became darker (higher MAC_{365}) with increasing BC/OA ratios (Saleh, 2020). The reason is that a fraction of BrC comprises organic precursors of BC whose conversion to BC was not completed during the combustion process (Saleh, 2020). Furthermore, the average BC/OA ratio in winter was 0.3 ± 0.2 higher than 0.2 ± 0.1 in summer. The average Abs_{365} in Karlsruhe was 2.8 ± 1.9 and 1.6 ± 0.5 M m^{-1} during winter and summer (Table 7). The average Abs_{365} values measured in Karlsruhe during winter were lower compared with European cities like Leipzig, Germany (6.8 ± 3.9 Mm^{-1}), and also rural sites like Melpitz, Germany (6.6 ± 3.5 Mm^{-1}) (Teich et al., 2017), and Magadino, Switzerland (5.6 ± 3.7 Mm^{-1}), but closer to observations in the city of Zurich, Switzerland (2.2 ± 1.6 Mm^{-1}) (Moschos et al., 2018). The main reason for the relatively lower absorption observed during winter in Karlsruhe is the substantial impact of storms and rain during almost half of the winter campaign (Figure 31.). In contrast, the Abs_{365} values in summer show similar values (1–2 M m^{-1}) in measurements at other cities, rural areas, and forest regions in Europe (Moschos et al., 2018; Teich et al., 2017).

Table 7 . Comparison of aerosol particle light absorption, mass absorption efficiency, and absorption Ångström exponent observed in Karlsruhe with other studies.

Sampling sites	Seasons	Abs_{365} (Mm^{-1})	MAE_{365} ($m^2\ g^{-1}$)	$AAE_{300\text{-}450}$	Remarks	References
Melpitz (rural)*, Germany	Summer	1.2 ± 0.3	0.3 ± 0.05	-	The Abs and MAE of BrC at 370 nm; the AAE of BrC in Athen at 470–950 nm	(Teich et al., 2017)
Melpitz (rural)*, Germany	Winter	6.6 ± 3.5	1.4 ± 0.5	-		(Teich et al., 2017)
Leipizig (urban)*, Germany	Winter	6.8 ± 3.9	1.5 ± 0.3	-		(Teich et al., 2017)
Waldstein (forest)*, Germany	Summer	0.9 ± 0.1	0.3 ± 0.03	-		(Teich et al., 2017)
Magadino (rural)**, Switzerland	Winter	5.6 ± 3.7	0.9	3.8	The Abs and MAE of BrC at 365 nm; the AAE of BrC at 300–400 nm	(Moschos et al., 2018)
Zurich (urban)**, Switzerland	Summer	1.0 ± 0.7	0.3	5.1		(Moschos et al., 2018)
Zurich (urban)**, Switzerland	Winter	2.2 ± 1.6	0.9	4.5		(Moschos et al., 2018)
Karlsruhe (urban), Germany	Autumn	-	12.9 ± 2.8	2.6 ± 0.8	The MAE of refractory black carbon (rBC) at 445 nm; the AAE of rBC at 445–532 nm	(Linke et al., 2016)
Karlsruhe# (urban), Germany	Summer	1.6 ± 0.5	0.5 ± 0.2	5.6 ± 1.5	The Abs and MAE of BrC at 365 nm; the AAE of BrC at 300-400 nm	This study
Karlsruhe# (urban), Germany	Winter	2.8 ± 1.9	1.1 ± 0.3	4.7 ± 0.4		This study

*: alkaline solvent extraction; **: water extraction; #: methanol extraction

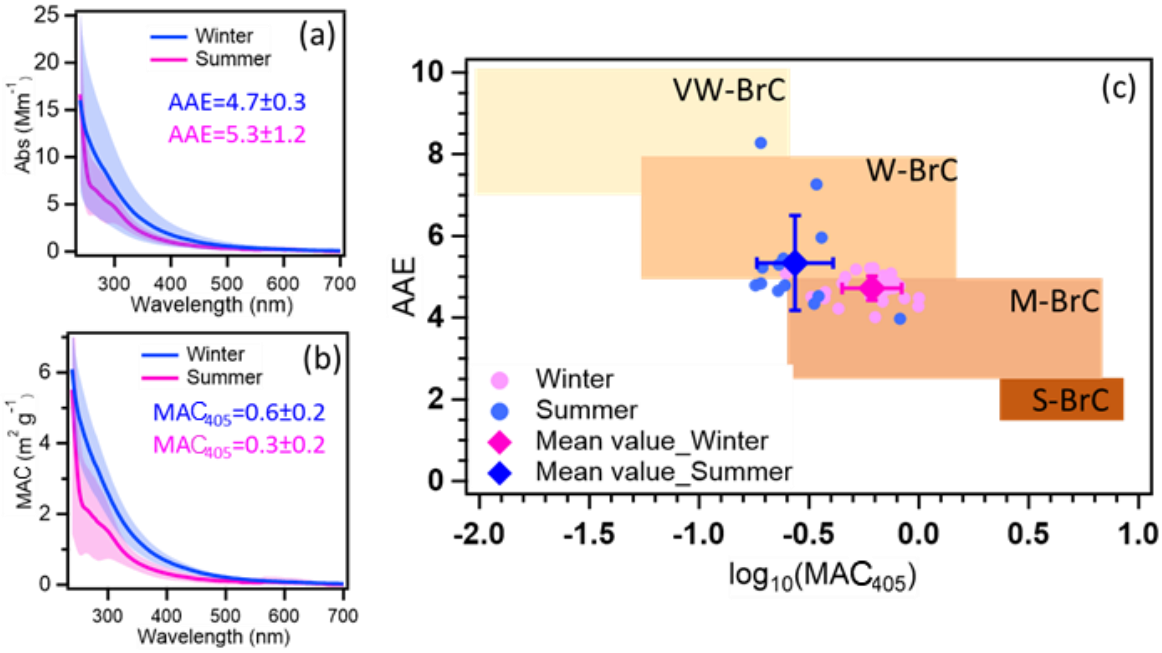

Figure 32. The average Abs (a) and MAC (b) of MS-BrC in winter (blue) and summer (pink). (c) Graphical representation of optical-based BrC classes in AAE-$\log_{10}$ (MAC_{405}) space with summer and winter data (Saleh, 2020; Hettiyadura et al., 2021). VW-BrC, W-BrC, M-BrC, and S-BrC, are very weakly absorbing, weakly absorbing, moderately absorbing, and strongly absorbing BrC. AAE reported in this work is calculated for a wavelength range of 300–450 nm. Please note that the small shoulder peak at ~300 nm for the average summer sample (a, b) is most likely due to some contamination e.g. from the filter. However, it only occurred in a few filter samples and does not affect our main results.

The average MAC_{365} in winter was 1.1 ± 0.3 m^2 g^{-1} higher than 0.5 ± 0.2 m^2 g^{-1} in summer (Table 7). And the average MAC from ultraviolet to visible wavelengths in summer was lower than in winter (Figure 32). The higher MAC values in winter indicate that the organic aerosol has a stronger absorbing capacity (Laskin et al., 2015). Similar values of MAC_{365} were reported for Melpitz, Leipzig, Magadino, and Zurich ranging between 1.0–1.5 and 0.3–0.5 m^2 g^{-1} during winter and summer, respectively (Moschos et al., 2018; Teich et al., 2017). The potential reasons are that similar sources contribute to OA in central Europe. The absorption Ångström exponents in the range of 300–450 nm ($AAE_{300–450}$) in summer and winter were 4.7 ± 0.4 and 5.5 ± 1.5, respectively (Figure 32a). The $AAE_{300–400}$ values show similar values measured at Zurich, which are 4.5 and 5.1 in winter and summer, respectively. However, lower values of 3.8 were observed in Magadino during winter (Moschos et al., 2018). Furthermore, comparing $AAE_{300–450}$ and log (MAC_{405}), the BrC in summer and winter can be classified as weakly absorptive BrC (WBrC) and moderately absorptive BrC (M-BrC), respectively (Figure 32c). Zeng et al. (2022) found that the brown carbon

in western United States wildfires was mainly moderately absorptive BrC. And Saleh (2020)found that the secondary BrC from aromatic volatile organic compound oxidation and biomass burning contributes to the very weakly or weakly absorptive BrC classes. The optical properties of BrC had seasonal characteristics due to different sources in winter and summer. In the following, we will discuss the potential MSBrC sources and chromophore characteristics.

3.3.3 EEM spectra and chromophores of methanol-soluble organic carbon

I used fluorescence spectra and a PARAFAC model to investigate chromophores and their potential sources of methanol-soluble organic carbon (MSOC) extracted from aerosol particles (Chen et al., 2020). With this approach, I identified four different characteristic components named C1, C2, C3, and C4 hereafter (Figure 33 and Figure S11, and Table S3). The methods were given in section 2.1.3. The excitation (Ex) and emission (Em) wavelengths of C1 range between < 240–330 nm and 350–395 nm, with peak (Ex / Em) values of < 240 and 363 nm, respectively. Compared with previous studies, a methanol-soluble chromophore component (Ex: < 250, Em: 388 nm) similar to C1 was enriched in biomass burning aerosol (Tang et al., 2020). Furthermore, (Chen et al., 2016) characterized a similar water-soluble chromophore component as less-oxygenated humic-like substances (HULIS) by correlation analysis of PARAFAC components and AMS data.

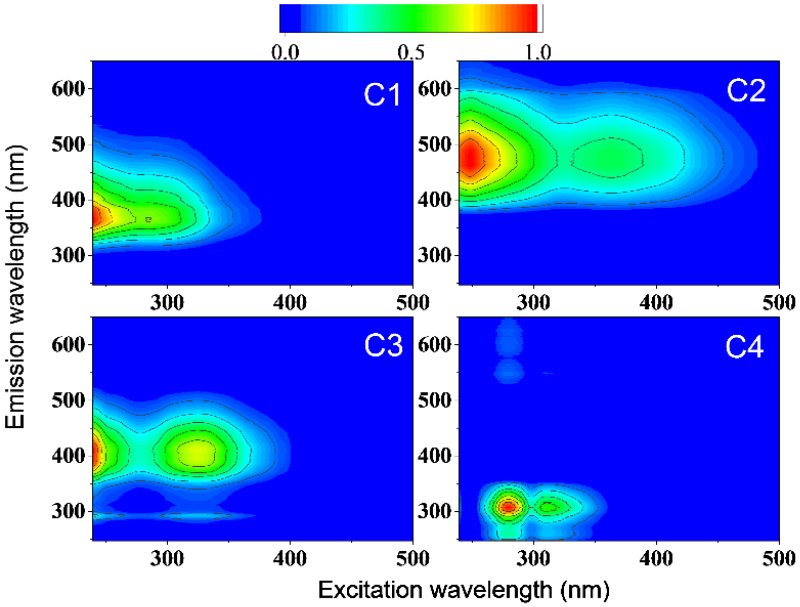

Figure 33. The four components were identified by the PARAFAC model analysis of the excitation–emission spectra from all filter extracts collected in summer and winter.

In contrast to C1, the maximum emission wavelengths of C2 and C3 range above 400 nm. This indicates that these emissions probably originate from conjugated systems (Matos et al., 2015; Cory and McKnight, 2005). Two fluorescence peaks of C2 at 248/362 nm (Ex) and 469 nm (Em) and two fluorescence peaks of C3 at 240/323 nm (Ex) and 408 nm (Em) were observed. Components with similar excitation and emission wavelengths as C2 and C3 were found in water-soluble organic carbon and considered highly oxygenated humic-like substances (Chen et al., 2021; Yan and Kim, 2017; Chen et al., 2016). The fluorescence peak (Ex/Em: 266/307 nm) of component C4 was located at the protein-like region which contains phenol and naphthalene compounds (Chen et al., 2016; Mladenov et al., 2011), since the peaks of shorter excitation wavelength (< 250 nm) and shorter emission wavelength (< 350 nm) were associated with aromatic proteins like tyrosine (Cory and McKnight, 2005). There was a low fluorescence peak at the right of the main peak in C4 component spectra. This could be the first-order Rayleigh scattering effect, but it does not affect the main results. Due to the significant similarity of the characteristic spectra identified using the PARAFAC model with the above literatures, I consider C1 to be a less-oxygenated HULIS (LO-HULIS) component, C2 to be a highly oxygenated HULIS (HO-HULIS) component, C3 to be a second HO-HULIS component, and C4 to be a phenol- and naphthalene-like component.

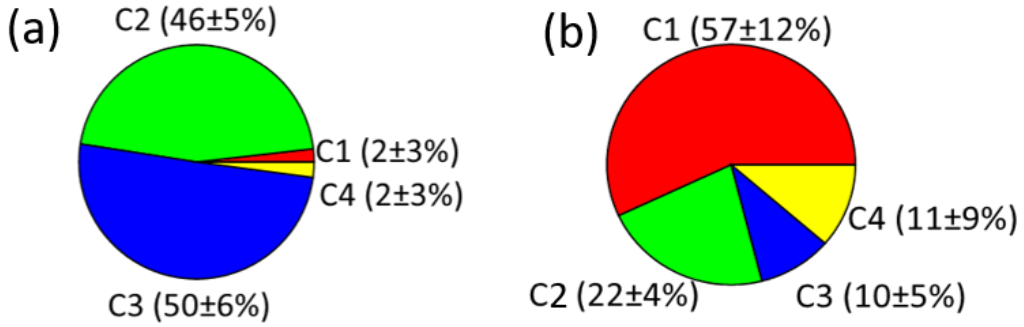

Figure 34. A comparison of relative contributions of the four components identified by PARAFAC model analysis to total fluorescence for summer (a) and winter (b).

As shown in Figure 34 and Figure 35a, there were different relative contributions of chromophore components in summer and winter. The LO-HULIS component (C1) has a high relative contribution of (57 ± 12) % in winter, but a low contribution of (2 ± 3) % in summer. The less-oxygenated HULIS originates most likely from primary emissions such as biomass burning, industrial sources, and other combustion sources (Chen et al., 2020). A similar chromophore component as C1 has also been identified in water-soluble organic carbon from the urban aerosol

in Aveiro, Portugal, showing relatively low contributions in a 1-year average (Matos et al., 2015). Therefore, primary emissions can be considered important sources for chromophore components in winter, but not in summer. In contrast, the HO-HULIS components C2 and C3 dominated (96 ± 6) % in summer and had much less but still substantial contributions with (31 ± 8) % in winter. Chen et al. (2020) and Lee et al. (2013) found that optically similar components as C2 and C3 had a high contribution in biogenic or anthropogenic secondary organic aerosol (SOA). Therefore, the chromophores from biogenic or anthropogenic SOA seem to have a substantial contribution in summer and still be significant in winter. The phenol- and naphthalene-like component C4 shows only lower contributions with (2 ± 4) % and (11 ± 9) % in summer and winter, respectively. A component optically similar to C4 has been identified in aerosol particles related to vehicle emissions (Tang et al., 2020). To substantiate this analysis including a first, yet not very specific, source apportionment, I will combine these findings with results from our high-solution time-of-flight aerosol mass spectrometer (HR-ToF-AMS, hereafter AMS) in the following section.

3.3.4 Sources of chromophores and organic aerosol

There are several factors of OA determined by PMF analysis of organic fragments measured by AMS in summer and winter (Figure S12 and Figure S13) (Ulbrich et al., 2009). As shown in Figure 35b, in brief, the HOA and COA were observed in summer and winter, classified as the primary organic aerosol. The HOA can be considered to stem mainly from traffic emissions in urban areas (Kasthuriarachchi et al., 2020). The contributions to total OA were on average (7 ± 2) % and (9 ± 6) % in summer and winter, respectively. The COA was associated with cooking activities in urban areas (Moschos et al., 2018; Mohr et al., 2012) and contributes on average (13 ± 4) % and (14 ± 8) % to total OA in summer and winter, respectively. The BBOA was only detected in winter and the average contribution to total OA was (23 ± 8) %. The BBOA can be considered to stem mainly from wood combustion used for residential heating during the wintertime in Europe (Moschos et al., 2021; Moschos et al., 2018). The SV-OOA and LV-OOA were observed both in summer and winter, mainly classified as secondary organic aerosol (Xiao et al., 2011). The average contributions of SV-OOA to total OA were (20 ± 4) % and (17 ± 8) % in summer and winter respectively. During the summer measurement, two different types of LV-OOA were observed LV-OOA1 (O/C: 0.70) and LV-OOA2 (O/C: 0.72). The average contributions of LV-OOA1 and LV-OOA2 to total OA were (28 ± 14) % and (32 ± 12) % respectively. Song et al. (2022) found that LV-OOA1 was mainly from regional transport and LV-OOA2 was mainly

from oxidation of biogenic VOC in summer. In contrast, the LV-OOA contributes on average (37 ± 20) % of the total OA during the winter period. Song et al. (2022) found that the LV-OOA in winter could be from regional transport. More details on the PMF analysis of AMS data are shown by Song et al. (2022).

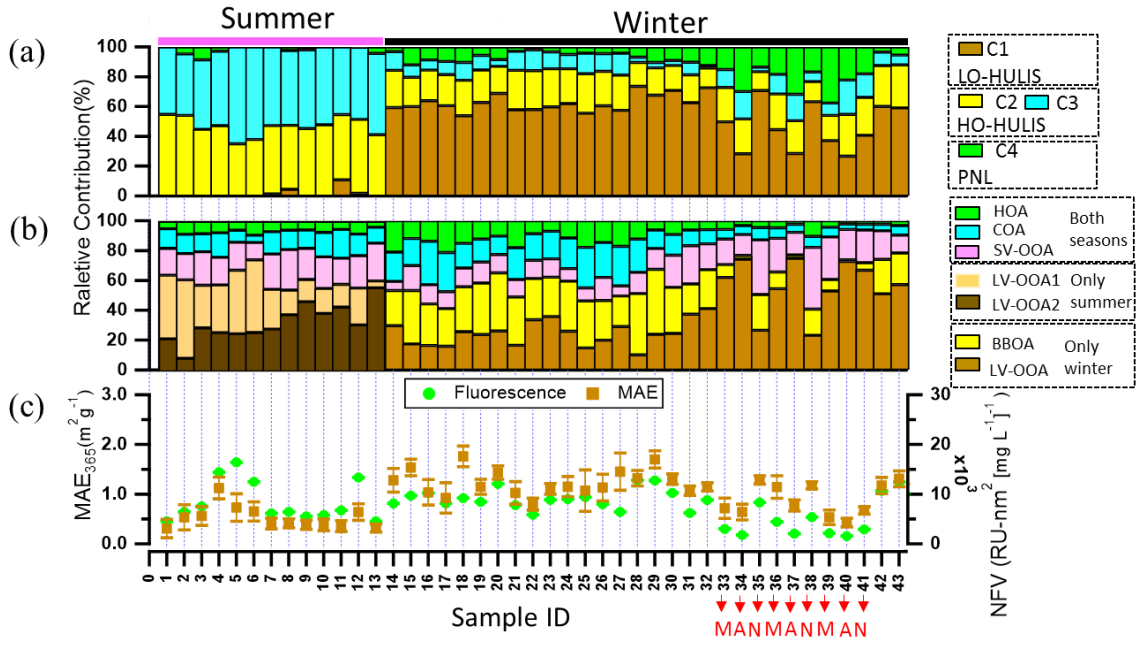

Figure 35. (a, b) Relative abundances of (a) the chromophore components, i.e. C1 is associated with less-oxygenated humic-like substances, C2 and C3 are associated with highly oxygenated HULIS, and C4 is associated with phenol- and naphthalene-like substance; (b) AMS-PMF factors, i.e. HOA, COA, SV-OOA, and LV-OOA1 for both seasons, LV-OOA2 only in summer, and BBOA and LV-OOA only in winter; and (c) the normalized fluorescence volume (NFV) (normalized to organic aerosol concentration) and mass absorption efficiency at 365 nm (MAC_{365}). Sample IDs 1–13 in summer and Sample IDs 14–43 in winter. Sample IDs 33, 36, and 39 in the morning (M); Sample IDs 34, 37, and 40 in the afternoon (A); Sample IDs 35, 38, and 41 at night (N). Sample IDs 1–32 and 42–43 for the whole day.

To potentially identify chromophore sources, I compared the factors from PMF analysis of AMS mass spectra and the components determined by the PARAFAC analysis of the excitation–emission spectra using a Pearson's correlation analysis based on relative abundances, as shown in Figure 36 and Figure S14. A significant correlation ($r = 0.8$, $p < 0.01$) can be seen between BBOA and LO-HULIS components in winter. Therefore, I consider LO-HULIS in winter to be mainly related to biomass burning organic aerosol. This is in agreement with a study that found the HULIS fraction of BrC was primarily related to biomass burning. This study conducted a dual carbon (13C and 14C) isotopic analysis on isolated HULIS (Yan and Kim, 2017). Residential wood burning was found to be the main source for HULIS in winter based on a strong correlation with K^+ no-dust ($R^2 > 0.7$) (Baduel et al., 2010). The HO-HULIS-1 component (C2) had a strong correlation

(r = 0.9, $p < 0.01$) with LV-OOA1, which is related to regional transport in summer. In addition, the HO-HULIS-2 component (C3) showed a significant correlation with LV-OOA2 (r = 0.7, $p <$ 0.7) (Baduel et al., 2010). As shown in Figure 35a, the phenol- and naphthalene-like component C4 had higher contributions to total fluorescence intensity for samples ID 33 to 41 (from 18 to 20 March 2020). Phenol in the gas phase also showed higher concentrations (Figure S15) during this period. Furthermore, as shown in Figure S15, the phenol- and naphthalene-like components had a good correlation (r = 0.7) with phenol, which most likely originates from biomass burning and fossil fuel combustion (Laskin et al., 2015; Sekimoto et al., 2013). Therefore, the phenol- and naphthalene-like component C4 may be related to biomass burning and fossil fuel combustion.

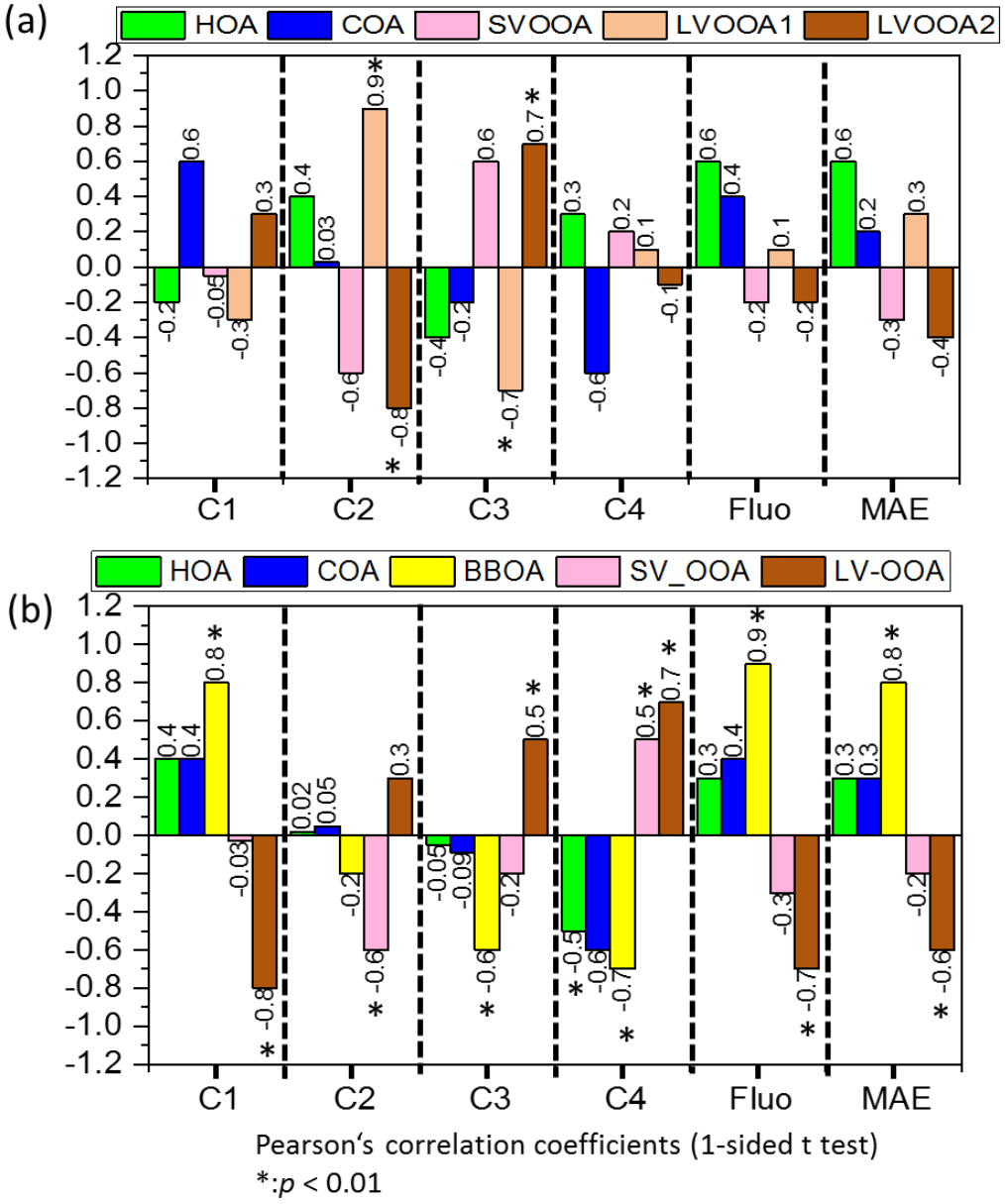

Figure 36. Pearson's correlation coefficients and significance levels (p,1-sided t test) of chromophore components and AMS-PMF factors. a: summer (n = 11), b: winter (n = 30).

The LO-HULIS and HO-HULIS components had variations of relative contributions during the winter campaign, especially diurnal variations. As shown in Table S2 in the Supplement, the samples with ID 33–41 were collected during different times of the day, such as morning (sample ID 33, 36, 39), afternoon (sample ID 34, 37, 40), and nighttime (sample ID 35, 38, 41). The contributions of LO-HULIS were lower in the morning and afternoon, but increased during the night. In contrast, HO-HULIS and phenol- and naphthalene-like chromophores showed an anti-

correlation with this diurnal evolution. Deng et al. (2022) also found that LO-HULIS components contributed more at nighttime and HO-HULIS obviously increased in daytime during the winter in Tianjin, northern China. The characteristics of LOHULIS are a low oxidizing state and high double bond equivalent. Furthermore, there is a negative correlation (Pearson's $r = -0.6$) between LO-HULIS and O_3 concentrations (Figure S16a). The HO-HULIS components (C2 and C3) have a high oxidation state and low double bond equivalents. They have significant correlations (Pearson's $r = 0.7$, $p < 0.01$) with O_3 in the wintertime (Figure S16b and c). Therefore, I consider that LO-HULIS may be oxidized into HO-HULIS. This is consistent with other studies (Deng et al., 2022; Chen et al., 2021).

The normalized fluorescence volume (NFV) has a high intensity in samples ID 5 and 6 but MAC_{365} (Figure 35c) is not significantly enhanced. This could be due to either contamination or specific species in these samples, as indicated e.g. by a higher fraction of LV-OOA1. During the wintertime measurements, the NFV and MAC_{365} had high correlation coefficients ($r = 0.9$ and 0.8, $p < 0.01$) with BBOA. Chen et al. (2016) found that the MAC_{266} and NFV values of water-soluble organic matter were positively correlated with $C_2H_4O_2^+$, an ion associated with organics from BBOA. In addition, MAC_{365} and NFV of MS-BrC were higher at nighttime and lowest in the afternoon. Satish et al. (2017) found that the absorption at 365 nm was higher in late evening, attributed to biomass burning, and lower in the middle of the day due to photobleaching and volatilization of BrC as well as rising boundary layer height. The sources of chromophores were identified well by combining chromophore components and AMS–PMF factors, but the BrC molecules are still unknown. The FIGAERO–CIMS can provide further insight into the aerosol (BrC) molecular composition.

3.3.5 Molecular composition of brown carbon during winter

Nitro-aromatic compounds (NACs) are typical brown carbon molecules. Therefore, I give here an overview of the main NACs I observed with their MAC_{365}, concentration range, and average concentration (Table 8). The highest average concentration showed 4-nitrocatechol with 0.6 ± 0.4 ng m^{-3}, followed by 2-methyl-4-nitrocatechol with 0.5 ± 0.4 ng m^{-3}. Lower average concentrations were observed for 2-methyl4-nitrophenol, 2-nitrophloroglucinol, and 4-nitrophenol, all with about ~0.2 ng m^{-3}. The sum of the five NACs varied between 0.7–3.6 ng m^{-3}, with an average concentration of 1.6 ± 0.9 ng m^{-3}, and contributes (0.02–0.08) % to the total organic mass concentrations measured by AMS. Teich et al. (2017) found mean NAC concentrations of 14.0 ng

m^{-3} in the city of Leipzig and somewhat lower values of 11.1 ng m^{-3} at the rural site of Melpitz, both Germany, during a winter campaign. NACs contributed on average ~0.5% of the total organic aerosol with a mean value of 20 ng m^{-3} in Detling, UK, in winter (Mohr et al., 2013). All these previous observations at different European locations show somewhat higher average NAC concentrations than I have observed. However, I think this difference can be explained mainly by the meteorological conditions during our winter campaign with long stormy periods with substantial precipitation. In contrast, the average concentrations of NACs were 173 ± 137 ng m^{-3}, with values ranging from 19 to 585 ng m^{-3} in Beijing, in winter (Li et al., 2020). This is just one example of more polluted regions of the world. Therefore, I conclude that NAC concentrations have levels between 1–20 ng m^{-3} in western Europe, which are substantially lower than in polluted regions. I calculated the light absorption of NACs by using molecular MAC_{365} (Xie et al., 2017). Based on this, the mean light absorption of the sum of the five NACs was calculated to be 0.014 ± 0.009 Mm^{-1}, contributing to 0.3 ± 0.1% of MS-BrC absorption at 365 nm, but they only contributed 0.03 ± 0.01% of the total organic mass. Mohr et al. (2013) found that the sum of five NACs. they found accounted for 4 ± 2% of UV light absorption by brown carbon, only contributing on average ~0.5% of the total OA mass. Li et al. (2020) found that the sum of 12 NACs contributed 17% of the total absorption by MS-BrC at 370 nm in Beijing, only accounting for 0.6% of the organic matter. Therefore, NACs are typical brown carbon molecules with typically lower mass contributions to total organic aerosol but relatively higher contributions to the total absorption.

Table 8. Nitro-aromatic compounds detected during the winter in Karlsruhe, including chemical formula, tentative structures, mass absorption coefficient at 365 nm (MAC_{365}), concentration range, and average concentration (mean ± standard deviation).

Molecule	Formula	Structure	MAC ($m^2\ g^{-1}$)*	Concentration Range ($ng\ m^{-3}$)	Average concentration ($ng\ m^{-3}$)
4-Methyl-5-nitrocatechol	C7H7O4N	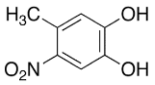	12.9	0.3–1.3	0.5 ± 0.4
2-Methyl-4-nitrophenol	C7H7O3N	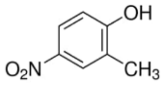	3.15	0.1–0.3	0.2 ± 0.05
2-Nitrophloroglucinol	C6H5O5N	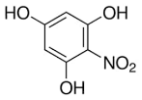	14	0.1–0.4	0.2 ± 0.1
4-Nitrocatechol	C6H5O4N	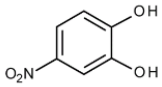	7.02	0.2–1.6	0.6 ± 0.4
4-Nitrophenol	C6H5O3N	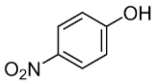	2.44	0.1–0.2	0.2 ± 0.05

* Xie et al., (2017).

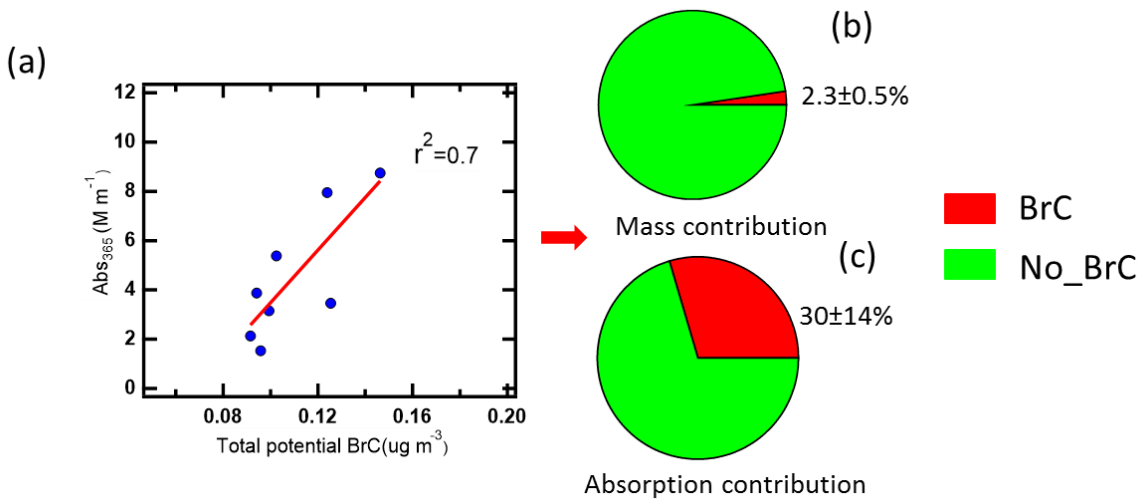

Figure 37. The correlation of Abs_{365} and total potential BrC (a). Mass (b) and absorption (c) contribution of the total potential BrC. The red pie: BrC; the green pie: No_BrC.

In order to identify potential brown carbon molecules besides the NAC from the about 2000 oxygenated organic molecules detected in the mass spectra of the FIGAERO–CIMS, I used the method described by Lin et al. (2018). From plotting a double bond equivalent (DBE) vs. a number of carbon atoms per molecule, I assigned 321 potential BrC molecules. Detailed information about

this method is shown in Supplement Figure S17. The mass fraction of potential BrC in 10 filters only accounted for 2.5 ± 0.6% of organic aerosol measured by AMS (Figure 37b). The mass of the total potential BrC molecules shows a good correlation (r^2=0.7) with MS-BrC absorption at 365 nm (Figure 37a). Furthermore, most of the individual potential BrC molecules correlated well with MS-BrC absorption at 365 nm. Therefore, this method seems to be useful to find potential or unknown brown carbon molecules in high-resolution mass spectra. Also applying the method described by Lin et al. (2018), Tang et al. (2020) found that high-molecular weight potential brown carbon molecules had good correlations (r = 0.9) with MAC_{365}. Xu et al. (2020) found 149 nitrogen-containing potential BrC chromophores from biomass burning emissions in the Tibetan Plateau. Since the MAC_{365} of most potential brown carbon molecules is still unknown, I assumed an average MAC_{365} of 9.5 m^2 g^{-1} for 316 potential brown carbon molecules. This is the average MAC_{365} of 12 typical NACs (Table S9) (Xie et al., 2020). Based on this assumption, I calculated a mean light absorption of the 316 potential BrC molecules of 1.2 ± 0.2 Mm^{-1}, accounting for 32 ± 15% of MS-BrC absorption at 365 nm (Figure 37c).

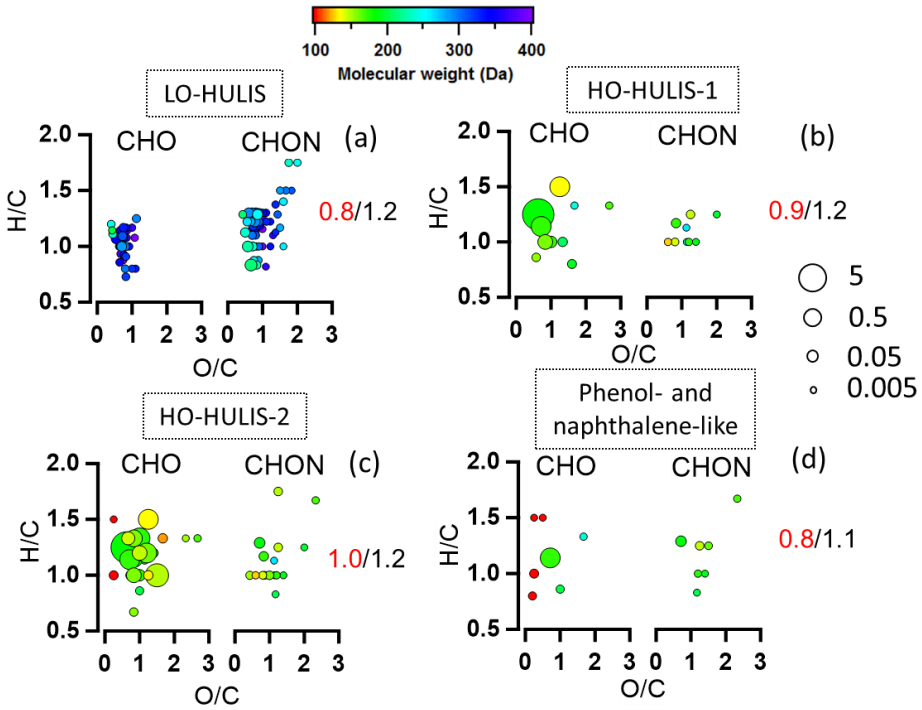

Figure 38. The van Krevelen plots of molecule families associated with each PARAFAC component (C1–C4). Data points are coloured by molecular weight. The molecules are split by $C_xH_yO_z$ and $C_xH_yO_zN_1$. The values in each plot are O/C ratios (red) and H/C ratios (black). The size of the circles is the relative contribution to the total brown carbon signals of each compound. (a) Molecules associated with the LO-HULIS component; (b) molecules associated with the HO-HULIS-1 component; (c) molecules associated with the HO-HULIS-2 component; (d) molecules associated with the phenol- and naphthalene-like component.

Table 9. Average properties of molecules associated with four characteristic chromophores in winter.

Chromophores	Average molecular mass [g mol^{-1}]	O/C ratio	DBE	AI_{mod}	Mass fraction of potential BrC [%]	Mass fraction of nitrogen containing molecules [%]
LO-HULIS (C1)	265 ± 2	0.8 ± 0.01	5.8 ± 0.04	0.23 ± 0.02	17 ± 4	62 ± 1
HO-HULIS-1 (C2)	170 ± 1	0.9 ± 0.01	3.6 ± 0.03	0.16 ± 0.01	14 ± 2	9 ± 0.3
HO-HULIS-2 (C3)	166 ± 1	1.0 ± 0.02	3.4 ± 0.02	0.10 ± 0.01	34 ± 4	9 ± 0.3
Phenol- and naphthalene-like (C4)	163 ± 8	0.8 ± 0.03	3.8 ± 0.06	0.20 ± 0.03	5 ± 1	32 ± 2

The potential BrC molecules could be assigned to the four different chromophore factors (C1–C4) identified by the PARAFAC analysis based on their individual correlations. The molecular weight, O/C, DBE, and modified aromaticity index (AI_{mod}) in Table 9 are intensity-weighted mean values. As shown in Table 9, 29% of the total potential BrC molecules are associated with LO-HULIS (component C1) and accounted for 17 ± 4% of the total potential BrC mass concentration. These molecules comprised 55 $C_xH_yO_zN_1$ molecules which accounted for 62 ± 1% of their mass concentration. Furthermore, these molecules show a relatively high average molecular weight of 265 ± 2 Da, a high DBE (5.8 ± 0.04), a high AI_{mod} (0.23 ± 0.02), and a relatively low average O/C ratio of 0.8 ± 0.01 (Figure 38a and Table 9). The LO-HULIS components were enriched with nitrogen-containing molecules with relatively high molecular weight and a relatively low oxidation state. The molecules associated with HO-HULIS1 (C2) accounted for 14 ± 2% of the total potential BrC mass concentration. The $C_xH_yO_zN_1$ molecules only account for 9 ± 0.3% of their mass concentration. The average O/C ratio, molecular weight, DBE, and AI_{mod} were 0.9 ± 0.01, 170 ± 1 Da, 3.6 ± 0.03, and 0.16 ± 0.01 respectively (Figure 38b and Table 9). Therefore, HO-HULIS-1 compounds are highly oxidized and have substantially lower nitrogen-containing molecules, as well as a lower molecular weight. In contrast, the molecules associated with HOHULIS-2 (C3) accounted for 34 ± 4% of the total potential BrC mass concentration. These molecules comprised 16 $C_xH_yO_zN_1$ molecules which only accounted for 9 ± 0.3% mass concentration. The average molecular weight, O/C ratio, DBE, and AI_{mod} of the HO-HULIS-2 molecules were 166 ± 1 Da, 1.0 ± 0.02, 3.4 ± 0.02, and 0.10 ± 0.01 respectively (Figure 38c and Table 9). The HO-HULIS

components had a relatively low molecular mass and a lower fraction of nitrogen-containing molecules compared to the LO-HULIS component. The phenol- and naphthalene-like components (C4) were associated with a few molecules which only accounted for 5 ± 1% of the total potential BrC mass concentration. The average O/C ratio, molecular weight, DBE, and AI_{mod} were 0.8 ± 0.03, 163 ± 8 Da, 3.8 ± 0.02, and 0.10 ± 0.01 (Figure 38d and Table 9). The $C_xH_yO_zN_1$ molecules account for 32 ± 2% of their mass concentration. In the above discussion, I conclude that NACs and the potential BrC molecules had a low contribution to organic mass concentration, but can explain a high contribution of absorption coefficients of BrC at 365 nm. The LO-HULIS associated molecules had a higher molecular weight, a higher DBE, a higher AI_{mod}, and higher contributions of nitrogen containing molecules compared to molecules associated with HO-HULIS chromophores.

3.3.6 Summary

In this chapter, the optical properties and chromophores of methanol-soluble brown carbon (MS-BrC) aerosol particles were investigated during July 2019 and February–March 2020 in downtown Karlsruhe, a city of about 300000 inhabitants in southwest Germany. The average Abs_{365} and MAE_{365} of MS-BrC were lower in the summer period (1.6 ± 0.5 Mm^{-1}, 0.5 ± 0.2 m^2 g^{-1}) than in the winter period (2.8 ± 1.9 Mm^{-1}, 1.1 ± 0.3 m^2 g^{-1}). In addition, the optical properties of MS-BrC in summer and winter can be classified as weakly absorptive BrC and moderately absorptive BrC, respectively, corresponding to the higher abundance and stronger light absorption of BrC in winter.

The excitation-emission analysis of the methanol soluble aerosol particle fraction showed that chromophores like HO-HULIS (C2 and C3) dominated the total fluorescence in summer with a relative fraction of 96 ± 6%. In winter, the LO-HULIS (C1) dominated the total fluorescence with 57 ± 12%, while the HO-HULIS still had a fraction of 31 ± 18%. This shows that the chromophore types substantially differ for winter and summer. The statistical analysis of AMS data (PMF) and Aqualog excitation-emission spectra (PRAFAC) showed that the LO-HULIS components in winter were mainly emitted from biomass burning. In contrast, the HO-HULIS components dominating in summer could be less volatile oxygenated organic aerosol from regional transport and oxidation of biogenic volatile organic compounds (VOC).

Furthermore, five nitro-aromatic compounds (NACs) were identified by CIMS ($C_7H_7O_3N$, $C_7H_7O_4N$, $C_6H_5O_5N$, $C_6H_5O_4N$, and $C_6H_5O_3N$) which contributed 0.03 ± 0.01% of total organic

mass, but can explain 0.3 ± 0.1% of the absorption coefficients of MS-BrC at 365 nm in winter. 316 potential brown carbon molecules were assigned accounting for 2.5 ± 0.6% of the organic mass, but explaining 32 ± 15% of the absorption at 365 nm, if assuming an average MAE_{365} of 9.5 m^2g^{-1}. This shows that a small fraction of brown carbon molecules dominates the overall absorption. This indicates the great importance to identify these molecules to predict aerosol absorption. The potential BrC molecules assigned to LO-HULIS chromophores, included more nitrogen-containing molecules (62 ± 1%), a higher average molecular weight (265 ± 2 Da), a higher double bond equivalent (5.8 ± 0.04), and a higher modified aromaticity index (0.23 ± 0.02) than the molecules assigned to the HO-HULIS chromophores.

3.4 Brown carbon at a rural site on KIT Campus Nord

In this chapter, I present an overview of field observations on KIT Campus Nord (3.4.1) and mass concentrations and volatility of brown carbon molecules (3.4.2). Furthermore, I present absorption concentration of 178 identified brown carbon molecules in particle phase. Finally, I present source and loss pathway of brown carbon in the gas and particle phase (3.4.3 and 3.4.5). These sections are mainly to answer these questions: 1) What are the chemical compositions and optical properties of brown carbon from mixed sources in field studies? 2) What is the link between chemical composition and optical properties of brown carbon aerosol? 3) What are the formation mechanisms and loss pathways of brown carbon aerosol in ambient environment? Detailed information on methods used at a rural site on KIT Campus Nord can be found in section 2.3.

3.4.1 Overview of the field observations

I performed particle and trace gas measurement from February 20th–March 16th March 2021 at KIT Campus Nord. Figure 39 and Figure 40 give an overview of meteorological parameters, traces gases, particle concentrations, and their optical properties during the winter campaign. The major wind directions at KIT Campus Nord, 3 km east of the village of Eggenstein-Leopoldshafen, were northeast and southwest (Figure 39) caused by channeling of the wind in the Rhine valley. The average wind speeds were 1.1 ± 0.8 (average ± standard deviation) m s^{-1}. Depending on meteorological conditions, local sources and regional transport had a major impact on air quality in Leopoldshafen in summer (Shen et al., 2019). As shown in Figure 39, O_3 had diurnal variations with peaks at daytime and an average of 41.3 ± 26.2 μg m^{-3} during the campaign. In contrast, the relative humidity (RH) showed diurnal variations with peaks at nighttime and an average of 68 ± 16% during the campaign. The average temperature during the winter campaign was 6.5 ± 5.6 °C and slowly increased from beginning to the end of the campaign. NO_2 had high concentrations at some periods e.g. from 20th to 23th February with 22 ± 8.6 μg m^{-3} and from 2nd to 4th March with 35 ± 14 μg m^{-3}. The SO_2 concentrations were 0.8 ± 1.0 μg m^{-3}, significantly lower than NO_2 concentrations. During the Saharan dust events, the $PM_{2.5}$ and PM_{10} mass concentrations were 21 ± 6 μg m^{-3} and 45 ± 20 μg m^{-3}, respectively, from 18th to 26th February and 19 ± 6 and 24 ± 7 μg m^{-3}, respectively, from 1st to 4th March as indicated by red boxes in the lowest panel of Figure 39. In addition, BC showed many spikes and a good correlation (r^2 = 0.8) with NO_2 (Figure 40). This indicates that there were many combustion activities during the campaign (Figure S18). The

absorption Ångström exponents of particles between 370 and 520 nm ($AAE_{370-520}$) and $AAE_{660-950}$ had diurnal variations with peaks at nighttime. I calculated the fraction of wood burning BC and fossil fuel BC as shown in Figure 40 using the Aethalometer model (Sandradewi et al., 2008a). During the winter campaign, the biomass burning BC was 0.73 ± 0.6 μg m^{-3}, mostly higher than 0.3 ± 0.3 μg m^{-3} for fossil fuel BC. The $AAE_{370–520}$, $AAE_{660–950}$, biomass burning BC, and NO_2 values were relatively enhances from 20th to 23th February and 2nd to 4th March. This indicates that strong biomass burning (BB) events were at these days. On these days, the BrC absorption accounted for ~40% of total absorption caused by BC and BrC. This points to the at least regional or seasonal importance of BrC absorption which has an important effect on air quality and climate.

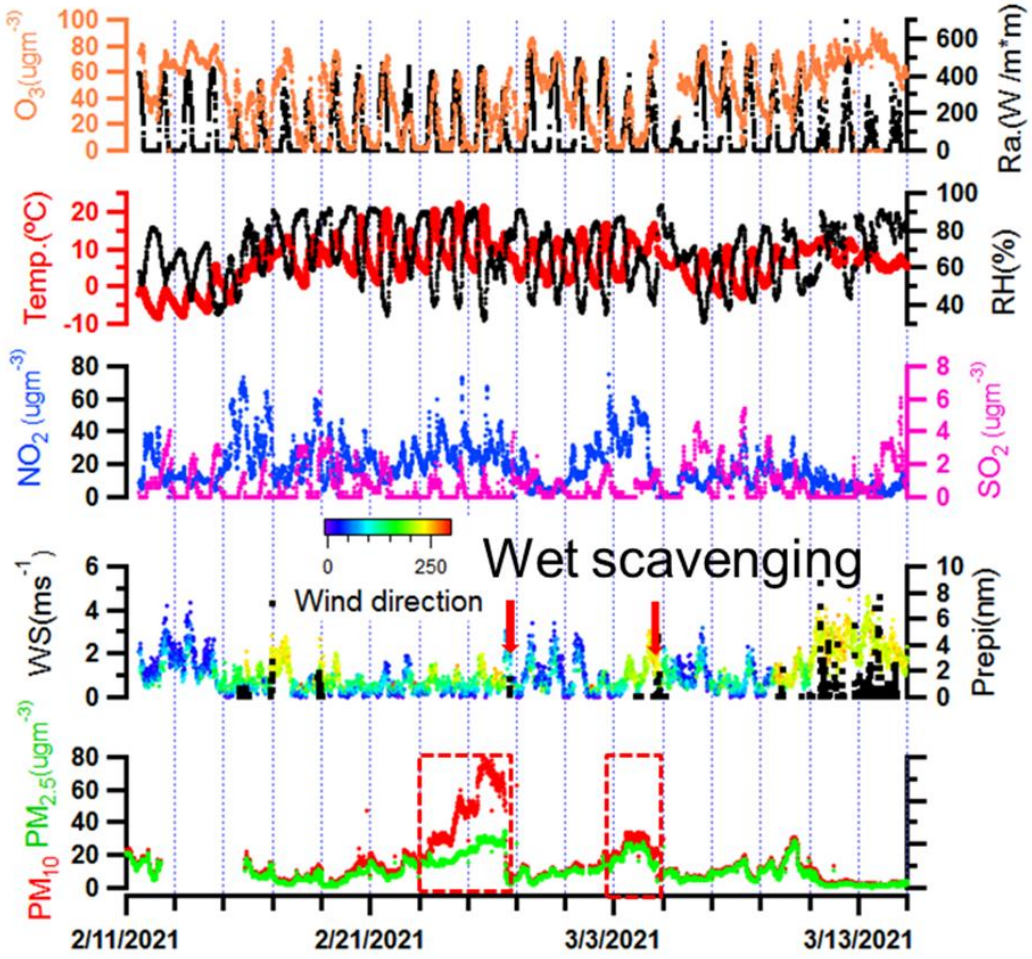

Figure 39 Overview of the meteorological parameters: trace gases (NO_2, O_3, and SO_2), temperature (T), radiation, relative humidity (RH), wind speed (WS), wind direction (WD), precipitation (Precipi), and $PM_{2.5}$ and PM_{10} during the campaign.

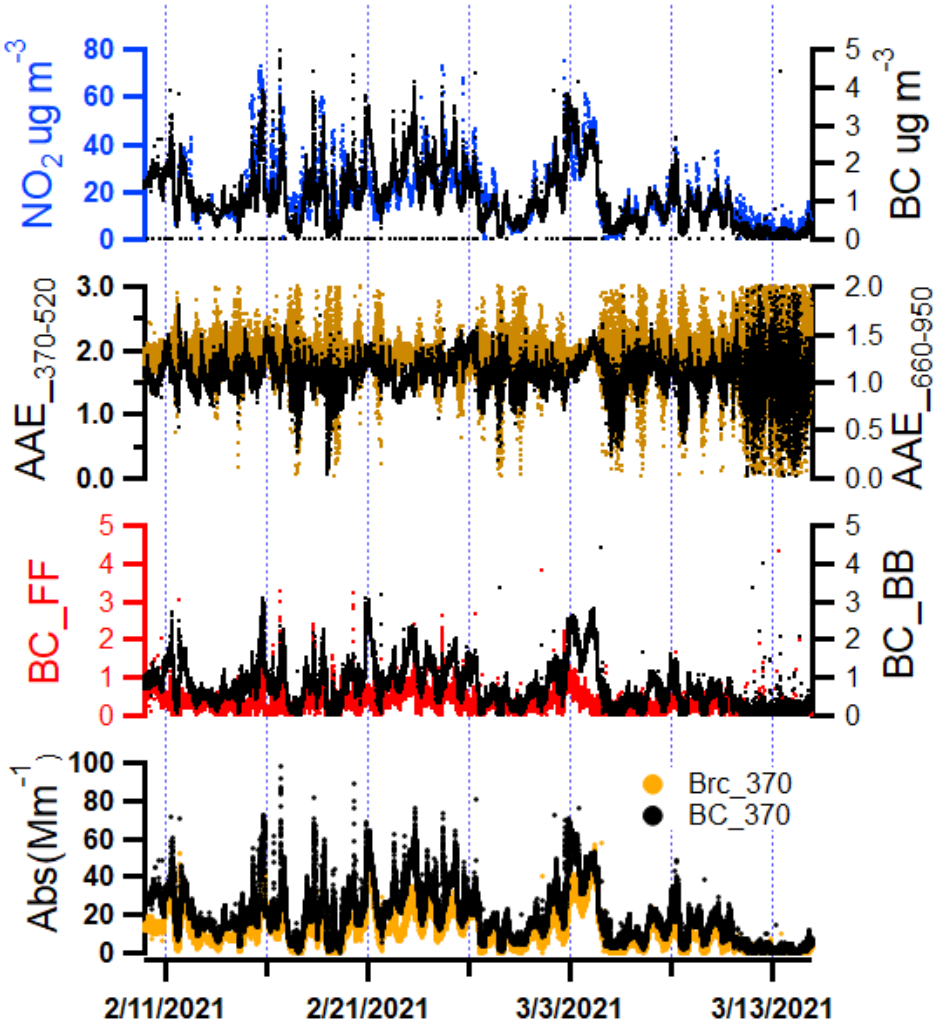

Figure 40. Overview of NO_2 and black carbon (BC), absorption Ångström exponents (AAE) at 370 to 520 nm ($AAE_{370-520}$), AAE at 660 to 950 ($AAE_{660-950}$), BC_FF, BC_BB, Abs_{370} of BrC, and Abs_{370} of BC.

3.4.2 Mass concentrations and volatility of brown carbon molecules

Figure 41 shows an overview of levoglucosan concentrations, BC concentrations, absorption of brown carbon at 370 nm (b_{brc370}), $AAE_{370-520}$, volatility and mass concentrations of 178 brown carbon molecules identified in the particle phase (Table S4) and 31 brown carbon molecules identified in the gas phase (Table S5) during the whole winter measurement. I identified 178 BrC molecules showing a good correlation (R=0.8) with the absorption at 370 nm (abs_{370}) of BrC (Figure S20). This indicates that it is meaningful to extract these 178 BrC molecules from more than two thousand molecules detected by FIGAERO-CIMS based on the double bond equivalent/carbon number ratio (DBE/C) of each molecule being higher than 0.5 and less than 0.9.

The levoglucosan had a good correlation (r=0.7) with BC. This also indicates that BC was mainly emitted from biomass burning during the winter campaign. Consistently, biomass burning BC accounted for 70% of total BC estimated by Aethalometer mode as I discussed above. The 178 BrC molecules detected in the particle phase correspond to an average mass concentration of 63 ± 32 ng m^{-3}. Mohr et al. (2013) found that five BrC molecules were 20 ng m^{-3} measured by CIMS during the winter in Detling, United Kingdom. Jiang et al. (2022) measured an average concentration of five BrC molecules measured of 1.6 ± 0.9 ng m^{-3} during the winter at a kerbside in downtown Karlsruhe. Therefore, the detection of the 178 BrC molecules allows more complete assessment of the BrC concentrations during this winter campaign. Their concentrations were significantly higher for biomass burning (BB) events e.g. 103 ± 31 ng m^{-3} at BB event 1 and 102 ± 34 ng m^{-3} at BB event 2, respectively. In addition, the absorption of brown carbon at 370 nm (b_{brc370}) had high peaks with ~100 Mm^{-1} and the $AAE_{370-520}$ of particles increased from ~1.5 to ~2 during the BB events. The average concentration of BrC in the gas phase was 6.2 ± 5.0 ng m^{-3} during the campaign. At BB events, their concentration can reach 26 ng m^{-3}. Therefore, biomass burning had a significant impact on optical properties of aerosol and brown carbon concentrations. The lowermost panel of Figure 41 shows the temporal variation of the average volatility of brown carbon molecules in the gas and particle phase. As expected, the average volatility ($\log_{10}C_{sat}$) of BrC in the particle phase was -1.1 ± 0.5 µg m^{-3} lower than 0.9 ± 0.6 µg m^{-3} of BrC in the gas phase during the campaign. Organic compounds with $\log_{10}C_{sat}$ lower than −4.5 µgm^{-3}, between −4.5 and −0.5 µgm^{-3}, between −0.5 and 2.5 µgm^{-3}, and between 2.5 and 6.5 µgm^{-3} are termed extremely low-volatility organic compounds (ELVOCs), low-volatility organic compounds (LVOCs), semi-volatile organic compounds (SVOCs), and intermediate-volatility organic compounds (IVOCs), respectively (Donahue et al., 2009). Therefore, BrC in the particle phase can be classified on average to the LVOCs and BrC in the gas phase to the SVOCs.

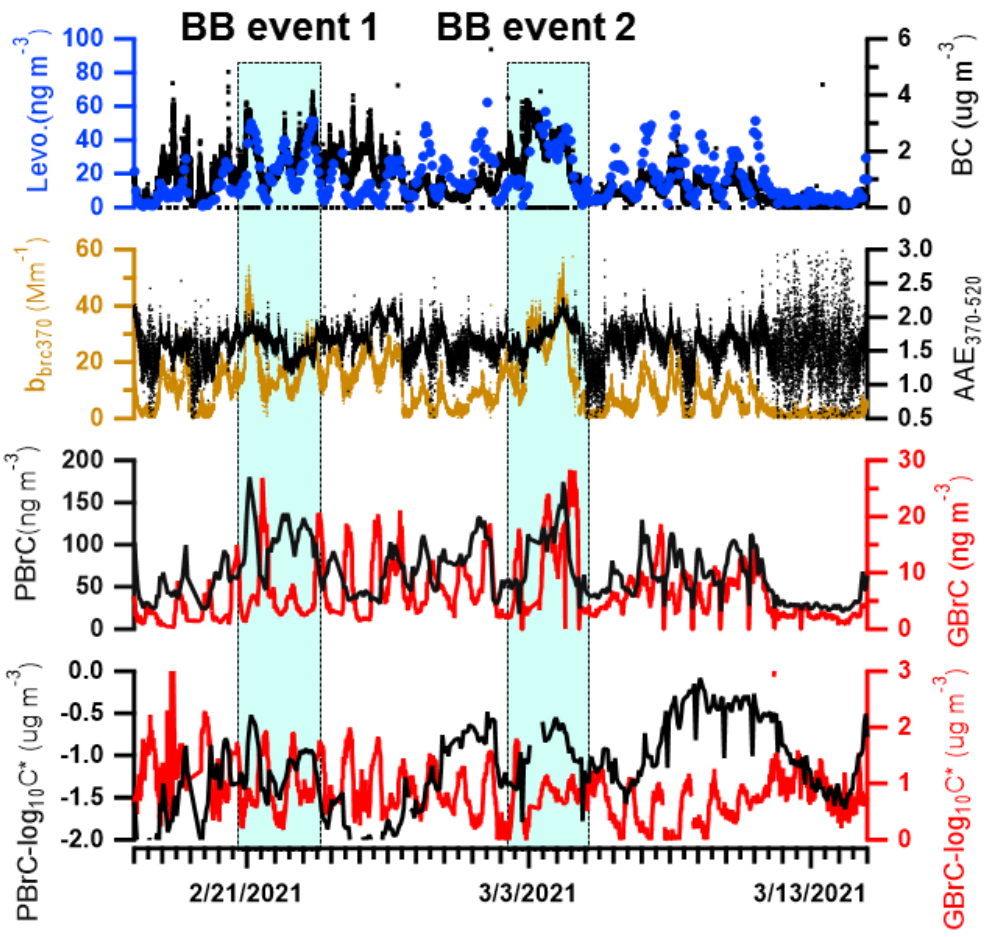

Figure 41. Time series of levoglucosan (Levo.) concentrations in particle phase from FIGAERO-CIMS, BC concentrations from aethalometer (AE33), absorption of brown carbon at 370 nm (brc_{370}), absorption Ångström exponents between 370 nm and 520 nm ($AAE_{370-520}$), brown carbon concentrations in particle phase (pBrC) and gas phase (gBrC), and volatility ($log_{10}C^*$) of brown carbon in particle phase (pBrC_$log_{10}C^*$) and gas phase (gBrC_$log_{10}C^*$) during the winter campaign.

3.4.3 Absorption contribution of 178 identified brown carbon molecules

Black carbon dominated light absorption of aerosol particles with a contribution of 100% at 880 nm and decreasing to 73% at 370 nm. With shorter wavelengths, the brown carbon absorption contribution significantly increased contributing to 27% of total aerosol absorption at 370 nm (Figure 42a). In order to calculate the light absorption from the 178 brown carbon molecules identified, I assumed an average MAC value of 9.5 m^2 g^{-1} tat 370 nm for all BrC molecules to estimate their absorption (Jiang et al., 2022). So far, the MAC_{370} of most potential brown carbon molecules is still unknown. Based on this assumption, I calculated the light absorption of the 178

brown carbon molecules identified to 0.6 ± 0.3 Mm^{-1} at 370 nm as average for the whole winter campaign (red bar in Figure 42). Jiang et al. (2022) found that a mean light absorption of 316 potential BrC molecules of 1.2 ± 0.2 Mm^{-1} at 365 nm at downtown Karlsruhe in winter. Since the online instrument to measure total organic aerosol mass, the AMS, wasn't available during this campaign, I estimated the total organic mass as fraction of 40% of $PM_{2.5}$ which is a typical fraction for this season and region (Song et al., 2022; Huang et al., 2019). Based on this assumption, the average organic aerosol mass concentration calculates to 4.2 ± 3.0 μgm^{-3}. Relative to this total organic aerosol particle mass and the measured brown carbon absorption, the 178 identified brown carbon molecules only accounted for 2.3 ± 1.5% of the total organic mass, but explain 14 ± 9% of total brown carbon absorption at 370 nm. Palm et al. (2020) found that particulate nitroaromatic compounds (BrC molecules) can explain 29 ± 15% of average BrC light absorption at 405 nm, despite accounting for just 4 ± 2% of average OA mass in fresh wildfire plumes. Mohr et al. (2013) found that five nitroaromatic compounds (BrC molecules) are potentially important contributors to absorption at 370 nm measured by an aethalometer and account for 4 ± 2% of UV light absorption by brown carbon in Detling, United Kingdom during Winter. Jiang et al. (2022) determined a mean light absorption of the 316 potential BrC molecules accounting for 32 ± 15% of methanol-soluble BrC absorption at 365 nm, but only accounted for 2.5 ± 0.6% of the organic aerosol mass. Therefore, only small mass fractions of strongly absorbing brown carbon molecules can dominate the brown carbon absorption.

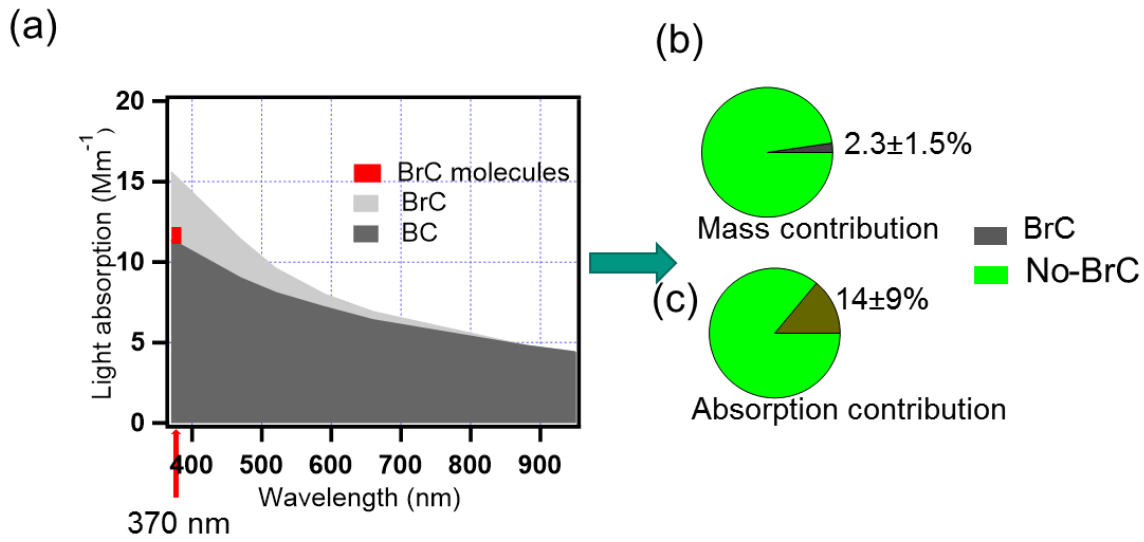

Figure 42. A stacked plot showing the main contributions to aerosol absorption from brown carbon and black carbon based on the seven wavelengths measured by the aethalometer AE33. The contribution of the identified brown carbon molecules to the total aerosol absorption is indicated in red at 370 nm. (b) Average mass contribution of the potential BrC molecules to estimated total organic mass and (c) absorption contribution of the potential BrC molecules identified to total absorption by BrC. The green pie: unidentified-BrC; the gray pie: identified BrC.

3.4.4 Sources of BrC in the gas phase

The 178 BrC molecules in the particle phase (PBrC) exhibited two peaks in the diurnal profile (Figure 43a) averaged over the whole winter campaign. They increased from 19:00 to 01:00 with a peak at 82 ± 35 μg m^{-3} around midnight. Then, the PBrC slowly decreased after midnight. However, they increased again from 6:00 to 08:00 and formed a second peak with 76 ± 50 μg m^{-3} in the morning. During the daytime, they decreased reaching the lowest values of 47 ± 24 μg m^{-3} at 14:00−15:00. During the nighttime and morning hours, the higher mass concentrations of PBrC were caused by residential wood burning emissions. Consistently, higher $PM_{2.5}$ concentration levels at nighttime at a rural site near Karlsruhe, Germany, could be assigned to wood burning emissions from wood stove operation during winter (Thieringer et al., 2022). The low mass concentrations of PBrC at the daytime could be explained to photobleaching and evaporation of BrC and/or dilution by the rising planetary boundary layer (Satish et al., 2017). Satish et al. (2017) found that BrC over the Indo-Gangetic Plain had two peaks of BrC in evening and morning hours, and the lowest value during daytime. Interestingly, gas-phase BrC (GBrC) molecules showed higher concentrations at daytime (09:00−17:00) and lower concentrations between evening and early morning (18:00−08:00). Salvador et al. (2021) also found that 16 gas-phase nitro-aromatic compounds (BrC molecules) measured by FIGAERO-CIMS were higher during daytime and

lower at nighttime during winter in rural China. As discussed above, strong biomass burning emission were mostly observed at evening and early morning hours. However, gas-phase BrC had no peaks during those time periods. Therefore, the primary emission from biomass burning was not a major source for GBrC at KIT Campus Nord. It seems to be mainly controlled by secondary formation (e.g. photochemical smog) or/and particle-to-gas partitioning (Salvador et al., 2021).

To demonstrate how the secondary formation and partitioning control the gas-phase BrC at KIT Campus Nord, I plotted diurnal profiles of the average volatility and volatility fractions of IVOC, SVOC, and LVOC of the gas-phase BrC (Figure 43b). The LVOC and SVOC of BrC increased at evenings and decreased at daytime. In contrast, the IVOC of BrC increased at daytime and reached ~17% of total $\log_{10}C^*$ (volatility) in gas-phase BrC while SVOC remained with a constant fraction. Furthermore, the IVOC fraction of BrC in the particle-phase was only 4% with a flat diurnal profile (Figure S21). The O/C ratio of gas-phase BrC also increased at daytime (Figure 43d). Therefore, the higher fraction of IVOC in the gas phase during daytime could be mainly caused by secondary formation e.g. photochemical aging because of higher concentrations of O_3 at same time (Figure 43c) (Salvador et al., 2021). Figure S22 shows that BrC in the gas phase had a good correlation (r=0.4) with temperature. This explains why the temperature shows a similar diurnal profile as the gas-phase BrC. Therefore, particle-to-gas partition was also an important source for gas-phase BrC. However, our results are not consistent with previous studies where 16 BrC molecules in gas phase were mainly from primary emissions during the biomass burning evenings and secondary formation during clear days in rural China (Salvador et al., 2021), since biomass burning emissions in rural Germany were lower than the polluted area in China. And the 31 BrC in the gas-phase in rural Germany was 6.2 ± 5.0 ng m^{-3}, significantly lower than 1720 ng m^{-3} of 16 BrC in polluted rural, China (Salvador et al., 2021). Cheng et al. (2021a) found that secondary formation was a strong source for five BrC molecules in the gas-phase Therefore, BrC in the gas-phase is less influenced from primary emissions from biomass burning but are mainly controlled by secondary formation and partitioning.

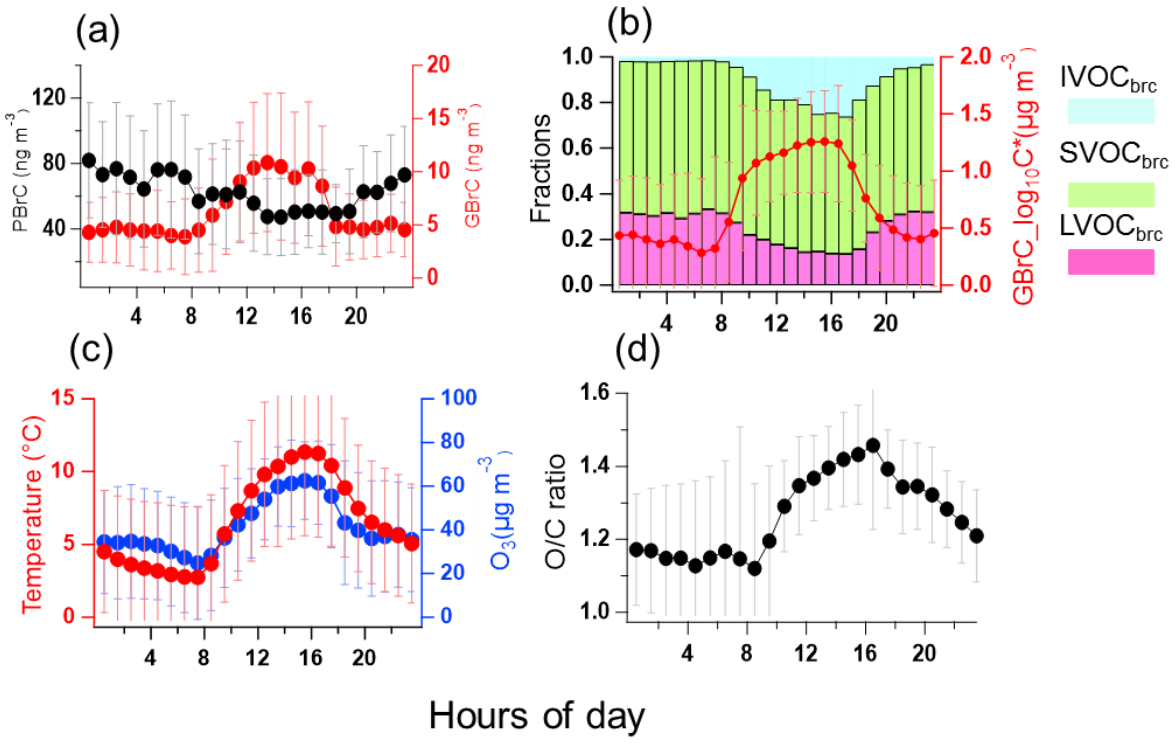

Figure 43. Diurnal profiles averaged over the whole winter campaign of (a) BrC in the particle (PBrC) and gas phase (GBrC), (b) BrC volatility fractions in $LVOC_{brc}$, $SVOC_{brc}$, $IVOC_{brc}$, and mean BrC volatility in the gas phase (red line), (c) temperature and ozone concentration. (d) O/C ratio of the oxidized organic components in the particle phase.

3.4.5 Sources and loss pathways of BrC in the particle phase

To determine the sources of brown carbon, I use the edge approach (Day et al., 2015). It allows to estimate the contribution of primary biomass burning to the measured BrC concentrations using levoglucosan as a primary source tracer. This approach is analogous to the widely used elemental carbon (EC) tracer approach, in which EC is used to distinguish the primary organic carbon (POC) and secondary organic carbon (SOC) in total organic carbon (OC) measurements (Day et al., 2015; Cabada et al., 2004). Levoglucosan (lev) and BrC were measured online by the same instruments and conditions. As discussed above, there is a good correlation (r=0.8) between levoglucosan and BC during the winter campaign. Therefore, levoglucosan is a suitable tracer for primary BB. Figure 44a shows that the blue points can be used as edge points to determine the ratio of BrC/levoglucosan at the primary emissions from biomass burning. The relative contributions of primary emission (BB) and secondary (sec) formation for total BrC molecules were estimated using the following expression:

$$BrC_{BB} = \left(\frac{[BrC]}{[lev]}_{BB}\right) * [lev.] \quad (12)$$

$$[BrC_{sec}] = [BrC_{Tot}] - [BrC_{BB}] \quad (13)$$

Where $([BrC]/[lev])_{BB}$ is the ratio of the concentration of the BrC to that of levoglucosan in the primary emissions from biomass burning and the value is 1.9 ± 0.1 (Figure 44a), BrC_{BB} and BrC_{sec} are the fractions of BrC generated through biomass burning and secondary production, respectively, BrC_{Tot} and lev. are the measured concentrations of BrC and levoglucosan during the winter campaign. Using this approach, I calculated the diurnal profiles of BrC from primary emission (BrC_{BB}) and secondary formation (BrC_{sec}) shown in Figure 43b. The mass fraction of BrC_{sec} increased at daytime and decreased in evening. This indicates that the secondary formation for BrC in the particle phase was enhanced during daytime, facilitated by the higher level of oxidants e.g. O_3 (Figure 43c). The mass fraction of BrC_{BB} had two peaks in early morning and evening hours, respectively. This may be caused by residential wood burning emissions. BrC_{BB} accounts for 39 ± 21% of total BrC as averaged for the whole measurement period. At biomass burning events, the BrC_{BB} is a major mass fraction for total BrC that accounts for 92% at BB-event1 and 82% at BB-event-2, respectively. Therefore, the primary emissions of BrC have a significant impact on BrC, especially, at biomass burning events. BrCsec dominates the mass fraction of BrC with 61 ± 7%. Therefore, the secondary formation was an important source for BrC in rural Germany. Consistently, Secondary sources for BrC were more important for absorption than primary ones in the Southeastern Margin of the Tibetan Plateau (Wang et al., 2019).

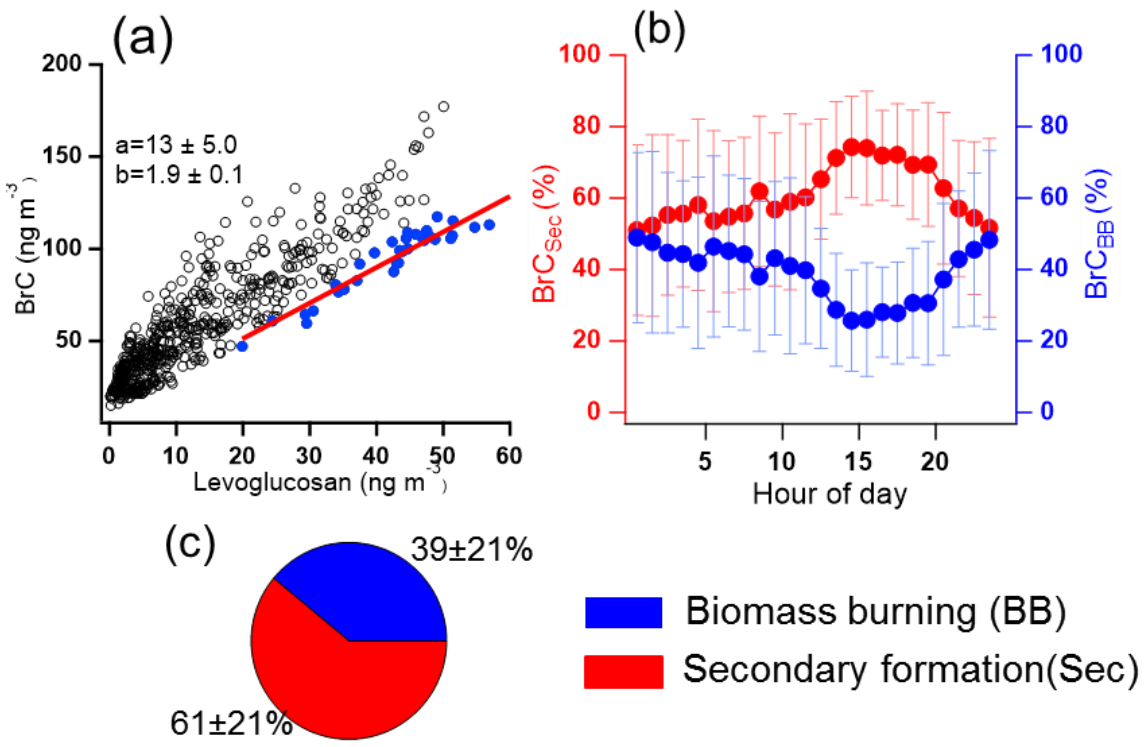

Figure 44. (a) Correlation analysis of BrC and levoglucosan in the particle phase for the analysis of the contribution of biomass burning using the edge method (Day et al., 2015). Blue points are the data used to determine $[BrC/lev.]_{BB}$. (b) diurnal profile of secondary-formation BrC and biomass-burning BrC for the whole measurement campaign. (c) Mass fractions of secondary formed BrC and biomass-burning primary BrC.

To further investigate the potential loss pathways of BrC in the particle phase, I plotted the diurnal profiles of O/C ratio of BrC during the whole measured campaign in Figure 45. The O/C ratio of BrC increased at daytime and decreased at nighttime. The O_3 had the same diurnal profile as O/C of BrC. In addition, the O/C of BrC had a positive correlation (r=0.8) with O_3. This indicates that the BrC was photo-oxidized by O_3 and led to an increase in the O/C ratio of BrC. In contrast, the light absorption of BrC at 370 nm (b_{brc370}) and double bond equivalent (DBE) decreased at daytime and increased at nighttime. Therefore, during daytime, the absorption of brown carbon at 370 nm decreased due to lower DBE and higher O/C of brown carbon oxidized by O_3. This is in accordance with previous studies where atmospheric photooxidation diminishes light absorption of primary brown carbon aerosol from biomass burning (Sumlin et al., 2017). Oxidative whitening can reduce light absorption of brown carbon during the day (Hems et al., 2021).

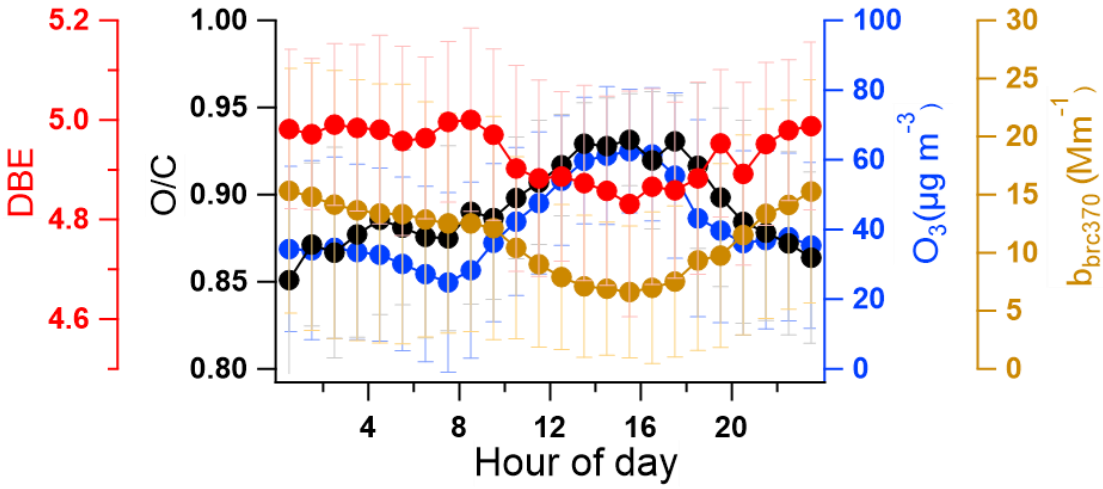

Figure 45. The diurnal profile of DBE (double bond equivalent), O/C ratio of BrC, O_3, and b_{brc370} (absorption of BrC at 370 nm) during the whole measured winter period.

3.4.6 Summary

Light absorption, sources, and loss pathways of brown carbon molecules were investigated during February−March 2021 in a rural area, at KIT Campus Nord in southwestern Germany. The 178 brown carbon molecules identified in the particle phase contributed on average 63 ± 32 ng m^{-3} to total aerosol mass and 31 brown carbon molecules identified in the gas phase contributed on average 6.2 ± 5.0 ng m^{-3} during the whole campaign. During biomass burning events, BrC concentrations in the particle phase were significantly higher reaching ~100 ng m^{-3}. The 178 brown carbon molecules identified only accounted for 2.3 ± 1.5% of the total organic mass, but explain 14 ± 9% of total brown carbon absorption at 370 nm, assuming an average MAC_{370} of 9.5 m^2 g^{-1}.

Diurnal variations show that the particle-phase BrC had two peaks at early morning and evening hours, respectively. These were mainly caused by residential wood burning emissions. In contrast, the gas-phase BrC showed higher concentrations at daytime and lower concentration at nighttime. During daytime, gas-phase BrC has higher O/C ratio and had a positive (r=0.4) correlation with ambient temperature. The gas-phase BrC molecules were mainly controlled by secondary formation (e.g. photochemical smog) and particle-to-gas partitioning. For the source of particle-phase BrC, primary emission from biomass burning accounted for 39 ± 21% of total BrC: Secondary formation dominates the mass fraction of BrC with 61 ± 7% during the whole winter campaign. During daytime, the secondary formation can contribute to 80% of particle-phase BrC. However, O/C of BrC increased at daytime and had a positive correlation (r=0.8) with O_3. In

addition, DBE of particle-phase decreased at daytime. This indicates that the absorption of brown carbon at 370 nm decreased due to lower DBE and higher O/C of brown carbon oxidized by O_3.

4. Conclusion and Outlook

4.1 Conclusions and atmospheric implications

In this dissertation, chemical composition and optical properties of brown carbon aerosol were investigated in simulation chamber experiments and field campaigns. Brown carbon was generated from primary emissions with different combustions fuels (straw, beech wood, cow dung, and plastic) and also from photooxidation of primary brown carbon. In addition, the brown carbon was formed by oxidation of toluene at different temperatures (253–313K) in presence of NO_2 and by oxidation of indole with/without NO_2 and seed particles simulating secondary BrC formation in chamber experiments. Besides the study of defined sources, brown carbon aerosol was also investigated in rural and urban areas in and near Karlsruhe.

Primary emissions from flaming combustion of straw, beech wood, cow dung, and plastic show as major brown carbon chromophores less oxygenated humic-like substances (LO-HULIS) and protein/phenol-like substances (PLS). This is consistent with study by Fan et al., (2020). Photo oxidation of the primary brown carbon containing aerosol resulted in smaller fractions of the PLS chromophore and higher fractions of highly oxygenated humic-like chromophores (HO-HULIS). The mass fraction of heavier molecules decreased and the O/C of ratio of organic aerosol increased. Both can be explained by gas phase oxidation of VOC leading to condensation of on average lighter and less or non-absorbing organic compounds on the primary aerosol particles. The PLS chromophores could also be depleted by photo-oxidation or converted into HO-HULIS. This was observed by Fan et al. (2020), who treated filter samples of biomass burning particles with very high concentrations (70 ppm) of ozone. They also found that O_3 aging induced the reduction of light absorption and fluorescence for the biomass-burning brown carbon. However, my studies provide a new insight on molecular level explaining the changing of chromophore and light absorption of brown carbon from primary emissions after photooxidation. The heavier molecules e.g. dimers (m/z 450–550) and trimers (m/z 550–650) were less abundant partially due to fragmentation but also due to gas to particle partitioning of lighter molecules formed by oxidation reactions in the gas phase e.g. $C_2H_2O_4$ and $C_3H_4O_4$. This is consistent with studies by (Bruns et al., 2015; Heringa et al., 2011). This study explains the aging of brown carbon aerosol from primary emissions in the atmosphere with decreasing mass absorption coefficients especially in the UV and with corresponding decreasing AAEs.

Toluene, which is as a typical anthropogenic precursor of brown carbon often emitted together with NO_x, is oxidized in presence of NO_2 to 4-methyl-5-nitrocatechol ($C_7H_7O_4N$), 2-methyl-4-nitrophenol ($C_7H_7O_3N$), and 4-nitrocatechol ($C_6H_5O_4N$). They dominated the nitrogen-containing products of toluene SOA with 8%–10%. Lin et al. (2015) also found the same brown carbon molecules in toluene SOA in presence of NO_2. Highest mass absorption coefficient of toluene SOA was observed for higher temperatures (313K) for which the SOA yields were lowest. Hence, toluene is an efficient BrC for warmer atmospheric conditions. Yalcin et al. (2020) found that the average concentration of toluene was 16 μg m^{-3} in the atmosphere of Balikesir, Turkey. This is a relatively typical concentration for urban areas (USEPS, 1988). Based on the yields and optical properties of toluene SOA that I have determined and typical toluene concentrations in the atmosphere, I estimated the potential average absorption of toluene SOA as 0.6 ± 0.06 Mm^{-1} at 365 nm. This value is on a similar level as the light absorption (0.5 ± 0.1 Mm^{-1} at 370 nm) of brown carbon in Waldstein, a forest site in Germany, in the ambient atmosphere (Teich et al., 2017). Therefore, brown carbon from the oxidation of toluene in presence of NO_2 has a significant impact on aerosol absorption, climate, and visibility, especially near urban areas. This work provides the basis to implement improved parameterizations of BrC formation from toluene in atmospheric transport models.

Only recently, indole was identified as a potentially important biogenic precursor of brown carbon. The major chromophore of indole SOA in absence of NO_2 was $C_8H_7O_3N$ contributing 20–30% of the light absorption of indole SOA. This new chromophore was observed also in a previous study (Montoya-Aguilera et al., 2017). In presence of seed particles and of NO_2, 3-nitroindole ($C_8H_6O_2N_2$) dominated the chemical composition with up to 76%. contributing around 50% of total absorption at 365 nm. Consistently, Baboomian et al. (2023) found that 3-nitroindole was a strong-absorbing chromophore in indole SOA in presence of NOx. The mass absorption coefficient of indole SOA is higher than of most other secondary brown carbon compounds. Atmospheric indole concentrations of ~1.8 and ~2.6 ppb were observed at daytime and nighttime, respectively during the spring flowering season (Gentner et al., 2014). Based on yields and optical properties of indole SOA that I have determined and these indole concentrations, I estimated that the potential absorption of indole SOA can reach 2.3 ± 0.2 Mm^{-1} and 3.2 ± 0.3 Mm^{-1} at 405 nm at daytime and nighttime, respectively. These values are higher than the total absorption at 370 nm (0.84 ± 0.24 Mm^{-1}) of brown carbon observed during the summer at a rural background site, Melpitz, Germany

(Moschos et al., 2018). These estimated absorption values are in the same range as total light absorption at 365 nm ($1.6 \pm 0.5\ Mm^{-1}$ at summer and $2.8 \pm 1.9\ Mm^{-1}$ at winter) of brown carbon aerosol in an urban area, the city of Karlsruhe (Jiang et al., 2022). This indicates that indole SOA can have a significant impact on aerosol absorption, climate, and visibility especially during the spring season. However, this may be limited to regions with corresponding emission sources like maize fields or down wind of animal husbandries. The regional importance should be determined with corresponding atmospheric models. However, significant improvements of indole emission factors are required to do this.

For a field campaign in an urban area, the optical properties and chromophores of methanol-soluble brown carbon (MS-BrC) aerosol particles were investigated during July 2019 and February–March 2020 in downtown Karlsruhe, a city of 300000 inhabitants in southwest Germany. The average Abs_{365} and MAE_{365} of MS-BrC were lower in the summer period ($1.6 \pm 0.5\ Mm^{-1}$, $0.5 \pm 0.2\ m^2\ g^{-1}$) than in the winter period ($2.8 \pm 1.9\ Mm^{-1}$, $1.1 \pm 0.3\ m^2\ g^{-1}$). The Excitation-emission analysis of the methanol soluble aerosol particle fraction showed that chromophores like HO-HULIS dominated the total fluorescence in summer with a relative fraction of 96 ± 6%. In winter, the LO-HULIS dominated the total fluorescence with 57 ± 12%, while the HO-HULIS still had a fraction of 31 ± 18%. LO-HULIS resulted from biomass burning in winter and the dominating HO-HULIS was low-volatility oxygenated organic aerosol from regional transport and oxidation of biogenic volatile organic compounds (VOCs) in summer. The molecules associated with LO-HULIS had a high molecular weight, a high double bond equivalent, a high modified aromaticity index, and high contributions of nitrogen-containing molecules. In contrast, HO-HULIS-associated molecules have a lower molecular weight, a lower double bond equivalent, a lower modified aromaticity index, and lower contributions of nitrogen-containing molecules. Also previous studies (Chen et al., 2016) found that LO-HULIS was associated with biomass burning aerosol. However, in contrast to Chen et al. (2016), I provide new insights into potential sources based on PMF analysis of AMS data and the detailed chemical composition of chromophores. Compared with previous studies (Devi et al., 2016; Costabile et al., 2017), this study explains the chemical composition and chromophores of brown carbon in central Europe.

I observed BrC also in a rural area at KIT Campus Nord in southwestern Germany. The optical properties, potential sources, and loss pathways of brown carbon molecules were investigated during February−March 2021. I identified 178 potential brown carbon molecules in the particle

phase and 31 brown carbon molecules in the gas phase. The 178 brown carbon molecules only accounted for 2.3 ± 1.5% of total organic particle mass, but explained 14 ± 9% of total brown carbon absorption at 370 nm, assuming an average MAC_{370} as 9.5 m^2 g^{-1}. This shows that a small fraction of brown carbon molecules can dominate the overall absorption. Therefore, it is of great importance to identify these molecules in order to estimate aerosol absorption. The gas-phase BrC molecules were mainly controlled by secondary formation (e.g. photochemical smog) and particle-to-gas partitioning. Secondary formation is an important source contributing to particle-phase BrC. During daytime, BrC in the particle phase can be oxidized leading to decreasing absorption of brown carbon aerosol. This is consistent with a previous study (Salvador et al., 2021). They found that 16 brown carbon molecules in the gas phase were mainly from secondary formation during the clear days and from primary emissions during polluted days.

Based on the results, it can be concluded that the dissertation answers all major research questions that were put forward in the beginning. This work demonstrates chemical compositions and optical properties of brown carbon aerosol from primary emissions, secondary formation, and in the ambient rural and urban atmosphere. This work helps to get better understanding of the link between chemical composition and optical properties of brown carbon aerosol. This work reveals that the temperatures, NO_2, and seed particles have a significant impact on chemical composition of brown carbon from oxidation of volatile organic compounds (toluene and indole) and lead to changing the optical properties of brown carbon. Besides, this work also reveals that photooxidation decreases the light absorption of brown carbon aerosol, and primary emission and secondary formation are major sources to contribute to brown carbon. This dissertation contributes to our fundamental understanding on physical and chemical properties of brown carbon aerosol, which improves our understanding for their impacts on visibility and climate. The major findings from this dissertation are summarized in a simplified concept in Figure 46.

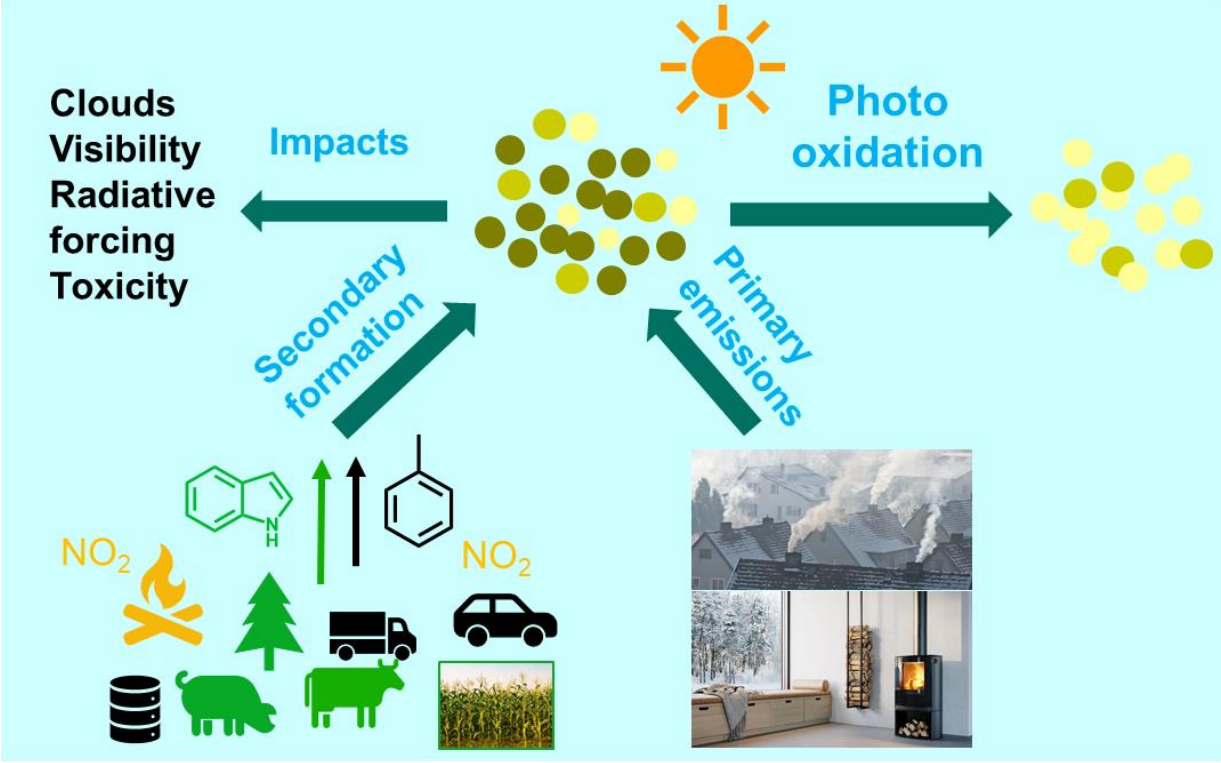

Figure 46. Schematic summary of results of my dissertation. Sources of toluene and indole are from anthropogenic and biogenic emissions. Secondary brown carbon is formed from oxidation of toluene and indole in presence of NOx or seed particles. Primary emissions of brown carbon are from biomass burning like a wood stove. The brown carbon VOC mixture can be photo-oxidized leading to the reduced average light absorption of aged brown carbon aerosol.

4.2 Outlook

This dissertation provides a comprehensive and substantial contribution to understanding chemical characterization and optical properties of brown carbon aerosol from primary emission, secondary formation and field campaigns with different sources. However, there are still some open scientific and technical questions which should be investigated in future studies:

1). There are strong biomass burning emissions at rural Germany and the black carbon concentration reached 5 μg m^{-3} at biomass burning events, since residences use wood stoves at home during the winter periods. Therefore, it needs more studies to demonstrate how biomass burning affects air quality in central Europe and how existing technologies could improve the situation. In addition, my findings may be a little contribution to achieve better regulations to control the biomass burning emissions in central Europe.

2). Indole is an important volatile organic compound in the atmosphere, especially near agricultural areas or animal husbandries. However, there are only a few studies to investigate the

indole emissions and concentration in field campaigns. Furthermore, chemical composition and formation mechanisms of indole secondary organic aerosol (SOA) at different conditions are still not yet well known.

3). 3-nitroindole has really high mass fraction of indole SOA in presence of NO_2 and seed particles. However, it still unclear whether surface chemistry, heterogeneous reactions, or volatility effects contribute to the efficient formation of 3-nitroindole. In addition, the 3-nitroindole is a really important product of indole SOA. It also needs more studies to investigate how 3-nitroindole affects human health and air quality.

4). FIGAERO-CIMS is a powerful instrument to measure the organic molecules in the gas and particle phases. I estimated BrC molecules from around two thousand molecules measured by FIGAERO-CIMS based on the double bond equivalent/carbon number ratio (DBE/C) of each molecule being higher than 0.5 and less than 0.9. Maybe one can refine the ways to identify brown carbon molecules from FIGAERO-CIMS measurements.

References

Baboomian, V. J., He, Q., Montoya-Aguilera, J., Ali, N., Fleming, L. T., Lin, P., Laskin, A., Laskin, J., Rudich, Y., and Nizkorodov, S. A.: Light absorption and scattering properties of indole secondary organic aerosol prepared under various oxidant and relative humidity conditions, Aerosol Science and Technology, 1-14, 10.1080/02786826.2023.2193235, 2023.

Baduel, C., Voisin, D., and Jaffrezo, J. L.: Seasonal variations of concentrations and optical properties of water soluble HULIS collected in urban environments, Atmospheric Chemistry and Physics, 10, 4085-4095, 10.5194/acp-10-4085-2010, 2010.

Bhattarai, H., Saikawa, E., Wan, X., Zhu, H. X., Ram, K., Gao, S. P., Kang, S. C., Zhang, Q. G., Zhang, Y. L., Wu, G. M., Wang, X. P., Kawamura, K., Fu, P. Q., and Cong, Z. Y.: Levoglucosan as a tracer of biomass burning: Recent progress and perspectives, Atmospheric Research, 220, 20-33, 10.1016/j.atmosres.2019.01.004, 2019.

Blake, R. S., Monks, P. S., and Ellis, A. M.: Proton-Transfer Reaction Mass Spectrometry, Chemical Reviews, 109, 861-896, 10.1021/cr800364q, 2009.

Bond, T. C., Doherty, S. J., Fahey, D. W., Forster, P. M., Berntsen, T., DeAngelo, B. J., Flanner, M. G., Ghan, S., Karcher, B., Koch, D., Kinne, S., Kondo, Y., Quinn, P. K., Sarofim, M. C., Schultz, M. G., Schulz, M., Venkataraman, C., Zhang, H., Zhang, S., Bellouin, N., Guttikunda, S. K., Hopke, P. K., Jacobson, M. Z., Kaiser, J. W., Klimont, Z., Lohmann, U., Schwarz, J. P., Shindell, D., Storelvmo, T., Warren, S. G., and Zender, C. S.: Bounding the role of black carbon in the climate system: A scientific assessment, Journal of Geophysical Research-Atmospheres, 118, 5380-5552, 10.1002/jgrd.50171, 2013.

Bruns, E. A., Krapf, M., Orasche, J., Huang, Y., Zimmermann, R., Drinovec, L., Močnik, G., El-Haddad, I., Slowik, J. G., Dommen, J., Baltensperger, U., and Prévôt, A. S. H.: Characterization of primary and secondary wood combustion products generated under different burner loads, Atmos. Chem. Phys., 15, 2825-2841, 10.5194/acp-15-2825-2015, 2015.

Budisulistiorini, S. H., Riva, M., Williams, M., Chen, J., Itoh, M., Surratt, J. D., and Kuwata, M.: Light-Absorbing Brown Carbon Aerosol Constituents from Combustion of Indonesian Peat and Biomass, Environ. Sci. Technol., 51, 4415-4423, 10.1021/acs.est.7b00397, 2017.

Cabada, J. C., Pandis, S. N., Subramanian, R., Robinson, A. L., Polidori, A., and Turpin, B.: Estimating the secondary organic aerosol contribution to PM2.5 using the EC tracer method, Aerosol Science and Technology, 38, 140-155, 10.1080/02786820390229084, 2004.

Canagaratna, M. R., Jayne, J. T., Jimenez, J. L., Allan, J. D., Alfarra, M. R., Zhang, Q., Onasch, T. B., Drewnick, F., Coe, H., Middlebrook, A., Delia, A., Williams, L. R., Trimborn, A. M., Northway, M. J., DeCarlo, P. F., Kolb, C. E., Davidovits, P., and Worsnop, D. R.: Chemical and microphysical characterization of ambient aerosols with the aerodyne aerosol mass spectrometer, Mass Spectrometry Reviews, 26, 185-222, 10.1002/mas.20115, 2007.

Chan, C. K., and Yao, X.: Air pollution in mega cities in China, Atmospheric Environment, 42, 1-42, 10.1016/j.atmosenv.2007.09.003, 2008.

Chen, Q. C., Miyazaki, Y., Kawamura, K., Matsumoto, K., Coburn, S., Volkamer, R., Iwamoto, Y., Kagami, S., Deng, Y. G., Ogawa, S., Ramasamy, S., Kato, S., Ida, A., Kajii, Y., and Mochida, M.: Characterization of Chromophoric Water-Soluble Organic Matter in Urban, Forest, and Marine Aerosols by HR-ToF-AMS Analysis and Excitation Emission Matrix Spectroscopy, Environ. Sci. Technol., 50, 10351-10360, 10.1021/acs.est.6b01643, 2016.

Chen, Q. C., Li, J. W., Hua, X. Y., Jiang, X. T., Mu, Z., Wang, M. M., Wang, J., Shan, M., Yang, X. D., Fan, X. J., Song, J. Z., Wang, Y. Q., Guan, D. J., and Du, L.: Identification of species and sources of atmospheric chromophores by fluorescence excitation-emission matrix with parallel factor analysis, Science of the Total Environment, 718, 10.1016/j.scitotenv.2020.137322, 2020.

Chen, Q. C., Hua, X. Y., Li, J. W., Chang, T., and Wang, Y. Q.: Diurnal evolutions and sources of water-soluble chromophoric aerosols over Xi'an during haze event, in Northwest China, Science of the Total Environment, 786, 10.1016/j.scitotenv.2021.147412, 2021.

Cheng, X., Chen, Q., Li, Y., Huang, G., Liu, Y., Lu, S., Zheng, Y., Qiu, W., Lu, K., Qiu, X., Bianchi, F., Yan, C., Yuan, B., Shao, M., Wang, Z., Canagaratna, M. R., Zhu, T., Wu, Y., and Zeng, L.: Secondary Production of Gaseous Nitrated Phenols in Polluted Urban Environments, Environ. Sci. Technol., 55, 4410-4419, 10.1021/acs.est.0c07988, 2021a.

Cheng, X., Chen, Q., Li, Y. J., Zheng, Y., Liao, K. R., and Huang, G. C.: Highly oxygenated organic molecules produced by the oxidation of benzene and toluene in a wide range of OH exposure and NOx conditions, Atmospheric Chemistry and Physics, 21, 12005-12019, 10.5194/acp-21-12005-2021, 2021b.

Clark, C. H., Kacarab, M., Nakao, S., Asa-Awuku, A., Sato, K., and Cocker, D. R.: Temperature Effects on Secondary Organic Aerosol (SOA) from the Dark Ozonolysis and Photo-Oxidation of Isoprene, Environ. Sci. Technol., 50, 5564-5571, 10.1021/acs.est.5b05524, 2016.

Cong, Z. Y., Kang, S. C., Dong, S. P., and Zhang, Y. L.: Individual Particle Analysis of Atmospheric Aerosols at Nam Co, Tibetan Plateau, Aerosol and Air Quality Research, 9, 323-331, 10.4209/aaqr.2008.12.0064, 2009.

Cory, R. M., and McKnight, D. M.: Fluorescence spectroscopy reveals ubiquitous presence of oxidized and reduced quinones in dissolved organic matter, Environ. Sci. Technol., 39, 8142-8149, 10.1021/es0506962, 2005.

Costabile, F., Gilardoni, S., Barnaba, F., Di Ianni, A., Di Liberto, L., Dionisi, D., Manigrasso, M., Paglione, M., Poluzzi, V., Rinaldi, M., Facchini, M. C., and Gobbi, G. P.: Characteristics of brown carbon in the urban Po Valley atmosphere, Atmospheric Chemistry and Physics, 17, 313-326, 10.5194/acp-17-313-2017, 2017.

Cuesta-Mosquera, A., Mocnik, G., Drinovec, L., Muller, T., Pfeifer, S., Minguillon, M. C., Briel, B., Buckley, P., Dudoitis, V., Fernandez-Garcia, J., Fernandez-Amado, M., De Brito, J. F., Riffault, V., Flentje, H., Heffernan, E., Kalivitis, N., Kalogridis, A. C., Keernik, H., Marmureanu, L., Luoma, K., Marinoni, A., Pikridas, M., Schauer, G., Serfozo, N., Servomaa, H., Titos, G., Yus-Diez, J., Ziola, N., and Wiedensohler, A.: Intercomparison and characterization of 23 Aethalometers under laboratory and ambient air conditions: procedures and unit-to-unit variabilities, Atmospheric Measurement Techniques, 14, 3195-3216, 10.5194/amt-14-3195-2021, 2021.

Day, M. C., Zhang, M. H., and Pandis, S. N.: Evaluation of the ability of the EC tracer method to estimate secondary organic carbon, Atmospheric Environment, 112, 317-325, 10.1016/j.atmosenv.2015.04.044, 2015.

De Haan, D. O., Corrigan, A. L., Smith, K. W., Stroik, D. R., Turley, J. J., Lee, F. E., Tolbert, M. A., Jimenez, J. L., Cordova, K. E., and Ferrell, G. R.: Secondary Organic Aerosol-Forming Reactions of Glyoxal with Amino Acids, Environ. Sci. Technol., 43, 2818-2824, 10.1021/es803534f, 2009.

De Haan, D. O., Jansen, K., Rynaski, A. D., Sueme, W. R. P., Torkelson, A. K., Czer, E. T., Kim, A. K., Rafla, M. A., De Haan, A. C., and Tolbert, M. A.: Brown Carbon Production by Aqueous-Phase Interactions of Glyoxal and SO2, Environ. Sci. Technol., 54, 4781-4789, 10.1021/acs.est.9b07852, 2020.

de Sa, S. S., Rizzo, L. V., Palm, B. B., Campuzano-Jost, P., Day, D. A., Yee, L. D., Wernis, R., Isaacman-VanWertz, G., Brito, J., Carbone, S., Liu, Y. J. J., Sedlacek, A., Springston, S., Goldstein, A. H., Barbosa, H. M. J., Alexander, M. L., Artaxo, P., Jimenez, J. L., and Martin, S. T.: Contributions of biomass-burning, urban, and biogenic emissions to the concentrations and light-absorbing properties of particulate matter in central Amazonia during the dry season, Atmospheric Chemistry and Physics, 19, 7973-8001, 10.5194/acp-19-7973-2019, 2019.

DeCarlo, P. F., Slowik, J. G., Worsnop, D. R., Davidovits, P., and Jimenez, J. L.: Particle morphology and density characterization by combined mobility and aerodynamic diameter measurements. Part 1: Theory, Aerosol Science and Technology, 38, 1185-1205, 10.1080/027868290903907, 2004.

DeCarlo, P. F., Kimmel, J. R., Trimborn, A., Northway, M. J., Jayne, J. T., Aiken, A. C., Gonin, M., Fuhrer, K., Horvath, T., Docherty, K. S., Worsnop, D. R., and Jimenez, J. L.: Field-deployable, high-resolution, time-of-flight aerosol mass spectrometer, Analytical Chemistry, 78, 8281-8289, 10.1021/ac061249n, 2006.

Deng, J. J., Ma, H., Wang, X. F., Zhong, S. J., Zhang, Z. M., Zhu, J. L., Fan, Y. B., Hu, W., Wu, L. B., Li, X. D., Ren, L. J., Pavuluri, C. M., Pan, X. L., Sun, Y. L., Wang, Z. F., Kawamura, K., and Fu, P. Q.: Measurement report: Optical properties and sources of water-soluble brown carbon in Tianjin, North China insights from organic molecular compositions, Atmospheric Chemistry and Physics, 22, 6449-6470, 10.5194/acp-22-6449-2022, 2022.

Devi, J. J., Bergin, M. H., McKenzie, M., Schauer, J. J., and Weber, R. J.: Contribution of particulate brown carbon to light absorption in the rural and urban Southeast US, Atmospheric Environment, 136, 95-104, 10.1016/j.atmosenv.2016.04.011, 2016.

Donahue, N. M., Robinson, A. L., and Pandis, S. N.: Atmospheric organic particulate matter: From smoke to secondary organic aerosol, Atmospheric Environment, 43, 94-106, 10.1016/j.atmosenv.2008.09.055, 2009.

Drinovec, L., Mocnik, G., Zotter, P., Prevot, A. S. H., Ruckstuhl, C., Coz, E., Rupakheti, M., Sciare, J., Muller, T., Wiedensohler, A., and Hansen, A. D. A.: The "dual-spot" Aethalometer: an improved measurement of aerosol black carbon with real-time loading compensation, Atmospheric Measurement Techniques, 8, 1965-1979, 10.5194/amt-8-1965-2015, 2015.

Du, Z. Y., He, K. B., Cheng, Y., Duan, F. K., Ma, Y. L., Liu, J. M., Zhang, X. L., Zheng, M., and Weber, R.: A yearlong study of water-soluble organic carbon in Beijing II: Light absorption properties, Atmospheric Environment, 89, 235-241, 10.1016/j.atmosenv.2014.02.022, 2014.

Eichler, P., Muller, M., D'Anna, B., and Wisthaler, A.: A novel inlet system for online chemical analysis of semi-volatile submicron particulate matter, Atmospheric Measurement Techniques, 8, 1353-1360, 10.5194/amt-8-1353-2015, 2015.

Fan, J. W., Wang, Y., Rosenfeld, D., and Liu, X. H.: Review of Aerosol-Cloud Interactions: Mechanisms, Significance, and Challenges, Journal of the Atmospheric Sciences, 73, 4221-4252, 10.1175/jas-d-16-0037.1, 2016.

Fan, X. J., Cao, T., Yu, X. F., Wang, Y., Xiao, X., Li, F. Y., Xie, Y., Ji, W. C., Song, J. Z., and Peng, P. A.: The evolutionary behavior of chromophoric brown carbon during ozone aging of fine particles from biomass burning, Atmospheric Chemistry and Physics, 20, 4593-4605, 10.5194/acp-20-4593-2020, 2020.

Feng, Y., Ramanathan, V., and Kotamarthi, V. R.: Brown carbon: a significant atmospheric absorber of solar radiation?, Atmospheric Chemistry and Physics, 13, 8607-8621, 10.5194/acp-13-8607-2013, 2013.

Gao, L., Song, J., Mohr, C., Huang, W., Vallon, M., Jiang, F., Leisner, T., and Saathoff, H.: Kinetics, SOA yields, and chemical composition of secondary organic aerosol from β-caryophyllene ozonolysis with and without nitrogen oxides between 213 and 313 K, Atmos. Chem. Phys., 22, 6001-6020, 10.5194/acp-22-6001-2022, 2022.

Gentner, D. R., Ormeno, E., Fares, S., Ford, T. B., Weber, R., Park, J. H., Brioude, J., Angevine, W. M., Karlik, J. F., and Goldstein, A. H.: Emissions of terpenoids, benzenoids, and other biogenic gas-phase organic compounds from agricultural crops and their potential implications for air quality, Atmospheric Chemistry and Physics, 14, 5393-5413, 10.5194/acp-14-5393-2014, 2014.

Goldstein, A. H., and Galbally, I. E.: Known and unexplored organic constituents in the earth's atmosphere, Environ. Sci. Technol., 41, 1514-1521, 10.1021/es072476p, 2007.

Graber, E. R., and Rudich, Y.: Atmospheric HULIS: How humic-like are they? A comprehensive and critical review, Atmospheric Chemistry and Physics, 6, 729-753, 10.5194/acp-6-729-2006, 2006.

Gundel, L. A., Dod, R. L., Rosen, H., and Novakov, T.: THE RELATIONSHIP BETWEEN OPTICAL ATTENUATION AND BLACK CARBON CONCENTRATION FOR AMBIENT AND SOURCE PARTICLES, Science of the Total Environment, 36, 197-202, 10.1016/0048-9697(84)90266-3, 1984.

Hagemann, R., Corsmeier, U., Kottmeier, C., Rinke, R., Wieser, A., and Vogel, B.: Spatial variability of particle number concentrations and NOx in the Karlsruhe (Germany) area obtained with the. mobile laboratory 'AERO-TRAM', Atmospheric Environment, 94, 341-352, 10.1016/j.atmosenv.2014.05.051, 2014.

He, Q. F., Li, C. L., Siemens, K., Morales, A. C., Hettiyadura, A. P. S., Laskin, A., and Rudich, Y.: Optical Properties of Secondary Organic Aerosol Produced by Photooxidation of Naphthalene under NOx Condition, Environ. Sci. Technol., 56, 4816-4827, 10.1021/acs.est.1c07328, 2022.

Hecobian, A., Zhang, X., Zheng, M., Frank, N., Edgerton, E. S., and Weber, R. J.: Water-Soluble Organic Aerosol material and the light-absorption characteristics of aqueous extracts measured over the Southeastern United States, Atmospheric Chemistry and Physics, 10, 5965-5977, 10.5194/acp-10-5965-2010, 2010.

Hems, R. F., Schnitzler, E. G., Liu-Kang, C., Cappa, C. D., and Abbatt, J. P. D.: Aging of Atmospheric Brown Carbon Aerosol, Acs Earth and Space Chemistry, 5, 722-748, 10.1021/acsearthspacechem.0c00346, 2021.

Herckes, P., Valsaraj, K. T., and Collett, J. L., Jr.: A review of observations of organic matter in fogs and clouds: Origin, processing and fate, Atmospheric Research, 132, 434-449, 10.1016/j.atmosres.2013.06.005, 2013.

Heringa, M. F., DeCarlo, P. F., Chirico, R., Tritscher, T., Dommen, J., Weingartner, E., Richter, R., Wehrle, G., Prevot, A. S. H., and Baltensperger, U.: Investigations of primary and secondary particulate matter of different wood combustion appliances with a high-resolution time-of-flight aerosol mass spectrometer, Atmospheric Chemistry and Physics, 11, 5945-5957, 10.5194/acp-11-5945-2011, 2011.

Hettiyadura, A. P. S., Garcia, V., Li, C., West, C. P., Tomlin, J., He, Q., Rudich, Y., and Laskin, A.: Chemical Composition and Molecular-Specific Optical Properties of Atmospheric Brown Carbon Associated with Biomass Burning, Environ. Sci. Technol., 10.1021/acs.est.0c05883, 2021.

Hildebrandt, L., Donahue, N. M., and Pandis, S. N.: High formation of secondary organic aerosol from the photo-oxidation of toluene, Atmospheric Chemistry and Physics, 9, 2973-2986, 10.5194/acp-9-2973-2009, 2009.

Hinks, M. L., Montoya-Aguilera, J., Ellison, L., Lin, P., Laskin, A., Laskin, J., Shiraiwa, M., Dabdub, D., and Nizkorodov, S. A.: Effect of relative humidity on the composition of secondary organic aerosol from the oxidation of toluene, Atmospheric Chemistry and Physics, 18, 1643-1652, 10.5194/acp-18-1643-2018, 2018.

Hoffer, A., Gelencser, A., Guyon, P., Kiss, G., Schmid, O., Frank, G. P., Artaxo, P., and Andreae, M. O.: Optical properties of humic-like substances (HULIS) in biomass-burning aerosols, Atmospheric Chemistry and Physics, 6, 3563-3570, 10.5194/acp-6-3563-2006, 2006.

Hoffer, A., Toth, A., Nyiro-Kosa, I., Posfai, M., and Gelencser, A.: Light absorption properties of laboratory-generated tar ball particles, Atmospheric Chemistry and Physics, 16, 239-246, 10.5194/acp-16-239-2016, 2016.

Huang, R. J., Yang, L., Cao, J. J., Chen, Y., Chen, Q., Li, Y. J., Duan, J., Zhu, C. S., Dai, W. T., Wang, K., Lin, C. S., Ni, H. Y., Corbin, J. C., Wu, Y. F., Zhang, R. J., Tie, X. X., Hoffmann, T., O'Dowd, C., and Dusek, U.: Brown Carbon Aerosol in Urban Xi'an, Northwest China: The Composition and Light Absorption Properties, Environ. Sci. Technol., 52, 6825-6833, 10.1021/acs.est.8b02386, 2018.

Huang, W., Saathoff, H., Shen, X. L., Ramisetty, R., Leisner, T., and Mohr, C.: Seasonal characteristics of organic aerosol chemical composition and volatility in Stuttgart, Germany, Atmospheric Chemistry and Physics, 19, 11687-11700, 10.5194/acp-19-11687-2019, 2019.

Jiang, F., Song, J., Bauer, J., Gao, L., Vallon, M., Gebhardt, R., Leisner, T., Norra, S., and Saathoff, H.: Chromophores and chemical composition of brown carbon characterized at an urban kerbside by excitation–emission spectroscopy and mass spectrometry, Atmos. Chem. Phys., 22, 14971-14986, 10.5194/acp-22-14971-2022, 2022.

Jiang, H. H., Frie, A. L., Lavi, A., Chen, J. Y., Zhang, H. F., Bahreini, R., and Lin, Y. H.: Brown Carbon Formation from Nighttime Chemistry of Unsaturated Heterocyclic Volatile Organic Compounds, Environmental Science & Technology Letters, 6, 184-190, 10.1021/acs.estlett.9b00017, 2019.

Jimenez, J. L., Canagaratna, M. R., Donahue, N. M., Prevot, A. S. H., Zhang, Q., Kroll, J. H., DeCarlo, P. F., Allan, J. D., Coe, H., Ng, N. L., Aiken, A. C., Docherty, K. S., Ulbrich, I. M., Grieshop, A. P., Robinson, A. L., Duplissy, J., Smith, J. D., Wilson, K. R., Lanz, V. A., Hueglin, C., Sun, Y. L., Tian, J., Laaksonen, A., Raatikainen, T., Rautiainen, J., Vaattovaara, P., Ehn, M., Kulmala, M., Tomlinson, J. M., Collins, D. R., Cubison, M. J., Dunlea, E. J., Huffman, J. A., Onasch, T. B., Alfarra, M. R., Williams, P. I., Bower, K., Kondo, Y., Schneider, J., Drewnick, F., Borrmann, S., Weimer, S., Demerjian, K., Salcedo, D., Cottrell, L., Griffin, R., Takami, A., Miyoshi, T., Hatakeyama, S., Shimono, A., Sun, J. Y., Zhang, Y. M., Dzepina, K., Kimmel, J. R., Sueper, D., Jayne, J. T., Herndon, S. C., Trimborn, A. M., Williams, L. R., Wood, E. C., Middlebrook, A. M., Kolb, C. E., Baltensperger, U., and Worsnop, D. R.: Evolution of Organic Aerosols in the Atmosphere, Science, 326, 1525-1529, 10.1126/science.1180353, 2009.

Kasthuriarachchi, N. Y., Rivellini, L. H., Adam, M. G., and Lee, A. K. Y.: Light Absorbing Properties of Primary and Secondary Brown Carbon in a Tropical Urban Environment, Environ. Sci. Technol., 54, 10808-10819, 10.1021/acs.est.0c02414, 2020.

Koch, B. P., and Dittmar, T.: From mass to structure: an aromaticity index for high-resolution mass data of natural organic matter, Rapid Communications in Mass Spectrometry, 20, 926-932, 10.1002/rcm.2386, 2006.

Kodros, J. K., Kaltsonoudis, C., Paglione, M., Florou, K., Jorga, S., Vasilakopoulou, C., Cirtog, M., Cazaunau, M., Picquet-Varrault, B., Nenes, A., and Pandis, S. N.: Secondary aerosol formation during the dark oxidation of residential biomass burning emissions, Environmental science: atmospheres, 2, 1221-1236, 10.1039/D2EA00031H, 2022.

Kong, X. R., Salvador, C. M., Carlsson, S., Pathak, R., Davidsson, K. O., Le Breton, M., Gaita, S. M., Mitra, K., Hallquist, A. M., Hallquist, M., and Pettersson, J. B. C.: Molecular characterization and optical properties of primary emissions from a residential wood burning boiler, Science of the Total Environment, 754, 10.1016/j.scitotenv.2020.142143, 2021.

Kroll, J. H., Donahue, N. M., Jimenez, J. L., Kessler, S. H., Canagaratna, M. R., Wilson, K. R., Altieri, K. E., Mazzoleni, L. R., Wozniak, A. S., Bluhm, H., Mysak, E. R., Smith, J. D., Kolb, C. E., and Worsnop, D. R.: Carbon oxidation state as a metric for describing the chemistry of atmospheric organic aerosol, Nature Chemistry, 3, 133-139, 10.1038/nchem.948, 2011.

Lambe, A. T., Zhang, J. Y., Sage, A. M., and Donahue, N. M.: Controlled OH radical production via ozone-alkene reactions for use in aerosol aging studies, Environ. Sci. Technol., 41, 2357-2363, 10.1021/es061878e, 2007.

Laskin, A., Laskin, J., and Nizkorodov, S. A.: Chemistry of Atmospheric Brown Carbon, Chemical Reviews, 115, 4335-4382, 10.1021/cr5006167, 2015.

Le Breton, M., Psichoudaki, M., Hallquist, M., Watne, A. K., Lutz, A., and Hallquist, A. M.: Application of a FIGAERO ToF CIMS for on-line characterization of real-world fresh and aged particle emissions from buses, Aerosol Science and Technology, 53, 244-259, 10.1080/02786826.2019.1566592, 2019.

Lee, B. H., Lopez-Hilfiker, F. D., Mohr, C., Kurten, T., Worsnop, D. R., and Thornton, J. A.: An Iodide-Adduct High-Resolution Time-of-Flight Chemical-Ionization Mass Spectrometer: Application to Atmospheric Inorganic and Organic Compounds, Environ. Sci. Technol., 48, 6309-6317, 10.1021/es500362a, 2014.

Lee, H. J., Laskin, A., Laskin, J., and Nizkorodov, S. A.: Excitation-Emission Spectra and Fluorescence Quantum Yields for Fresh and Aged Biogenic Secondary Organic Aerosols, Environ. Sci. Technol., 47, 5763-5770, 10.1021/es400644c, 2013.

Li, C. L., Windwer, E., Fang, Z., Nissenbaum, D., and Rudich, Y.: Correcting micro-aethalometer absorption measurements for brown carbon aerosol, Science of the Total Environment, 777, 10.1016/j.scitotenv.2021.146143, 2021a.

Li, X., Wang, Y. J., Hu, M., Tan, T. Y., Li, M. R., Wu, Z. J., Chen, S. Y., and Tang, X. Y.: Characterizing chemical composition and light absorption of nitroaromatic compounds in the winter of Beijing, Atmospheric Environment, 237, 10.1016/j.atmosenv.2020.117712, 2020.

Li, Y. X., Zhao, J. Y., Wang, Y., Seinfeld, J. H., and Zhang, R. Y.: Multigeneration Production of Secondary Organic Aerosol from Toluene Photooxidation, Environ. Sci. Technol., 55, 8592-8603, 10.1021/acs.est.1c02026, 2021b.

Lin, P., Liu, J., Shilling, J. E., Kathmann, S. M., Laskin, J., and Laskin, A.: Molecular characterization of brown carbon (BrC) chromophores in secondary organic aerosol generated from photo-oxidation of toluene, Physical Chemistry Chemical Physics, 17, 23312-23325, 10.1039/c5cp02563j, 2015.

Lin, P., Fleming, L. T., Nizkorodov, S. A., Laskin, J., and Laskin, A.: Comprehensive Molecular Characterization of Atmospheric Brown Carbon by High Resolution Mass Spectrometry with Electrospray and Atmospheric Pressure Photoionization, Analytical Chemistry, 90, 12493-12502, 10.1021/acs.analchem.8b02177, 2018.

Linke, C., Ibrahim, I., Schleicher, N., Hitzenberger, R., Andreae, M. O., Leisner, T., and Schnaiter, M.: A novel single-cavity three-wavelength photoacoustic spectrometer for atmospheric aerosol research, Atmospheric Measurement Techniques, 9, 5331-5346, 10.5194/amt-9-5331-2016, 2016.

Liu, D., Li, S., Hu, D., Kong, S., Cheng, Y., Wu, Y., Ding, S., Hu, K., Zheng, S., Yan, Q., Zheng, H., Zhao, D., Tian, P., Ye, J., Huang, M., and Ding, D.: Evolution of Aerosol Optical Properties from Wood Smoke in Real Atmosphere Influenced by Burning Phase and Solar Radiation, Environ. Sci. Technol., 55, 5677-5688, 10.1021/acs.est.0c07569, 2021a.

Liu, S., Huang, D., Wang, Y., Zhang, S., Liu, X., Wu, C., Du, W., and Wang, G.: Synergetic effects of NH3 and NOx on the production and optical absorption of secondary organic aerosol formation from toluene photooxidation, Atmos. Chem. Phys., 21, 17759-17773, 10.5194/acp-21-17759-2021, 2021b.

Lopez-Hilfiker, F. D., Mohr, C., Ehn, M., Rubach, F., Kleist, E., Wildt, J., Mentel, T. F., Lutz, A., Hallquist, M., Worsnop, D., and Thornton, J. A.: A novel method for online analysis of gas and particle composition: description and evaluation of a Filter Inlet for Gases and AEROsols (FIGAERO), Atmospheric Measurement Techniques, 7, 983-1001, 10.5194/amt-7-983-2014, 2014.

Lopez-Hilfiker, F. D., Iyer, S., Mohr, C., Lee, B. H., D'Ambro, E. L., Kurten, T., and Thornton, J. A.: Constraining the sensitivity of iodide adduct chemical ionization mass spectrometry to multifunctional organic molecules using the collision limit and thermodynamic stability of iodide ion adducts, Atmospheric Measurement Techniques, 9, 1505-1512, 10.5194/amt-9-1505-2016, 2016.

Martinsson, J., Eriksson, A. C., Nielsen, I. E., Malmborg, V. B., Ahlberg, E., Andersen, C., Lindgren, R., Nystrom, R., Nordin, E. Z., Brune, W. H., Svenningsson, B., Swietlicki, E., Boman, C., and Pagels, J. H.: Impacts of Combustion Conditions and Photochemical Processing on the Light Absorption of Biomass Combustion Aerosol, Environ. Sci. Technol., 49, 14663-14671, 10.1021/acs.est.5b03205, 2015.

Matos, J. T. V., Freire, S., Duarte, R., and Duarte, A. C.: Natural organic matter in urban aerosols: Comparison between water and alkaline soluble components using excitation-emission matrix fluorescence spectroscopy and multiway data analysis, Atmospheric Environment, 102, 1-10, 10.1016/j.atmosenv.2014.11.042, 2015.

Mayorga, R., Chen, K., Raeofy, N., Woods, M., Lum, M., Zhao, Z., Zhang, W., Bahreini, R., Lin, Y.-H., and Zhang, H.: Chemical Structure Regulates the Formation of Secondary Organic Aerosol and Brown Carbon in Nitrate Radical Oxidation of Pyrroles and Methylpyrroles, Environ. Sci. Technol., 10.1021/acs.est.2c02345, 2022.

Mladenov, N., Alados-Arboledas, L., Olmo, F. J., Lyamani, H., Delgado, A., Molina, A., and Reche, I.: Applications of optical spectroscopy and stable isotope analyses to organic aerosol source discrimination in an urban area, Atmospheric Environment, 45, 1960-1969, 10.1016/j.atmosenv.2011.01.029, 2011.

Mohr, C., DeCarlo, P. F., Heringa, M. F., Chirico, R., Slowik, J. G., Richter, R., Reche, C., Alastuey, A., Querol, X., Seco, R., Penuelas, J., Jimenez, J. L., Crippa, M., Zimmermann, R., Baltensperger, U., and Prevot, A. S. H.: Identification and quantification of organic aerosol from cooking and other sources in Barcelona using aerosol mass spectrometer data, Atmospheric Chemistry and Physics, 12, 1649-1665, 10.5194/acp-12-1649-2012, 2012.

Mohr, C., Lopez-Hilfiker, F. D., Zotter, P., Prevot, A. S. H., Xu, L., Ng, N. L., Herndon, S. C., Williams, L. R., Franklin, J. P., Zahniser, M. S., Worsnop, D. R., Knighton, W. B., Aiken, A. C., Gorkowski, K. J., Dubey, M. K., Allan, J. D., and Thornton, J. A.: Contribution of Nitrated Phenols to Wood Burning Brown Carbon Light Absorption in Detling, United Kingdom during Winter Time, Environ. Sci. Technol., 47, 6316-6324, 10.1021/es400683v, 2013.

Moise, T., Flores, J. M., and Rudich, Y.: Optical Properties of Secondary Organic Aerosols and Their Changes by Chemical Processes, Chemical Reviews, 115, 4400-4439, 10.1021/cr5005259, 2015.

Montoya-Aguilera, J., Horne, J. R., Hinks, M. L., Fleming, L. T., Perraud, V., Lin, P., Laskin, A., Laskin, J., Dabdub, D., and Nizkorodov, S. A.: Secondary organic aerosol from atmospheric photooxidation of indole, Atmospheric Chemistry and Physics, 17, 11605-11621, 10.5194/acp-17-11605-2017, 2017.

Morville, S., Scheyer, A., Mirabel, P., and Millet, M.: A multiresidue method for the analysis of phenols and nitrophenols in the atmosphere, Journal of Environmental Monitoring, 6, 963-966, 10.1039/b408756a, 2004.

Moschos, V., Kumar, N. K., Daellenbach, K. R., Baltensperger, U., Prevot, A. S. H., and El Haddad, I.: Source Apportionment of Brown Carbon Absorption by Coupling Ultraviolet-Visible Spectroscopy with Aerosol Mass Spectrometry, Environmental Science & Technology Letters, 5, 302-+, 10.1021/acs.estlett.8b00118, 2018.

Moschos, V., Gysel-Beer, M., Modini, R. L., Corbin, J. C., Massabo, D., Costa, C., Danelli, S. G., Vlachou, A., Daellenbach, K. R., Szidat, S., Prati, P., Prevot, A. S. H., Baltensperger, U., and El Haddad, I.: Source-specific light absorption by carbonaceous components in the complex aerosol matrix from yearly filter-based measurements, Atmospheric Chemistry and Physics, 21, 12809-12833, 10.5194/acp-21-12809-2021, 2021.

Mukherjee, A., Dey, S., Rana, A., Jia, S. G., Banerjee, S., and Sarkar, S.: Sources and atmospheric processing of brown carbon and HULIS in the Indo-Gangetic Plain: Insights from compositional analysis, Environmental Pollution, 267, 10.1016/j.envpol.2020.115440, 2020.

Murphy, K. R., Stedmon, C. A., Graeber, D., and Bro, R.: Fluorescence spectroscopy and multi-way techniques. PARAFAC, Analytical Methods, 5, 6557-6566, 10.1039/c3ay41160e, 2013.

Ng, N. L., Kroll, J. H., Chan, A. W. H., Chhabra, P. S., Flagan, R. C., and Seinfeld, J. H.: Secondary organic aerosol formation from m-xylene, toluene, and benzene, Atmospheric Chemistry and Physics, 7, 3909-3922, 10.5194/acp-7-3909-2007, 2007.

Nguyen, T. B., Laskin, A., Laskin, J., and Nizkorodov, S. A.: Brown carbon formation from ketoaldehydes of biogenic monoterpenes, Faraday Discussions, 165, 473-494, 10.1039/c3fd00036b, 2013.

Palm, B. B., Peng, Q. Y., Fredrickson, C. D., Lee, B., Garofalo, L. A., Pothier, M. A., Kreidenweis, S. M., Farmer, D. K., Pokhrel, R. P., Shen, Y. J., Murphy, S. M., Permar, W., Hu, L., Campos, T. L., Hall, S. R., Ullmann, K., Zhang, X., Flocke, F., Fischer, E. V., and Thornton, J. A.: Quantification of organic aerosol and brown carbon evolution in fresh wildfire plumes, Proceedings of the National Academy of Sciences of the United States of America, 117, 29469-29477, 10.1073/pnas.2012218117, 2020.

Park, R. J., Kim, M. J., Jeong, J. I., Youn, D., and Kim, S.: A contribution of brown carbon aerosol to the aerosol light absorption and its radiative forcing in East Asia, Atmospheric Environment, 44, 1414-1421, 10.1016/j.atmosenv.2010.01.042, 2010.

Poschl, U.: Atmospheric aerosols: composition, transformation, climate and health effects, Angew Chem Int Ed Engl, 44, 7520-7540, 10.1002/anie.200501122, 2005.

Posfai, M., Simonics, R., Li, J., Hobbs, P. V., and Buseck, P. R.: Individual aerosol particles from biomass burning in southern Africa: 1. Compositions and size distributions of carbonaceous particles, Journal of Geophysical Research-Atmospheres, 108, 10.1029/2002jd002291, 2003.

Pucher, M., Wunsch, U., Weigelhofer, G., Murphy, K., Hein, T., and Graeber, D.: staRdom: Versatile Software for Analyzing Spectroscopic Data of Dissolved Organic Matter in R, Water, 11, 10.3390/w11112366, 2019.

Ramanathan, V., Li, F., Ramana, M. V., Praveen, P. S., Kim, D., Corrigan, C. E., Nguyen, H., Stone, E. A., Schauer, J. J., Carmichael, G. R., Adhikary, B., and Yoon, S. C.: Atmospheric brown clouds:

Hemispherical and regional variations in long-range transport, absorption, and radiative forcing, Journal of Geophysical Research-Atmospheres, 112, 10.1029/2006jd008124, 2007.

Ravindra, K., Sokhi, R., and Van Grieken, R.: Atmospheric polycyclic aromatic hydrocarbons: Source attribution, emission factors and regulation, Atmospheric Environment, 42, 2895-2921, 10.1016/j.atmosenv.2007.12.010, 2008.

Rizzo, L. V., Artaxo, P., Muller, T., Wiedensohler, A., Paixao, M., Cirino, G. G., Arana, A., Swietlicki, E., Roldin, P., Fors, E. O., Wiedemann, K. T., Leal, L. S. M., and Kulmala, M.: Long term measurements of aerosol optical properties at a primary forest site in Amazonia, Atmospheric Chemistry and Physics, 13, 2391-2413, 10.5194/acp-13-2391-2013, 2013.

Saarikoski, S., Niemi, J. V., Aurela, M., Pirjola, L., Kousa, A., Ronkko, T., and Timonen, H.: Sources of black carbon at residential and traffic environments obtained by two source apportionment methods, Atmospheric Chemistry and Physics, 21, 14851-14869, 10.5194/acp-21-14851-2021, 2021.

Saathoff, H., Naumann, K. H., Mohler, O., Jonsson, A. M., Hallquist, M., Kiendler-Scharr, A., Mentel, T. F., Tillmann, R., and Schurath, U.: Temperature dependence of yields of secondary organic aerosols from the ozonolysis of alpha-pinene and limonene, Atmospheric Chemistry and Physics, 9, 1551-1577, 10.5194/acp-9-1551-2009, 2009.

Saleh, R., Robinson, E. S., Tkacik, D. S., Ahern, A. T., Liu, S., Aiken, A. C., Sullivan, R. C., Presto, A. A., Dubey, M. K., Yokelson, R. J., Donahue, N. M., and Robinson, A. L.: Brownness of organics in aerosols from biomass burning linked to their black carbon content, Nature Geoscience, 7, 647-650, 10.1038/ngeo2220, 2014.

Saleh, R., Cheng, Z. Z., and Atwi, K.: The Brown-Black Continuum of Light-Absorbing Combustion Aerosols, Environmental Science & Technology Letters, 5, 508-513, 10.1021/acs.estlett.8b00305, 2018.

Saleh, R.: From Measurements to Models: Toward Accurate Representation of Brown Carbon in Climate Calculations, Current Pollution Reports, 6, 90-104, 10.1007/s40726-020-00139-3, 2020.

Salo, K., Hallquist, M., Jonsson, A. M., Saathoff, H., Naumann, K. H., Spindler, C., Tillmann, R., Fuchs, H., Bohn, B., Rubach, F., Mentel, T. F., Muller, L., Reinnig, M., Hoffmann, T., and Donahue, N. M.: Volatility of secondary organic aerosol during OH radical induced ageing, Atmospheric Chemistry and Physics, 11, 11055-11067, 10.5194/acp-11-11055-2011, 2011.

Salvador, C. M. G., Tang, R. Z., Priestley, M., Li, L. J., Tsiligiannis, E., Le Breton, M., Zhu, W. F., Zeng, L. M., Wang, H., Yu, Y., Hu, M., Guo, S., and Hallquist, M.: Ambient nitro-aromatic compounds - biomass burning versus secondary formation in rural China, Atmospheric Chemistry and Physics, 21, 1389-1406, 10.5194/acp-21-1389-2021, 2021.

Sanchez, J., Tanner, D. J., Chen, D. X., Huey, L. G., and Ng, N. L.: A new technique for the direct detection of HO2 radicals using bromide chemical ionization mass spectrometry (Br-CIMS): initial characterization, Atmospheric Measurement Techniques, 9, 3851-3861, 10.5194/amt-9-3851-2016, 2016.

Sandradewi, J., Prevot, A. S. H., Szidat, S., Perron, N., Alfarra, M. R., Lanz, V. A., Weingartner, E., and Baltensperger, U.: Using aerosol light absorption measurements for the quantitative determination of wood burning and traffic emission contributions to particulate matter, Environ. Sci. Technol., 42, 3316-3323, 10.1021/es702253m, 2008a.

Sandradewi, J., Prevot, A. S. H., Weingartner, E., Schmidhauser, R., Gysel, M., and Baltensperger, U.: A study of wood burning and traffic aerosols in an Alpine valley using a multi-wavelength Aethalometer, Atmospheric Environment, 42, 101-112, 10.1016/j.atmosenv.2007.09.034, 2008b.

Satish, R., Shamjad, P., Thamban, N., Tripathi, S., and Rastogi, N.: Temporal Characteristics of Brown Carbon over the Central Indo-Gangetic Plain, Environ. Sci. Technol., 51, 6765-6772, 10.1021/acs.est.7b00734, 2017.

Seinfeld, J., and Pandis, S.: Atmospheric Chemistry and Physics From Air Pollution to Climate Change, Hoboken, NJ, USA, John Wiley&Sons, in, Inc, 2006.

Sekimoto, K., Inomata, S., Tanimoto, H., Fushimi, A., Fujitani, Y., Sato, K., and Yamada, H.: Characterization of nitromethane emission from automotive exhaust, Atmospheric Environment, 81, 523-531, 10.1016/j.atmosenv.2013.09.031, 2013.

Shen, X., Vogel, H., Vogel, B., Huang, W., Mohr, C., Ramisetty, R., Leisner, T., Prévôt, A. S. H., and Saathoff, H.: Composition and origin of PM2.5 aerosol particles in the upper Rhine valley in summer, Atmos. Chem. Phys. Discuss., 2019, 1-30, 10.5194/acp-2019-441, 2019.

Shen, Z. X., Zhang, Q., Cao, J. J., Zhang, L. M., Lei, Y. L., Huang, Y., Huang, R. J., Gao, J. J., Zhao, Z. Z., Zhu, C. S., Yin, X. L., Zheng, C. L., Xu, H. M., and Liu, S. X.: Optical properties and possible sources of brown carbon in PM2.5 over Xi'an, China, Atmospheric Environment, 150, 322-330, 10.1016/j.atmosenv.2016.11.024, 2017.

Siemens, K., Morales, A., He, Q., Li, C., Hettiyadura, A. P. S., Rudich, Y., and Laskin, A.: Molecular Analysis of Secondary Brown Carbon Produced from the Photooxidation of Naphthalene, Environ. Sci. Technol., 56, 3340-3353, 10.1021/acs.est.1c03135, 2022.

Song, J. W., Saathoff, H., Gao, L. Y., Gebhardt, R., Jiang, F., Vallon, M., Bauer, J., Norra, S., and Leisner, T.: Variations of PM2.5 sources in the context of meteorology and seasonality at an urban street canyon in Southwest Germany, Atmospheric Environment, 282, 10.1016/j.atmosenv.2022.119147, 2022.

Stefenelli, G., Pospisilova, V., Lopez-Hilfiker, F. D., Daellenbach, K. R., Huglin, C., Tong, Y. D., Baltensperger, U., Prevot, A. S. H., and Slowik, J. G.: Organic aerosol source apportionment in Zurich using an extractive electrospray ionization time-of-flight mass spectrometer (EESI-TOF-MS) - Part 1: Biogenic influences and day-night chemistry in summer, Atmospheric Chemistry and Physics, 19, 14825-14848, 10.5194/acp-19-14825-2019, 2019.

Sumlin, B. J., Pandey, A., Walker, M. J., Pattison, R. S., Williams, B. J., and Chakrabarty, R. K.: Atmospheric Photooxidation Diminishes Light Absorption by Primary Brown Carbon Aerosol from Biomass Burning, Environmental Science & Technology Letters, 4, 540-545, 10.1021/acs.estlett.7b00393, 2017.

Sundberg, R.: The chemistry of indoles, Elsevier, 2012.

Svendby, T. M., Lazaridis, M., and Torseth, K.: Temperature dependent secondary organic aerosol formation from terpenes and aromatics, Journal of Atmospheric Chemistry, 59, 25-46, 10.1007/s10874-007-9093-7, 2008.

Tang, J., Li, J., Su, T., Han, Y., Mo, Y. Z., Jiang, H. X., Cui, M., Jiang, B., Chen, Y. J., Tang, J. H., Song, J. Z., Peng, P. A., and Zhang, G.: Molecular compositions and optical properties of dissolved brown carbon in biomass burning, coal combustion, and vehicle emission aerosols illuminated by excitation-emission matrix spectroscopy and Fourier transform ion cyclotron resonance mass spectrometry analysis, Atmospheric Chemistry and Physics, 20, 2513-2532, 10.5194/acp-20-2513-2020, 2020.

Teich, M., van Pinxteren, D., Wang, M., Kecorius, S., Wang, Z. B., Muller, T., Mocnik, G., and Herrmann, H.: Contributions of nitrated aromatic compounds to the light absorption of water-soluble and particulate brown carbon in different atmospheric environments in Germany and China, Atmospheric Chemistry and Physics, 17, 1653-1672, 10.5194/acp-17-1653-2017, 2017.

Thieringer, J. R. D., Szabadi, J., Meyer, J., and Dittler, A.: Impact of Residential Real-World Wood Stove Operation on Air Quality concerning PM2.5 Immission, Processes, 10, 545, 2022.

Ulbrich, I. M., Canagaratna, M. R., Zhang, Q., Worsnop, D. R., and Jimenez, J. L.: Interpretation of organic components from Positive Matrix Factorization of aerosol mass spectrometric data, Atmospheric Chemistry and Physics, 9, 2891-2918, 10.5194/acp-9-2891-2009, 2009.

Updyke, K. M., Nguyen, T. B., and Nizkorodov, S. A.: Formation of brown carbon via reactions of ammonia with secondary organic aerosols from biogenic and anthropogenic precursors, Atmospheric Environment, 63, 22-31, 10.1016/j.atmosenv.2012.09.012, 2012.

Wang, Q. Y., Han, Y. M., Ye, J. H., Liu, S. X., Pongpiachan, S., Zhang, N. N., Han, Y. M., Tian, J., Wu, C., Long, X., Zhang, Q., Zhang, W. Y., Zhao, Z. Z., and Cao, J. J.: High Contribution of Secondary Brown Carbon to Aerosol Light Absorption in the Southeastern Margin of Tibetan Plateau, Geophysical Research Letters, 46, 4962-4970, 10.1029/2019gl082731, 2019.

Washenfelder, R. A., Attwood, A. R., Brock, C. A., Guo, H., Xu, L., Weber, R. J., Ng, N. L., Allen, H. M., Ayres, B. R., Baumann, K., Cohen, R. C., Draper, D. C., Duffey, K. C., Edgerton, E., Fry, J. L., Hu, W. W., Jimenez, J. L., Palm, B. B., Romer, P., Stone, E. A., Wooldridge, P. J., and Brown, S. S.: Biomass burning dominates brown carbon absorption in the rural southeastern United States, Geophysical Research Letters, 42, 653-664, 10.1002/2014gl062444, 2015.

West, C. P., Hettiyadura, A. P. S., Darmody, A., Mahamuni, G., Davis, J., Novosselov, I., and Laskin, A.: Molecular Composition and the Optical Properties of Brown Carbon Generated by the Ethane Flame, Acs Earth and Space Chemistry, 4, 1090-1103, 10.1021/acsearthspacechem.0c00095, 2020.

Wu, G.-M., Cong, Z.-Y., Kang, S.-C., Kawamura, K., Fu, P.-Q., Zhang, Y.-L., Wan, X., Gao, S.-P., and Liu, B.: Brown carbon in the cryosphere: Current knowledge and perspective, Advances in Climate Change Research, 7, 82-89, 2016.

Xiao, R., Takegawa, N., Zheng, M., Kondo, Y., Miyazaki, Y., Miyakawa, T., Hu, M., Shao, M., Zeng, L., Gong, Y., Lu, K., Deng, Z., Zhao, Y., and Zhang, Y. H.: Characterization and source apportionment of submicron aerosol with aerosol mass spectrometer during the PRIDE-PRD 2006 campaign, Atmospheric Chemistry and Physics, 11, 6911-6929, 10.5194/acp-11-6911-2011, 2011.

Xie, M., Chen, X., Hays, M. D., Lewandowski, M., Offenberg, J., Kleindienst, T. E., and Holder, A. L.: Light Absorption of Secondary Organic Aerosol: Composition and Contribution of Nitroaromatic Compounds, Environ. Sci. Technol., 51, 11607-11616, 10.1021/acs.est.7b03263, 2017.

Xie, M. J., Zhao, Z. Z., Holder, A. L., Hays, M. D., Chen, X., Shen, G. F., Jetter, J. J., Champion, W. M., and Wang, Q. G.: Chemical composition, structures, and light absorption of N-containing aromatic compounds emitted from burning wood and charcoal in household cookstoves, Atmospheric Chemistry and Physics, 20, 14077-14090, 10.5194/acp-20-14077-2020, 2020.

Xiong, R., Li, J., Zhang, Y. Z., Zhang, L., Jiang, K., Zheng, H., Kong, S. F., Shen, H. Z., Cheng, H. F., Shen, G. F., and Tao, S.: Global brown carbon emissions from combustion sources, Environmental Science and Ecotechnology, 12, 10.1016/j.ese.2022.100201, 2022.

Xu, J. Z., Hettiyadura, A. P. S., Liu, Y. M., Zhang, X. H., Kang, S. C., and Laskin, A.: Regional Differences of Chemical Composition and Optical Properties of Aerosols in the Tibetan Plateau, Journal of Geophysical Research-Atmospheres, 125, 10.1029/2019jd031226, 2020.

Xu, L., Kollman, M. S., Song, C., Shilling, J. E., and Ng, N. L.: Effects of NOx on the Volatility of Secondary Organic Aerosol from Isoprene Photooxidation, Environ. Sci. Technol., 48, 2253-2262, 10.1021/es404842g, 2014.

Xue, J., Ma, F., Elm, J., Chen, J., and Xie, H. B.: Atmospheric Oxidation Mechanism and Kinetics of Indole Initiated by ·OH and ·Cl: A Computational Study, Atmos. Chem. Phys. Discuss., 2022, 1-23, 10.5194/acp-2022-88, 2022.

Yalcin, E., Tecer, L. H., Yurdakul, S., and Tuncel, G.: Potential sources and measured concentrations of VOCs in Balikesir ambient atmosphere, Atmosfera, 33, 269-284, 10.20937/atm.52646, 2020.

Yan, C. Q., Zheng, M., Bosch, C., Andersson, A., Desyaterik, Y., Sullivan, A. P., Collett, J. L., Zhao, B., Wang, S. X., He, K. B., and Gustafsson, O.: Important fossil source contribution to brown carbon in Beijing during winter, Scientific Reports, 7, 10.1038/srep43182, 2017.

Yan, G., and Kim, G.: Speciation and Sources of Brown Carbon in Precipitation at Seoul, Korea: Insights from Excitation-Emission Matrix Spectroscopy and Carbon Isotopic Analysis, Environ. Sci. Technol., 51, 11580-11587, 10.1021/acs.est.7b02892, 2017.

Yan, J., Wang, X., Gong, P., Wang, C., and Cong, Z.: Review of brown carbon aerosols: Recent progress and perspectives, Science of the Total Environment, 634, 1475-1485, 10.1016/j.scitotenv.2018.04.083, 2018.

Yang, L. H., Takeuchi, M., Chen, Y. L., and Ng, N. L.: Characterization of thermal decomposition of oxygenated organic compounds in FIGAERO-CIMS, Aerosol Science and Technology, 55, 1321-1342, 10.1080/02786826.2021.1945529, 2021.

Yang, Z., Tsona, N. T., George, C., and Du, L.: Nitrogen-Containing Compounds Enhance Light Absorption of Aromatic-Derived Brown Carbon, Environ. Sci. Technol., 10.1021/acs.est.1c08794, 2022.

Yassine, M. M., Harir, M., Dabek-Zlotorzynska, E., and Schmitt-Kopplin, P.: Structural characterization of organic aerosol using Fourier transform ion cyclotron resonance mass spectrometry: Aromaticity equivalent approach, Rapid Communications in Mass Spectrometry, 28, 2445-2454, 10.1002/rcm.7038, 2014.

Yuan, B., Koss, A. R., Warneke, C., Coggon, M., Sekimoto, K., and de Gouw, J. A.: Proton-Transfer-Reaction Mass Spectrometry: Applications in Atmospheric Sciences, Chemical Reviews, 117, 13187-13229, 10.1021/acs.chemrev.7b00325, 2017.

Yuan, Q., Xu, J. Z., Liu, L., Zhang, A. X., Liu, Y. M., Zhang, J., Wan, X., Li, M. M., Qin, K., Cong, Z. Y., Wang, Y. H., Kang, S. C., Shi, Z. B., Posfai, M., and Li, W. J.: Evidence for Large Amounts of Brown Carbonaceous Tarballs in the Himalayan Atmosphere, Environmental Science & Technology Letters, 8, 16-23, 10.1021/acs.estlett.0c00735, 2021.

Yue, S. Y., Zhu, J. L., Chen, S., Xie, Q. R., Li, W., Li, L. J., Ren, H., Su, S. H., Li, P., Ma, H., Fan, Y. B., Cheng, B. R., Wu, L. B., Deng, J. J., Hu, W., Ren, L. J., Wei, L. F., Zhao, W. Y., Tian, Y., Pan, X. L., Sun, Y. L., Wang, Z. F., Wu, F. C., Liu, C. Q., Su, H., Penner, J. E., Poschl, U., Andreae, M. O., Cheng, Y. F., and Fu, P. Q.: Brown carbon from biomass burning imposes strong circum-Arctic warming, One Earth, 5, 293-304, 10.1016/j.oneear.2022.02.006, 2022.

Zeng, L., Dibb, J., Scheuer, E., Katich, J. M., Schwarz, J. P., Bourgeois, I., Peischl, J., Ryerson, T., Warneke, C., Perring, A. E., Diskin, G. S., DiGangi, J. P., Nowak, J. B., Moore, R. H., Wiggins, E. B., Pagonis, D., Guo, H., Campuzano-Jost, P., Jimenez, J. L., Xu, L., and Weber, R. J.: Characteristics and Evolution of Brown Carbon in Western United States Wildfires, Atmos. Chem. Phys. Discuss., 2022, 1-45, 10.5194/acp-2022-70, 2022.

Zhang, Q., Jimenez, J. L., Canagaratna, M. R., Allan, J. D., Coe, H., Ulbrich, I., Alfarra, M. R., Takami, A., Middlebrook, A. M., Sun, Y. L., Dzepina, K., Dunlea, E., Docherty, K., DeCarlo, P. F., Salcedo, D., Onasch, T., Jayne, J. T., Miyoshi, T., Shimono, A., Hatakeyama, S., Takegawa, N., Kondo, Y., Schneider, J., Drewnick, F., Borrmann, S., Weimer, S., Demerjian, K., Williams, P., Bower, K., Bahreini, R., Cottrell, L., Griffin, R. J., Rautiainen, J., Sun, J. Y., Zhang, Y. M., and Worsnop, D. R.: Ubiquity and dominance of oxygenated species in organic aerosols in anthropogenically-influenced Northern Hemisphere midlatitudes, Geophysical Research Letters, 34, 10.1029/2007gl029979, 2007.

Zheng, G. J., He, K. B., Duan, F. K., Cheng, Y., and Ma, Y. L.: Measurement of humic-like substances in aerosols: A review, Environmental Pollution, 181, 301-314, 10.1016/j.envpol.2013.05.055, 2013.

Zikova, N., and Zdimal, V.: Precipitation scavenging of aerosol particles at a rural site in the Czech Republic, Tellus Series B-Chemical and Physical Meteorology, 68, 10.3402/tellusb.v68.27343, 2016.

Publications during the PhD study

[1] **Jiang, F.,** Song, J., Bauer, J., Gao, L., Vallon, M., Gebhardt, R., Leisner, T., Norra, S., and Saathoff, H.: Chromophores and chemical composition of brown carbon characterized at an urban kerbside by excitation–emission spectroscopy and mass spectrometry, Atmos. Chem. Phys., 22, 14971-14986, 10.5194/acp-22-14971-2022, 2022.

[2] Gao, L., Song, J., Mohr, C., Huang, W., Vallon, M., **Jiang, F.**, Leisner, T., and Saathoff, H.: Kinetics, SOA yields, and chemical composition of secondary organic aerosol from β-caryophyllene ozonolysis with and without nitrogen oxides between 213 and 313 K, Atmos. Chem. Phys., 22, 6001–6020, https://doi.org/10.5194/acp-22-6001-2022, 2022.

[3] Vallon, M., Gao, L., **Jiang, F.**, Krumm, B., Nadolny, J., Song, J., Leisner, T., and Saathoff, H.: LED-based solar simulator to study photochemistry over a wide temperature range in the large simulation chamber AIDA, Atmos. Meas. Tech., 15, 1795–1810, https://doi.org/10.5194/amt-15-1795-2022, 2022.

[4] Song, J., Saathoff, H., Gao, L., Gebhardt, R., **Jiang, F.**, Vallon, M., Bauer, J., Norra, S., and Leisner, T.: Variations of $PM_{2.5}$ sources in the context of meteorology and seasonality at an urban street canyon in Southwest Germany, Atmos. Envi., 282 (2022), 119147, https://doi.org/10.1016/j.atmosenv.2022.119147.

Appendix A: Supplement for Results and Discussion

Note: Part of the tables in Appendix A are reprinted with permission from: Jiang, F., Song, J., Bauer, J., Gao, L., Vallon, M., Gebhardt, R., Leisner, T., Norra, S., and Saathoff, H.: Chromophores and chemical composition of brown carbon characterized at an urban kerbside by excitation–emission spectroscopy and mass spectrometry, Atmos. Chem. Phys., 22, 14971-14986, 10.5194/acp-22-14971-2022, 2022.

Table S1. A list of Teflon filters sampled for FIGAERO-CIMS analysis at Durlacher Tor, Karlsruhe.

Filter No.	Starting time	Ending time	Duration (min)	Sampling flow (L min^{-1})	Volume (L)	Time
1	03/17/2020 08:35	03/17/2020 10:35	120	5.2	624	Morning
2	03/17/2020 10:42	03/17/2020 14:14	212	5.2	1102	Afternoon
3	03/17/2020 20:59	03/17/2020 22:50	111	5.2	577	Night
4	03/18/2020 08:50	03/18/2020 11:20	150	5.2	780	Morning
5	03/18/2020 12:36	03/18/2020 16:30	234	5.2	1217	Afternoon
6	03/18/2020 21:35	03/18/2020 23:10	95	5.2	494	Night
7	03/19/2020 08:40	03/19/2020 11:20	160	5.2	832	Morning
8	03/19/2020 11:30	03/19/2020 16:05	275	5.2	1430	Afternoon
9	03/19/2020 20:00	03/19/2020 22:04	124	5.2	645	Night
10	03/20/2020 09:05	03/20/2020 11:30	145	5.2	754	Morning
11	03/20/2020 12:00	03/20/2020 14:20	140	5.2	728	Afternoon

Table S2. A list of quartz filters sampled for Aqualog analysis at Durlacher Tor, Karlsruhe.

Sample IDs.	Starting time	Ending time	Duration(h)	Sampling flow (m^3h^{-1})	Volume (m^3)	Times
2019 Summer						
1	07/07/2019 12:30	07/08/2019 12:00	23.5	2.3	54	One day
2	07/08/2019 12:30	07/09/2019 12:00	23.5	2.3	54	One day
3	07/10/2019 12:30	07/11/2019 12:00	23.5	2.3	54	One day
4	07/12/2019 12:30	07/13/2019 12:00	23.5	2.3	54	One day
5	07/14/2019 12:30	07/15/2019 12:00	23.5	2.3	54	One day
6	07/15/2019 12:30	07/16/2019 12:00	23.5	2.3	54	One day
7	07/16/2019 12:30	07/17/2019 12:00	23.5	2.3	54	One day
8	07/17/2019 12:30	07/18/2019 12:00	23.5	2.3	54	One day
9	07/18/2019 12:30	07/19/2019 12:00	23.5	2.3	54	One day
10	07/19/2019 12:30	07/20/2019 12:00	23.5	2.3	54	One day
11	07/20/2019 12:30	07/21/2019 12:00	23.5	2.3	54	One day
12	07/21/2019 12:30	07/22/2019 12:00	23.5	2.3	54	One day
13	07/23/2019 12:30	07/24/2019 12:00	23.5	2.3	54	One day
2020Winter						
14	02/27/2020 09:30	02/28/2020 09:00	23.5	2.3	54	One day
15	02/28/2020 09:30	02/29/2020 09:00	23.5	2.3	54	One day
16	02/29/2020 09:30	03/01/2020 09:00	23.5	2.3	54	One day
17	03/01/2020 09:30	03/02/2020 09:00	23.5	2.3	54	One day
18	03/02/2020 09:30	03/03/2020 09:00	23.5	2.3	54	One day
19	03/03/2020 09:30	03/04/2020 09:00	23.5	2.3	54	One day
20	03/04/2020 09:30	03/05/2020 09:00	23.5	2.3	54	One day
21	03/05/2020 09:30	03/06/2020 09:00	23.5	2.3	54	One day
22	03/06/2020 09:30	03/07/2020 09:00	23.5	2.3	54	One day
23	03/07/2020 09:30	03/08/2020 09:00	23.5	2.3	54	One day
24	03/09/2020 09:30	03/10/2020 09:00	23.5	2.3	54	One day
25	03/10/2020 09:30	03/11/2020 09:00	23.5	2.3	54	One day
26	03/11/2020 09:30	03/12/2020 09:00	23.5	2.3	54	One day
27	03/12/2020 09:30	03/13/2020 09:00	23.5	2.3	54	One day
28	03/13/2020 09:30	03/14/2020 09:00	23.5	2.3	54	One day
29	03/14/2020 09:30	03/15/2020 09:00	23.5	2.3	54	One day
30	03/15/2020 09:30	03/16/2020 09:00	23.5	2.3	54	One day
31	03/16/2020 09:30	03/17/2020 09:00	23.5	2.3	54	One day
32	03/17/2020 09:30	03/18/2020 09:00	23.5	2.3	54	One day
33	03/18/2020 09:30	03/18/2020 12:10	2.7	2.3	6	Morning
34	03/18/2020 12:12	03/18/2020 18:25	6.2	2.3	14	Afternoon
35	03/18/2020 18:30	03/19/2020 08:42	14.1	2.3	60	Night
36	03/19/2020 08:45	03/19/2020 11:33	2.8	2.3	6	Morning
37	03/19/2020 11:33	03/19/2020 19:40	8.1	2.3	19	Afternoon

38	03/19/2020 19:43	03/20/2020 09:05	13.4	2.3	31	Night
39	03/20/2020 09:10	03/20/2020 12:00	2.8	2.3	7	Morning
40	03/20/2020 12:03	03/20/2020 18:22	6.3	2.3	15	Afternoon
41	03/20/2020 18:30	03/21/2020 09:00	14.5	2.3	33	Night
42	03/21/2020 09:30	03/22/2020 09:00	23.5	2.3	54	One day
43	03/22/2020 09:30	03/23/2020 09:00	23.5	2.3	54	One day
44	03/23/2020 09:30	03/24/2020 09:00	23.5	2.3	54	One day
45	03/24/2020 09:30	03/25/2020 09:00	23.5	2.3	54	One day
46	03/25/2020 09:30	03/26/2020 09:00	23.5	2.3	54	One day
47	03/26/2020 09:30	03/27/2020 09:00	23.5	2.3	54	One day

Table S3. Spectral characteristics of the four PARAFAC components identified in the EEM datasets of methanol extracts from aerosol particles collected during summer and winter.

PARAFAC component	Excitation wavelength (nm)	Emission wavelength (nm)	Component characteristics from this study	Associated AMS-PMF factors	Associated molecular characteristics (winter)	Similar component characteristics from references
C1	< 240	363	Less-oxygenated HULIS	BBOA	High nitrogen-containing molecules, high molecular weight, and low oxidation status	Humic-like component and less oxygenated species. (Chen et al., 2016) Enriched in biomass burning aerosols (Tang et al., 2020)
C2	248, 362	469	Highly oxygenated HULIS-1	LVOOA1 (summer)	Low nitrogen-containing molecules, low molecular weight, and high oxidation status	Highly oxygenated species and humic-like substance (Chen et al., 2016) An intermediate contribution in urban aerosol (Matos et al., 2015)
C3	< 240, 323	408	Highly oxygenated HULIS-2	LVOOA2 (summer) LVOOA (winter)	Low nitrogen-containing molecules, low molecular weight, and high oxidation status	Highly oxygenated species and humic-like substance (Chen et al., 2016) The highest contribution in urban aerosol (Matos et al., 2015)
C4	266	307	Phenol- and naphthalene-like substances	SV-OOA and LV-OOA (winter)	High nitrogen-containing molecules, low molecular weight, and low oxidation status	Protein-like and non-N-containing species. (Chen et al., 2016) More intense in vehicle exhaust particles. (Tang et al., 2020)

Table S4 Assignment of 178 potential brown carbon molecules in the particle phase detected in KIT Campus Nord, including mass, formula, double bone equivalent (DBE), the ratio of O/C, and the H/C ratio.

Number	Mass (g mol^{-1})	Formula	DBE	O/C	H/C
1	75	C2H4O3	1.5	1.5	1.5
2	104	C3H4O4	2	1.3	1.3
3	120	C3H4O5	2	1.7	1.3
4	152	C3H4O7	2	2.3	1.3
5	168	C3H4O8	2	2.7	1.3
6	103	C3H5O3N1	2	1.0	1.7
7	135	C3H5O5N1	2	1.7	1.7
8	151	C3H5O6N1	2	2.0	1.7
9	167	C3H5O7N1	2	2.3	1.7
10	183	C3H5O8N1	2	2.7	1.7
11	84	C4H4O2	3	0.5	1.0
12	116	C4H4O4	3	1.0	1.0
13	132	C4H4O5	3	1.3	1.0
14	148	C4H4O6	3	1.5	1.0
15	164	C4H4O7	3	1.8	1.0
16	178	C4H4O7N1	3	1.8	1.3
17	180	C4H4O8	3	2.0	1.0
18	99	C4H5O2N1	3	0.5	1.3
19	131	C4H5O4N1	3	1.0	1.3
20	147	C4H5O5N1	3	1.3	1.3
21	163	C4H5O6N1	3	1.5	1.3
22	179	C4H5O7N1	3	1.8	1.3
23	125	C5H4O3	4	0.6	0.8
24	205	C5H4O8	4	1.6	0.8
25	221	C5H4O1	4	0.2	0.8
26	80	C5H4O3	4	0.6	0.8
27	112	C5H4O4	4	0.8	0.8
28	128	C5H4O5	4	1.0	0.8
29	144	C5H4O6N1	4	1.2	1.0
30	174	C5H4O7	4	1.4	0.8
31	176	C5H4O8	4	1.6	0.8
32	208	C5H5O1	3	0.2	1.2
33	111	C5H5O2	3	0.4	1.2
34	97	C5H5O3N1	4	0.6	1.0
35	127	C5H5O3	3	0.6	1.2
36	113	C5H5O4N1	4	0.8	1.0
37	129	C5H5O5N1	4	1.0	1.0
38	159	C5H5O6N1	4	1.2	1.0

39	191	C5H5O7	3	1.4	1.2
40	177	C5H5O8N1	4	1.6	1.0
41	207	C5H5O8	3	1.6	1.2
42	112	C5H6O3	3	0.6	1.2
43	114	C5H6O4	3	0.8	1.2
44	130	C5H6O5	3	1.0	1.2
45	160	C5H6O6	3	1.2	1.2
46	176	C5H6O7	3	1.4	1.2
47	178	C5H6O7N1	3	1.4	1.4
48	192	C5H6O8	3	1.6	1.2
49	194	C5H6O8N1	3	1.6	1.4
50	99	C5H7O3N1	3	0.6	1.4
51	115	C5H7O4N1	3	0.8	1.4
52	131	C5H7O5N1	3	1.0	1.4
53	147	C5H7O6N1	3	1.2	1.4
54	163	C5H7O7N1	3	1.4	1.4
55	193	C5H7O8N1	3	1.6	1.4
56	195	C5H7O9N1	3	1.8	1.4
57	153	C6H3O10	5	1.7	0.7
58	138	C6H4O4	5	0.7	0.7
59	140	C6H4O5	5	0.8	0.7
60	156	C6H4O5N1	5	0.8	0.8
61	186	C6H4O7	5	1.2	0.7
62	218	C6H4O9	5	1.5	0.7
63	220	C6H5N1	5	0.0	0.8
64	123	C6H5O3N1	5	0.5	0.8
65	139	C6H5O4N1	5	0.7	0.8
66	141	C6H5O5N1	5	0.8	0.8
67	171	C6H5O6N1	5	1.0	0.8
68	187	C6H5O7N1	5	1.2	0.8
69	203	C6H5O7	4	1.2	1.0
70	189	C6H5O8	4	1.3	1.0
71	235	C6H5O9	4	1.5	1.0
72	110	C6H6O3	4	0.5	1.0
73	126	C6H6O4	4	0.7	1.0
74	142	C6H6O4N1	4	0.7	1.2
75	156	C6H6O5	4	0.8	1.0
76	172	C6H6O6	4	1.0	1.0
77	204	C6H6O8	4	1.3	1.0
78	222	C6H6O10	4	1.7	1.0
79	111	C6H7O3N1	4	0.5	1.2

80	141	C6H7O4N1	4	0.7	1.2
81	157	C6H7O5N1	4	0.8	1.2
82	173	C6H7O6N1	4	1.0	1.2
83	175	C6H7O7N1	4	1.2	1.2
84	207	C6H7O8N1	4	1.3	1.2
85	199	C7H3O7	6	1.0	0.6
86	154	C7H6O4	5	0.6	0.9
87	170	C7H6O5	5	0.7	0.9
88	218	C7H6O8	5	1.1	0.9
89	232	C7H6O8N1	5	1.1	1.0
90	153	C7H7O3N1	5	0.4	1.0
91	169	C7H7O4N1	5	0.6	1.0
92	155	C7H7O4	4	0.6	1.1
93	185	C7H7O5N1	5	0.7	1.0
94	171	C7H7O5	4	0.7	1.1
95	201	C7H7O6N1	5	0.9	1.0
96	187	C7H7O6	4	0.9	1.1
97	217	C7H7O7N1	5	1.0	1.0
98	203	C7H7O7	4	1.0	1.1
99	233	C7H7O8N1	5	1.1	1.0
100	219	C7H7O8	4	1.1	1.1
101	140	C7H8O3	4	0.4	1.1
102	156	C7H8O4	4	0.6	1.1
103	172	C7H8O5	4	0.7	1.1
104	188	C7H8O6	4	0.9	1.1
105	204	C7H8O7	4	1.0	1.1
106	220	C7H8O8	4	1.1	1.1
107	236	C7H8O9	4	1.3	1.1
108	250	C7H8O9N1	4	1.3	1.3
109	155	C7H9O3N1	4	0.4	1.3
110	171	C7H9O4N1	4	0.6	1.3
111	187	C7H9O5N1	4	0.7	1.3
112	203	C7H9O6N1	4	0.9	1.3
113	219	C7H9O7N1	4	1.0	1.3
114	235	C7H9O8N1	4	1.1	1.3
115	251	C7H9O9N1	4	1.3	1.3
116	267	C7H9O10N1	4	1.4	1.3
117	182	C8H6O5	6	0.6	0.8
118	213	C8H7O6N1	6	0.8	0.9
119	199	C8H7O6	5	0.8	1.0
120	229	C8H7O7N1	6	0.9	0.9

121	215	C8H7O7	5	0.9	1.0
122	168	C8H8O4	5	0.5	1.0
123	184	C8H8O5	5	0.6	1.0
124	200	C8H8O6	5	0.8	1.0
125	216	C8H8O7	5	0.9	1.0
126	230	C8H8O7N1	5	0.9	1.1
127	183	C8H9O4N1	5	0.5	1.1
128	199	C8H9O5N1	5	0.6	1.1
129	215	C8H9O6N1	5	0.8	1.1
130	231	C8H9O7N1	5	0.9	1.1
131	295	C8H9O11N1	5	1.4	1.1
132	228	C9H8O7	6	0.8	0.9
133	211	C9H9O5N1	6	0.6	1.0
134	229	C9H9O7	5	0.8	1.1
135	259	C9H9O8N1	6	0.9	1.0
136	307	C9H9O11N1	6	1.2	1.0
137	182	C9H10O4	5	0.4	1.1
138	198	C9H10O5	5	0.6	1.1
139	214	C9H10O6	5	0.7	1.1
140	230	C9H10O7	5	0.8	1.1
141	262	C9H10O9	5	1.0	1.1
142	213	C9H11O5N1	5	0.6	1.2
143	229	C9H11O6N1	5	0.7	1.2
144	293	C9H11O10N1	5	1.1	1.2
145	309	C9H11O11N1	5	1.2	1.2
146	242	C10H10O7	6	0.7	1.0
147	257	C10H11O7N1	6	0.7	1.1
148	273	C10H11O8N1	6	0.8	1.1
149	305	C10H11O10N1	6	1.0	1.1
150	353	C10H11O13N1	6	1.3	1.1
151	282	C11H6O9	9	0.8	0.5
152	284	C11H8O9	8	0.8	0.7
153	347	C11H9O12N1	8	1.1	0.8
154	286	C11H10O9	7	0.8	0.9
155	285	C11H11O8N1	7	0.7	1.0
156	301	C11H11O9N1	7	0.8	1.0
157	349	C11H11O12N1	7	1.1	1.0
158	256	C11H12O7	6	0.6	1.1
159	272	C11H12O8	6	0.7	1.1
160	288	C11H12O9	6	0.8	1.1
161	287	C11H13O8N1	6	0.7	1.2

162	303	C11H13O9N1	6	0.8	1.2
163	319	C11H13O10N1	6	0.9	1.2
164	300	C12H12O9	7	0.8	1.0
165	332	C12H12O11	7	0.9	1.0
166	348	C12H12O12	7	1.0	1.0
167	282	C13H14O7	7	0.5	1.1
168	330	C13H14O10	7	0.8	1.1
169	394	C13H14O14	7	1.1	1.1
170	345	C13H15O10N1	7	0.8	1.2
171	393	C13H15O13N1	7	1.0	1.2
172	326	C14H14O9	8	0.6	1.0
173	324	C15H16O8	8	0.5	1.1
174	356	C15H16O10	8	0.7	1.1
175	372	C15H16O11	8	0.7	1.1
176	403	C15H17O12N1	8	0.8	1.1
177	368	C16H16O10	9	0.6	1.0
178	366	C17H18O9	9	0.5	1.1

Table S5. Assignment of 31 potential brown carbon molecules in the gas phase detected in KIT Campus Nord, including mass, formula, double bone equivalent (DBE), the ratio of O/C, and the H/C ratio.

Number	Mass (g mol^{-1})	Formula	DBE	O/C	H/C
1	135	C3H4O6	2	2.0	1.3
2	151	C3H5O6N1	2	2.0	1.7
3	84	C4H4O2	3	0.5	1.0
4	196	C4H4O9	3	2.3	1.0
5	163	C4H5O6N1	3	1.5	1.3
6	179	C4H5O7N1	3	1.8	1.3
7	206	C5H4O9	4	1.8	0.8
8	159	C5H5O6N1	4	1.2	1.0
9	175	C5H5O7N1	4	1.4	1.0
10	177	C5H5O8N1	4	1.6	1.0
11	114	C5H6O4	3	0.8	1.2
12	208	C5H6O9	3	1.8	1.2
13	147	C5H7O6N1	3	1.2	1.4
14	163	C5H7O7N1	3	1.4	1.4
15	123	C6H5O3N1	5	0.5	0.8
16	139	C6H5O4N1	5	0.7	0.8
17	156	C6H6O5	4	0.8	1.0
18	220	C6H6O9	4	1.5	1.0
19	222	C6H6O10	4	1.7	1.0
20	173	C6H7O6N1	4	1.0	1.2
21	175	C6H7O7N1	4	1.2	1.2
22	207	C6H7O8N1	4	1.3	1.2
23	221	C6H7O9N1	4	1.5	1.2
24	153	C7H7O3N1	5	0.4	1.0
25	169	C7H7O4N1	5	0.6	1.0
26	203	C7H9O6N1	4	0.9	1.3
27	219	C7H9O7N1	4	1.0	1.3
28	235	C7H9O8N1	4	1.1	1.3
29	184	C8H8O5	5	0.6	1.0
30	183	C8H9O4N1	5	0.5	1.1
31	262	C9H10O9	5	1.0	1.1

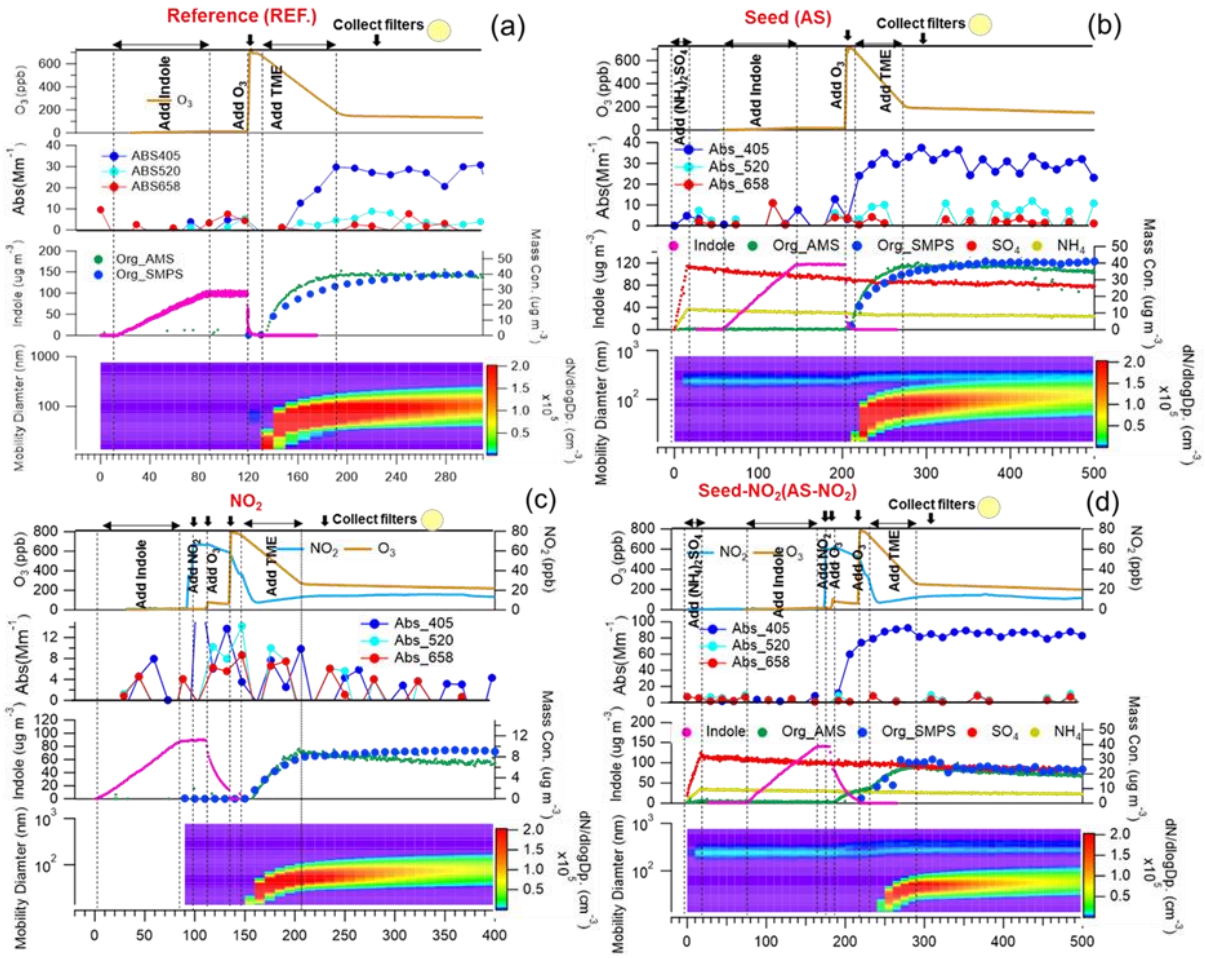

Figure S1. Evolution of trace gases, light absorption, particle mass, and size distribution of indole oxidation at REF. (a), AS (b), NO_2 (c), and NO_2-AS (d).

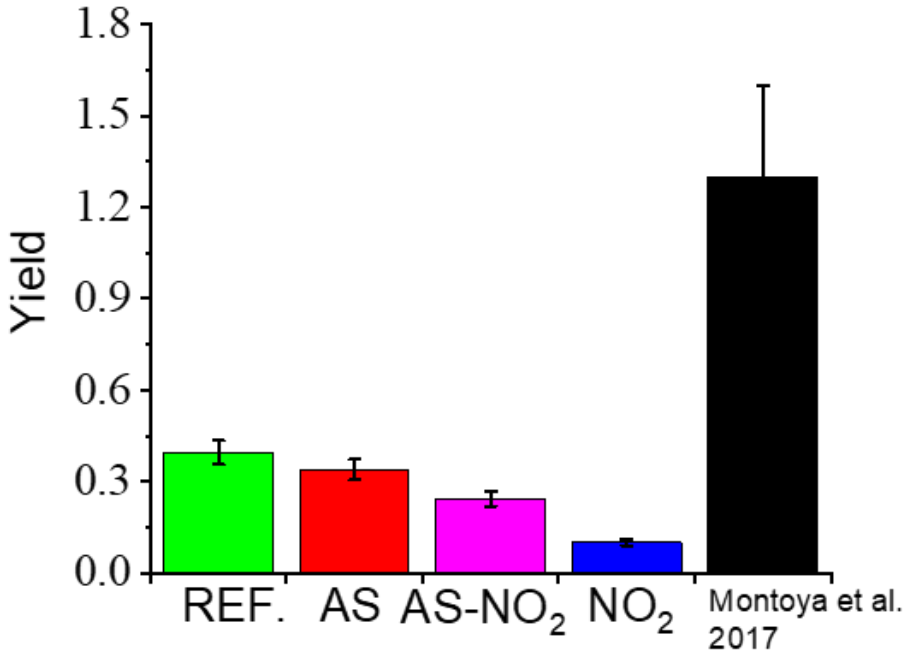

Figure S2. Yields of ind-SOA during stable period recorded in the REF (pink), AS (green), AS-NO_2 (black) and NO_2 (red) experiments. Black bar shows previously reported data by Montoya et al. The yields were calculated under stable periods for one hour (plateau level). (no wall loss-correction).

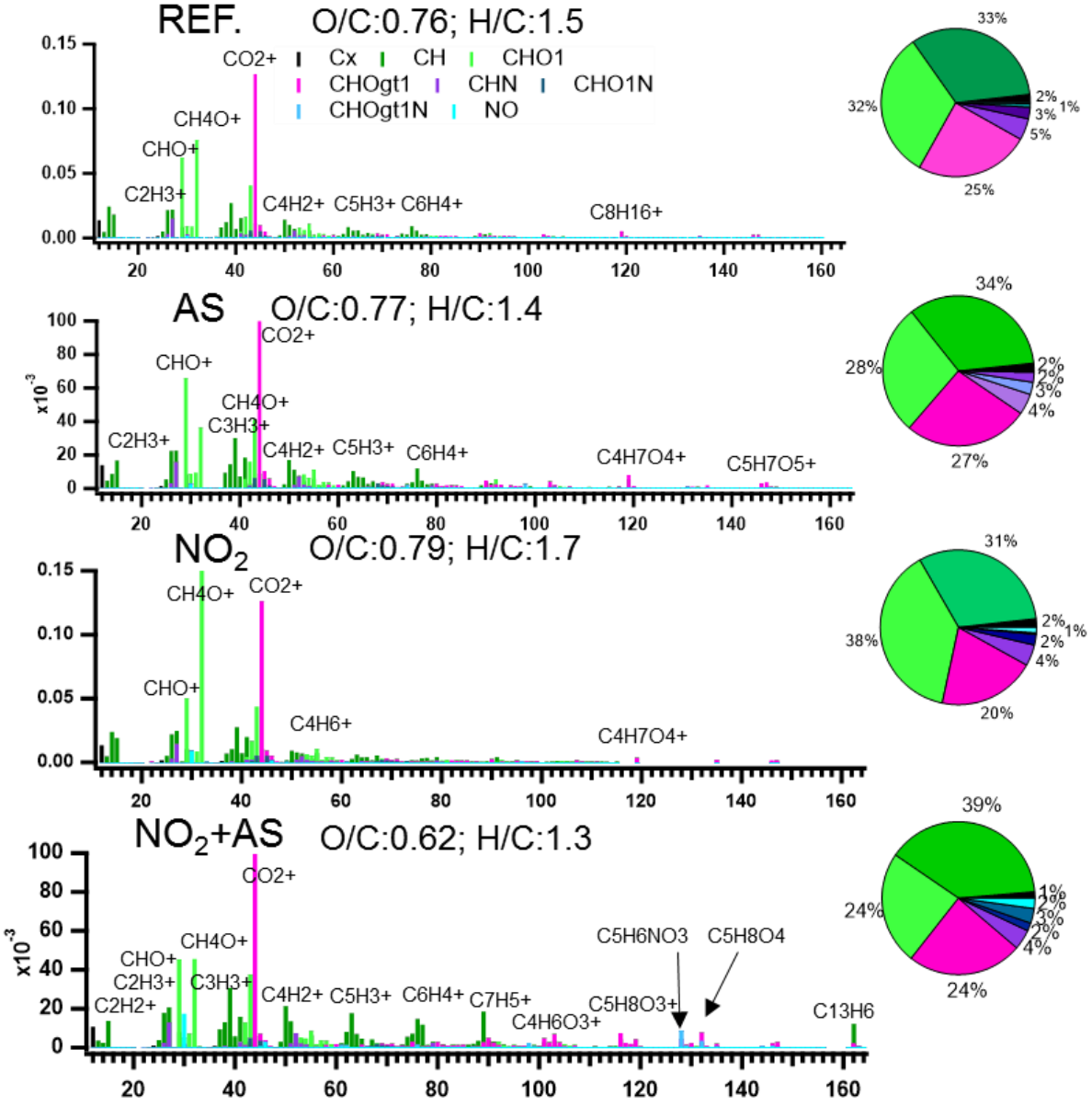

Figure S3. High-resolution AMS mass spectra of ind-SOA generated in the REF., AS, NO_2, and NO_2-AS experiments. Eight ion groups are grouped for clarity as C_x (black), CH_+ (dark green), CHO_1 (green), $CHOg_{t1}$ (pink), CHN (purple).

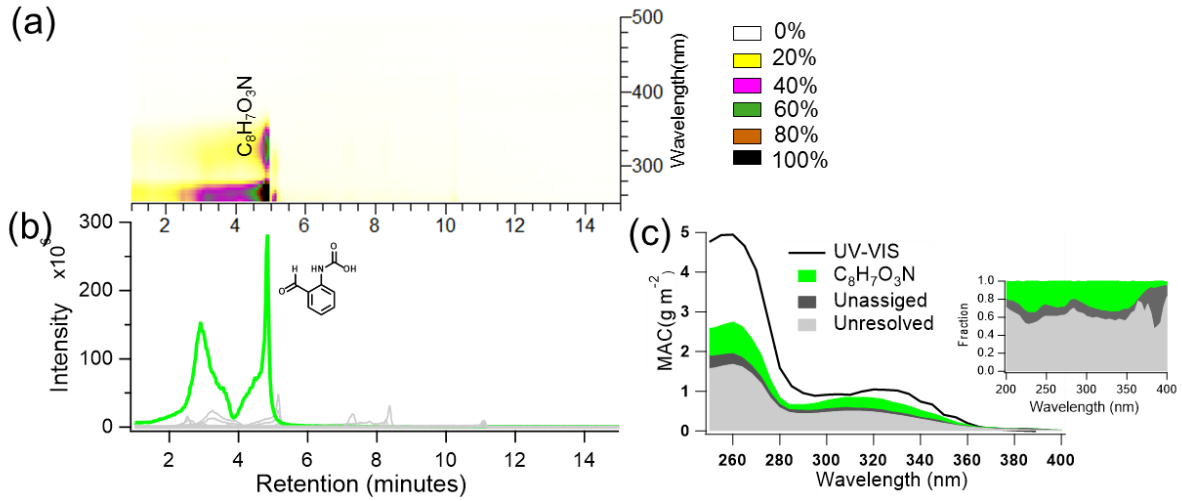

Figure S4. Molecular characteristics of individual components identified in the indole SOA at the reference condition. The pane (a) is the normalization of UPLC-PDA chromatograms and identified chromophore molecules. The panel (b) shows a compilation of the selected extracted ion chromatograms (EICs) and molecular structure of the most abundant peaks. The pane (c) shows the MAC from UV-visible spectrometer and UPLC-PDA measurement and absorption fractions. Unresolved chromophores (grey), unassigned absorbing chromophores (black grey), and $C_8H_7O_3N$ (green).

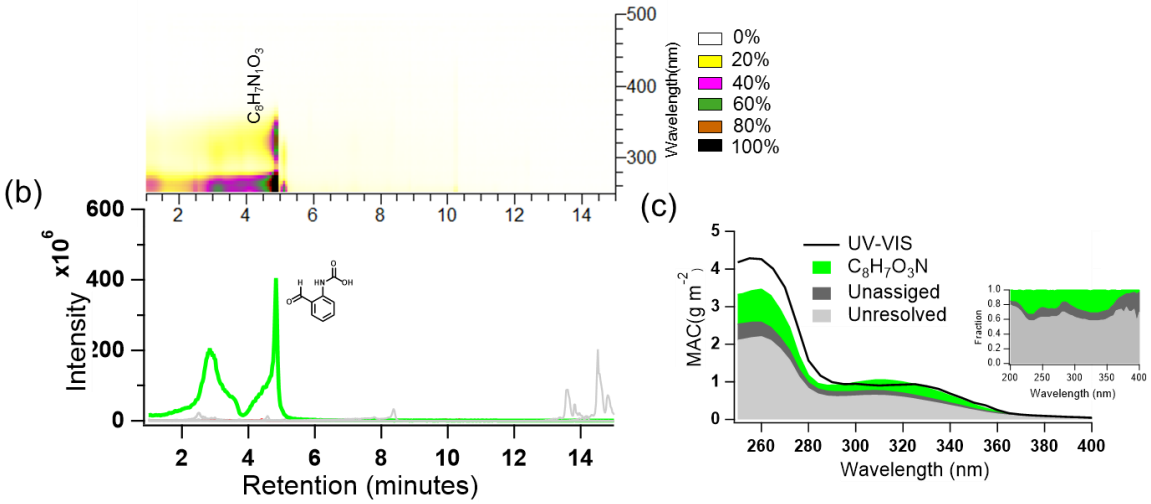

Figure S5. Molecular characteristics of individual components identified in the indole SOA at the AS condition. The pane (a) is the normalization of UPLC-PDA chromatograms and identified chromophore molecules. The panel (b) shows a compilation of the selected extracted ion chromatograms (EICs) and molecular structure of the most abundant peaks. The pane (c) shows the MAC from UV-visible spectrometer and UPLC-PDA measurement and absorption fractions. Unresolved chromophores (grey), unassigned absorbing chromophores (black grey), and $C_8H_7O_3N$ (green).

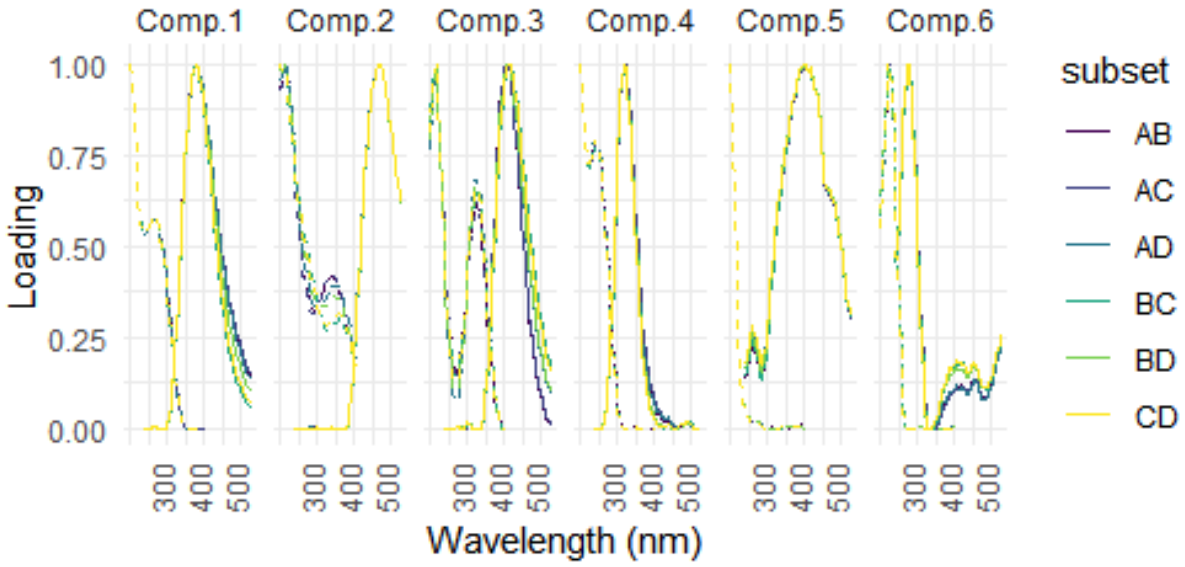

Figure S6. Split analysis of 6 component PARAFAC model with the split style 'S4C6T3' for all EEMs. The data are split into four subsets (A, B, C, and D) and recombined to compare one-half of the data to the other in different combinations (AB-CD, AD-BC, AC-DB) (Pucher et al., 2019).

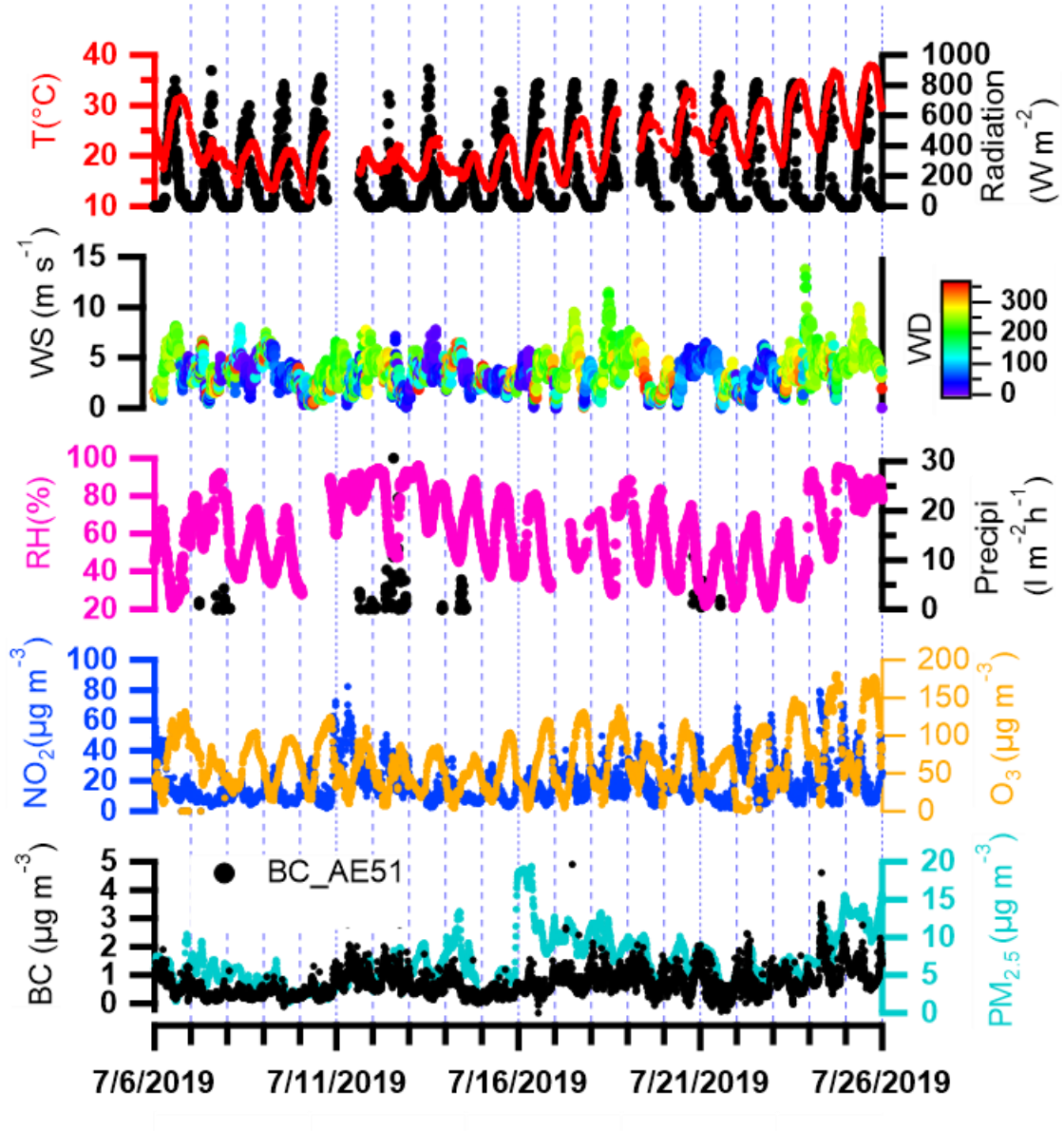

Figure S7. Overview of the meteorological parameters: temperature (T), radiation, wind speed (WS), wind direction (WD), relative humidity (RH), precipitation (Precipi), trace gases (NO_2 and O_3), black carbon (BC), and $PM_{2.5}$ in summer.

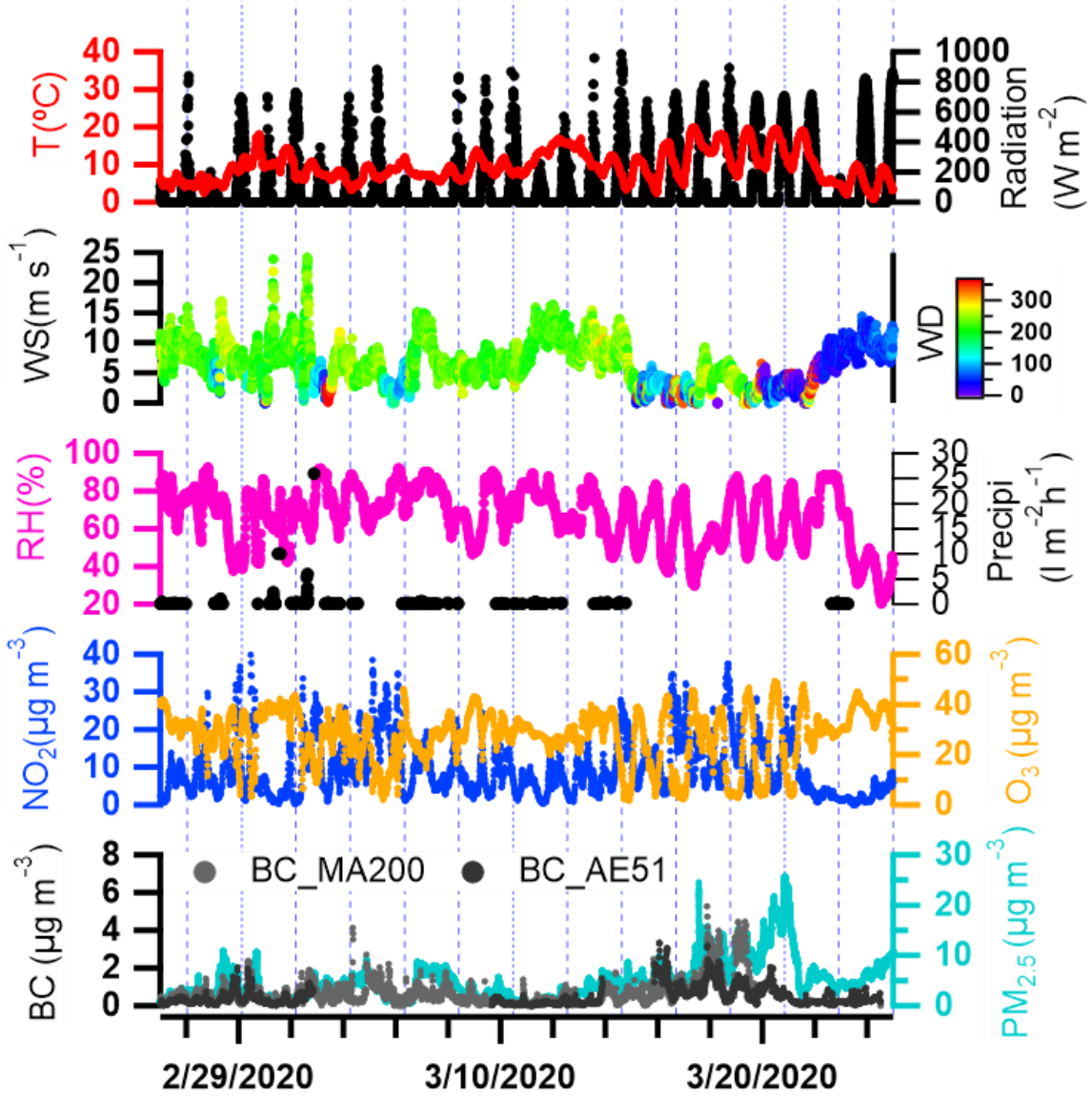

Figure S8. Overview of the meteorological parameters: temperature (T), radiation, windspeeds (WS), wind direction (WD), relative humidity (RH), precipitation (Precipi), trace gases (NO_2 and O_3), black carbon (BC), and $PM_{2.5}$ in winter.

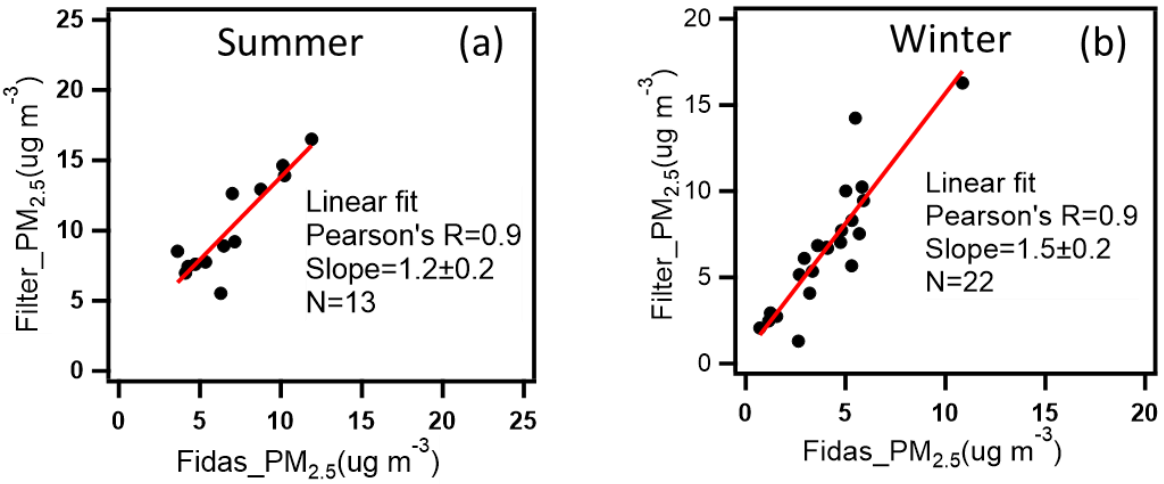

Figure S9. Linear correlation of $PM_{2.5}$ mass concentrations from gravimetric analysis of filter and Fidas-OPC in summer (a) and winter (b).

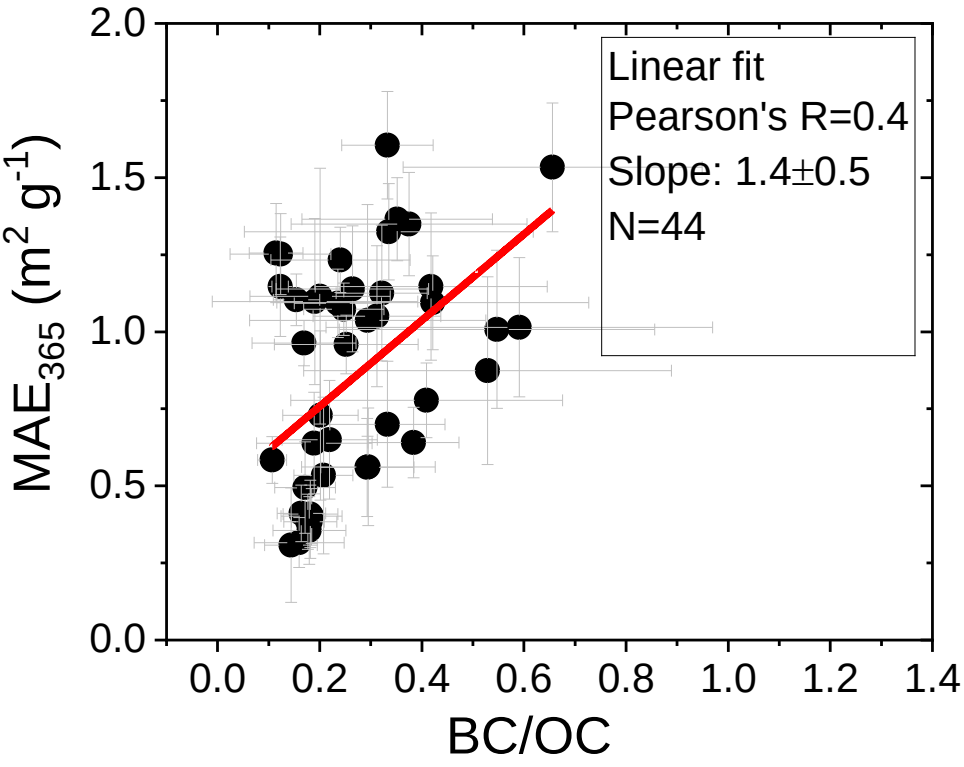

Figure S10. Linear correlation between the MAE_{365} and the BC/OC ratio.

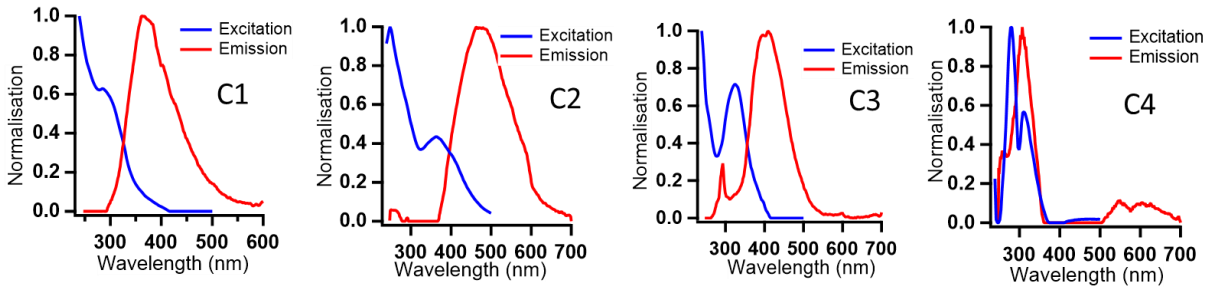

Figure S11. Normalization of spectral loading of C1, C2, C3, and C4.

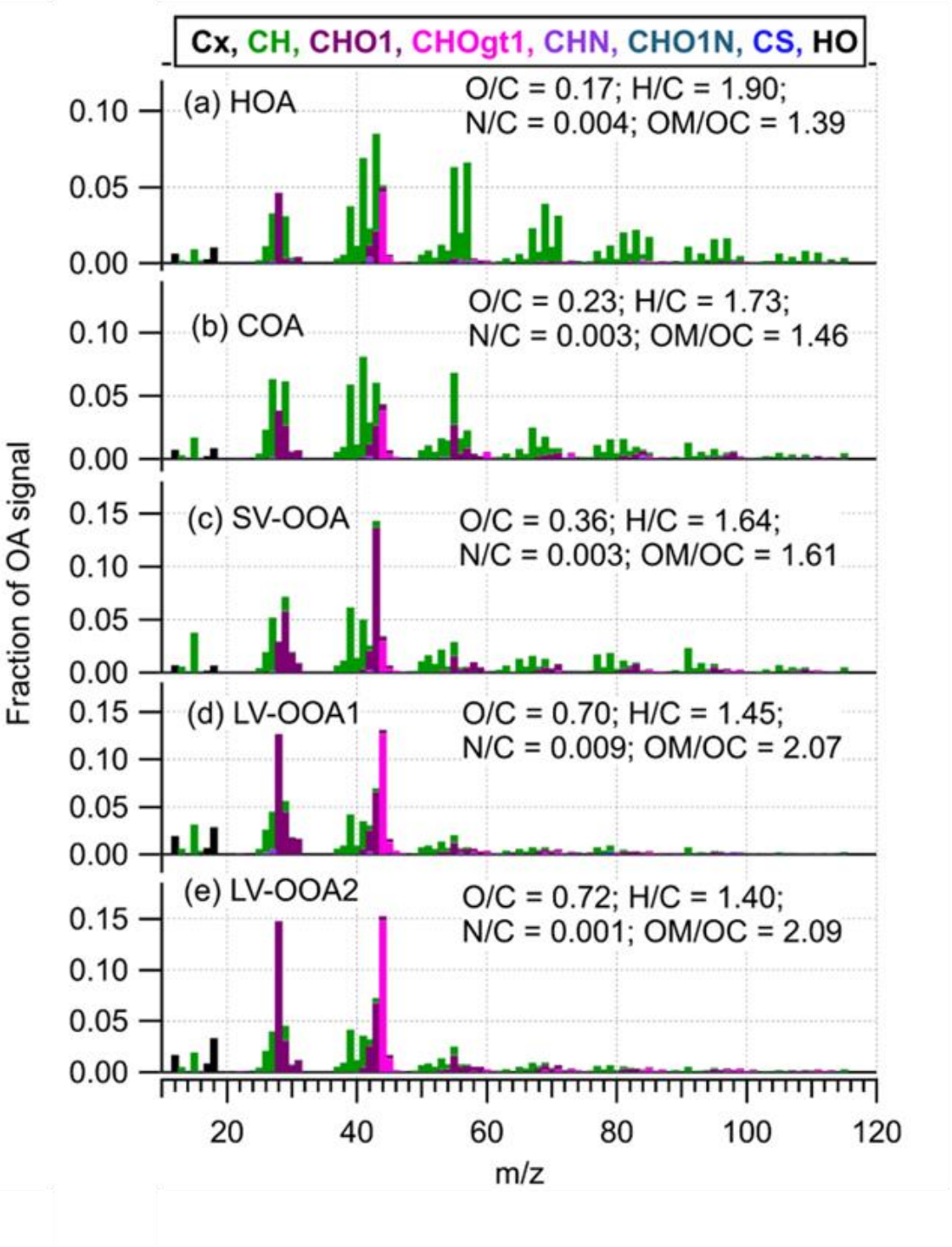

Figure S12. Mass spectra of five PMF-resolved organic aerosol (OA) factors at Durlacher Tor, Karlsruhe in summer 2019. HOA = hydrocarbon-like OA; COA = cooking-related OA; SV-OOA = semi-volatile oxidized OA and LV-OOA = low-volatile oxygenated OA (LV-OOA1 and LV-OOA2).

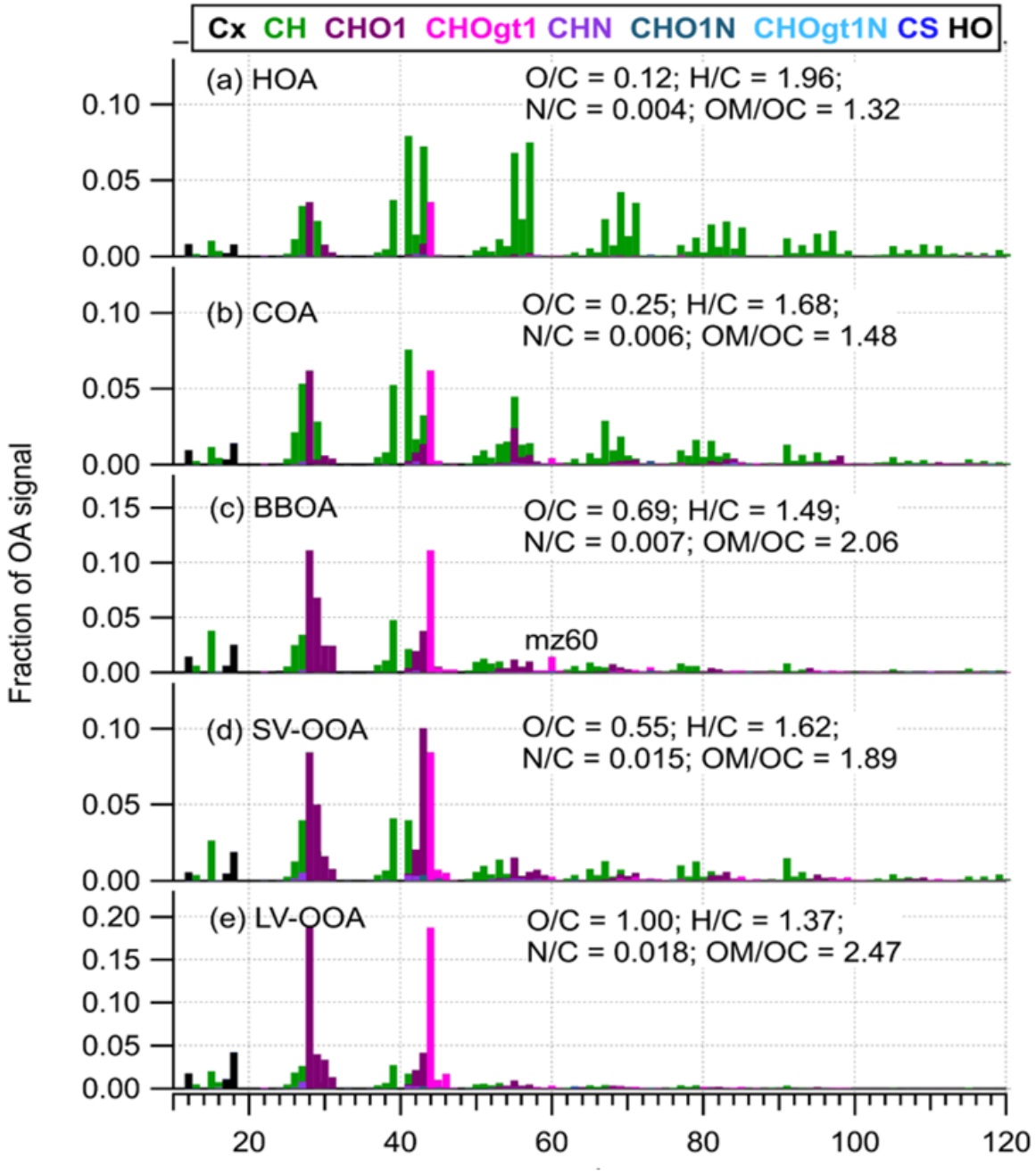

Figure S13. Mass spectra of five PMF-resolved organic aerosol (OA) factors at Durlacher Tor, Karlsruhe in winter 2020. HOA = hydrocarbon-like OA; COA = cooking-related OA; BBOA = biomass burning-related OA; SV-OOA = semi-volatile oxygenated OA; LV-OOA = low-volatile oxygenated OA.

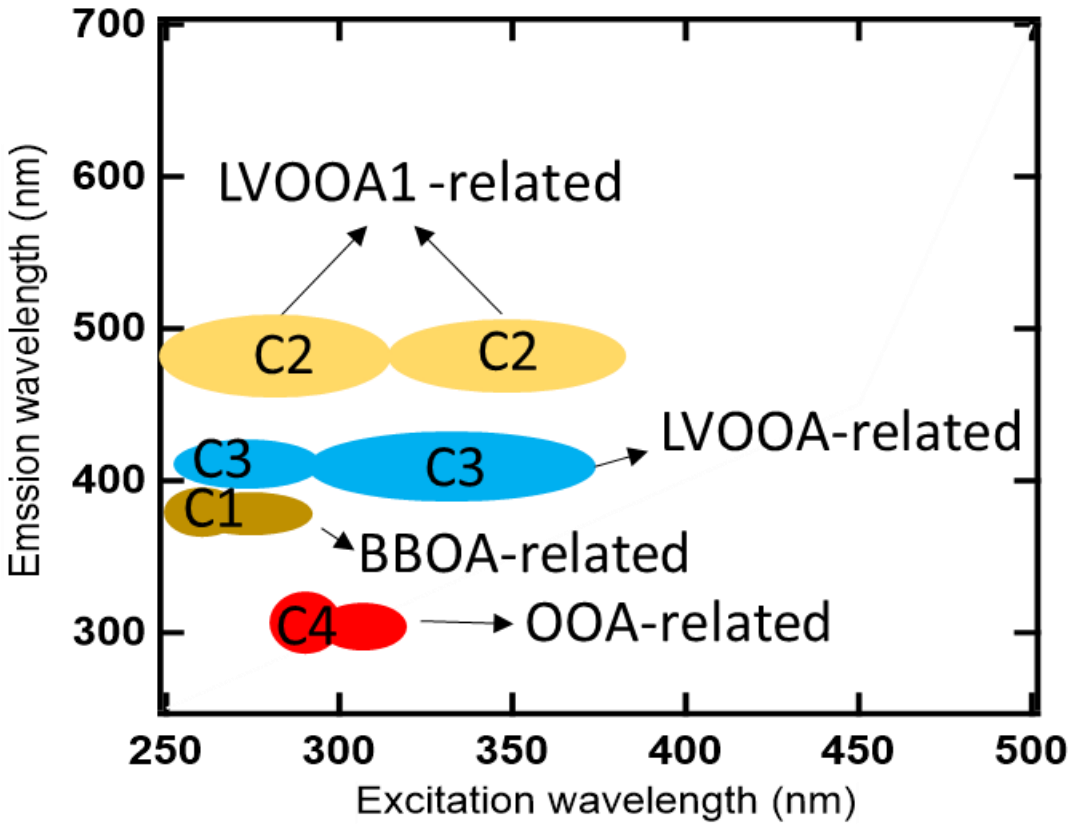

Figure S14. Diagram of the association of the EEM profiles with AMS-PMF factors.

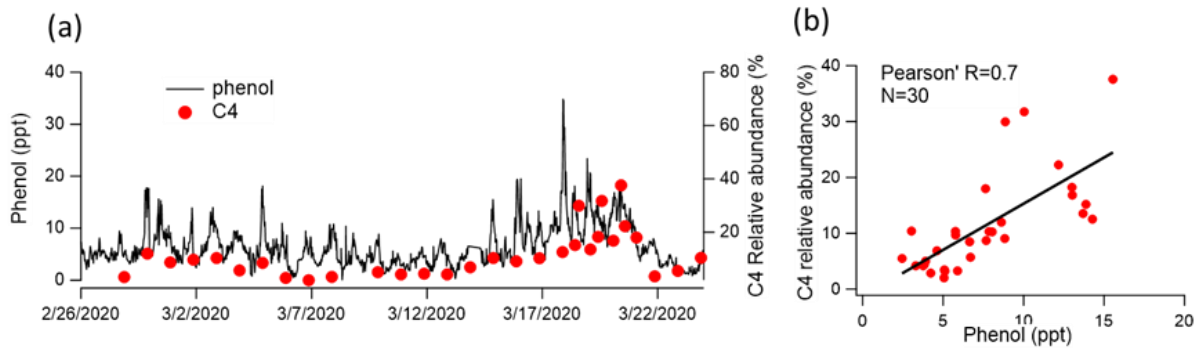

Figure S15. Time series of phenol in gas phase and component 4 (C4) in particle phase (a). Correlation analysis of C4 and phenol (b). Phenol measurement were provided by my colleague Junwei Song.

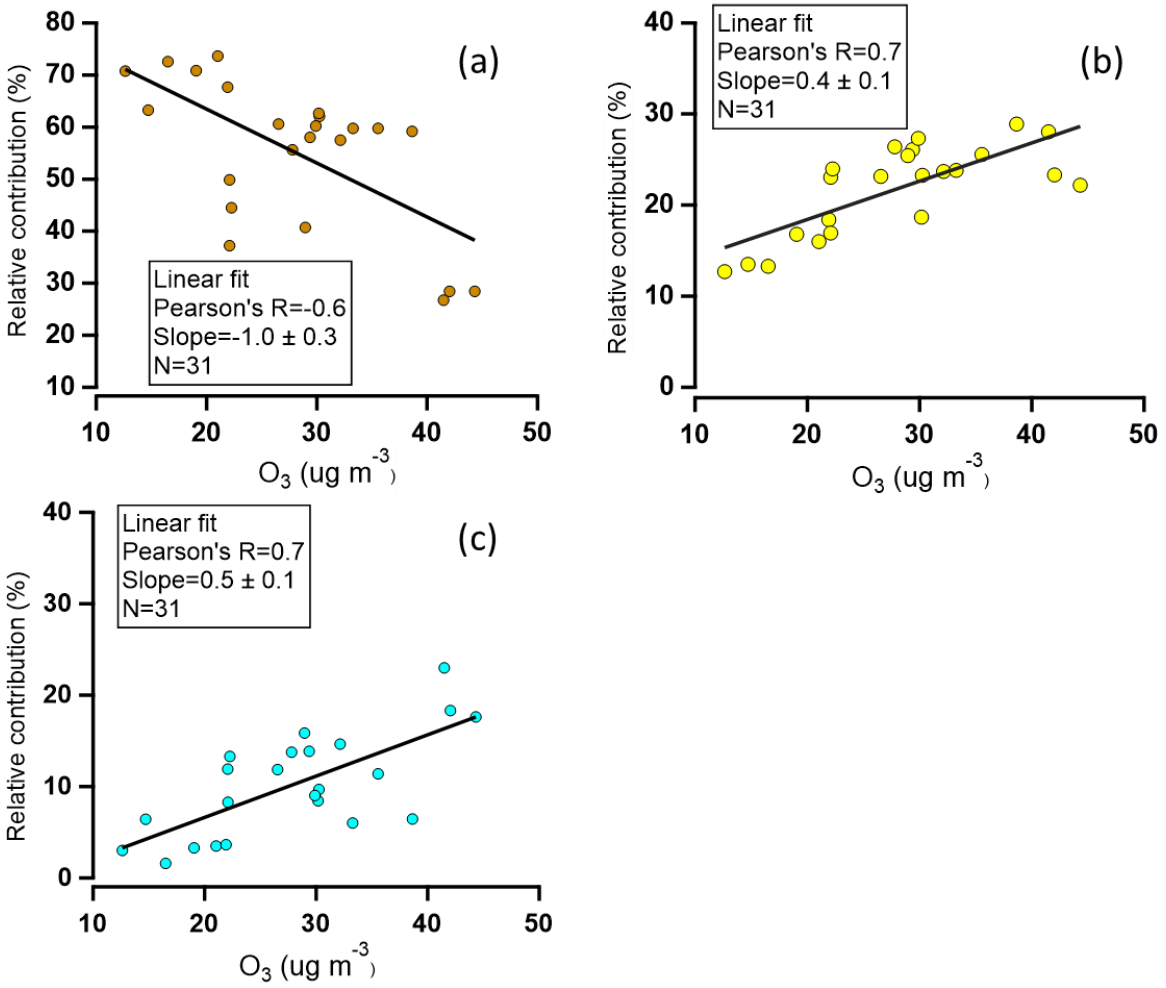

Figure S16. The linear correlations between chromophore components with O_3, LO-HULIS (a), HO-HULIS-1 (b), and HO-HULIS-2 (c).

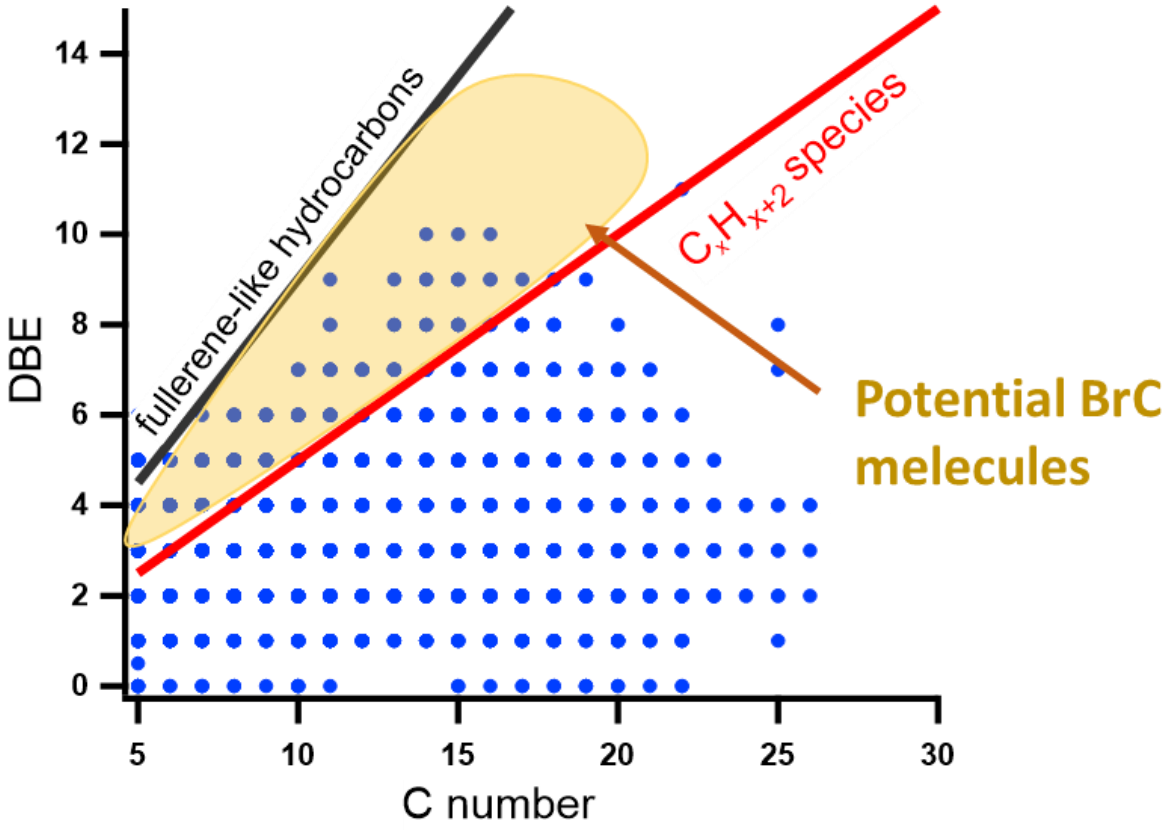

Figure S17. The plot of the double bond equivalent (DBE) vs a number of carbon atoms according to our measurements following the procedure described by Lin et al. (2018). The lines indicate DBE reference values of linear conjugated polyenes C_xH_{x+2} (red solid line) and fullerene-like hydrocarbons with DBE=0.9*c (black solid line). Data points inside the yellow shaded area are potential BrC molecules. (cf. Lin et al. 2018).

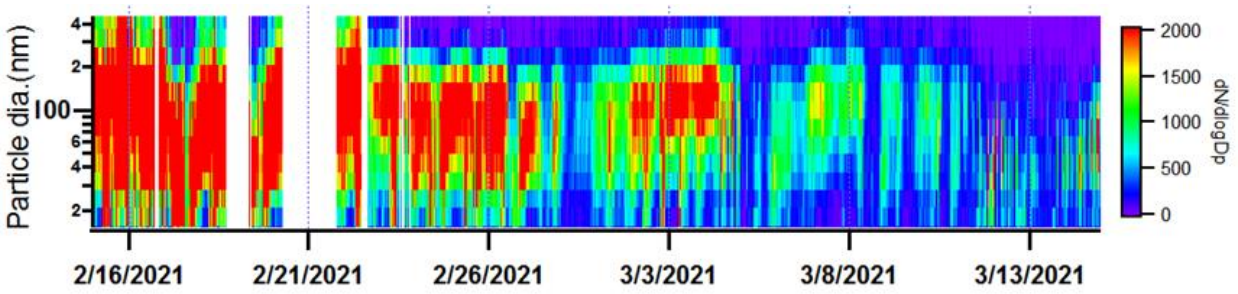

Figure S18. Particle size distribution measured with NanoScan.

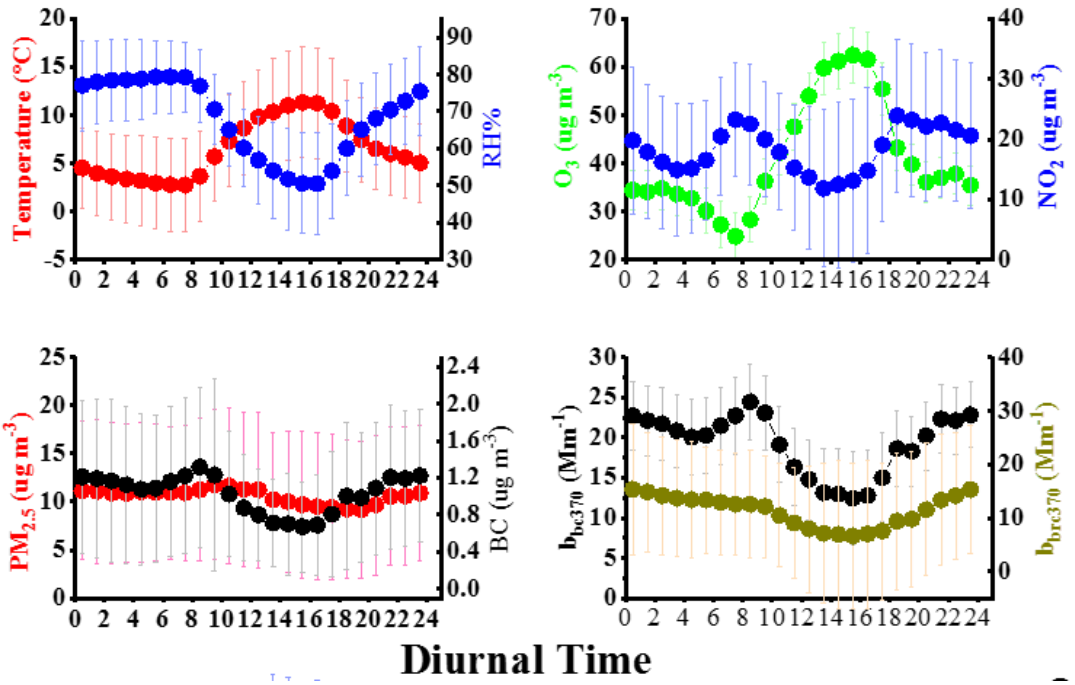

Figure S19. Diurnal variation of temperature, relative humidity, O_3, NO_2, $PM_{2.5}$, BC, b_{bc370} and b_{brc370} for the whole measurement period.

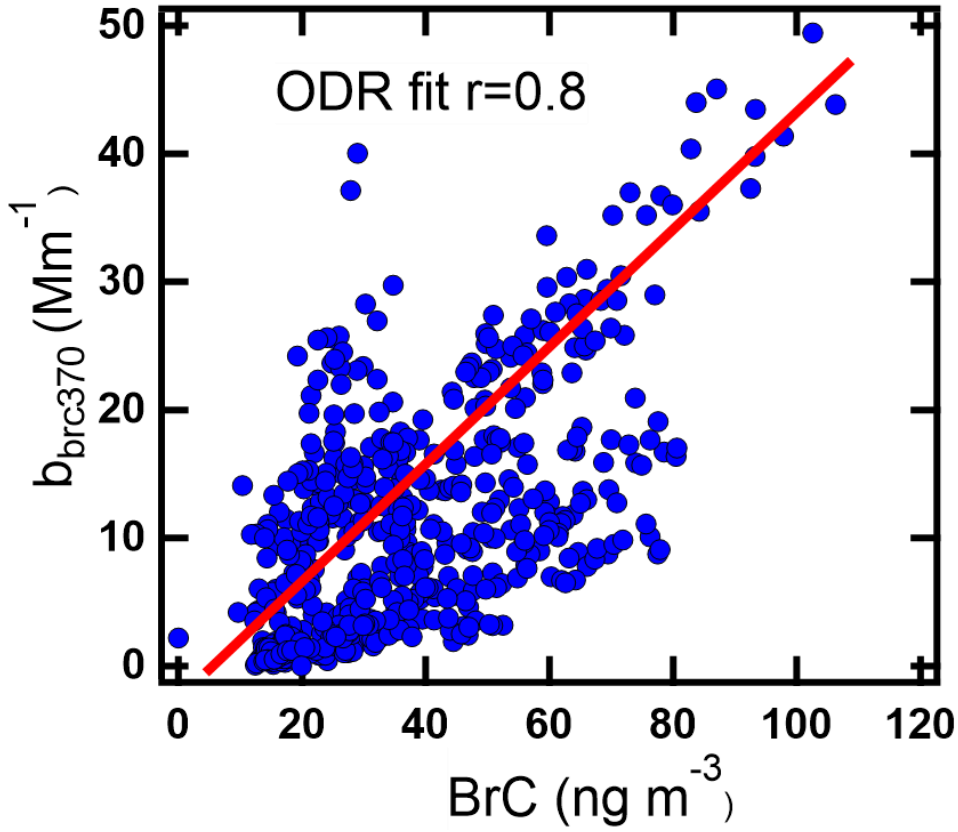

Figure S20. The correlation of BrC molecules and b_{brc370}.

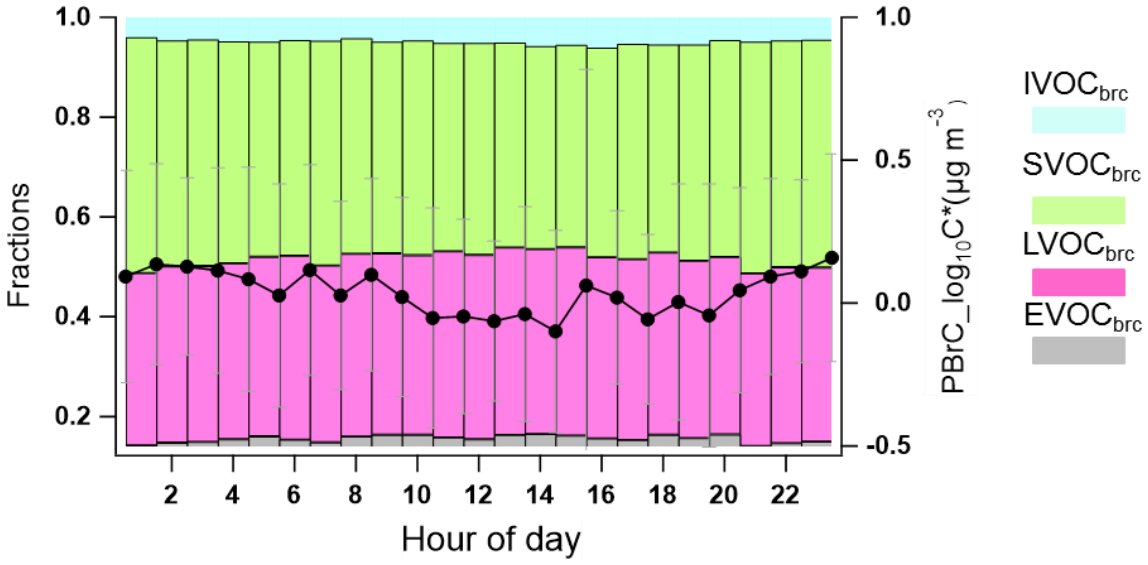

Figure S21. Diurnal profiles of $LVOC_{brc}$, $SVOC_{brc}$, $IVOC_{brc}$, $EVOC_{brc}$, and the average BrC volatility in the particle phase for the whole campaign.

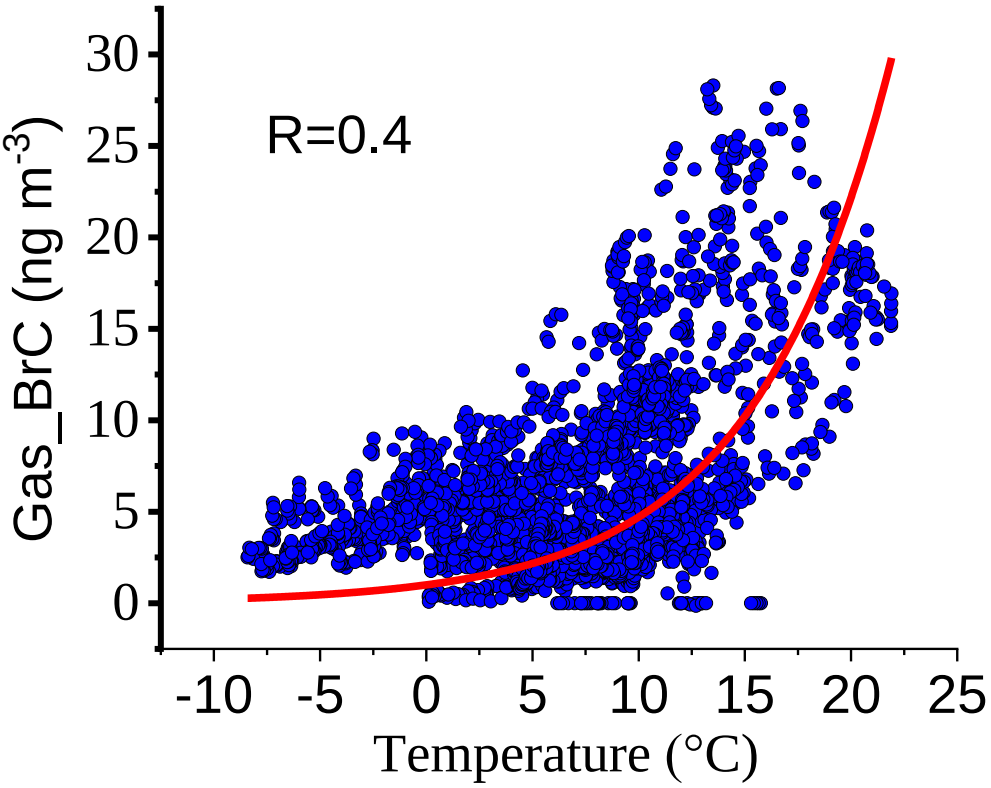

Figure S22. The correlation of gas-phase BrC and temperature based on exponential function.

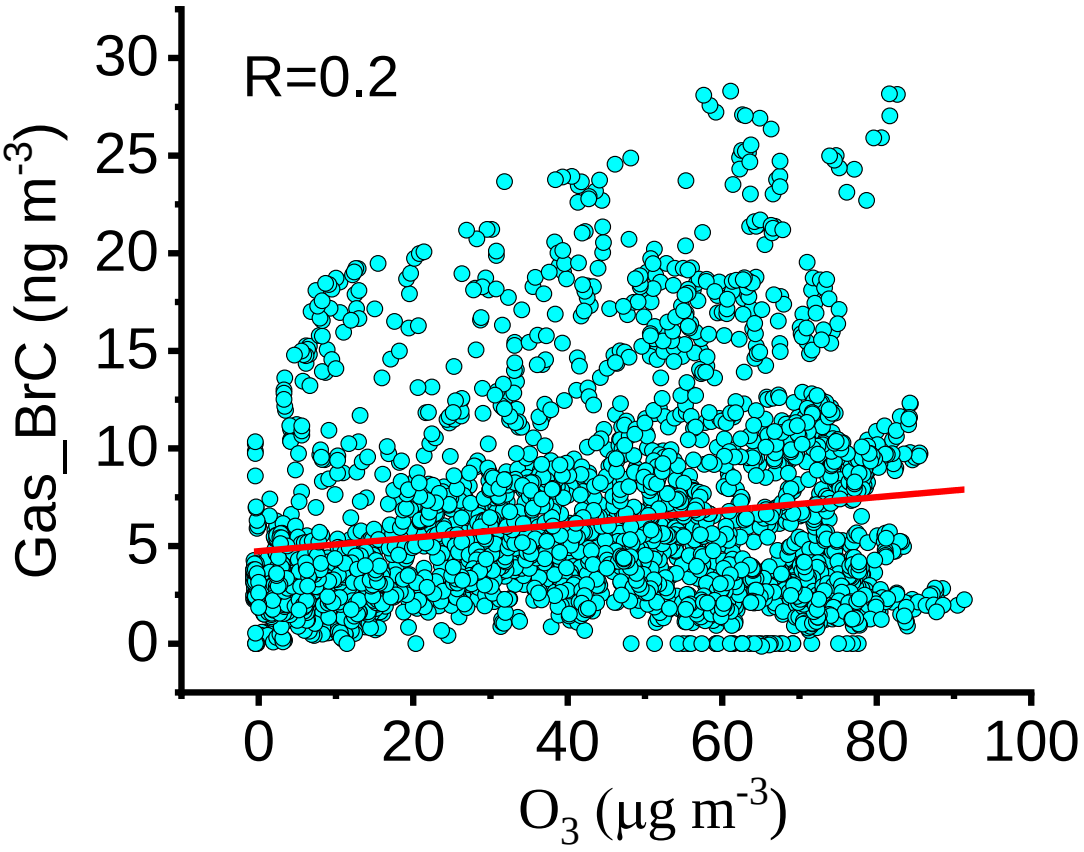

Figure S23. The correlation of gas-phase BrC and O_3 based on linear function.